Lecture Notes on Beam Instrumentation and Diagnostics

Peter Forck
Gesellschaft für Schwerionenforschung (GSI)
Darmstadt, Germany
e-mail: p.forck@gsi.de

Joint University Accelerator School
January – March 2009

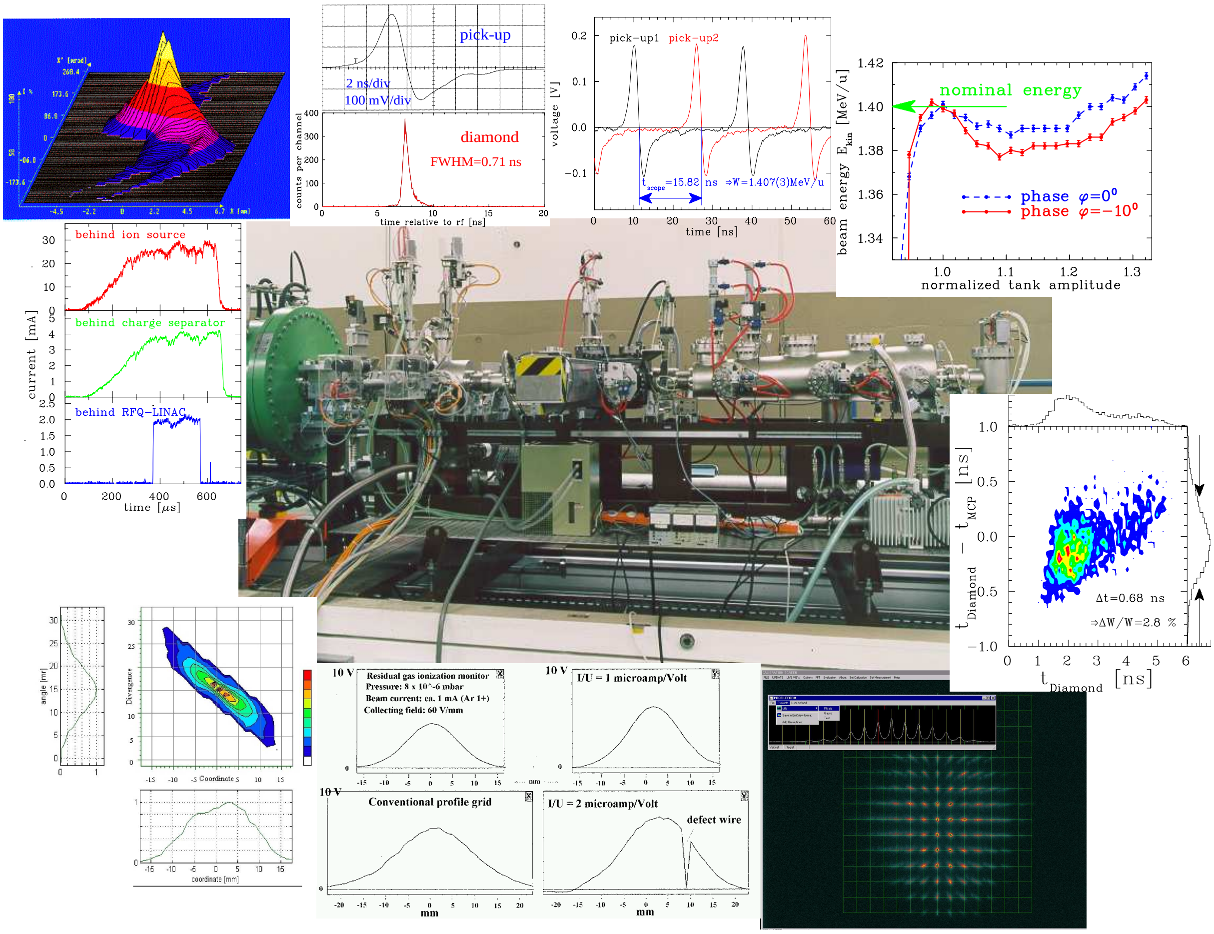

A picture of the mobile test bench including some measurements, as provided for the commissioning of the high current injector at GSI in 1999.

Contents

Chapter 1

Demands for beam diagnostics

Beam diagnostics is an essential constituent of any accelerator. It is the 'organ of sense' showing the properties and the behavior of the beam. It deals with the real beam including all possible imperfections of a real technical installation. Without adequate diagnostics one would 'blindly grope around in the dark' for the accelerator settings and improvements are hardly achievable. There are three categories of diagnostic demands at any facility:

- Reliable, quick measurements to determine the basic parameters of a machine setting used as a fast check of the general functionality. The readings from the instrumentation give a single number or simple plots. These devices should be non-destructive for the beam, yielding an online information. A prominent example is the current measurement by a transformer as shown in Fig. 2.11 accompanied by the display of the average current in form of one single number.

- Instrumentation built for a daily check of performance and stability, or for the control of wanted parameter changes in the accelerator setting. It can also be used for solving simpler machine problems in case of any malfunction. An example is the profile determination, in most cases performed by a destructive device as discussed in Chapter 3; in Fig. 3.6 profiles are shown as display in the control room at the GSI facility during the regular operation procedure.

- Complex instrumentation for the commissioning of a new accelerator component, for the development of higher performance and for solving more serious problems in case of a malfunction. The devices can be more complex to use and might be destructive for the beam. The importance is the creation of reliable information about the complex beam behavior allowing a clear interpretation. The determination of the beam emittance is an important example for the commissioning of a LINAC, these methods are discussed n Chapter 4. For a synchrotron the measurement of lattice parameters, like tune, chromaticity or β-function are required to achieve higher performance and for the comparison to theoretical calculations; related methods are discussed in Chapter 5.9 and 5.10.

The frontiers between these points are smooth, but should give a guideline for the construction and usage of the diagnostics.

An additional application is the active influence of the beam settings after the detection of the beam's properties. This is called feedback of a given parameter to yield an improved beam delivery. An example is the reading of the beam position and the correction of the orbit to its nominal value. Quite different reaction times are common, from less than μs to s, depending on the application. Such feedback systems involves the beam diagnostics as the input of the correction calculation. These extensive systems for beam control are out of the scope of this lecture and will not be discussed here.

Beam quantity		**LINAC, transfer line**	**Synchrotron**
current I	*general*	transformer (dc, pulsed)	transformer (dc)
		Faraday cup	
	special	particle detector	normalized pick-up signal
		(Scint. IC, SEM)	
position $\overline{x}$	*general*	pick-up	pick-up
	special	using profile measurement	cavity excitation (e^-)
profile x_{width}	*general*	SEM-grid, wire scanner	residual gas monitor
		viewing screen, OTR-screen	synch. radiation (e^-)
			wire scanner
	special	grid with ampl. (MWPC)	
trans. emittance ϵ_{trans}	*general*	slit grid	residual gas monitor
		quadrupole scan	wire scanner
	special	pepper-pot	transverse Schottky pick-up
			wire scanner
momentum p and $\Delta p/p$	*general*	pick-up (TOF)	pick-up
		magn. spectrometer	
	special		Schottky noise pick-up
bunch width $\Delta\varphi$	*general*	pick-up	pick-up
			wall current monitor
	special	particle detector	streak camera (e^-)
		secondary electrons	
long. emittance ϵ_{long}	*general*	magn. spectrometer	
		buncher scan	
	special	TOF application	pick-up + tomography
tune, chromaticity Q, ξ	*general*	—	exciter + pick-up (BTF)
	special	—	transverse Schottky pick-up
beam loss r_{loss}	*general*	particle detector	
polarization P	*general*	particle detector	
	special	Compton scattering with laser	
luminosity $\mathcal{L}$	*general*	particle detector	

Table 1.1: Beam parameters and the most commonly used beam diagnostics.

There is a large variety of beam parameters to be measured. For a good alignment of the beam all relevant parameters should be controllable. Table 1.1 gives an overview of the most important beam quantities and the commonly used diagnostic devices and methods. Only the general properties for most of these devices will be discussed in this lecture, without going deeply into details; i.e., the lecture gives a reasonable coverage at the expense of a detailed description. For some parameters, the type of instrumentation differs for LINACs and synchrotrons, due to their different accelerating principles. An important example is, that in a LINAC or a transfer line, the beam passes only once, while in a synchrotron the behavior of thousands of passages have to be determined. For a synchrotron non-destructive methods are preferred to monitor the beam behavior without any modifying influence. Moreover, electron beams have a quite different behavior as compared to protons or heavy ions. A simple example is the fact, that electrons are relativistic just after the first LINAC modules, while for protons several 100 m long LINACs or even a synchrotron is needed to reach significant relativistic conditions. Another difference is the emission of synchrotron radiation by electrons, while this process occurs for protons only at the highest reachable energies, like in LHC. As seen from Table 1.1 the same beam quantity can be determined with different devices. Which of these are most suited depends on the various beam parameters themselves. On the other hand, several beam quantities can be determined with one type of instrument.

The diagnostics are a vital part of any accelerator. About 3 % to 10 % of the total cost of an accelerator facility must be dedicated to diagnostic instrumentation. But due to the complex physics and techniques involved, the amount of man-power for the design, operation and further development exceeds 10 % in most cases.

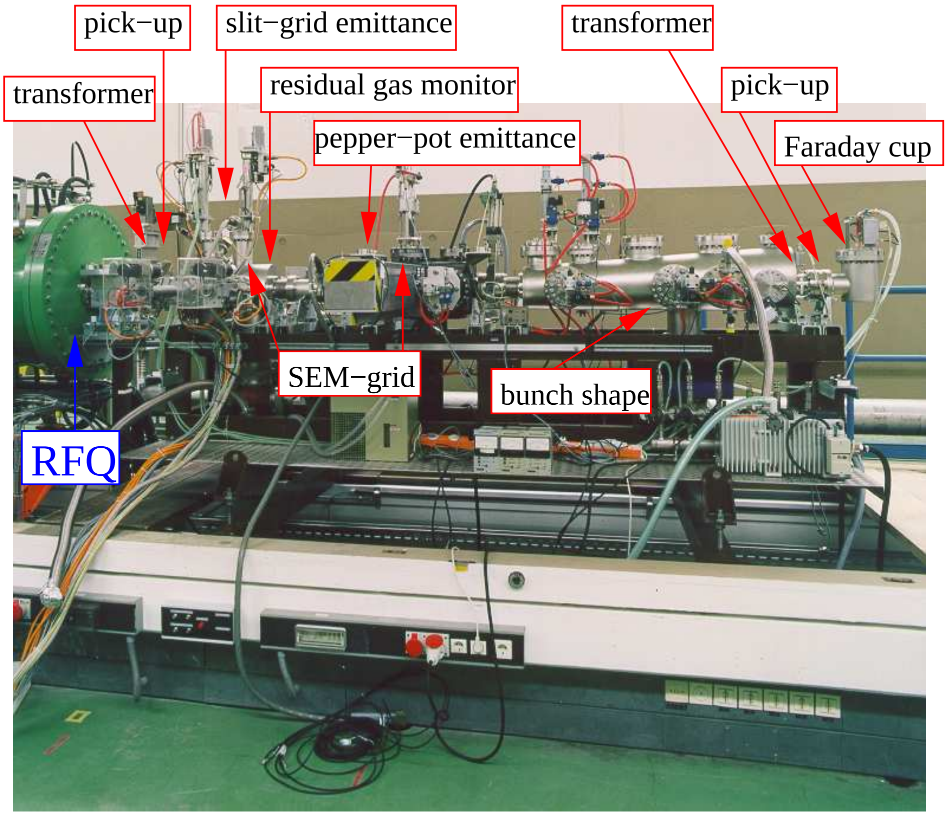

Figure 1.1: Picture of a movable test bench provided for commissioning of the new high current RFQ of GSI (green tank on the left).

As a first look at 'real life', Fig. 1.1 shows an instrumental assembly installed behind the heavy ion LINAC at GSI during its commissioning phase. With this equipment all relevant beam parameters had been measured extensively during a several week long period for each LINAC module. The beam quantities were: Current, transverse profile, transverse emittance, energy, bunch position, bunch structure and longitudinal emittance in dependence of various parameter settings. Now the equipment is installed behind the last module for permanent use during operation and for further developments.

Most of the diagnostic instrumentation is based on one of the following physical processes:

- The electro-magnetic influence of moving charges on the environment as described by classical electro-dynamics. The technique is based on a voltage or current measurement on a low or high frequency scale. Examples are beam transformers or pick-ups.

- The emission of photons by accelerated charges. This diagnostic is only important for relativistic particles, i.e. electrons or very highly energetic protons. The technique is based on optical methods spanning the visible range up to the x-ray region. Examples are synchrotron radiation monitors for beam profile and time measurements.

- The Coulomb interaction of charged particles penetrating matter, described by atomic or solid state physics. The energy release due to electronic stopping gives the dominant fraction of the detected signal. The technique is based on current measurements or the observation of light by optical methods. Examples are scintillators, viewing screens, secondary electron emission grids, ionization chambers and residual gas monitors.

- The nuclear- or elementary particle physics interaction between the accelerated particles and a fixed target or between colliding beams. From the known cross sections, the beam quantity can be deduced. The technique is based on nuclear- or elementary particle physics detectors. Examples are polarimeters, luminosity monitors, or beam loss monitors used for machine protection and alignment.
- The interaction of the particles with a photon beam. The technique is based on lasers, their associated optics and on detectors used for high energy physics. Examples are laser scanners or Compton polarimeters. Due to the special application, this is not discussed in this lecture.

In this lecture we can only describe the principles of some commonly used devices, not all can be covered. Excellent introductory descriptions for beam diagnostics exist, as well as several books related to a variety of related topics [1]. Information on particular realizations can be found in the proceedings of dedicated beam diagnostics conferences and as a part of the general accelerator conferences [2]. In the literature one can find extensive descriptions for the full instrumentation used at an ion synchrotron (RHIC, Brookhaven [3]) and an electron-positron collider (KEKB. Japan [4]).

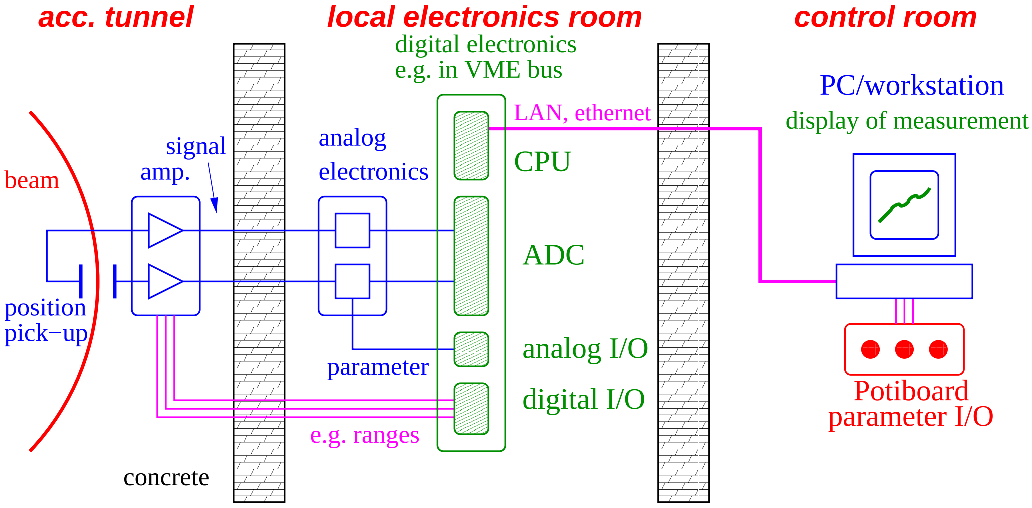

Figure 1.2: Schematics of typical beam diagnostics (here a position pick-up). The beam signal is modified by analogue electronics and digitized in a local electronics room. From the control room the parameters of the measurement, as well as for the beam can be influenced.

Normally the yield of information from the diagnostic devices follows three successive steps from the measurement up to the display of the quantity of interest, as shown in Fig. 1.2 for the case of a electromagnetic beam position monitor:

- There is first the interaction of the beam with the detector. This signal has to be amplified and shaped. Low noise processing is important at this step. In most cases this is done close to the beam pipe.
- The amplified signal is transferred out of the accelerator area to a local electronics room. The distance between these two locations can be several 100 m. Further shaping can

proceed here and the signal might be combined with other parameters as given by the accelerator settings. This is done in most cases with analogue electronics. The modified signal is then digitized and stored. This can be done using an oscilloscope or a digital bus system. Example for bus systems are field buses like CAN- or PROFI-bus, or crate based systems like CAMAC, VME, PXI or CompactPCI. The control of the analogue electronics can also be done using these busses.

- The data, or in most cases a reduced subset of the data, are passed to a PC or a workstation located in the operator's control room. Here the visualization is done providing only the necessary information. Also the parameters for the accelerator, like magnet currents or rf voltages, are changed from the control room to influence the beam. The resulting effect on the beam is then observed with a new set of measured data.

In this lecture we focus on the principle of the action of the beam on the detector. For several systems, raw data are shown to visualize the general detector functionality. The preceding analogue electronics are only discussed briefly. The technique of digitalization is not treated here, even though it is of great importance and occupies a significant effort. Digital electronics is not a pure diagnostics subject, and the realization is comparable to a great variety of other control applications. From the data analysis on the PC or workstation only typical results are presented, the algorithms are not discussed here. The associated software at the various steps is not described either.

Fig. 1.3 shows a view into the control room at GSI, where the information from the beam diagnostic instruments is displayed in connection with other controls of the accelerator. The various parameters of the accelerator are changed from this control room.

Figure 1.3: One section of the operator control room at GSI.

Most of the examples in this lecture are measured at the GSI facility, because the author is most familiar with these realizations. This does not mean, that GSI has the most advanced systems; at other facilities better installations might exist. The GSI accelerator facility, as shown in Fig. 1.4, consist of two pulsed LINACs running on 36 MHz and 108 MHz, respectively to accelerate all ions from different ion sources up to 18 MeV/u, corresponding to a velocity of $\beta = v/c = 0.19$. This energy is well above the so-called Coulomb barrier, where nuclear reactions

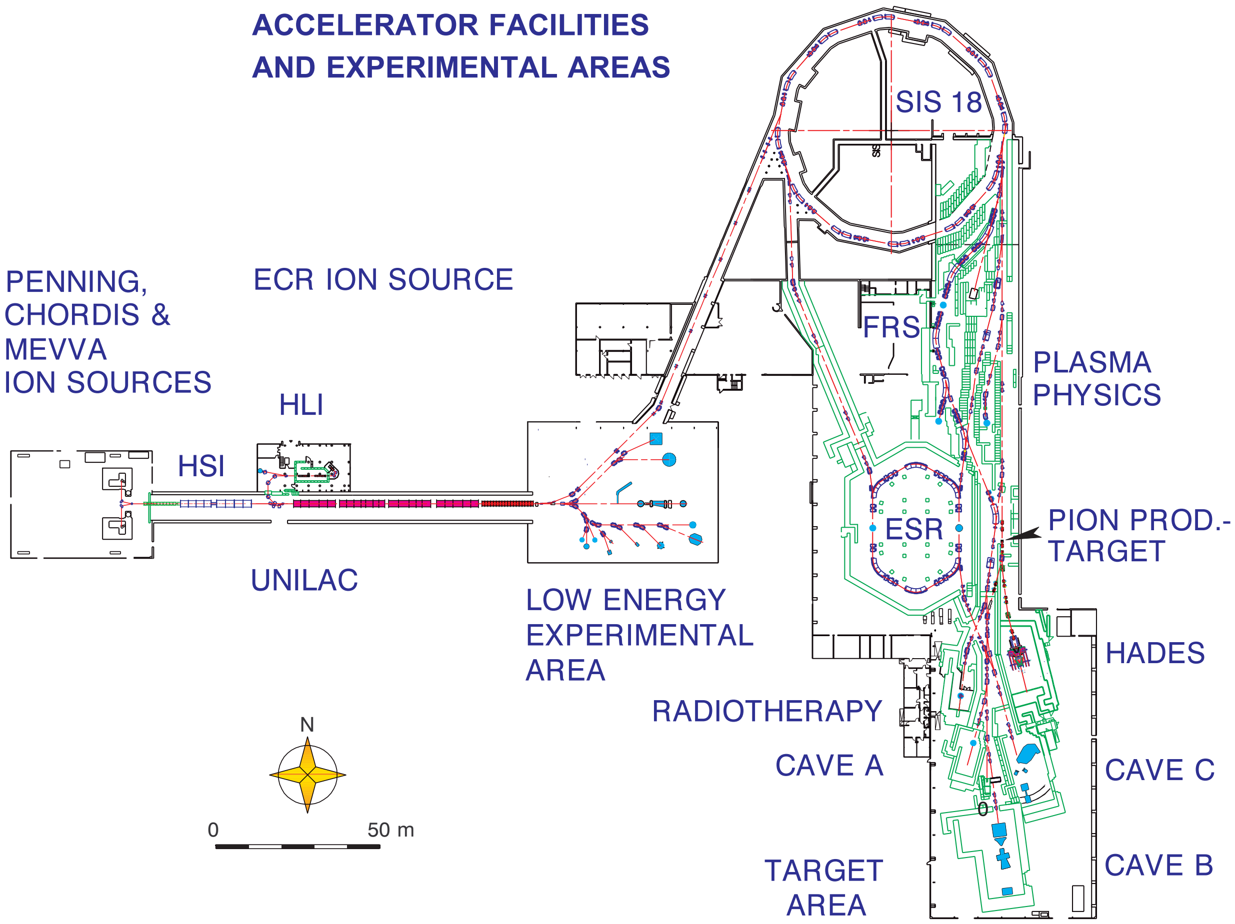

Figure 1.4: The GSI heavy ion accelerator facility.

are possible. Experiments with this beam are performed in the low energy experimental hall. For achieving higher energies up to 2 GeV/u, corresponding to $\beta = 0.95$, a synchrotron with 218 m circumference, the SIS, is used. The beam can be transferred to the storage ring ESR with a single bunch transfer (so-called fast extraction). Alternatively, it can be sent to fixed target experiments in this fast mode, or using slow extraction lasting from 1 to 10 s. The physics at these targets are related to nuclear, atomic or plasma physics, as well as human cancer therapy.

We restrict the lecture to the instrumentation of accelerators for stable particles, having a moderate current range. Typical applications at these facilities are experiments in atomic, solid state, biological, nuclear and particle physics, as well as the use as synchrotron radiation sources. We do not treat the diagnostic needs e.g. for radioactive beams (having a very low current) or the high current beam produced by induction accelerators. Moreover, the special diagnostics for negative H^- beams are not treated. The measurement of polarization and luminosity at colliders uses particle detectors and well known cross sections for secondary particle production; this will not be discussed here.

At the end of the introduction we have to state that the beam diagnostics have to help getting a stable operation with the best possible beam quality needed for the physics experiments.

Chapter 2

Measurement of beam current

The total electrical current is one of the most important parameters for the operation of a particle accelerator. In the daily operation a first check concerns the current in almost all accelerator laboratories. In most cases it is measured with a beam transformer. This device works for electron and proton LINACs and synchrotrons, even for short pulses, like the transfer between synchrotrons, as well as for dc-beams, like in a storage ring. These devices are commercially available [5], even though quite different types are used. They are all non-intercepting. Their principle is the detection of the magnetic field carried by the beam. Only for very low currents, transformers cannot be used due to noise limitations. For these low current regions, particles detectors are used instead. For most parameters this is a intercepting methods. Here the energy loss of the charged particle traveling through matter is detected. Either the particles are counted directly, or the particle flux can be calculated with the help of a calibration.

From the first days of accelerators, Faraday cups were used. The cup gives a direct measurement of the particle beam's charge. The particles have to be stopped in the cup. For high current this destructive method can not be applied, because the total energy carried by the beam can destroy the intercepting material. For higher energetic particles the penetration depth reaches more than several cm and Faraday cups are not useful any more.

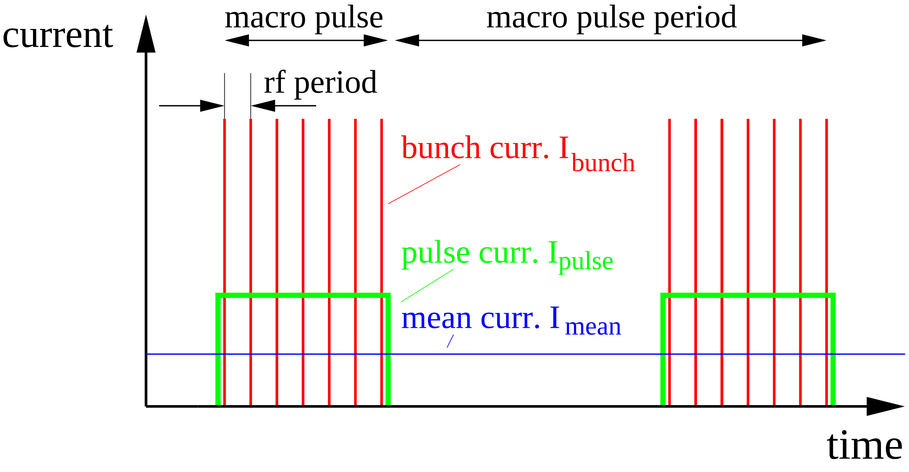

Figure 2.1: The time structure of the different currents at a pulsed LINAC.

Before discussing the devices we define the time structure of a pulsed LINAC according to Fig. 2.1:

- The average or mean current I_{mean} in the long time average as given in units of A.
- The macro pulse current I_{pulse} is the time average during the beam delivery. In most cases

this is given in units of A.

- The current within a bunch I_{bunch}, sometimes also called the micro pulse current. In most cases this is given in number of particles or charges per bunch.

A typical example of such a structure is given in Fig. 2.2 for a pulse length of 5 ms and an rf period of 27 MHz as recorded at the GSI heavy ion LINAC.

Having a long train of bunches, the number of charges within a bunch is not determined with a transformer, as it's bandwidth is too low for this purpose. Here capacitive pick-ups, which detect the electrical field, are well suited. Both plots on the right are recorded with these devices, see also Chapter 5.

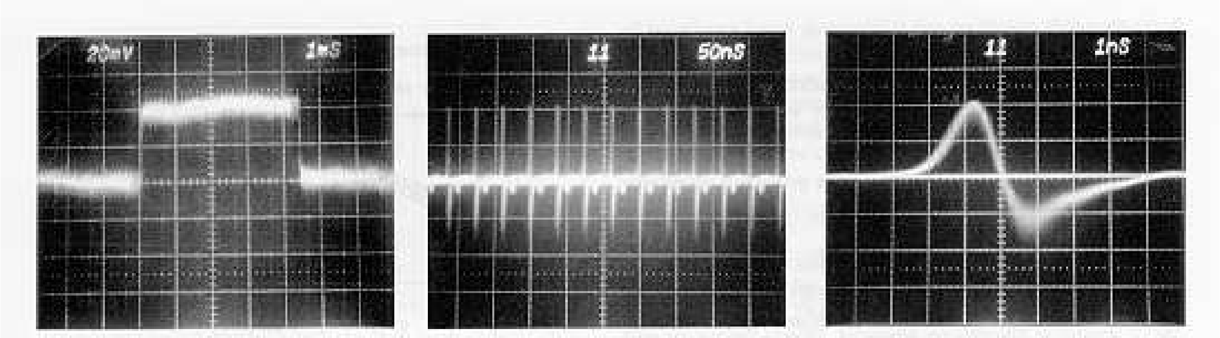

Figure 2.2: Pictures of measured currents. Left: macro pulse current, measured by a beam transformer with 1 ms/div, center: bunch signals within the macro pulse at 50 ns/div, right: differentiated single bunch signal from a capacitive pick-up on an enlarged scale of 1 ns/div.

Pulsed LINACs or pulsed cyclotrons can be used as an injector to a synchrotron, where only a typical pulse length of 100 μs is needed for a multi-turn injection. For a single-turn injection the time is of the order of 10 μs. For other applications, like in atomic or nuclear physics, a cw (continuous wave) accelerator is used. Here the bunches are delivered for a 'infinitely' long time. The macro pulse current I_{pulse} then equals the average current I_{mean}, but the bunch structure still remains due to the rf acceleration by a LINAC or a cyclotron. There exist also types of accelerators not producing bunched beams, examples are Van-de-Graaff- and Cockcroft-Walton types, using electrostatic acceleration. Here all three types of current are equal.

2.1 Current transformer for pulsed beams

2.1.1 General considerations and passive transformer

In an accelerator the current is formed by N particles of charge state q per unit of time t or unit of length l and velocity $\beta = v/c$. The electrical current is

$$I_{beam} = \frac{qeN}{t} = \frac{qeN}{l} \cdot \beta c \tag{2.1}$$

with e being the elementary charge. The magnetic field B of a current can be calculated according to the Biot-Savart law

$$d\vec{B} = \mu_0 I_{beam} \cdot \frac{d\vec{l} \times \vec{r}}{4\pi r^3} \tag{2.2}$$

with $\mu_0 = 4\pi \cdot 10^{-7}$ Vs/Am is the permeability of the vacuum, $d\vec{l}$ the length in direction of the beam and $\vec{r}$ the distance between the center of the beam and the point the field is measured. For a cylindrical symmetry only the azimuthal component has to be considered along the unitary vector $\vec{e}_\varphi$ as shown in Fig. 2.3

$$\vec{B} = \mu_0 \frac{I_{beam}}{2\pi r} \cdot \vec{e}_\varphi . \tag{2.3}$$

For a beam current of 1 μA and a distance of 10 cm the magnetic field has a value of only 2 pT. To put this into perspective, the constant and homogeneous earth magnetic field has a value of about 50 μT.

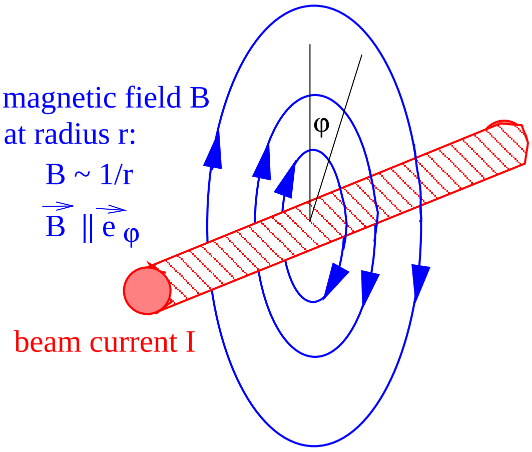

Figure 2.3: The magnetic field of a current.

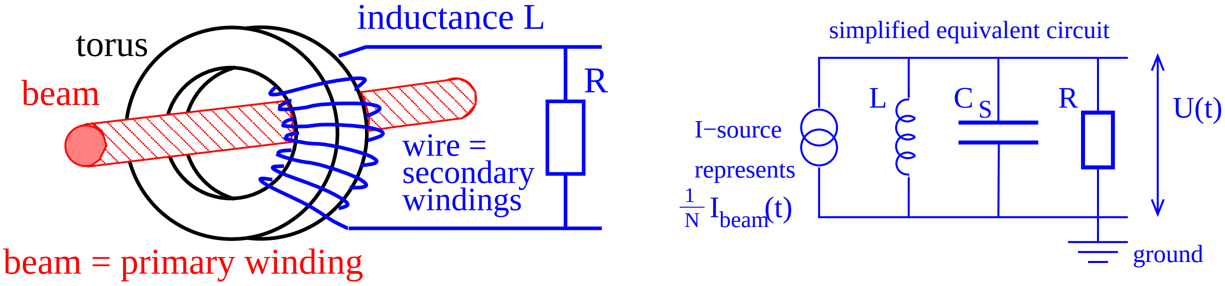

Figure 2.4: Scheme of a current transformer built as a ring-core (torus) around the beam (left) and the simplified equivalent circuit (right).

The beam current can be determined by monitoring the accompanied magnetic field with a current transformer schematically shown in Fig. 2.4. The beam passes through a highly permeable torus as the 'primary winding'. An insulated wire, wound around the torus with N turns, serves as the 'secondary winding' of the transformer with the inductance L. The inductance for a torus material of length l in beam direction, inner radius r_i and outer radius r_o having a relative permeability μ_r and N windings is given by

$$L = \frac{\mu_0 \mu_r}{2\pi} \cdot l N^2 \cdot \ln \frac{r_o}{r_i} . \tag{2.4}$$

One reason for the torus is to guide the field-lines, so only the azimuthal component is measured and the signal strength is nearly independent of the beam position inside the vacuum pipe.

Generally for an ideal current transformer loaded with a low value of ohmic resistance R the ratio between the primary current I_{prim} and secondary current I_{sec} is given by

$$I_{sec} = \frac{N_{prim}}{N_{sec}} \cdot I_{prim} \quad \Longrightarrow \quad I_{sec} = \frac{1}{N} \cdot I_{prim} \quad \text{due to} \quad N_{prim} = 1 \tag{2.5}$$

with $N_{prim} = 1$ is the winding number on the primary side, which is one due to the single pass of the beam through the torus. N_{sec} is the winding number on the secondary side and for simplicity it is called N further-on.

For most practical cases a measurement of a voltage U is preferred, therefore the resistance R is introduced leading to

$$U = R \cdot I_{sec} = \frac{R}{N} \cdot I_{beam} \quad . \tag{2.6}$$

The ratio between the usable signal voltage U and the beam current I_{beam} is called sensitivity S (or transfer impedance, for a more stringent discussion see Chapter 5.1)

$$U = S \cdot I_{beam} \quad . \tag{2.7}$$

To understand the design criteria for the various applications one has to consider the electrical properties of the transformer in more detail. With different external electrical elements the response to a given time structure of the beam can widely be influenced. We first consider the characteristics of a so-called passive transformer, where the voltage at a 50 Ω resistor is recorded. The equivalent circuit of the secondary transformer side is depicted in Fig. 2.4 on the right side. The beam current is modeled by a current source with a reduction given by the number of windings N according to Eq. 2.5. One has to take also some stray capacitances C_S into account, which are caused by the capacitance between the windings, the windings and the torus and along the shielded cable to the resistor R. To determine the voltage $U(t)$ the impedance of the parallel shunt of the three elements in dependence of the excitation frequency f or $\omega = 2\pi f$ is

$$\frac{1}{Z} = \frac{1}{i\omega L} + \frac{1}{R} + i\omega C_S \quad . \tag{2.8}$$

Using some algebra, this is equivalent to

$$Z = \frac{i\omega L}{1 + i\omega L/R + \omega L/R \cdot \omega R C_S} \quad . \tag{2.9}$$

This equation can be analyzed for three different frequency ranges:

- **Low frequency range assuming $\omega \ll \frac{R}{L}$:**
  In this case, the second and third term in the denominator of Eq. 2.9 can be neglected. The resulting impedance is then
  $$Z \to i\omega L \quad . \tag{2.10}$$
  The meaning of this equation is, that the usable signal at the resistor R decreases proportional to the excitation frequency because the inductance acts as a short circuit for the considered low frequencies. In particular, at $\omega = 0$ no signal is recordable. This reflects the well known fact, that a transformer can not handle dc-currents.

- **High frequency range assuming $\omega \gg \frac{1}{RC_S}$:**
  In this case, the first and second term in the denominator of Eq. 2.9 can be neglected. The impedance is then
  $$Z \to \frac{1}{i\omega C_S} \quad . \tag{2.11}$$
  This reflects the fact that for high frequencies the current is mainly flowing through the capacitor and therefore the voltage drop at the resistor R is low.

- **Working region $\frac{R}{L} \ll \omega \ll \frac{1}{RC_S}$:**
  For this case the second term in the denominator of Eq. 2.9 dominates and term one and three can be neglected. The impedance is then
  $$Z \simeq R \quad . \tag{2.12}$$

This is the usable working region, where the voltage drop at the resistor is significant. The working region is very broad due to the values of the electronic elements. In particular, the low value of the resistor $R = 50\ \Omega$ to ground annihilates the flowing current, resulting in an over-damping of possible oscillations.

The above mentioned frequencies restrict the working region with a true response of the measured signal with respect to the beam current. At the lower frequency boundary the signal decreases; the point of factor 2 decrease is called the low cut-off frequency and is given by $\omega_{low} = R/L$. At the upper boundary the corresponding value $\omega_{high} = RC_S$ is called upper cut-off frequency.

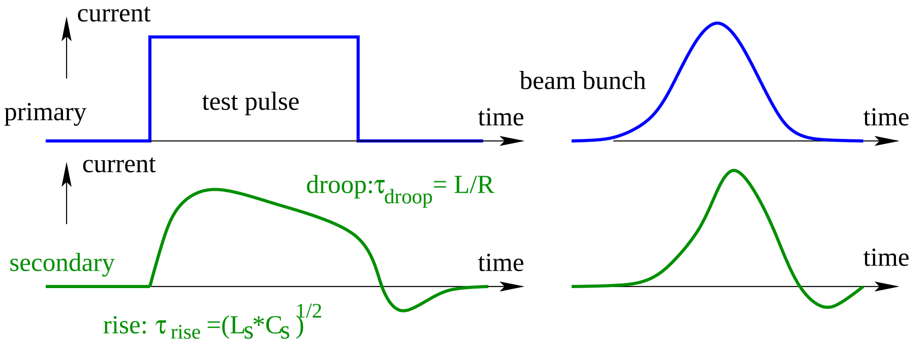

Figure 2.5: The response of an ac-transformer to a rectangular pulse and a more realistic beam pulse.

For the discussion we are more interested on the time response of the measurement device to a given beam pulse. Therefore, we define the rise time and droop time as depicted in Fig. 2.5: The rise time τ_{rise} is the time needed for the amplitude going from 10 % to 90 % described by an exponential function if the excitation is given by a step-function. It is linked to the upper cut-off frequency by

$$\tau_{rise} = \frac{\ln 0.9 - \ln 0.1}{\omega_{high}} = \frac{\ln 9}{2\pi f_{high}} \simeq \frac{1}{3 f_{high}} \quad . \tag{2.13}$$

Correspondingly, the droop time constant is linked to the lower cut-off frequency as

$$\tau_{droop} \simeq \frac{1}{3 f_{low}} \quad . \tag{2.14}$$

The two equations above have a general meaning and will be used to transfer the bandwidth, as given in the frequency domain, into the response description in the time domain. For the passive current transformer as described by the equivalent circuit of Fig. 2.4 the rise and droop time constant are given by

$$\tau_{rise} = RC_S \quad \text{and} \quad \tau_{droop} = \frac{L}{R} \quad . \tag{2.15}$$

A more realistic case of the passive transformer is shown in Fig. 2.6. The main difference is the additional loss resistivity in the cables, which is represented by a serial resistor R_L. Moreover, we have also a stray inductance between the windings, which is best modeled by a serial insertion of an inductance L_S. For the higher frequencies response one has to consider the frequency dependence of the permeability μ_r of the torus made of CoFe-based amorphous alloy (so called Vitrovac©) with $\mu_r \sim 10^5$ for low frequencies. But the permeability decreases above $f \sim 100$ kHz with a scaling $\mu_r \propto 1/f$ and therefore also the inductance of the torus decreases. For frequencies above ~ 100 MHz the stray inductance is the dominant contribution. With these two modifications the rise and droop times are modified to yield

$$\tau_{rise} = \sqrt{L_S C_S} \qquad \text{and} \qquad \tau_{droop} = \frac{L}{R + R_L} \quad . \tag{2.16}$$

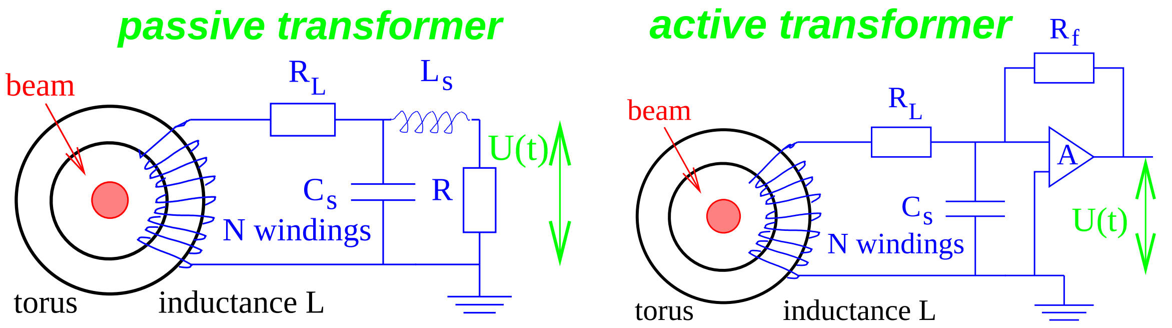

Figure 2.6: Equivalent circuits of a passive beam transformer (left) and an active transformer (right).

Passive transformers are mainly used when short beam pulses have to be observed. Examples are the observation of the bunch structure during acceleration inside a synchrotron or the fast extraction from a synchrotron within one revolution. For the latter case the passive transformer is installed in the beam pipe outside the synchrotron. The beam pulse length is typically between 1 ns and 10 μs. Moreover, with the passive transformer, the bunch structure in time can be observed and a bandwidth up to 500 MHz (corresponding to a rise time of $\tau_{rise} \leq 1$ ns) can be achieved. The specifications of the GSI device are listed in Table 2.1 and a measurement is shown in Fig. 2.7. Careful matching is necessary between the torus and the 50 Ω resistor R, where the voltage drop is measured.

Torus radii	$r_i = 70$ mm, $r_o = 90$ mm
Torus thickness	$l = 16$ mm
Torus material	Vitrovac 6025: $(\mathrm{CoFe})_{70\%}(\mathrm{MoSiB})_{30\%}$
Torus permeability	$\mu_r \simeq 10^5$ for $f < 100$ kHz, $\mu_r \propto 1/f$ above
Number of windings	10
Sensitivity	4 V/A at $R = 50\ \Omega$, 10^4 V/A with amplifier
Resolution for $S/N = 1$	40 $\mu\mathrm{A}_{rms}$ for full bandwidth
$\tau_{droop} = L/R$	0.2 ms
$\tau_{rise} = \sqrt{L_S C_S}$	1 ns
Bandwidth	2 kHz to 300 MHz

Table 2.1: Some basic specification of the GSI passive transformer.

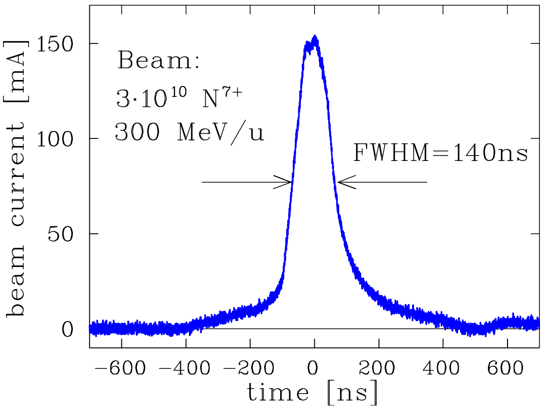

Figure 2.7: The signal from a passive transformer for a single beam bunch extracted from the GSI synchrotron.

To get the right choice of the parameters of a passive transformer we have some requirements:

1. For a high sensitivity i.e. a large voltage U a low number of windings is preferred, according to $U(t) \propto 1/N$ in Eq. 2.6.
2. For a long droop time constant, i.e. the possibility of measuring long beam pulses, a large inductance has to be used. The scaling is $L \propto N^2$ and $L \propto \mu_r$ as given in Eq. 2.4. Therefore materials with a high permeability are used e.g. CoFe-based amorphous alloy (so called Vitrovac©) with $\mu_r \sim 10^5$. For higher frequencies μ_r decreases and therefore also the torus inductance L. A typical cut-off frequency is 100 kHz with a scaling for higher frequencies $\mu_r \propto 1/f$.
3. To achieve a fast rise time and therefore a fast response, the stray capacity C_s should be low due to $\tau_{rise} \propto \sqrt{L_s C_s}$

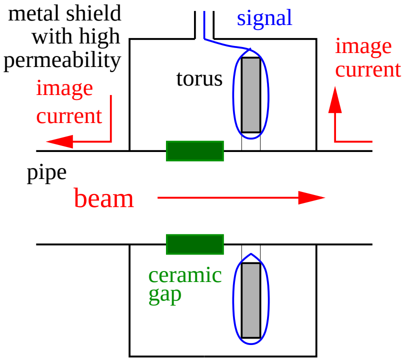

Figure 2.8: Scheme of a transformer housing used as an image current pass and a shielding against external magnetic fields.

An additional general point is, that close to the transformer the electrical conductivity of the beam pipe has to be interrupted as schematically shown in Fig. 2.8. This is done with an insulator, either a ceramic gap or a plastic vacuum seal. The reason is to prevent a flow of image current inside of the transformer torus. This image current has the opposite sign and without the gap, the fields of the image current and beam current add up to zero. The image current has to be bypassed outside of the transformer torus by some metallic housing. It is surrounded of high permeability μ-metal, also used for the shielding of the transformer against external magnetic fields. A general review on transformers is presented in [6].

2.1.2 Active ac-transformer

For the observation of beam pulses longer than several μs, the droop of a passive transformer leads to a significant deformation of the measured signal, as schematically shown in Fig. 2.5. The droop time constant can be made much longer by using an operational amplifier (op-amp), with feedback resistor R_f and amplification A, instead of a constant resistor to measure the voltage. The equivalent circuit is shown in Fig. 2.6, right side. The effect is the reduction of the op-amp input resistance by a factor of R_f/A. This is the setup of a so called trans-impedance amplifier or current to voltage converter. The remaining resistance is then only given by the cable resistivity R_L because $R_f/A \ll R_L$. The droop is now only

$$\tau_{droop} = \frac{L}{R_f/A + R_L} \simeq \frac{L}{R_L}. \tag{2.17}$$

Droop time constants up to 1 second are possible. (Typical values of the cable resistance is $R_L \sim 1\ \Omega$.) An additional winding (not shown in Fig. 2.6 right) has to be used to compensate the 'natural', known droop. In addition, the feedback resistor R_f of the operational amplifier can be used for range switching. This principle is called the active transformer.

The rise time τ_{rise} for this active type is much larger than for the passive type. This is mainly due to the choice of a low bandwidth (low value of the upper cut-off frequency) of the operational amplifier to obtain a significant reduction of the amplifier's high frequency noise. This results in the high sensitivity of an active transformer.

Torus radii	$r_i = 30$ mm, $r_o = 45$ mm
Torus thickness	$l = 25$ mm
Torus material	Vitrovac 6025: $(\mathrm{CoFe})_{70\%}(\mathrm{MoSiB})_{30\%}$
Torus permeability	$\mu_r \simeq 10^5$
Number of windings	2×10 with opposite orientation
Maximal sensitivity	10^6 V/A
Ranges of the beam current	10 μA to 100 mA
Resolution for $S/N = 1$	0.2 $\mu\mathrm{A}_{rms}$ for full bandwidth
Droop	< 0.5 % for 5 ms pulse length
Maximum pulse length	8 ms

Table 2.2: Some basic specification of the GSI LINAC transformer.

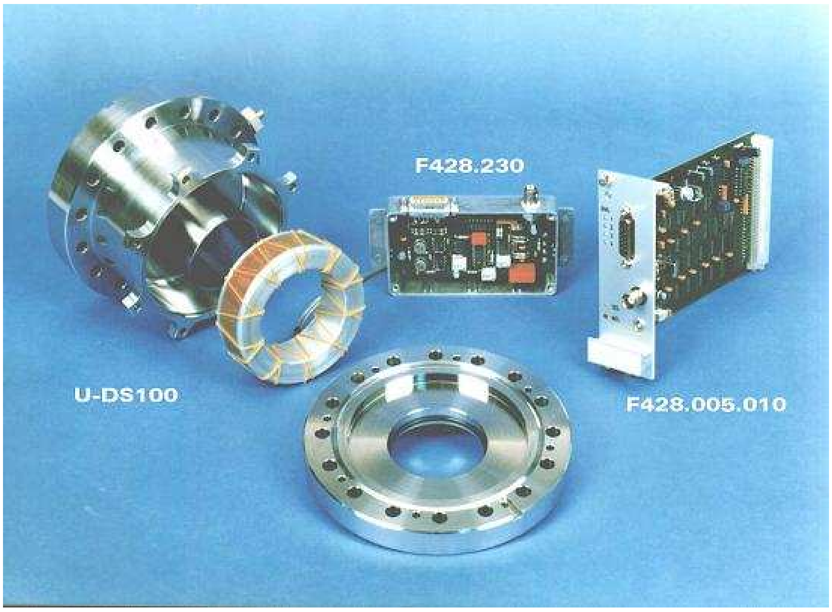

Figure 2.9: Photo of an ac-current transformer used at the pulsed heavy ion LINAC at GSI. The torus with the differential winding is shown left, the used electronic modules at the right.

We discuss a typical device [7] used at the heavy ion LINAC at GSI with pulse length of 100 μs (used for the filling of a synchrotron) and 5 ms (used directly by the experiments). The values of the macro pulse current ranges from the low detection threshold of ~ 200 nA up to 100 mA. The very large dynamic range depends on the experiment's needs and on the maximum current the ion source can deliver. In Fig. 2.9 and Fig. 2.10 the hardware is shown. A specification is given in Table 2.2.

The device has a rise time of 1 μs and a maximum droop of only 0.5% for 5 ms long pulses. The torus material is made of amorphous alloy $(\mathrm{CoFe})_{70\%}(\mathrm{MoSiB})_{30\%}$ (Vitrovac$^{\copyright}$), to enable a large sensitivity. Besides the high permeability of $\mu_r \simeq 10^5$ it has a high electrical resistance resulting in fast decay of eddy currents. The torus is made of flat strips of 25 μm thickness

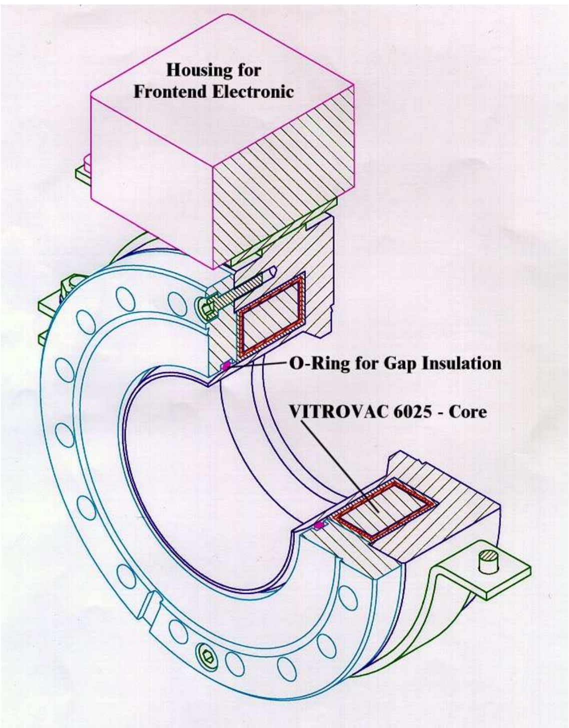

Figure 2.10: Schematic drawing for the ac current transformer used at the pulsed heavy ion LINAC at GSI.

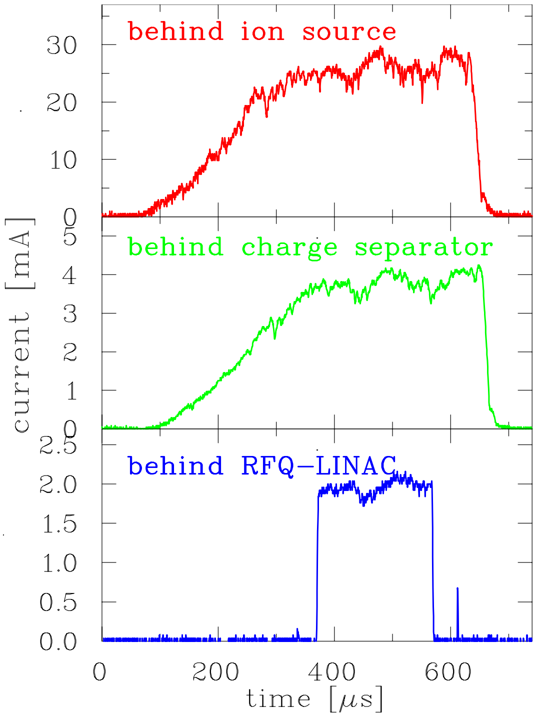

Figure 2.11: Transmission determination by ac-transformers at three different locations at the GSI LINAC using a Ni^{2+} beam from a high current source. The upper curve shows the current after the ion source where all charge states are present. The second curve is after filtering one ionic state. The third curve is the current after the first LINAC module.

with a thin insulation and is wound to get the final thickness of $r_o - r_i = 15$ mm. Another important material constant is the change of the inductance as a function of external stress, the magnetostriction. A low value prevents the micro-phonic pick-up of vibrations produced e.g. by vacuum pumps.

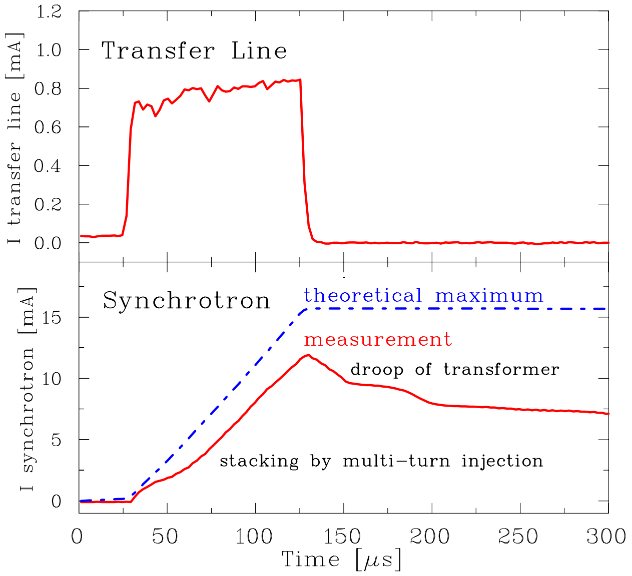

Figure 2.12: The multi-turn injection at GSI measured with two ac-transformers. The upper curve is the current delivered by the LINAC and the lower curve is the stored current in the synchrotron. In this case 20 turns are used and 70 % efficiency is reached for this Ni^{26+} beam.

A measurement done with these types of transformers is shown in Fig. 2.11, where one macro-pulse is recorded at three locations starting at the ion source until the end of the first LINAC tank. A high current ion beam is generated in the source with ~ 0.5 ms length. The slow rise of the beam current before the LINAC is due to the build-up of the space charge compensation of the un-bunched beam. A chopper in front of the LINAC is used to generate the needed pulse length. Transformers are essential to determine and maximize the transmission through the accelerator, in particular if the ion source conditions are not very stable. A non-destructive method is needed to follow the beam pulse for its pass through the full accelerator. During the operation of the accelerator, these transformers are the most frequently used diagnostics.

To control the filling of a synchrotron by a pulse from a LINAC, transformers of the described type are used. One of them is mounted in the external beam line, measuring the delivered current, and the other one is installed inside the synchrotron to determine the stored current. The used multi-turn injection is done with some bumper magnets to fill the large horizontal acceptance of the synchrotron by the LINAC pulse, which is much longer than the revolution period. Such a measurement at the GSI facility [8] is shown in Fig. 2.12 where the injection takes place over 20 turns and an accumulation by a factor ~ 15 is achieved. For each beam setting optimization of the injection process is an important task to achieve a maximal matching. The transformer inside the synchrotron has a higher bandwidth to see modulations within a fraction of the revolution period, resulting in a larger droop of ~ 20 % within 100 μs.

2.2 The dc-transformer

An important task for beam diagnostics is the measurement of a coasting (dc) beam current. The application is either a LINAC running in a dc-mode or a synchrotron with storage times from seconds to several days. The transformers discussed in the previous sections only work for a pulsed beam, even though the droop time constant can be made to be of the order of a second.

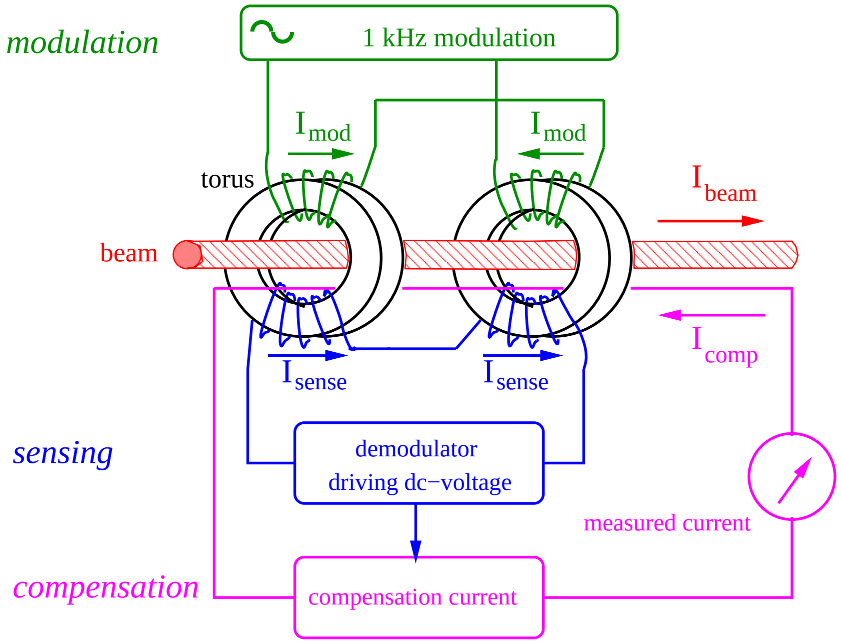

Figure 2.13: Schematics of a dc-transformer, see text.

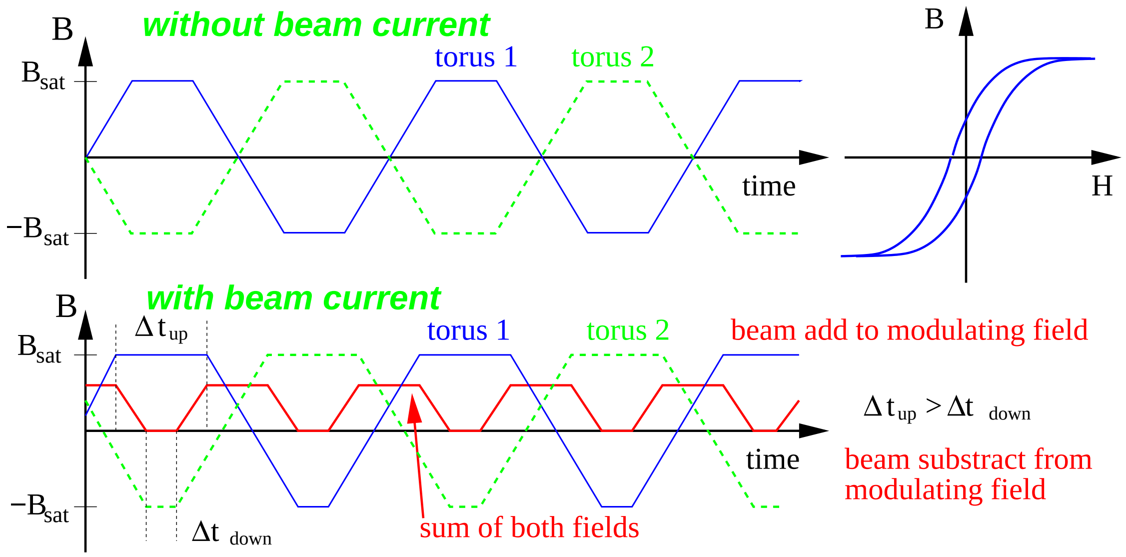

Figure 2.14: The fluxes in the two tori of a dc-transformer without and with a beam. The magnetic field of the beam adds to the modulated field for one modulation phase and 180^o degree later it is subtracted. The sum of the maximum magnetization gives the measured signal. The scheme is drawn for a triangular-modulation, for a realistic sine-modulation the edges are smoother.

The dc transformer principle [5, 7, 9] is shown schematically in Fig. 2.13. It consist of two tori with three types of windings each. The first windings of each torus with opposite orientation are used as a modulator. The modulation frequency is typically 1-10 kHz. The amplitude of the modulation current is high enough to force the torus into magnetic saturation of $B_{sat} \simeq 0.6$ T, two times for each period. The secondary windings with equal orientation act as a detector for the modulated signal, see Fig. 2.14. Assuming perfectly identical magnetic characteristics of both tori, the detector signal, as shown in the scheme, should be exactly zero if there is no beam current flowing through the tori. However, an asymmetric shifting of the hysteresis curve

Figure 2.15: The dc-transformer installed at the GSI synchrotron. The left torus is the dc-transformer (two tori mounted closely together), the middle is the ac-transformer used for the feedback of the dc-type and the right one is the ac-transformer for the control of the injection.

Torus radii	$r_i = 135$ mm, $r_o = 145$mm
Torus thickness	10 mm
Torus material	Vitrovac 6025: $(CoFe)_{70\%}(MoSiB)_{30\%}$
Torus permeability	$\mu_r \simeq 10^5$
Isolating gap	Al_2O_3
Number of windings	16 for modulation and sensing 12 for feedback
Ranges for beam current	300 μA to 1 A
Resolution for $S/N = 1$	2 μA
Bandwidth	dc to 20 kHz
rise time	20 μs
Offset compensation	± 2.5 μA in auto mode < 15 μA/day in free run
temperature coeff.	1.5 μA/^{o}C

Table 2.3: The specification of the dc-transformer installed at the GSI synchrotron.

results if a dc-beam is fed through the toroids, because of the additional magnetic field from the beam. The sum signal U_S is different from zero with a modulation twice the modulation frequency. In the demodulator stage this signal is rectified. The dc-current is measured by means of the current generated in the feedback compensation circuit which forces the output signal back to zero. The applied feedback current flows through the third winding of both tori. The detector can even be use at even harmonics of the modulation frequency, which results in higher sensitivity and an improvement of the signal to noise ratio. Due to the extremely specific requirements concerning the matching of the magnetic characteristics for a pair of tori, the design of a magnetic modulator with high resolution and dc-stability is rather complex and the success depends very much on the selection and treatment of the core-material as discussed in more detail in [9]. The applied feedback circuit for the zero flux compensation makes the device very sensitive and linear. To get a fast response, the signal from an ac-transformer is added into the feedback circuit. With this enhancement, the time resolution of the full device is in the range of 20 μs.

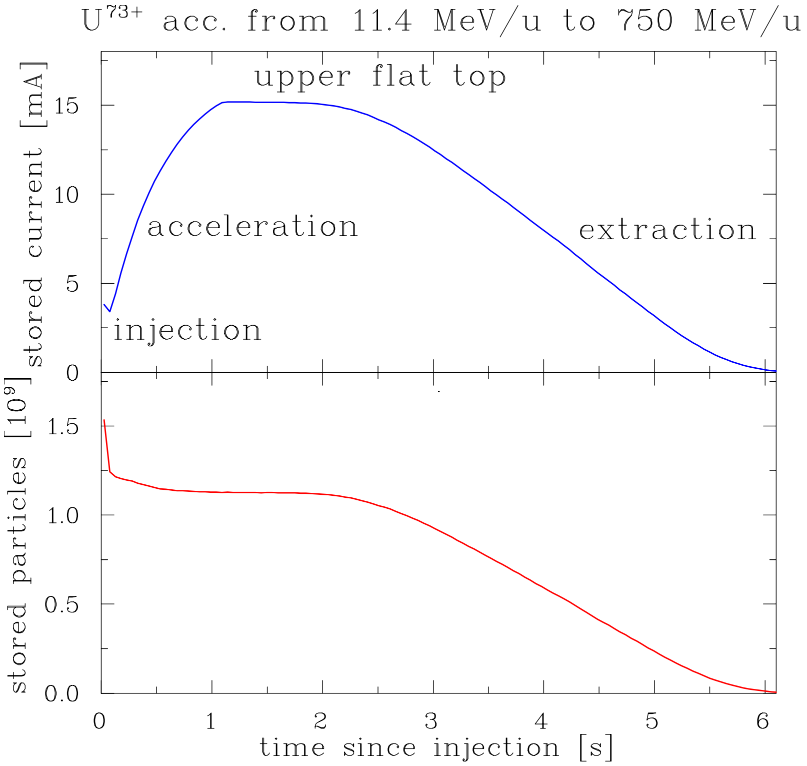

Figure 2.16: The signal of a dc-transformer for a $^{238}U^{73+}$ beam at the GSI synchrotron. The electrical current is shown at the top and the number of stored particles at the bottom. The acceleration needs about 1 s. After a delay of about 0.5 s, the slow extraction of 4 s length follows.

The specification of a typical dc-transformer developed for the heavy ion synchrotron at GSI is given in Table 2.3 and a photo in Fig. 2.15. The resolution is about 1 μA. The offset drift, mainly caused by the magnetic properties of the tori, are of the order of 20 μA per day. The offset can be improved by an automatic zero compensation at times the synchrotron does not contain any current e.g., after the ramp down phase of the magnets.

An example of a dc-transformer measurement is shown in Fig. 2.16. The electrical current and the number of stored particles are shown. A $^{238}U^{73+}$ beam is injected in the synchrotron and the acceleration starts shortly after the injection. A loss of particles is seen, during the rf bunching process due to some misalignments. During the acceleration the slope of the magnetic field $dB/dt = 1.3$ T/s is constant, resulting in a constant rise of of the particle momentum. The current grows linearly only for non-relativistic velocities due to the decrease of the revolution time, inversely proportional to the velocity. For the maximal energy of 750 MeV/u, corresponding to $\beta = 84$ %, the relativistic increase of the mass starts to be significant. After reaching the maximum energy, a ~ 0.5 s flat top is seen for the de-bunching phase. The slow extraction of several seconds is done by changing the tune using a fast quadrupole to get close to a 1/3-resonance to blow up the transverse beam dimension. The resonant beam particles are then separated from the circulating stable beam by an electrostatic septum and are extracted.

2.3 The low current limit of transformers

The very low magnetic field carried by the beam is detected with a transformer; the detection threshold or the signal-to-noise ratio has to be discussed briefly:

1. A first general limitation is the thermal noise of the load resistor. The effective thermal noise voltage U_{eff} is given by

$$U_{eff} = \sqrt{4k_B T \cdot R \cdot \Delta f} \tag{2.18}$$

   with T is the temperature of the resistor R, k_B the Boltzmann constant and Δf the required bandwidth. A general rule is that the noise is lower for a smaller bandwidth. For a passive transformer $R = 50\ \Omega$ for the load resistor. For an active transformer the amplifier noise dominates.

2. Regarding the magnetization of the core-material on a atomic (or solid state physics) scale, we have the so called Weiss domains. In a domain the maximum magnetization is reached, but the magnetization of the different domains do not have the same orientation. By applying an external field the Weiss domains change their orientations in a jerky way. This results in a noisy behavior as schematically demonstrated in Fig 2.17. The effect is called Barkhausen noise. This effect is the limitation of the dc-transformer, because the working principle is the modulation, which drives the tori into saturation. For an ac-transformer the Barkhausen noise is of no importance, because the low resistive coupling of the secondary winding (50 Ω for the passive type and low impedance input of the op-amp for the active type) prevent magnetization of the torus.

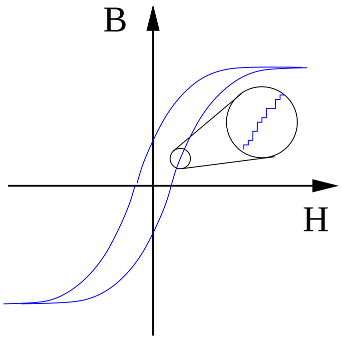

Figure 2.17: Barkhausen noise generated by the change of the orientation of the Weiss domains.

3. A careful choice of the magnetic core-material is important to have a low temperature influence, as well as a low disturbance of mechanical vibration (low magnetostriction).

4. Even if the local magnetic field is measured precisely, it might not be the field of the beam. In particular eddy currents in the torus or in the surrounding might give rise to a noisy or wrong reading. To reduce eddy currents, a spiral wound flat ribbon (∼ 25 μm thickness) with high resistivity and insulation between layers is used.

5. The transformer has to be well shielded against external magnetic fields. In particular against the fields from the bending and focusing magnets and from the fields produced by turbo pumps.

6. One has to prevent the flow of secondary electrons, created by the beam hitting the vacuum pipe, through the transformer. This can be a large error contribution to the reading. Shielding within the vacuum pipe is difficult in most cases. Therefore the beam steering has to be controlled carefully.

The actual value of the minimum detected beam current depends on the design of the device. For most cases it is about 1 μA.

2.4 Faraday cups for low currents

A Faraday cup is a beam stopper supposed to measure the electrical current of the beam. The basic cup design is shown in Fig. 2.18: An isolated metal cup is connected to a current sensitive pre-amplifier. As shown for an active beam transformer, the pre-amplifier consist of a low impedance input and a conversion to a voltage. Range switching is achieved by using different feedback resistors for the operational-amplifier. With a Faraday cup, much lower currents can be measured as compared to a transformer. A measurement of 10 pA even for a dc-beam is possible with a low noise current-to-voltage amplifier and careful mechanical design; this is 5 orders of magnitude more sensitive than a dc-transformer. Low current measurement is important e.g., for the acceleration of radioactive beams.

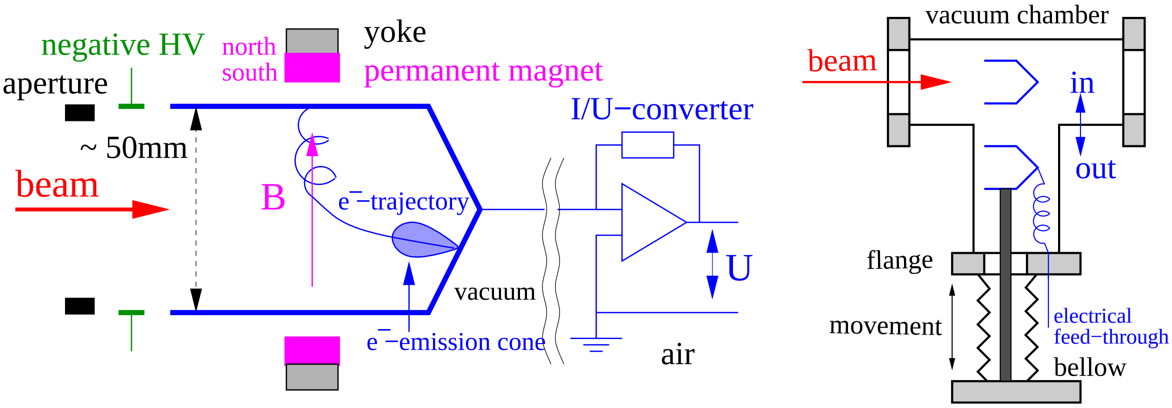

Figure 2.18: Left: Scheme of an uncooled Faraday cup with magnetic and electric secondary electron suppression. Right: Scheme for inside and outside position of destructive diagnostics devices.

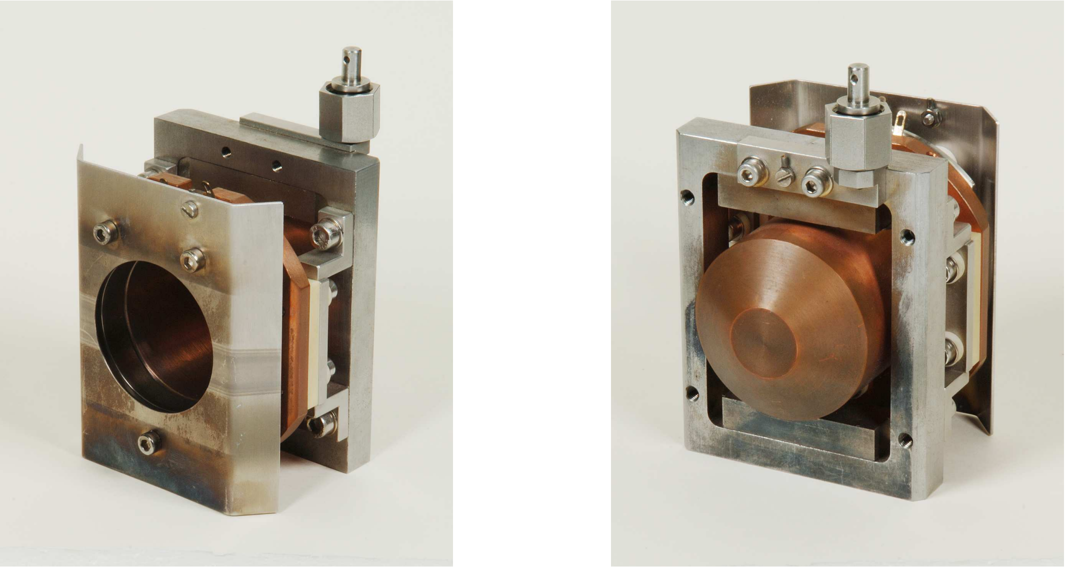

Figure 2.19: Photo of an Ø50 mm uncooled Faraday cup with magnetic and electric secondary electron suppression.

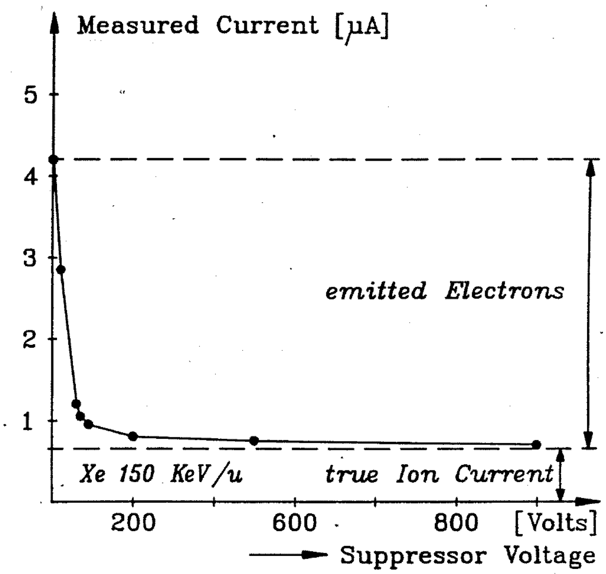

Figure 2.20: The suppression of secondary electrons in a Faraday cup as a function of the applied voltage.

When an accelerated particle hits a surface, secondary electrons are liberated (see also Chapter 2.7.3). The flux of these electrons is proportional to $\cos\theta$, where θ is the angle of the electron trajectory with respect to the surface. Their average energy is below 10 eV. If these electrons leave the insulated cup, the reading of the beam current is wrong by this amount. A secondary electron suppression has to be foreseen. It can be done by:

- Very long cups, where the length in beam direction is much greater than the diameter. The contribution of the lost electrons is low for this geometry.

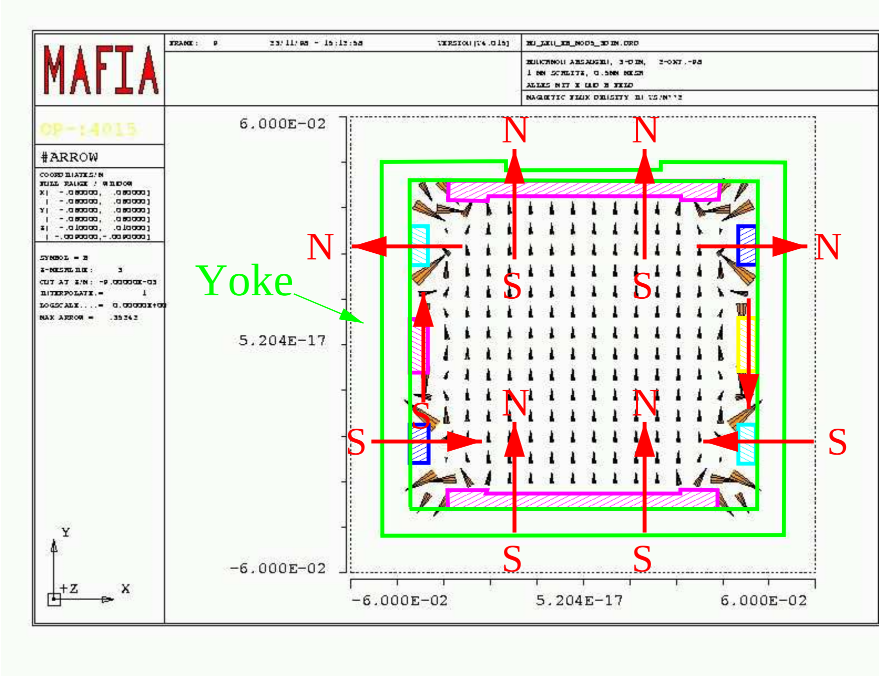

Figure 2.21: Arrangement of Co-Sm permanent magnets within the yoke and the calculated magnetic field lines. The homogeneous field strength is $B \sim 0.1$ T.

- Using a high voltage suppression close to the entrance of the cup. By applying a voltage well above the mean energy of the secondary electrons, they are pushed back to the cup surface. A measurement using this suppression voltage is shown in Fig. 2.20. The disadvantage of this method is related to the fact that the electrical field on the beam axis is lower that on the edges, while for the emission of the electrons it is vice versa.
- By using a magnetic field created by permanent magnets. In this field B, the secondary electrons spiral around the magnetic field lines with the cyclotron radius r_c

  $$r_c = \frac{\sqrt{2m_e E_{kin}}}{eB} = 3.37 \frac{\sqrt{E_{kin}[\mathrm{eV}]}}{B[\mathrm{mT}]} \ [\mathrm{mm}] \tag{2.19}$$

  with m_e the electron mass, e its charge and E_{kin} the kinetic energy component perpendicular to the field lines. For $E_{kin} = 10$ eV and a field of 10 mT the radius $r_c \sim 1$ mm, which is short compared to the mechanical dimensions. With permanent magnets, field lines perpendicular to the beam axis can be created relatively easily, see Fig. 2.21.

2.5 Energy loss and ranges of particles in matter

For the discussion of the cup, as for all intercepting diagnostics, we need the energy loss and the related range of the particles penetrating through matter. The energy loss of a proton or an ion is mainly due to the collision of the projectile with the electrons of the stopping target, the so called electronic stopping. Due to the different masses of the ion and the electron, the energy transfer per collision is in most cases below 100 eV. The electronic stopping is described by the Bethe-Bloch formula

$$-\frac{dE}{dx} = 4\pi N_A r_e^2 m_e c^2 \cdot \frac{Z_t}{A_t}\rho \cdot \frac{Z_p^2}{\beta^2}\left[\ln\frac{2m_e c^2\gamma^2\beta^2}{I} - \beta^2\right] \tag{2.20}$$

with the constants: N_A the Avogadro number, m_e and r_e the mass and classical radius of an electron and c the velocity of light. The target parameters are: ρ density of the target with nuclear mass A_t and nuclear charge Z_t; the quantity $\frac{Z_t}{A_t}\rho$ correspond to the electron density. I is the mean ionization potential for the target. The projectile parameters are: Z_p nuclear charge of the ion with velocity β and $\gamma = (1-\beta^2)^{-1/2}$. For more details see [10, 11, 12]. This formula has to be modified due to the fact that ions traveling through matter are not bare nuclei, but have some inner electrons. An effective charge is used instead of Z_p calculated by e.g. semi-empirical methods described by [13]. The result of such a calculation is shown in Fig. 2.22 for different ions into copper. The energy loss is maximal for ions with a kinetic energy around 100 keV/u to 7 MeV/u (corresponding to velocities $\beta \sim 1.5$ % to 12 %) depending on the ion species. These are typical energies of a proton/heavy ion LINAC. Below 100 keV/u the energy loss decreases and nuclear stopping becomes significant. Energies below 10 keV/u are typical for proton/heavy ion sources mounted on a high voltage platform. For relativistic energies above 1 GeV/u the energy loss is nearly constant. These are typical energies of synchrotrons.

For the consideration of a Faraday cup, the range in material is important. Copper is often used for cups, due to its high heat conductivity. For a particle accelerated to E_{kin}, the range R is calculated numerically from the stopping power via

$$R = \int_0^{E_{kin}} \left(\frac{dE}{dx}\right)^{-1} dE \tag{2.21}$$

and has an approximately scaling above $\simeq 10$ MeV/u [10]

$$R \propto E_{kin}^{1.75} \ . \tag{2.22}$$

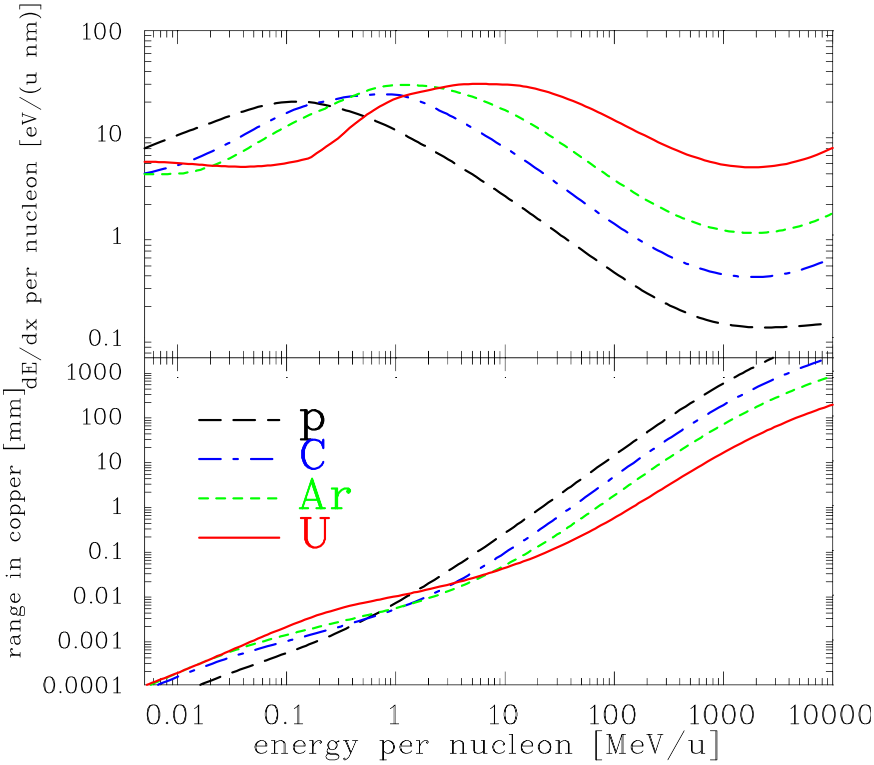

Figure 2.22: The energy loss per nucleon at the surface and the range in copper as a function of the kinetic energy for several ions. The energy range is plotted from 5 keV/u to 10 GeV/u and the range from 100 nm to 1m. The calculation of the electronic and nuclear stopping uses SRIM [13].

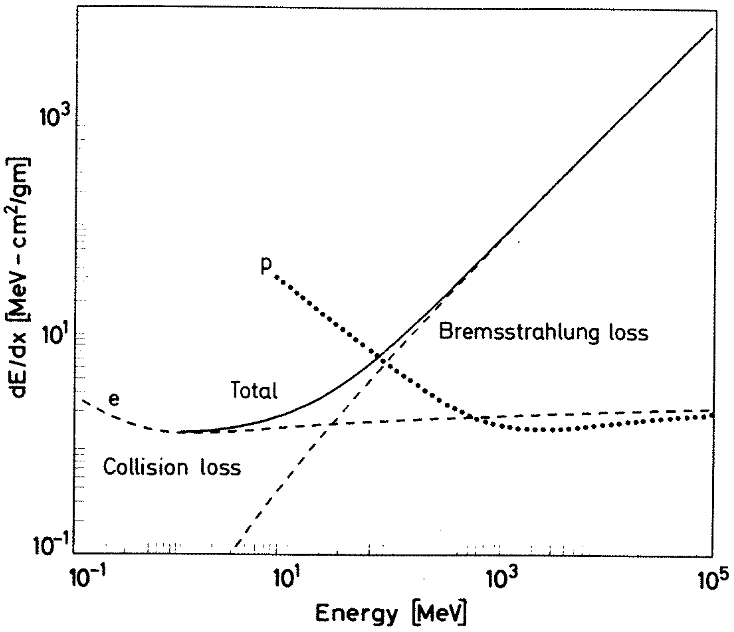

Figure 2.23: The energy loss of electrons in copper for collision and radiation losses [10]. For comparison the loss of protons are also shown.

The results are shown in Fig. 2.22. This range should be much shorter than the mechanical dimension for a practical cup design. For energies below 100 MeV/u the range is less than 1 cm. Or, in other words, cups are only useful at LINACs or cyclotrons. For higher energies, the range is too large and other techniques are applied. In addition for particles above the nuclear Coulomb barrier nuclear reactions are possible and charged secondary particles might leave the material resulting in a wrong reading.

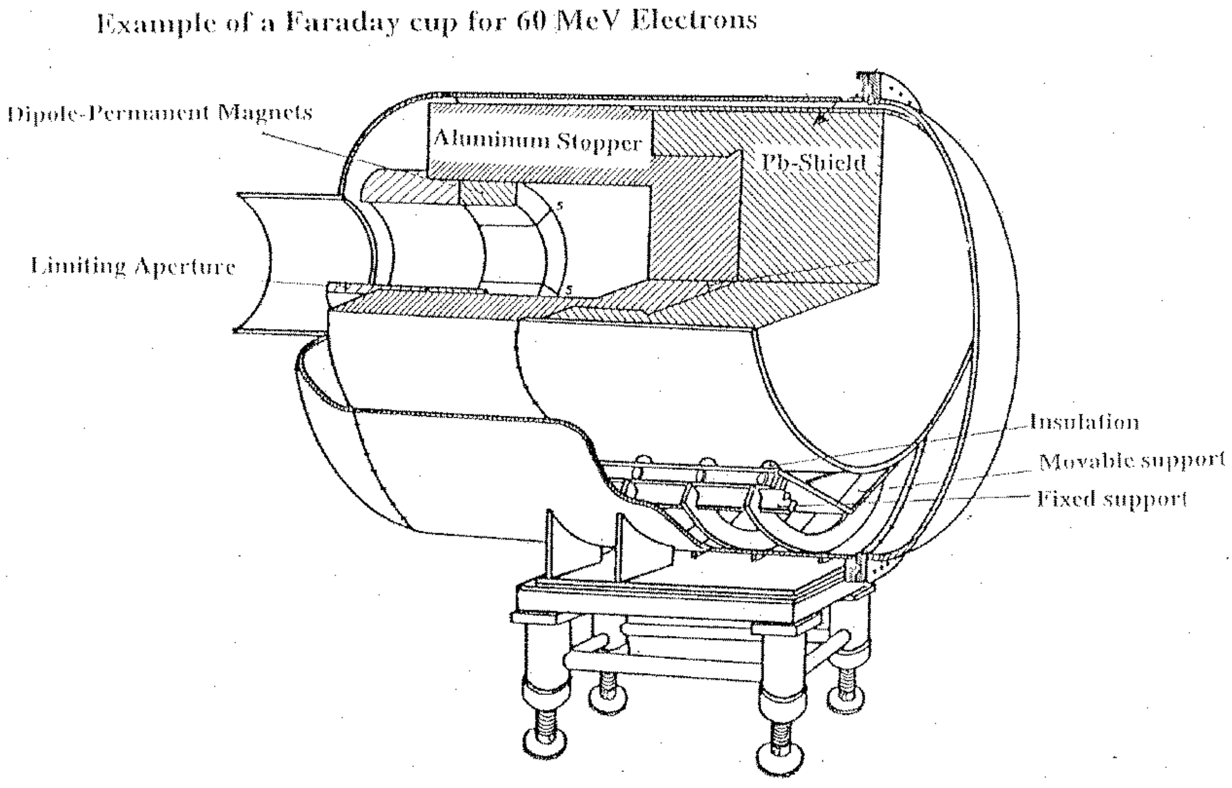

Figure 2.24: A drawing of a cup used for 60 MeV electrons.

The stopping of electrons differs from protons and ions. The collisional loss due to electronic stopping is also described by Bethe-Bloch, but for energies above a few 10 MeV the radiation loss by Bremsstrahlung is dominant, see Fig. 2.23 and e.g. [10]. The trajectories in the material are much less straight than for ions, due to the possible high energy- and momentum transfer in a single collision. Also the range distribution is much wider. Faraday cups for electrons have to be made even larger than for ions, see Fig. 2.24. Here the electrons are relatively gently stopped in the low Z material aluminum to limit the production of high energy Bremsstrahlungs-photons. In addition, one has to prevent the escape of charged particles, e.g., electrons or positrons, created by the Bremstrahlungs-photons. For this reason a Pb shield is included. Due to the long range, the use of cups is restricted to the first few modules of an electron LINAC.

2.6 Faraday cups for high currents

Faraday cups are sometimes used for higher beam currents, where measurements are also possible with ac-transformers, because their electronics are simpler. In addition cups serve as beam dumps. Like for all intercepting diagnostic devices, the heating by the beam's energy loss has to considered. An example of the temperature rise is shown in Fig. 2.25, where a pulsed beam (in this case an Ar^{10+} beam with 10 mA electrical current) of pulse length 1 ms and a repetition

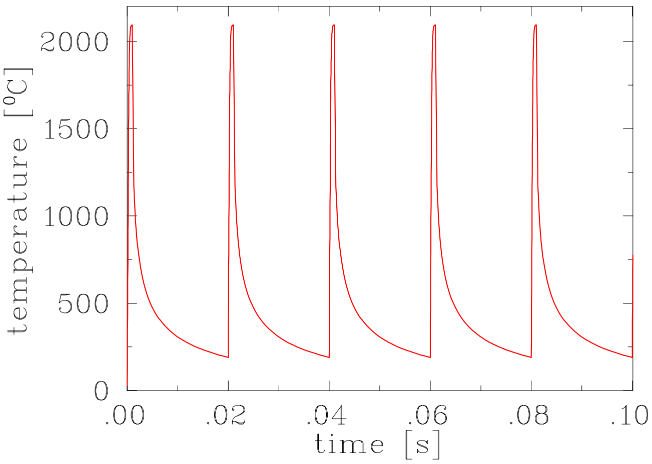

Figure 2.25: Temperature increase for a 1 μm thin tantalum foil (emissivity of $\epsilon = 0.49$) irradiated by a 10 mA Ar^{10+} beam of length 1 ms and repetition time of 20 ms with 11.4 MeV/u. The beam size is 5 mm FWHM in both directions and the absorbed power is ~ 40 kW/mm^2.

time of 20 ms hits an uncooled foil. The heat source is the energy loss of the particles, while the heat sink is the radiation power per area P_r as described by the Stefan-Boltzmann law

$$P_r = \epsilon \sigma T^4 \qquad (2.23)$$

with T the temperature and $\sigma = 5.67 \cdot 10^{-8}$ W/m^{2}K^4 the Stefan-Boltzmann constant. ϵ is the emissivity of the material with typical values $0.1 < \epsilon < 0.9$. Radiation is a fast cooling process only for high temperatures. The heat conductivity is a relatively slow process, compared to the heating by a short intense beam pulse. The foil is heated close to its melting temperature during the pulse (here about 2000 ^{o}C). In the intervals it cools down to 200 ^{o}C again and the average temperature is only $\sim 550^o$C. But the material has to survive the high temperature during the beam delivery. The beam parameters in the example are moderate. At GSI, higher currents are possible. The typical current needed for a neutron spallation source is also higher.

For a quantitative analysis for a massive material the partial differential equation of heat transfer inside the material has to be calculated numerically

$$\frac{\partial T(\vec{x},t)}{\partial t} = \frac{\lambda}{\rho c} \text{div grad } T + \frac{1}{\rho c} \eta(\vec{x},t) \qquad (2.24)$$

for the temperature T as a function of time t at each position $\vec{x}$ inside the material. λ is the heat conductivity, ρ the density and c the specific heat. The source term $\eta(\vec{x},t)$ is the volumetric power deposition by the beam, which depends on position and time. For a more detailed discussion of an optimized material and geometric arrangement see e.g. [14].

An example of such a calculation is given in Fig. 2.26 for a cylindrical cup for a high power U ion beam at the end of the macro pulse. The value is set to the design power of the high current in the 1 MW LINAC at GSI. One solution to dissipate this large power is to increase the surface area of the irradiated material by a cone-like construction, as shown in Fig. 2.27. The ions at the GSI LINAC have ranges below 1 mm. A 1 mm thin layer of tantalum is used to stop the ions, because tantalum has a high melting temperature. Underlying copper is used for its high heat conductivity. The water cooling can only dissipate the average power and an equilibrium temperature is reached. For pulsed beams the maximum value at the surface, or more precisely, close to the penetration depth of the particles, is much higher than the equilibrium value. This high temperature is what mainly deteriorates the device. Water-cooling is normally used to dissipate the average beam power. To have a low electrical conductivity de-mineralized

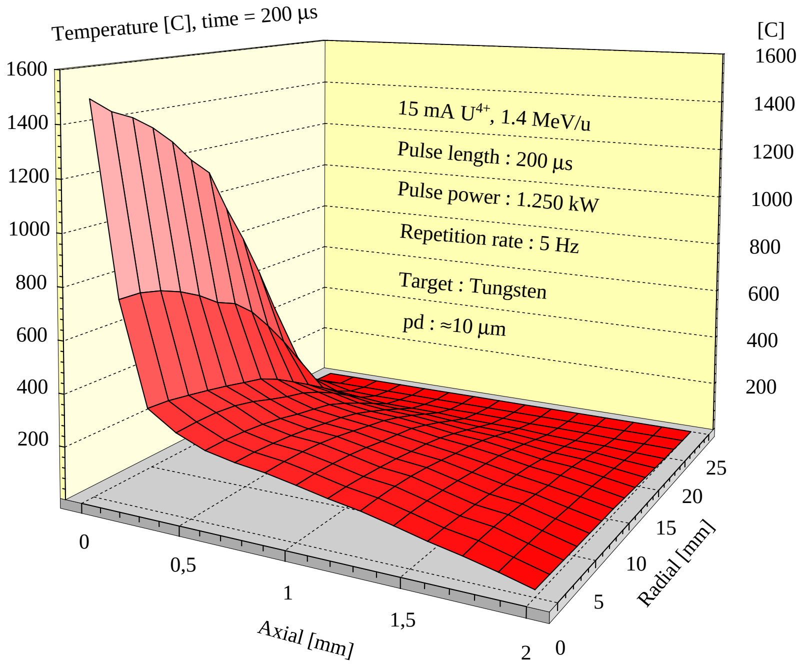

Figure 2.26: A 1.4 MeV/u U^{4+} beam of 15 mA electrical current and 0.2 ms pulse length hitting a cooled cylindrical Faraday cup. The distribution of the temperature is calculated by finite element method.

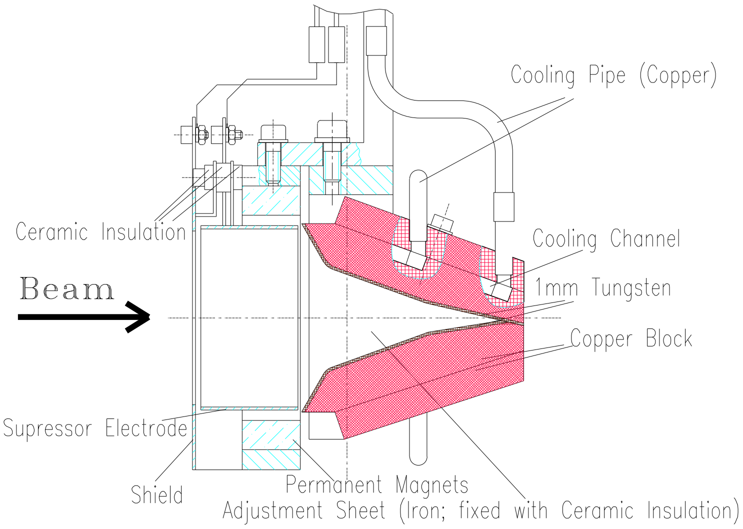

Figure 2.27: A Faraday cup and beam stopper of high intensity beams as installed at the high current LINAC at GSI. The opening of the cup is Ø 50 mm

water is used, but for a precise current reading the finite and temperature dependent electrical conductivity has to be taken into account. Therefore, cooled cups have a much lower sensitivity than isolated, uncooled cups. A careful design has to be done and the beam parameters have to be controlled to prevent the destruction of cups and beam dumps for higher power LINACs and cyclotrons.

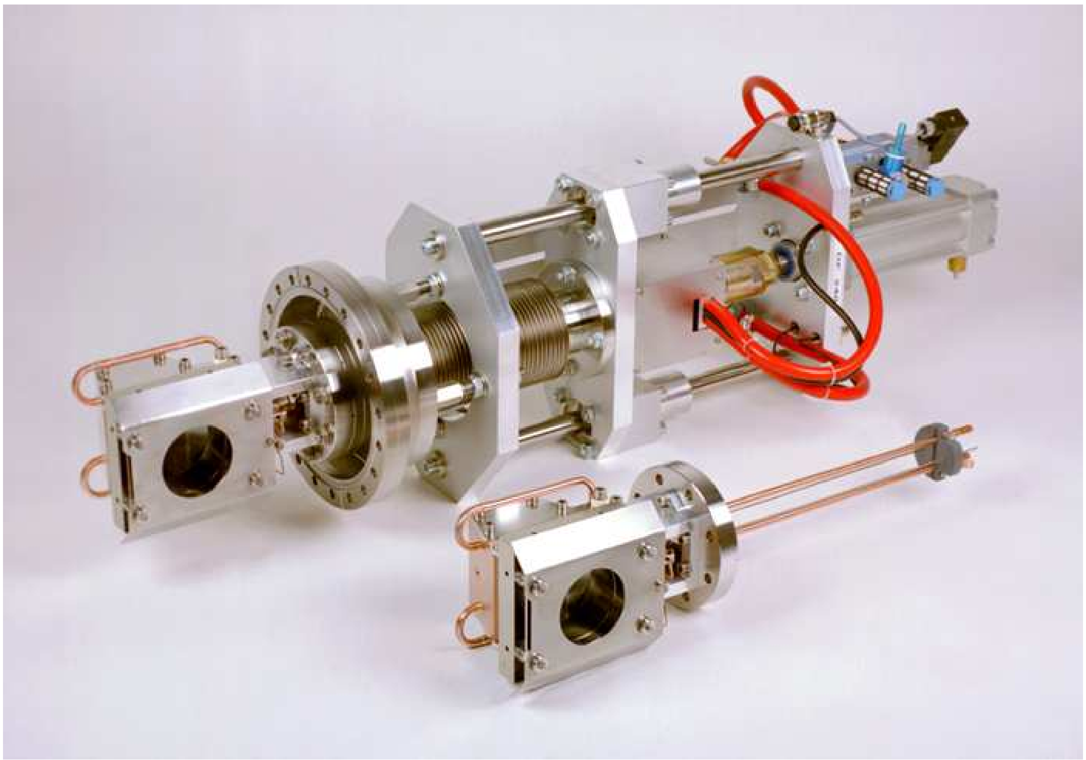

Figure 2.28: Photo of a Faraday cup and beam stopper for high intensity beams as installed at the high current LINAC at GSI. The pneumatic feed-through is mounted on a Ø 150 mm flange.

2.7 Low current measurement used for slow extraction

A lot of experiments in particle, atomic or nuclear physics use protons or ions in the energy range of synchrotrons, i.e., higher than $\sim$100 MeV/u. Due to their detectors, a dc-beam, as generated by a slow extraction, is preferred. Typical data from a dc-transformer has been shown in Fig. 2.16. The current ranges from only 10^3 up to 10^{12} particles per second, which corresponds to an electrical current from 10^{-15} to 10^{-6} A. This is well below the resolution of a dc-transformer. Due to the high energy, the range of the particles is too large for the use of Faraday cups, as shown in Fig. 2.22 for copper. In addition, a lot of secondary particles would be created in the cup material. The techniques of particle detectors are used instead. An overview of the typical detectors is presented in Fig. 2.29:

- For the current below 10^6 s^{-1}, the individual particles can be counted by scintillators.
- For the medium range from about 10^4 to 10^9 s^{-1} the energy loss in a gas is measured by an ionization chamber (IC).
- For the higher range from about 10^8 s^{-1} the emission of secondary electrons from a metal surface forced by the primary ion's energy loss is determined by secondary electron monitors (SEM).

The design of such a system is described in e.g. [15, 16, 17].

2.7.1 Scintillation counter

When a particle penetrates a scintillating material, the electronic energy loss by the collision of the beam particles with the target electrons create some fluorescence photons. These photons can

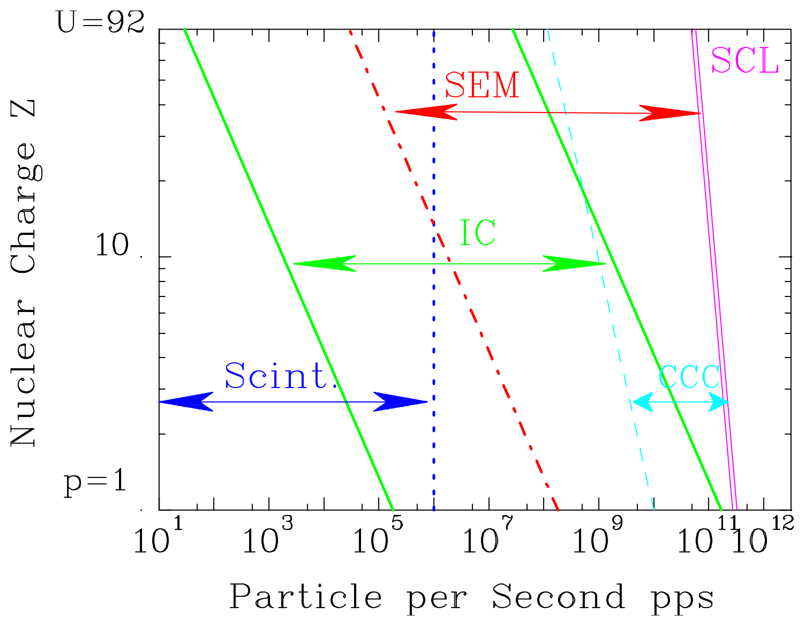

Figure 2.29: Overview of the different detector systems used for slow extraction at the GSI synchrotron. The numbers are given for the different ions with an kinetic energy of 1 GeV/u, extracted within 1 s and a spot size of 1 cm^2. With a scintillator up to 10^6 particles can be counted. The lower limit of the IC and SEM correspond to a secondary current of 1 pA, the upper threshold of the IC is 30 Gray/s. The CCC (cryogenic current comparator) measures the magnetic field. SCL means the incoherent space-charge limit of the synchrotron at injection energy.

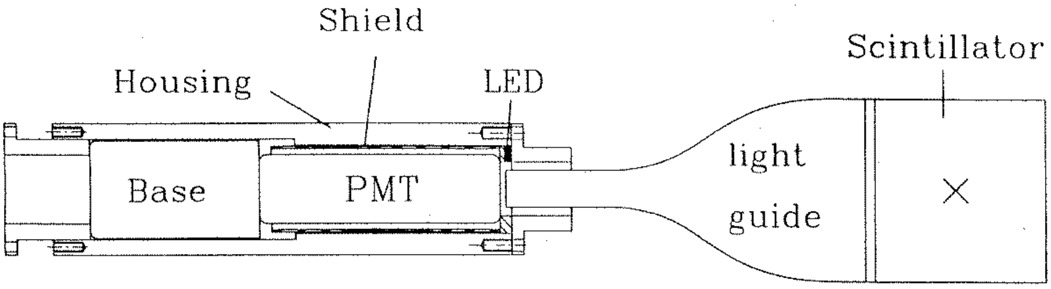

Multiplier Tube:	Scintillator:
Philips XP2972 (1")	Pilot U
Gain ≅ $10^4 \ldots 10^6$	75 x 75 x 1.0 mm^3
Anode rise time < 2 ns	Pulse Width 1.2 ns

Figure 2.30: The scheme of a plastic scintillation counter connected to the photo-multiplier via a plastic light guide.

be detected and amplified by a photo-multiplier, converted to a logical pulse by a discriminator and finally counted by a scaler. Scintillators should have some general properties (for more details see [10, 11]):

- The light output should be linear to the energy loss.
- The fluorescence should decay as fast as possible to get a high count rate.

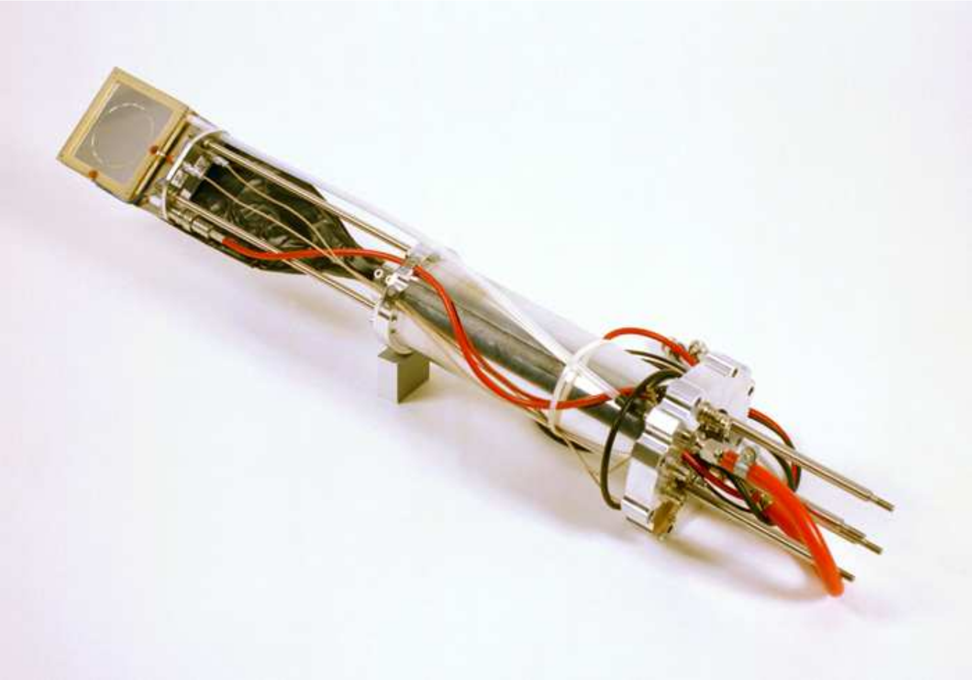

Figure 2.31: The hardware of the scintillators (wrapped in black tape) and the IC installed at GSI.

- The scintillator material should be transparent for the fluorescence light and the index of refraction should be around $n = 1.5$ for the use of light guides.
- The material should be easy to form and it should be possible to get large sizes, about a factor of two larger than the maximum beam size.
- The wavelength of the light should be within the spectral range of the photo-cathode of the photo-multiplier: 350 nm $< \lambda <$ 500 nm is preferred, i.e., near UV to green light. The photo-cathode of the photo-multiplier converts the light into electrons. These electrons are amplified by ~ 10 stages of so called dynodes, where electro-static fields and secondary emission are applied to accelerate and multiply the electrons.
- The scintillator material should be radiation hard, so it will not be destroyed by the incident particles.

In most cases plastic scintillators are used. They are cheap and easy to produce in nearly every mechanical shape. As an example, the arrangement used at GSI is shown in Fig. 2.30 and a photo together with an ionization chamber in Fig. 2.31. A large size of 75×75 mm^2 has been chosen with a thickness in beam direction of 1 mm. The plastic scintillator (in this case BC 400) has a short decay time in the range of ns. A typical pulse is displayed in Fig. 2.32, recorded with a medium energy heavy ion beam. The energy resolution is quite good, which is important because it yields good accuracy of this absolute measurement. Due to the used several 100 m long cables between the detector in the beam pipe and the electronic processing, the cable dispersion broadens the peak. Before pile-ups start to play a role, count rates up to several 10^7 s^{-1} can be accepted. A typical measurement of an extracted current is shown in Fig. 2.33, where the particle rate as determined by a scintillator and an ionization chamber are compared. This is corroborated with the signal of the dc-transformer measuring the stored current in the synchrotron.

The disadvantage of the plastic scintillators is the very low radiation hardness, due to their complex organic molecular structure. Inorganic crystal have a much higher radiation hardness.

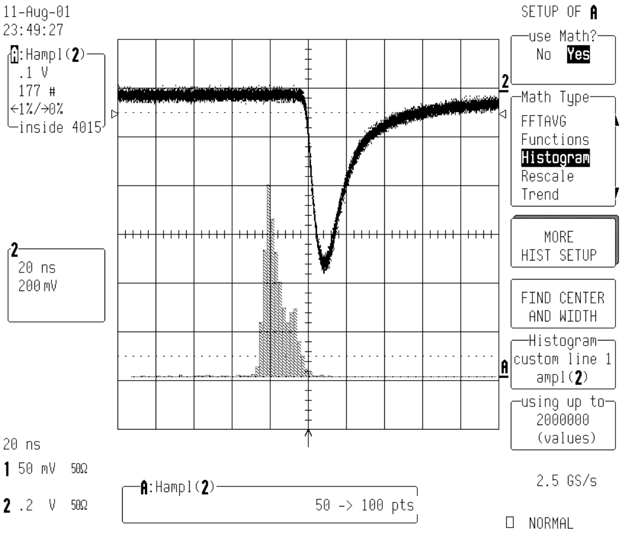
11-Aug-01
23:49:27

A:Hampl(2)
.1 V
177 #
←1%/→0%
inside 4015

2
20 ns
200 mV

20 ns
1 50 mV 50Ω
2 .2 V 50Ω

A:Hampl(2)
50 -> 100 pts

SETUP OF A
use Math? No Yes
Math Type: FFTAVG Functions Histogram Rescale Trend
Histogram custom line 1 ampl(2)
using up to 2000000 (values)

2.5 GS/s
☐ NORMAL

Figure 2.32: Analogue pulses from a plastic scintillator recorded with a low current 300 MeV/u Kr beam; the scaling is 20 ns/div and 100 mV/div. The lower curve is the pulse-height distribution.

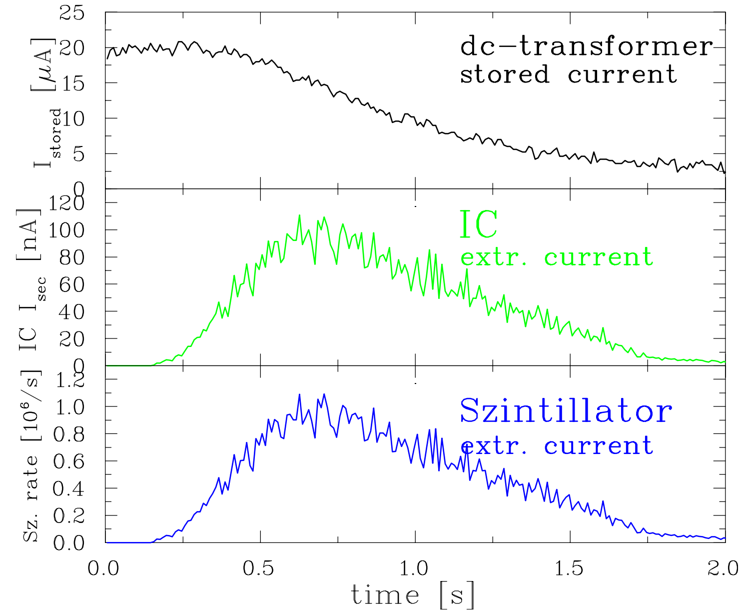

Figure 2.33: The extracted current measured with an IC (middle, given in nA for the secondary current) and a scintillator (bottom, given in particles per second) as compared to the current inside the GSI synchrotron determined by dc-transformer (top, given in μA) for one extraction of a 250 MeV/u ^{208}Pb^{67+} beam with a total amount of 10^6 particles.

In most case Ce activated materials are used [11]. But these inorganic scintillators are difficult to produce in larger sizes, because they are made of single crystals.

2.7.2 Ionization chamber

For the medium particle range the current is determined by the energy loss in a gas inside an ionization chamber (IC). A general description can be found in [11, 18]. Due to the large statistics, the average energy for the production of an electron-ion pair is a well known number, the so called W-value. The W-value of some gases are given in Table 2.4. The arrangement of

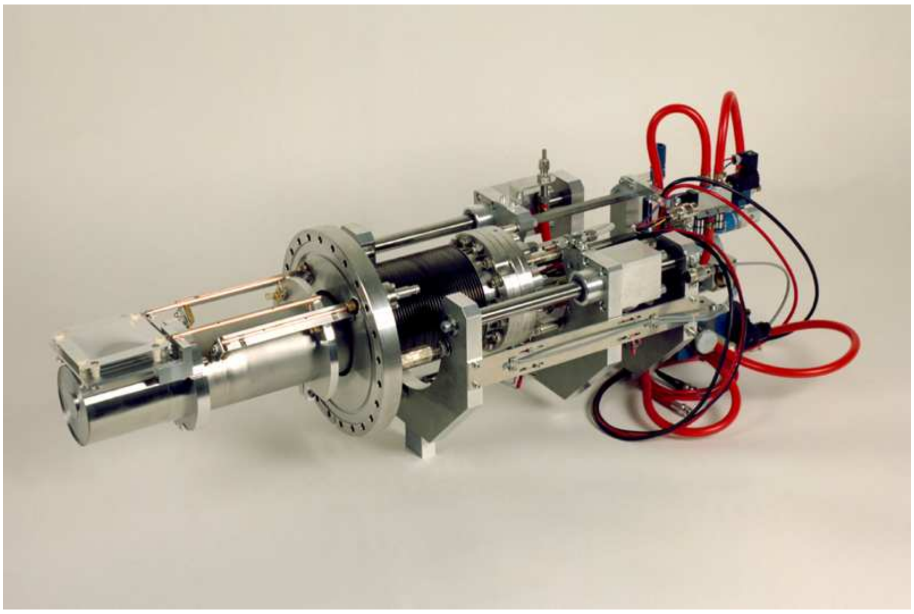

Figure 2.34: The feed-through mounted on a Ø200 mm flange containing the scintillator and IC inside the pocket at atmospheric pressure and the SEM in the vacuum.

Gas	ionization potential [eV]	W-value [eV]
H_2	15.6	36.4
He	24.5	42.7
N_2	15.5	36.4
O_2	12.5	32.2
Ar	15.7	26.3
CH_4	14.5	29.1
CO_2	13.7	33.0

Table 2.4: Ionization potential and W-values for some gases.

an IC is displayed in Fig. 2.35 and a photo in Fig. 2.31. The beam passes a 5 mm thick active gas volume and creates electron-ion pairs. In most cases pure Ar is used, sometimes also mixed with about 10% of molecular gases, like CH_4 or CO_2. The active gas volume is confined by two metalized plastic foils. One of these metalized electrodes is biased with about 1 kV to separate the charges. The other electrode measures the amount of secondary charge with a sensitive current amplifier. A secondary current down to the pA region can be measured precisely, see e.g. [19]. The IC, filled with gas at atmospheric pressure is separated from the vacuum by a metallic foil of typically 100 μm thickness. This thickness has to be chosen so no significant energy loss takes place in the foil. The specification of the IC at GSI is given in Table 2.5.

With the help of the W-values and the calculated energy loss dE/dx, the number of primary ions I_{beam} is determined from the secondary current I_{sec}

$$I_{sec} = \frac{1}{W} \cdot \frac{dE}{dx} \Delta x \cdot I_{beam} \tag{2.25}$$

generated in the active length Δx. The precision of such a measurement depends mainly on the accuracy of the energy loss calculation. For energies above 1 GeV/u the value of dE/dx is only weakly dependent on the energy E, see Fig. 2.22. When the energies of the beam particles are below this, calibrations have to be done to reach an accuracy in the range of 1 %. This calibration

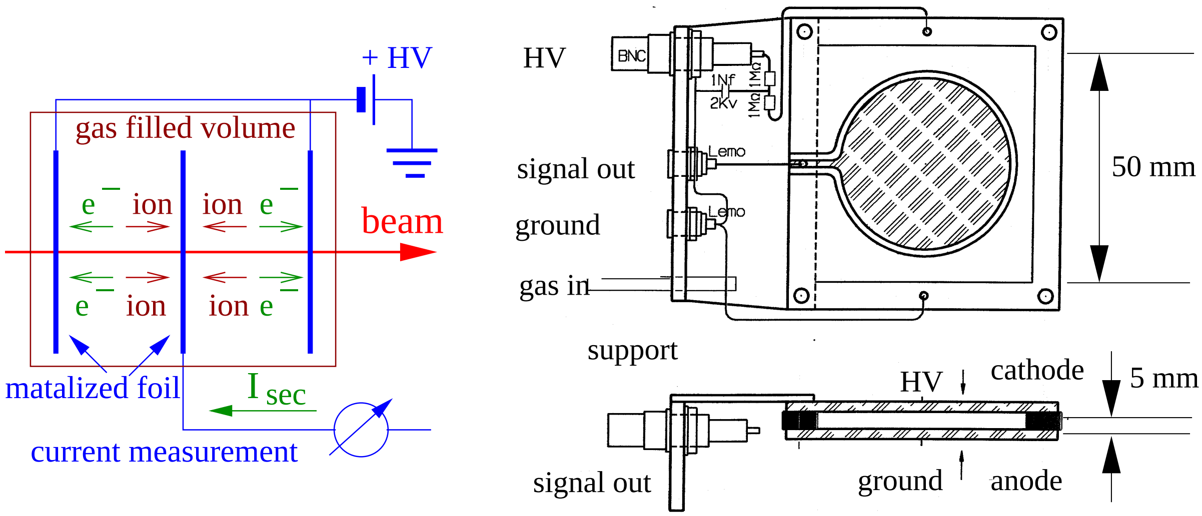

Figure 2.35: The scheme of an IC (left) and its realization with a 5 mm active length (right).

active surface	64×64 mm^2
active length	5 mm
electrode material	1.5 μm Mylar
coating	100 μg/cm^2 silver
gas (flowing)	80 % Ar + 20 %CO$_2$
pressure	1 bar
voltage	500 ... 2000 V

Table 2.5: The specifications of the IC at GSI.

can be done with respect to a scintillator, where an absolute measurement is performed, like shown in Fig. 2.33. From the number of counted particles and the secondary current of the IC a calibration factor can be determined. The result for different ions and energies as performed at GSI [17] is summarized in Fig. 2.36. Due to the different ions, three orders of magnitude are covered, from 10^{-16} C/ion up to 10^{-13} C/ion. The linearity is very good.

The lower limit of an IC is given by the minimum secondary current, which is about 1 pA. Taking this current, the line in Fig. 2.29 is determined. The upper limit is demonstrated in Fig. 2.37. We first discuss the characteristic line of the IC with a moderate primary current: The proportional region is reached after applying a moderate voltage of 500 V, corresponding to 1 kV/cm. The output is then independent of the voltage (or the applied electric field). There is no gas amplification, which starts only above $\sim$ 10 kV/cm. The characteristic line is determined by comparison to the SEM (see below) to get the efficiency. For a higher primary current the plateau is not reached any more. A higher voltage cannot be applied without the risk of sparks. This decrease in efficiency is due to the recombination of the liberated electrons with the positive gas ions, like $Ar^+ + e^- \rightarrow Ar$. The drift time of the ions toward the electrodes depends on the applied electric field, while the drift time for the electrons is nearly constant for the given parameters [11]. The collision frequency of electrons and ions is proportional to their concentration n_e and n_i. The recombination rate is

$$\frac{dn_e}{dt} = \frac{dn_i}{dt} = \alpha \cdot n_e n_i \propto I_{beam}^2 \tag{2.26}$$

with α the rate coefficient. The loss rate is therefore proportional to the square of the primary beam current. Typical values are summarized in Table 2.6. One can conclude that the secondary

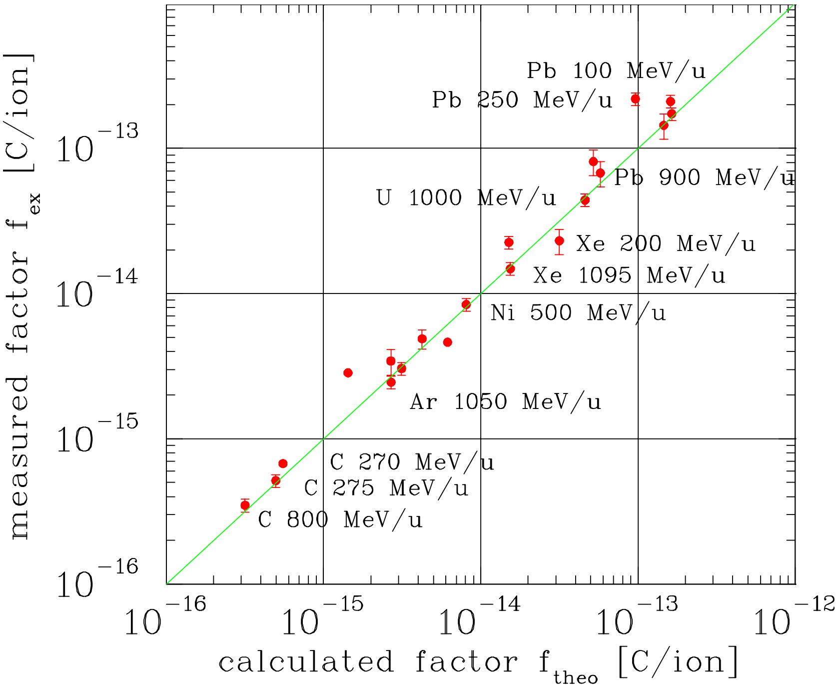

Figure 2.36: The measured calibration factor of an IC and calculated value using energy loss for various slowly extracted ion from the GSI synchrotron [17].

current for the used IC should be below ~ 1 μA for typical parameters, corresponding to a dose rate of about 30 Gray/s [16]. To get the value of the primary current the calibration factor using the energy loss or the values from Fig. 2.36 have to be used.

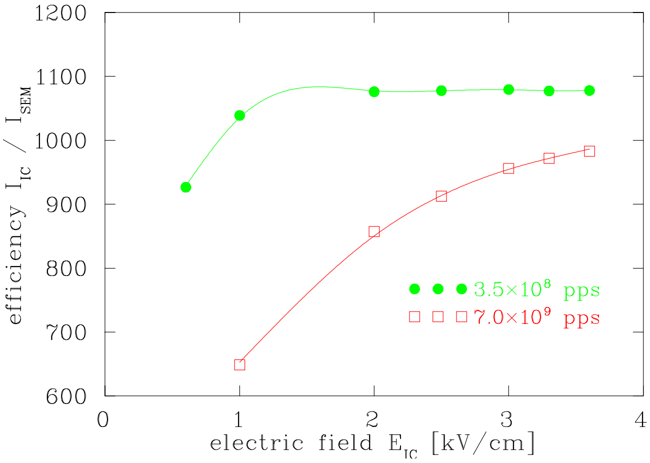

Figure 2.37: The characteristic line for the IC as determined of the 300 MeV/u Ne^{10+} beam. The efficiency, as measured by the ratio of the secondary current of the IC and the SEM as a function of the applied electric field [16]. For low primary current a plateau is reached, while for a high current the recombination leads to a decrease of the secondary charges.

To get a large upper threshold the use of gases with high electron affinity, like O_2 and H_2O, has to be avoided. The electron affinity describes the probability of an electron capture like $O_2 + e^- \rightarrow O_2^-$. The presence of negative ions enhances the recombination with positive ions, like $O_2^- + O^+ \rightarrow O_3$, resulting in a smaller amount of measured secondary charge. In particular an IC should not contain any air.

	Ions	Electrons
drift velocity w^{drift}	0.1 mm/μs	20 mm/μs
drift time t^{drift}	50 μs	0.1 μs
saturation density n^{sat}	$2 \cdot 10^9$ 1/cm^3	$4 \cdot 10^6$ 1/cm^3
secondary current I_{IC}	1 μA	
dose rate D_{IC}	30 Gy/s	
aver. rate coefficient α	10^{-9} cm^3/s	

Table 2.6: Properties of the IC close to the saturation point, see text.

2.7.3 Secondary electron monitor

To cover the high current range, the emission of secondary electrons from a metallic surface can be used. Such a setup is shown in Fig. 2.38, where three 100 μm thick Al-foils are visible, installed on the vacuum side of the feed-through. The outer two foils are biased by typically +100 V to sweep out the free electrons. The middle foil is connected to a sensitive current amplifier. The secondary emission current is given by

$$I_{sec} = Y \cdot \frac{dE}{\rho dx} \cdot I_{beam} \tag{2.27}$$

with Y being the yield factor describing the amount of secondary emission per unit of energy loss at the surface of the Al foil. A calibration has to be done experimentally to determine the value of Y, yielding a precision of 5 %, see Fig. 2.39. The accuracy is lower than for an IC, because the actual value of the yield is determined by the surface structure of the material, which might vary, depending on the production and cleaning method. Eq. 2.27 reflects the fact that only electrons liberated close to the surface have enough energy to overcome the work-function. Most of the free electrons are emitted with a relatively small kinetic energy of less than 10 eV, due to the thermalization process inside the material. The physics of the SEM is also used for profile measurements, see Chapter 3.2.

The material Al is often used due to its well suited mechanical properties. In particular it is stiff enough to prevent micro-phonic pick-up by external vibrations caused e.g., by turbo

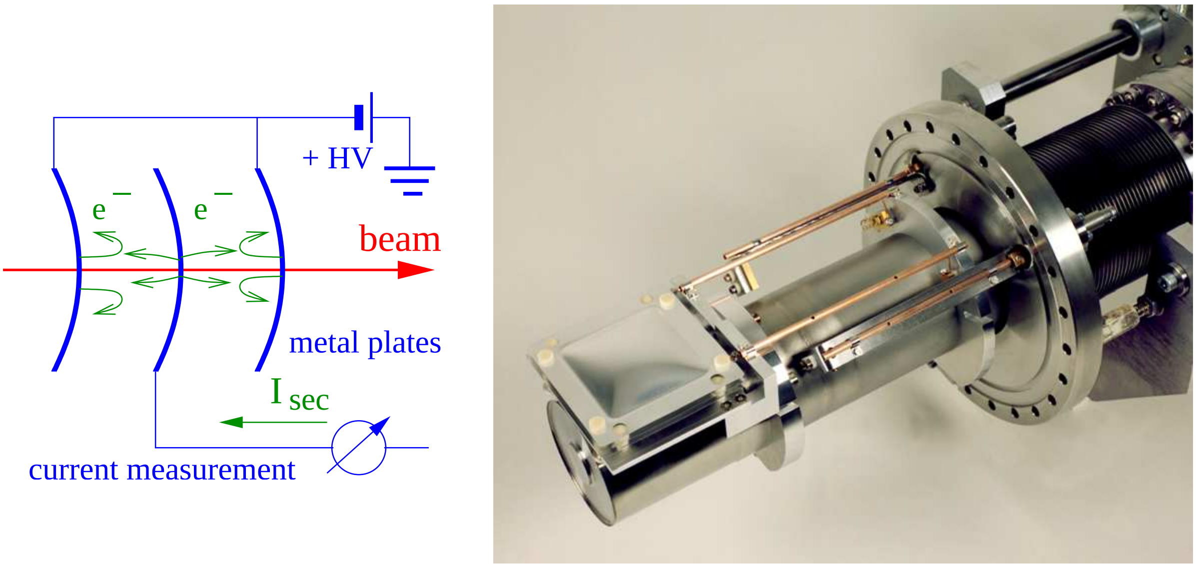

Figure 2.38: Scheme of a SEM (left) and a photo of the SEM part made of 3 Al foils with thickness of 100 μm of the feed-through used for slow extraction current measurements at GSI.

material	pure Al (≃99.5%)
thickness	100 μm
number of electrodes	3
active surface	80 × 80 mm^2
distance between electrode	5 mm
voltage	100 V

Table 2.7: Specification of the SEM at GSI.

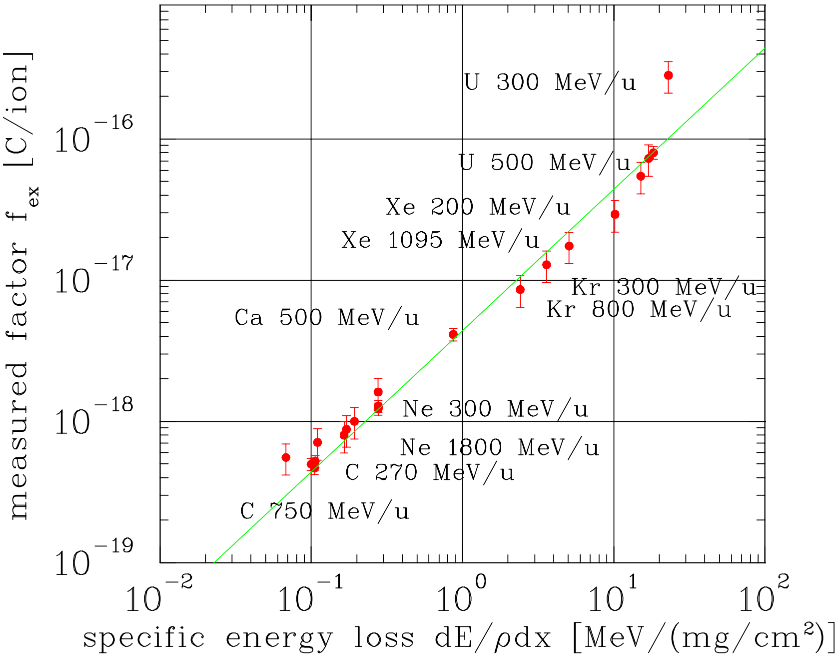

Figure 2.39: The measured calibration factor of a SEM and calculated value using energy loss and a fitted value of $Y = 27.4\ e^-/(\mathrm{MeV/mg/cm^2})$ for various slowly extracted ion from the GSI synchrotron [17].

vacuum pumps. But the emission yield Y might change with irradiation. This is caused by modifications of the surface, which changes the work-function and therefore the average yield Y. Measurements have shown a significant degradation by a factor of two after 10^{18} proton/cm^2 with 450 GeV proton at CERN SPS [20]. Here Ti-foils have a much lower sensitivity to radiation. Radiation hardness is important, because these devices are often used in front of the target as a permanent current monitor.

A totally different approach for low current measurement in the nA region is related to the determination of the magnetic field. Instead of the transformer principle, the field is measured by a SQUID (super-conducting quantum interference device). We refer to [21] for details.

Chapter 3

Measurement of beam profile

The beam profile can be influenced by quadrupole magnets installed in all accelerating structures and in transfer lines. A measurement is important to control the beam width, as well as the transverse matching between different part of an accelerating facility. The large number of bending, focusing and correction magnets gives rise to the need for many profile measurement stations. Depending on the beam particles, current and energy, a very large variety of devices exists. We can only briefly discuss the most popular ones. The beam spot can be directly observed by intercepting it with scintillator screens and viewing the emitted fluorescence with a CCD camera. Secondary electron emission grids are widely used as an electronic alternative to get a very large dynamic range. A grid of wires with typically 1 mm spacing is inserted. Instead of a fixed grid, one single wire can be scanned through the beam to get high spatial resolution. A third approach is a residual gas monitor or ionization profile monitor, where the ionization products of the interaction of the beam with the residual gas atoms or molecules inside the (non-perfect) vacuum of the tube are detected. In these devices the resulting electrons or ions are accelerated by an external electrical field to a detector having a spatial resolution. A profile can also be obtained by the observation of the light emitted by the residual gas molecules excited by the beam interaction. These residual gas monitors and beam induced fluorescence monitors are well suited as non-destructive methods for a synchrotron. When charged particles with relativistic velocities pass a metallic foil, radiation is emitted as described by classical electrodynamics. This light is monitored to receive the beam profile. Electron beams emit synchrotron radiation if the trajectory is curved. Monitoring this light yields direct information about the beam spot. Normally the size of an electron beam is less than 1 mm, while proton or heavy ion beams have large diameters, up to some cm. In particular, in a synchrotron with multi-turn injection, several cm can be reached.

The beam width is mainly given by the settings of the focusing magnets and the beam emittance ϵ. Knowing the lattice, i.e., the β-function $\beta(s)$ and the dispersion $D(s)$ at the monitor location s, the measured beam width $\sigma(s)$ is given by

$$\sigma_x^2(s) = \epsilon_x \beta_x(s) + \left(D(s) \frac{\Delta p}{p} \right)^2 \qquad \text{and} \qquad \sigma_y^2(s) = \epsilon_y \beta_y(s). \tag{3.1}$$

In a synchrotron the lattice functions are well known, or can be measured separately. If also the momentum spread $\Delta p/p$ is known, the emittance can be calculated. (In the vertical direction the dispersion is zero in most cases, because only horizontal bending magnets are used.) Nevertheless, the contribution due to the dispersion has to be taken into account for the interpretation of the beam width. In a LINAC, the lattice functions are not so precisely fixed due to the variable input emittance orientation, leading to a less stringent relation between profile width and emittance.

3.1 Scintillation screen

The most direct way of beam observation is the light emitted from a scintillation screen, monitored by a commercial video or CCD camera, see e.g. [22] for an overview. These devices are installed in nearly all accelerators from the source up to the target.

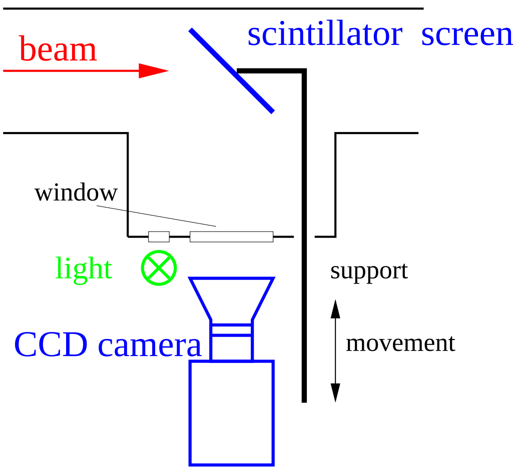

Figure 3.1: Scheme of a intercepting scintillator screen.

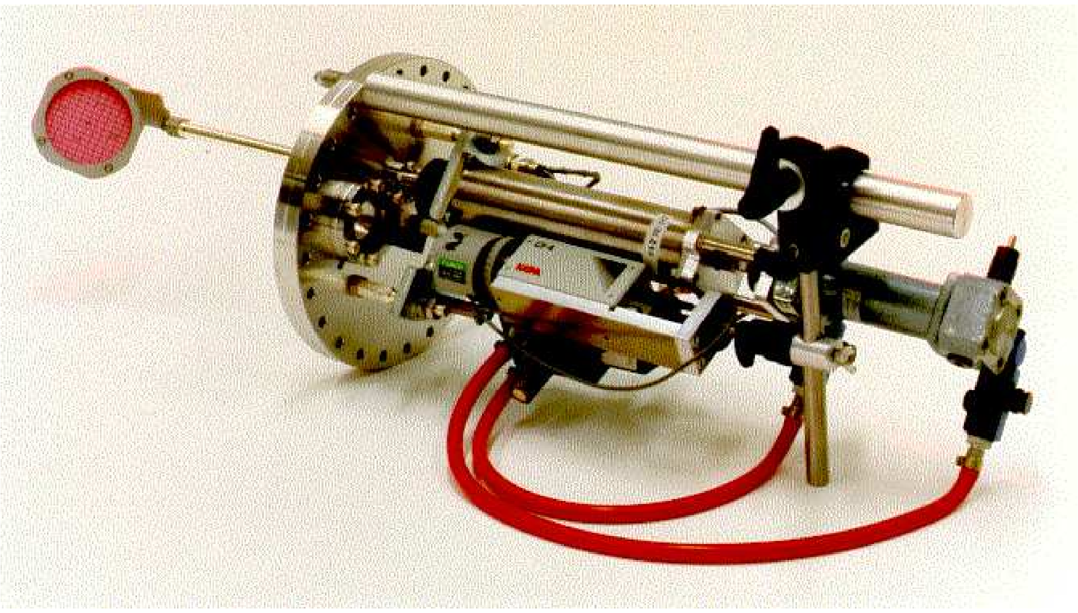

Figure 3.2: A Chromolux scintillation screen of Ø70 mm mounted on a Ø200 mm feed-through including the CCD camera.

When a charged particle penetrates a material the energy loss can be transformed to fluorescence light, as discussed in the previous Chapter 2.7.1. The important properties of such a scintillator are:

- High light output matched to the optical system of the CCD camera in the optical or UV wavelength range (300 nm $< \lambda <$ 700 nm).
- High dynamic range, i.e., a good linearity between the incident particle flux and the light output. In particular, a possible saturation of the light gives rise to a deformation of the recorded profile.

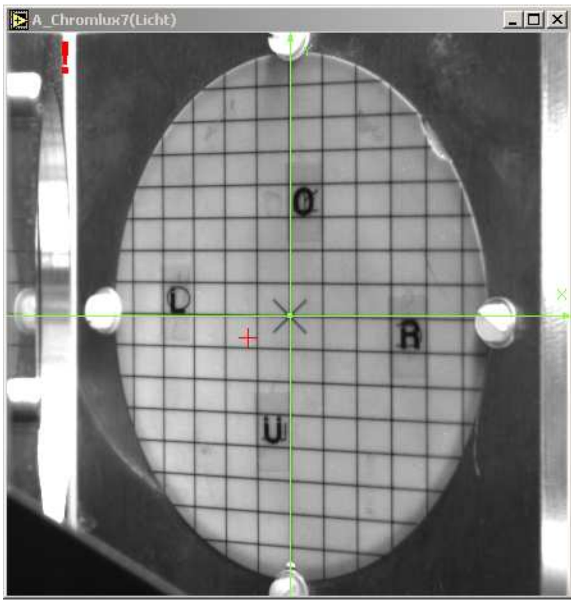

Figure 3.3: View of a Chromolux screen with a camera. The screen is illuminated by an external light. The lines have a separation of 5mm.

- No absorption of the emitted light to prevent artificial broadening by the stray light inside the material.
- Fast decay time, to enable the observation of possible variations of the beam size.
- Good mechanical properties for producing up to Ø100 mm large screens.
- Radiation hardness to prevent permanent damage.

As stated, plastic scintillators have only low radiation hardness and various kinds of inorganic material are used instead. In Table 3.1 some properties are given [22]; for more details see [11].

Abbreviation	Material	Activator	max. emission	decay time
Quartz	SiO_2	none	optical	< 10 ns
	CsI	Tl	550 nm	1 μs
	ZnS	Ag	450 nm	0.2 μs
Chromolux	Al_2O_3	Cr	700 nm	100 ms
	Li glass	Ce	400 nm	0.1 μs
P43	Gd_2O_2S	Tb	545 nm	1 ms
P46	$Y_3Al_5O_{12}$	Ce	530 nm	0.3 μs
P47	$Y_2Si_5O_5$	Ce	400 nm	50 ns

Table 3.1: Chemical composition and some basic optical properties of inorganic scintillation screens. The matrix Al_2O_3 and Li-glass are ceramics in form of glasses, the last three are so called phosphor screens, where powder is deposited on glass or metal plates.

The material Chromolux is a ceramic, which can be fabricated like pure Al_2O_3, used widely as an insulating material. The scintillation is due to the Cr activators; chemically it is comparable to ruby. The disadvantages are its long decay time of ~100 ms and the large absorption inside the material. Nevertheless, due to its robustness, it is quite often used. The well known Ce activated crystal materials like YAG ($Y_3Al_5O_{12}$) have better optical properties and are widely used for particle counting applications [11]. But it is difficult to get crystalline disks of about 10 cm diameter out of this material. Instead of the expensive single crystal disk, one can use small grains of $\sim 10\ \mu$m size, deposited on several mm thick glass or metal disks. These phosphor screens are also used very frequently in analogue oscilloscopes, electron microscopes and image intensifiers.

The sensitivities of the different materials might span several orders of magnitude and depend on the particle species as well, see e.g. [23]. They are used in pulsed and cw-LINACs, for the transfer between different synchrotrons with pulses in the μs range (e.g. [24]) and for slow extraction from a synchrotron (e.g. [25]). A practical realization using a P43 screen for a slowly extracted C^{6+} beam with 127 MeV/u and about 10^8 particles per second is shown in Fig. 3.4.

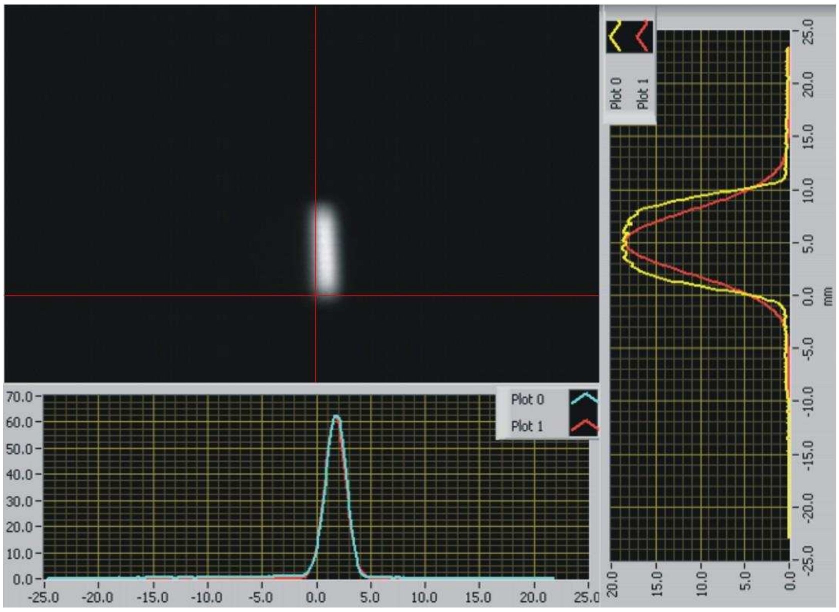

Figure 3.4: Beam spot of a 127 MeV/u C^{6+} beam extracted for the GSI synchrotron on a P43 screen recorded with a camera exposure of 20 ms. The projection on the two axis are shown in connecting with Gaussian fits with 5 mm/div.

For high intensity beams, one has to make sure that the material in not destroyed by the power absorption. In particular, for slow heavy ions this restricts the use, see also the discussion in Chapter 2.5. A disadvantage of the screen is related to the interception. The used material is so thick (several mm) that it causes a large energy loss, so it can never be used for the diagnostics of a circulating beam inside a synchrotron.

The screen is observed with a CCD camera. In older applications with video (i.e. analogue) output, the digitalization is done with a frame grabber. A modern approach uses a digital link, with a digital data transfer of the CCD pixel values. In most cases fiber optic links are used to get fast data rates and larger cable length without signal degeneration, see e.g. [25]. A problem is the radiation sensitivity of the CCD sensor and the digital equipment. At high levels of radiation, the old fashioned analogue VIDICON cameras are used.

3.2 Secondary electron emission (SEM) grid

When particles hit a surface, secondary electrons are liberated, escaping form the surface, as described in Chapter 2.7.3. For the profile determination, individual wires or ribbons interact with the beam; this is called a **S**econdary **E**lectron **EM**ission grid or a harp. A review article can be found [26]. Each of the wires has an individual current-to-voltage amplifier. This is an electronic alternative to a scintillation screen with a much higher dynamic range i.e., the ratio of minimal to maximal detectable current is orders of magnitude larger. For the metallic wires or flat ribbons W-Re alloys are often used for their excellent refractory properties. In particular at low energy LINACs this is important, because no cooling can be applied due to the geometry. A photo of such a device is shown in Fig. 3.5 and the specifications are given in Table 3.2.

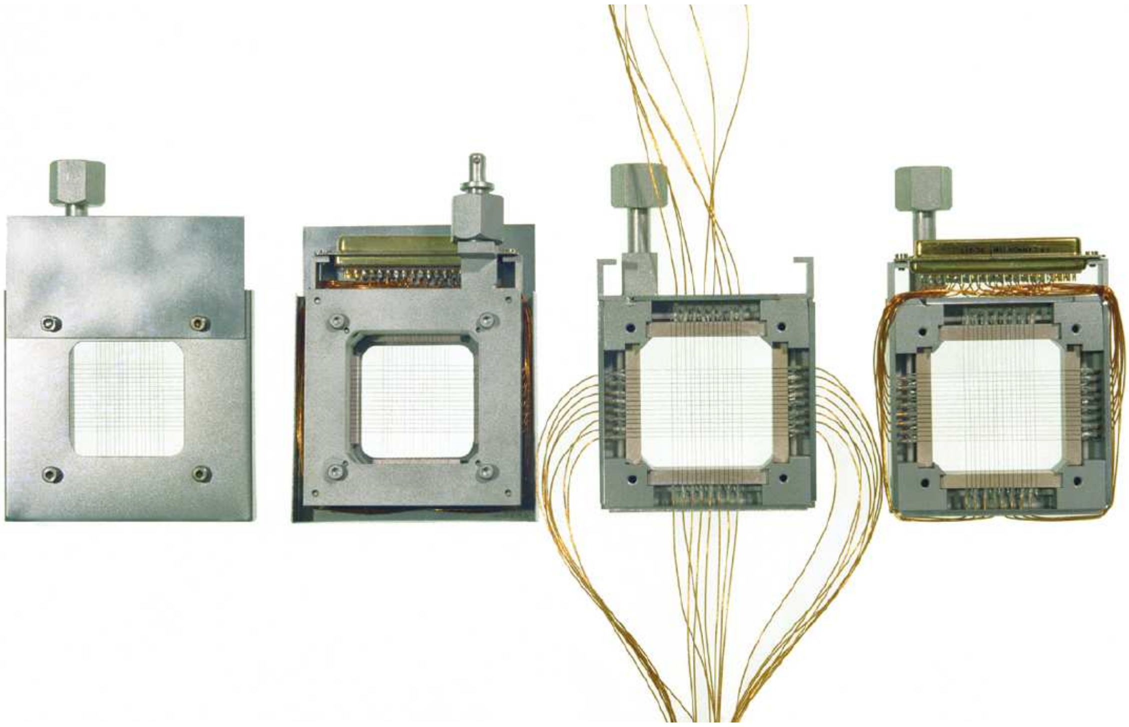

Figure 3.5: Profile grid for both planes with 15 wires spaced by 1.5 mm each in a different steps of the manufacturing. The individual wires are insulated with glass-ceramics. The device is mounted on a pneumatic feed-through to move it in and out of the beam (not shown).

Diameter of the wires	0.05 to 0.5 mm
Spacing	0.5 to 2 mm
Length	50 to 100 mm
Material	W or W-Re alloy
Insulation of the frame	glass or Al_2O_3
number of wires	10 to 100
Max. power rating in vacuum	1 W/mm
Min. sensitivity of I/U-conv.	1 nA/V
Dynamic range	1:10^6
Number of ranges	10 typ.
Integration time	1 μs to 1 s

Table 3.2: Typical specification for a profile grid used at proton and heavy ion LINACs.

For low energies at proton or heavy ion LINACs the particles are stopped in the material or undergo a significant energy loss. The ratio diameter-to-spacing of the wires determines the attenuation of the beam current (and of course also the signal strength on the individual wires). Typically only 10 % of the beam area is covered by the wires and in this sense the profile measurement is nearly non-destructive. For energies above 1 GeV/u the relative energy loss is negligible and large size ribbons are used. A typical example of the SEM-grid measurement used for beam optimization is shown in Fig. 3.6 for a transfer line.

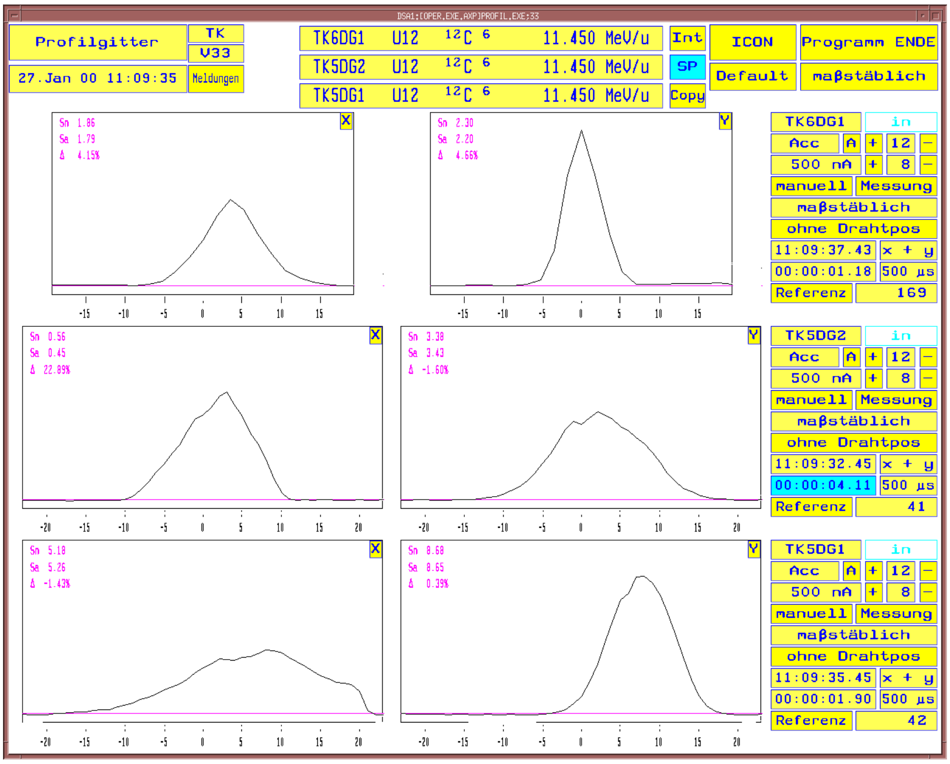

Figure 3.6: The measured profiles of SEM grids in one transfer line at the GSI heavy ion LINAC, displaying the horizontal profile left and the vertical right in mm.

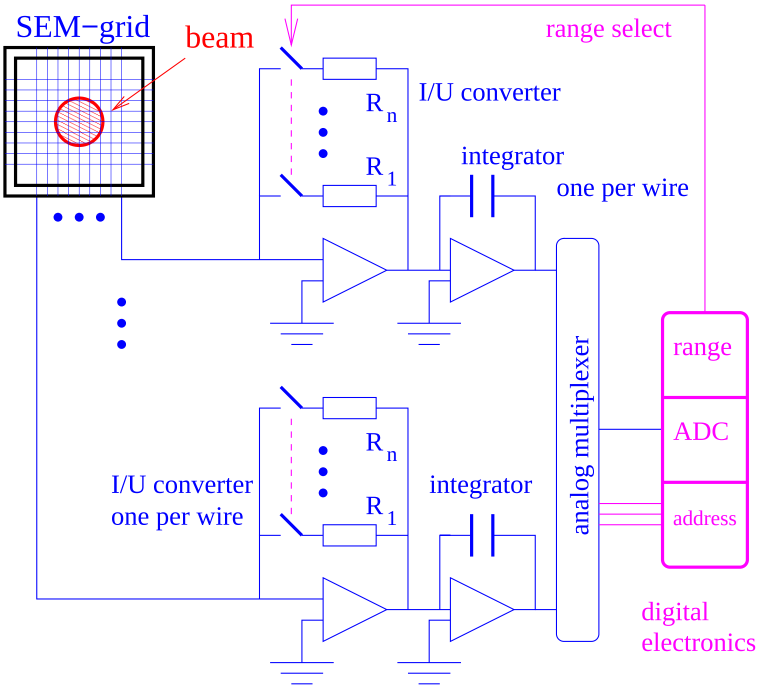

Figure 3.7: Typical analog signal processing for a SEM-grid.

Each wire has a individual pre-amplifier, in most cases an I/U converter, followed by a sample-and-hold circuit, see Fig. 3.7. These electronics have to be installed close to the accelerator hardware. With a multiplexer, the analog values are transported to an ADC located outside of the accelerator tunnel. Readout of a full SEM-grid in less than a ms is typical for the use of pulsed or dc beams.

Application: Betatron mismatch for synchrotron injection

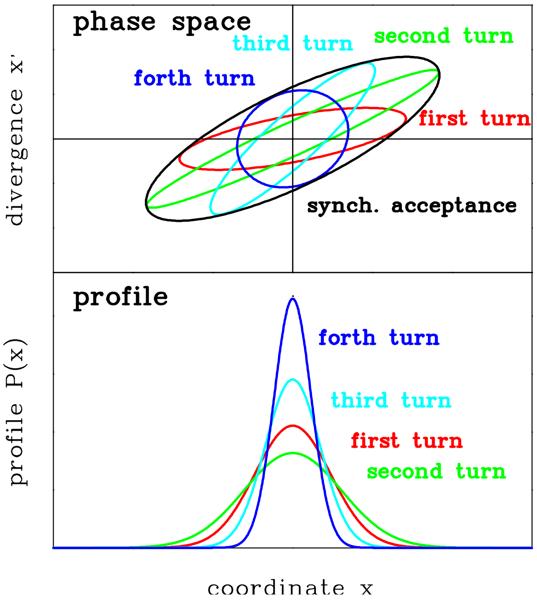

Figure 3.8: Schematics for the betatron mismatched injection into a synchrotron. If the orientation of the injected beam emittance does not fit the acceptance, variations of the beam profile occur.

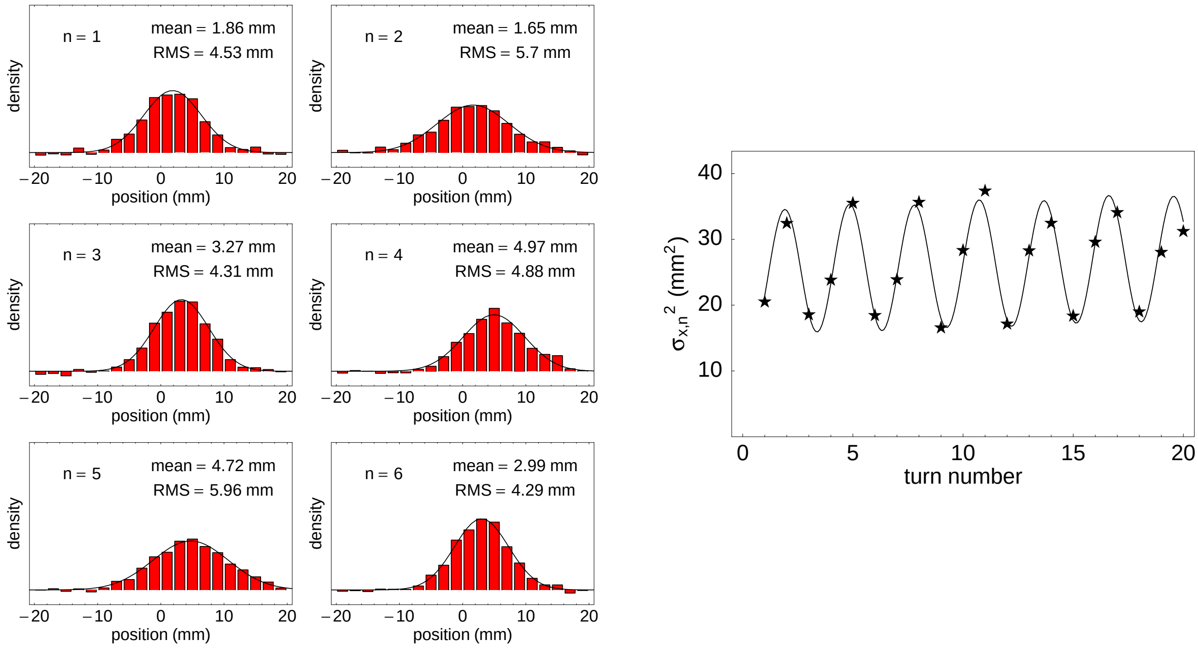

Figure 3.9: Profile measurement for a mismatched injection into the CERN PS synchrotron for the first $n = 1...6$ turns and the fitted square of the beam width as a function of time, from [33].

An interesting application for a profile measurement is the control of the injection into a synchrotron. If the orientation of the injected beam emittance is wrong due to a misaligned focusing, beam storage is still possible. But then the emittance ellipse starts to rotate with an angle per revolution as given by the fractional part q of the tune Q of the synchrotron as shown in Fig. 3.8. A rotating ellipse is equivalent to a variation in the beam profile from turn to turn. After several hundred turns, the full synchrotron acceptance is filled due to the de-coherence of the single particle phases, leading to a larger circulating beam and an emittance blow-up. The mismatch can be determined by recording the profile width on a turn-by-turn basis. An example is shown in Fig. 3.9 for a proton injection into the CERN PS synchrotron with 1.4 GeV energy and a bunch length of 80 ns [33, 34]. The revolution period is 2.2 μs. Thin SEM grids are used and the data are digitized each revolution of the short bunch. The energy loss of the protons in the wires is too low to influence this measurement during only a few turns. The oscillation of the profile width is seen and the fitted Gaussian width is plotted as a function of the turn number. It results in a blow-up of the stored emittance by ~ 10 %. A better injection is created by changing the setting of the quadrupole magnets in the transfer line.

3.3 Wire scanner

Instead of using several wires with individual, expensive electronics, a single wire can be swept through the beam[26]. The advantage is that the resolution is not limited by the wire spacing and therefore this technique is often used at electron accelerators with beam sizes in the sub-mm range. It can also be applied in proton synchrotrons due to the small amount of intercepting matter.

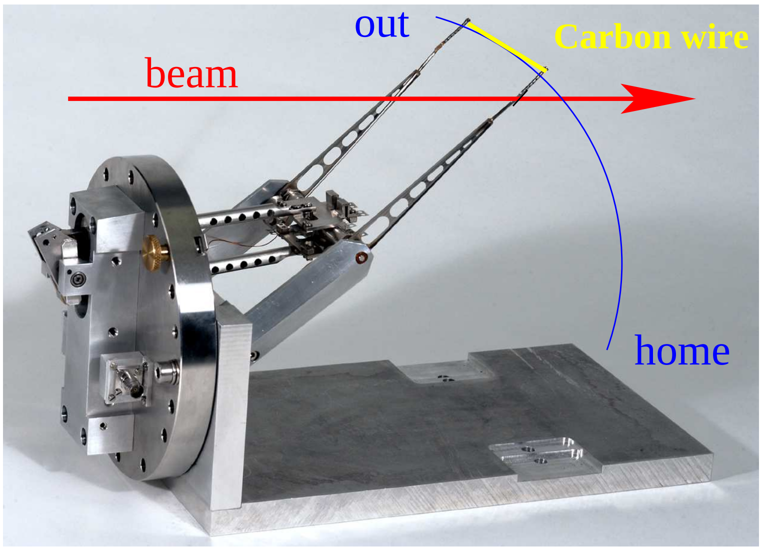

Figure 3.10: Pendulum scanner or 'flying wire' used at CERN synchrotron [27].

An arrangement with a straight wire on a fast pendulum mechanics in shown in Fig. 3.10, from [27, 28]. Scanning velocities up to 10 m/s can be achieved with a special pneumatic mechanism. Sometimes this setup is also called flying wire. As the wire material, carbon or SiC is used due to its low weight and low nuclear charge Z, resulting in a low energy deposition in the wire (Bethe-Bloch Eq. 2.20 gives $dE/dx \propto \rho \cdot Z/A$). In addition, these materials can withstand high temperatures without melting. The thickness can be down to 10 μm. But due to the scanned single wire the profile is not taken at a single instant, even with high scanning velocity. Therefore only the steady state distribution can be probed.

For the display of the profile, the position of the wire, determined by the position encoder, is plotted on the horizontal axis. The beam signal for the vertical axis can be deduced from the current given by the emitted secondary electrons, like for a SEM-grid. This is done in particular for low energy protons and heavy ions. In most cases for beam energies larger than 150 MeV/u for ions (the threshold for π-meson production) or 10 MeV for electrons the signal is deduced by monitoring the secondary particles outside of the beam pipe, see Fig. 3.11. These secondaries might be hadrons created by the nuclear interaction of the proton or heavy ion projectiles and the wire, having enough kinetic energy to leave the vacuum chamber. For the case of electron accelerators, the secondaries are mainly Bremsstrahlung-photons. The detector is just a type of well suited beam loss monitor, e.g. a scintillator installed several meters away (see also Chapter 8). The count-rate is plotted as a function of the wire position as a precise representation of the beam profile.

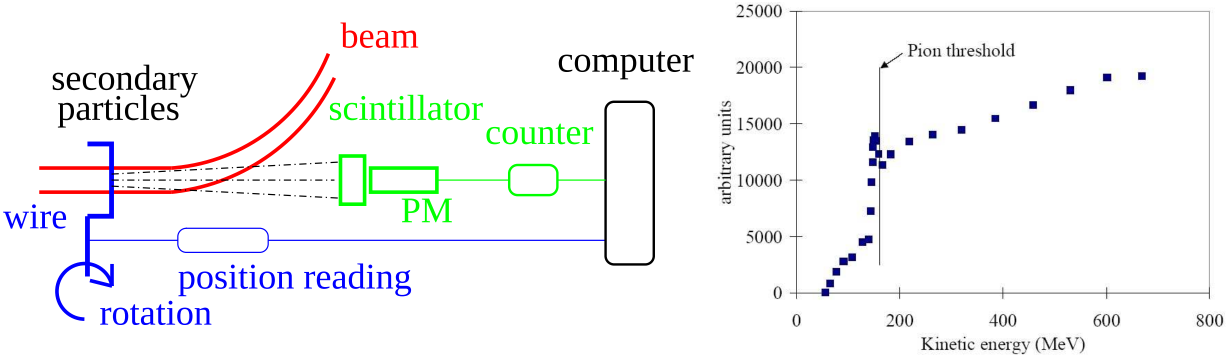

Figure 3.11: Left: Scheme of a wire scanner using the production of secondary particles as the signal source. Right: The total rate from a wire scanner under proton impact at CERN PS-Booster, showing the rate increase above the π-threshold at ~ 150 MeV, from [29].

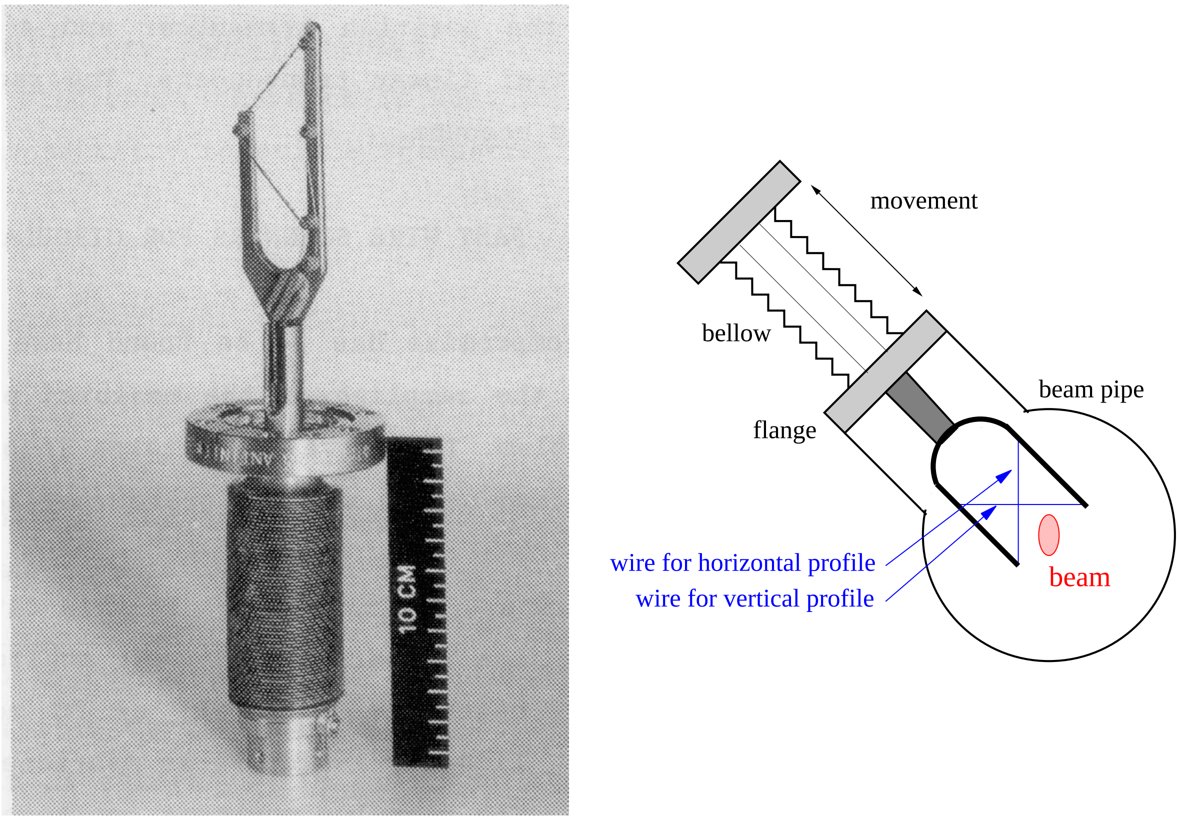

Figure 3.12: Linear scanner used at CERN [30].

For the fast movement, vibration of the wire restricts the orbital resolution. A much higher precision can be achieved with a much slower movement of, for example, only 0.1 m/s with a linear feed-through as shown in Fig. 3.12 [30]. With these types a resolution of 1 μm is reached in electron accelerators [31]. To get this low beam width σ_{beam}, a deconvolution of the contribution of the wire (4μm thick carbon wire in this case) from the measured width σ_{meas} has to be done according to

$$\sigma^2_{beam} = \sigma^2_{meas} - 4 \cdot r^2_{wire} \quad . \tag{3.2}$$

In most cases, the wire is mounted on a fork, which is inserted into the beam pass by a feed-through mounted on 45^o. Then only one feed-trough is sufficient for measuring both transverse planes by mounting the wires in a crossed orientation, as shown in Fig. 3.12. If the signal generation is performed by reading the secondary emission current than two isolated wires can be mounted in a compact manner. If the signal is generated by beam loss monitors outside the beam pipe, the two wires have to separated (as shown in the Fig. 3.12 left), so the wires cross the beam one after the other.

A comparison of the wire scanner and the SEM-grid shows the advantages and disadvantages of both types [26]:

- With a SEM-grid the beam intensity is sampled concurrently, whereas a moving wire samples the parts of the profile at different locations at different times. Therefore variations of the beam intensity in time will be mixed with transverse intensity variations using a scanning device.
- In case of pulsed beams further complications may arise from the demand for exact synchronization, which can be solved without any problems in case of SEM-grid application.
- The resolution of a SEM-grid is fixed by the wire spacing (typically 1 mm), while a wire scanner can can have much higher resolution, down to 10 μm, due to its constant movement. (For high resolution mechanical vibration has to be avoided.)
- The electronics for data acquisition is cheaper for a scanning system. A SEM-grid requires one channel per wire.
- For the cost of the mechanics it is vice versa: The precise vacuum actuator for the scanner is more expensive than the pneumatic feed-trough needed for a SEM-grid.

3.4 Multi-wire proportional chamber MWPC

For slowly extracted beams from a synchrotron, the current is much too low to be measured by a SEM-grid. One can use the amplification of electrons in a gas as done in a **M**ulti-**W**ire **P**roportional **C**hamber **MWPC**. For the principle of operation see e.g. [11]. As discussed for the ionization chamber for current measurements in Chapter 2.7.2, the primary particles traverse a gas (like 90 % Ar mixed with 10 % CH_4 or CO_2), creating secondary electrons. A MWPC consists of a grid held at a high voltage, typically several kV, and a grounded grid, which is read by a charge-sensitive pre-amplifier, like for SEM-grids. The distance between the anode and the cathode plane is typically 1 cm and the spacing of the wires about 1 mm. The principle is shown in Fig. 3.13. Close to the anode wires, having typically 25 μm diameter, the electrical field increases with $\propto 1/r$, see Fig. 3.14. After reaching a threshold, the energy of the electrons accelerated toward the wires is high enough to knock out additional electrons from the gas atom/molecules. This gives rise to an avalanche, which results in a $\sim 10^4$ amplification of the number of electrons. This amplification inside the detector volume is nearly noise free due to the electrically spoken high source impedance of the free charge carriers. The resulting low noise could not be achieved by an electric amplifier due to its thermal noise. The following electronics (further amplifier and ADC) and the way of displaying is comparable to the procedure for SEM-grids.

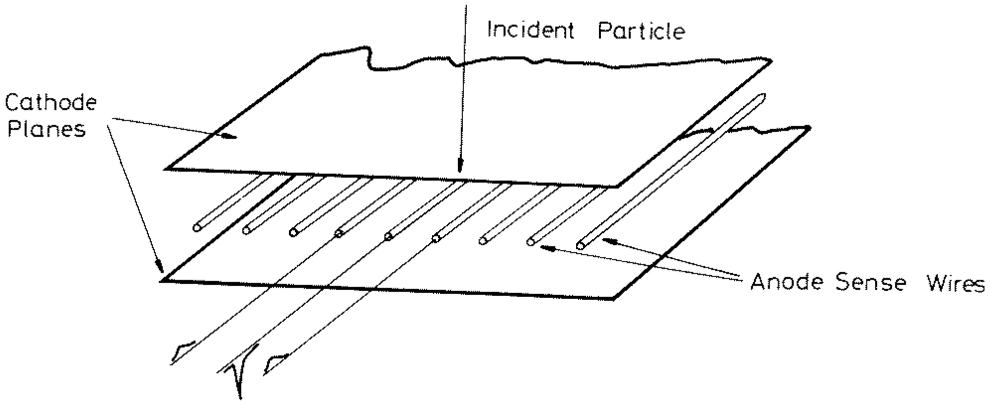

Figure 3.13: The scheme of a MWPC for one plane showing the type of signal generating by a particle interaction.

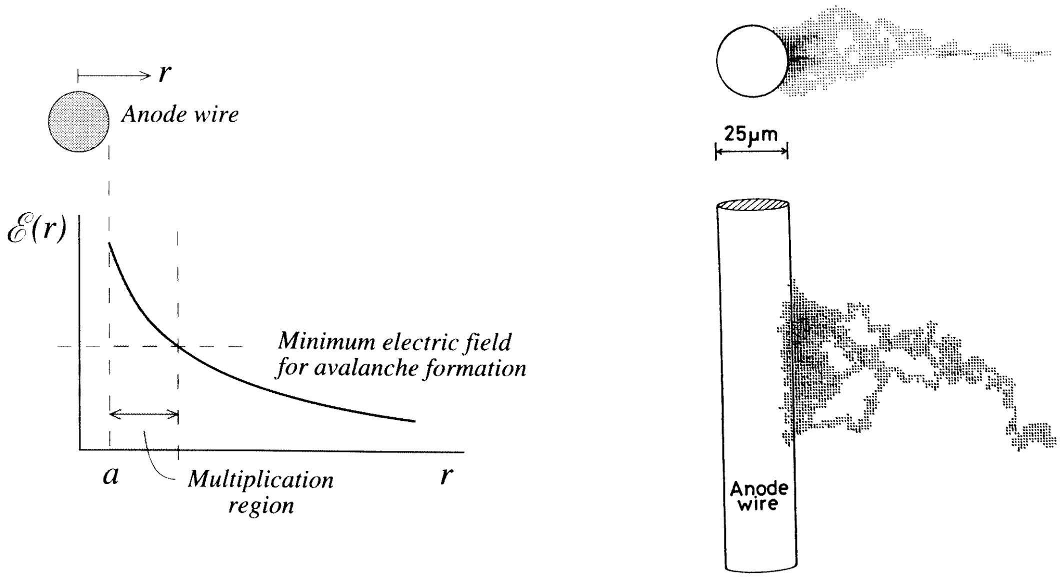

Figure 3.14: The electric field close to the anode wires with the region of amplification indicated (left). A Monte-Carlo simulation shows the concentration of the electron avalanche by the gray shading (right), from [32].

3.5 Residual gas monitor

A frequently used non-destructive method for the profile determination is the **R**esidual **G**as **M**onitor **RGM**; it is sometimes also called **I**onization **P**rofile **M**onitor **IPM**. These are installed in nearly every proton/heavy ion synchrotron for the detection of beam sizes between some mm and several cm, a review is given in [35]. For electron synchrotrons, they are not used so often, due to the smaller electron beam dimensions. The idea is to detect the ionized products from a collision of the beam particles with the residual gas atoms or molecules present in the vacuum pipe. Typical pressures for LINACs and transfer lines are in the range $10^{-8} - 10^{-6}$ mbar containing mainly N_2 and O_2 and for synchrotrons $10^{-11} - 10^{-9}$ mbar containing mainly H_2. The different compositions are due to the different vacuum pumps used. A scheme for such a monitor is shown in Fig. 3.16. Due to electronic stopping, electrons are liberated and electron-ion pairs are generated. An estimation of the signal strength can be obtained by Bethe-Bloch formula.

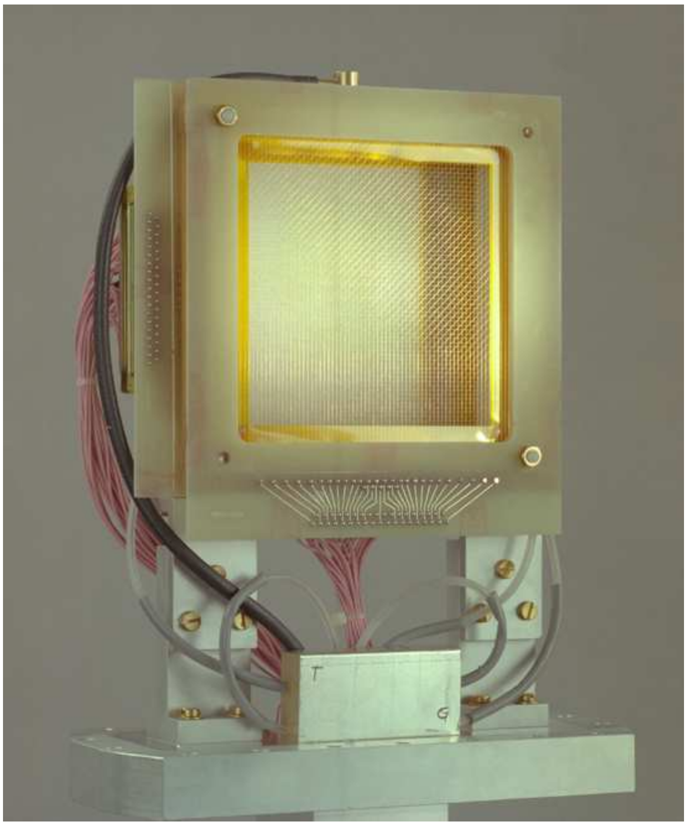

Figure 3.15: The MWPC used for profile measurement of slowly extracted ion beams at the GSI.

But due to the single collision behavior, W-values (see Chapter 2.7.2) are only a first order approximation for the conversion of the energy loss to the numbers of secondaries. To separate the electron-ion pairs, an external electric field is applied of the order of 1 kV/cm by metallic plates installed in the vacuum pipe, but outside the beam path. To get a more homogeneous field, guide strips are installed at the side to get a smooth transition from the HV side to the ground plane. Normally the residual gas ions are detected in this setup. A realization from the GSI synchrotron is shown in Fig. 3.16 having a large opening of 17 cm [36].

For the LINAC case, the vacuum pressure is high and the energy loss is larger due to the lower beam energy. Enough electron-ion pairs are generated to give a measurable current (down to 0.1 nA per strip) of secondary ions for direct detection by a sensitive SEM-grid like wire array [37]. In a synchrotron the pressure and the stopping power is lower. A multi channel plate (MCP) particle detector is used as a 'pre-amp'. A MCP is made of a 1 mm thick glass plate with round channels of ~ 10 μm, see Fig. 3.17. These channels are coated with high resistivity materials and a voltage of $\sim$ 1kV is applied across them. When a residual gas ion (or electron) hits the surface, secondary electrons are liberated, i.e., the ions are converted to electrons. These electrons are multiplied like in a photo-multiplier by a factor of typically 10^3 per MCP. Due to the diameter of the channels, the spatial resolution of a single step MCP is in the order of 0.03 mm. For higher amplifications a two step device (s.c. Chevron geometry) with a gain of $\sim 10^6$ is used resulting in a resolution of about 0.1 mm.

For the detection of the secondary electrons at the MCP output, three types of anodes can be used:

- A SEM-grid made of wires with $\sim$ 0.5 mm diameter and 1 mm spacing. The advantage is the fast readout possibly using appropriate electronics [38]. The disadvantage is the

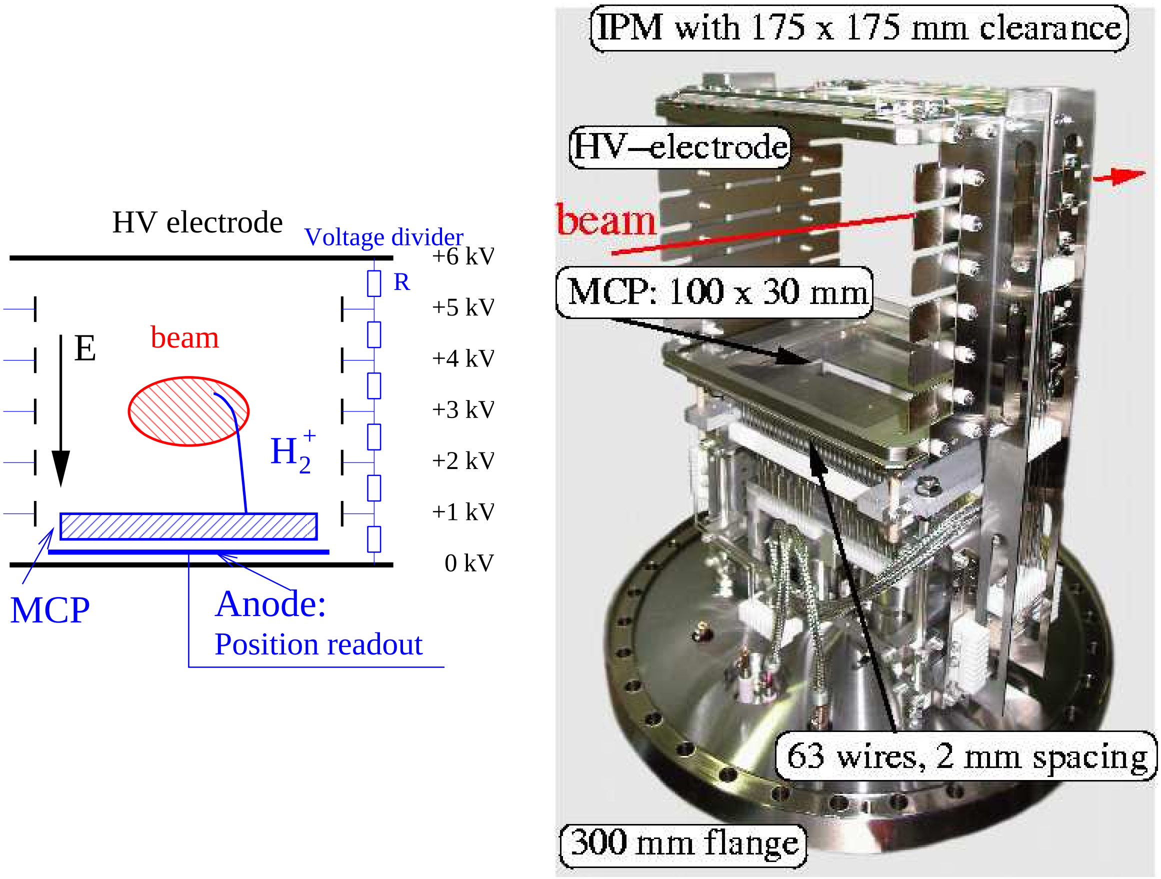

Figure 3.16: *Left:* Scheme of a residual gas monitor for the horizontal profile determination. *Right:* The large aperture residual gas monitor installed at the GSI synchrotron for the horizontal direction, the clearance is 175×175 mm^2. The monitor is mounted on a Ø 300 mm flange. The read-out behind the MCP (bottom) is done with an array of 63 wires with 2 mm spacing.

limited spatial resolution.

- An anode type using particle detection schemes, like wedge and strip anodes or resistive anodes, see e.g. [39]. It is based on the detection of single particles, leading to the advantage that the resolution can be improved by collecting data with high statistics up to the spatial resolution limit of the MCP.

- A phosphor screen installed close to the MCP back side. The secondary electrons create a light pulse, which is imaged by a CCD camera. The advantage is the high resolution due to several hundreds of pixels for one plane and the cheap and direct data acquisition system supplied by the commercial CCD camera. But with this technique the time resolution and the image repetition rate is limited by the CCD camera frame-rate of about 100 frames per second. For faster readout the CCD is replaced by a photo-multiplier or avalanche diode, e.g. [40].

During the acceleration of a beam inside a synchrotron, the beam width should shrink. This is related to the fact that the emittance is defined in the lab-frame by the angle between the transverse- and longitudinal velocity. During acceleration, the longitudinal velocity increases (for the non-relativistic case), while the transverse component remains. Therefore the angle between both decreases. This is called transverse adiabatic damping by the conservation of the normalized emittance, see also the discussion for Eq. 4.18. In Fig. 3.18 this decrease of

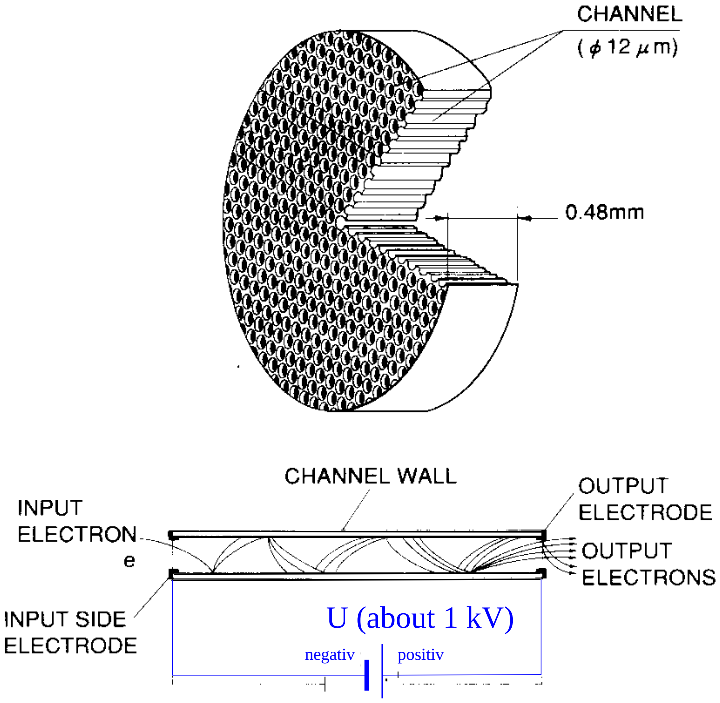

Figure 3.17: Scheme of a single MCP made of a glass plate with small channels, where the amplification of the secondary electrons takes place.

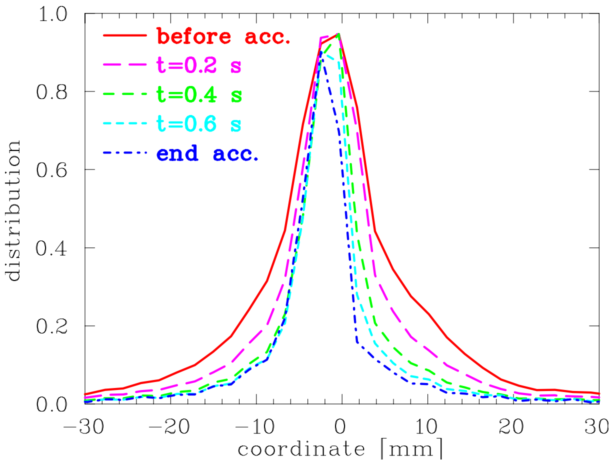

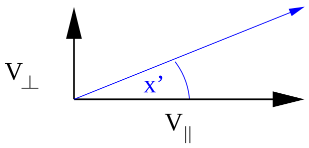

Figure 3.18: The evolution of the beam profile during the acceleration of U^{73+} from 11 MeV/u to 500 MeV/u within 0.8 s at the GSI synchrotron.

the beam width is demonstrated for the acceleration of an U^{73+} ion beam from 11 MeV/u, corresponding to $\beta = 15\%$ to 500 MeV/u, corresponding to $\beta = 75\%$. A residual gas monitor is a non-intercepting device, well suited for long-time observation without any influence on the beam.

Application: Transverse cooling

An example for the importance of a profile measurement is shown in Fig. 3.19 at the GSI synchrotron, where beam cooling is applied. Cooling is often used to get a high brilliance beam by a shrinkage of the transverse emittance and momentum distribution. This is important for high resolution experiments or for the increase of the number of stored particles using so called stacking methods. This is performed by electron cooling (see e.g. [42]) or stochastic cooling (see e.g. [43]). In Fig. 3.19 the effect of transverse cooling is clearly seen.

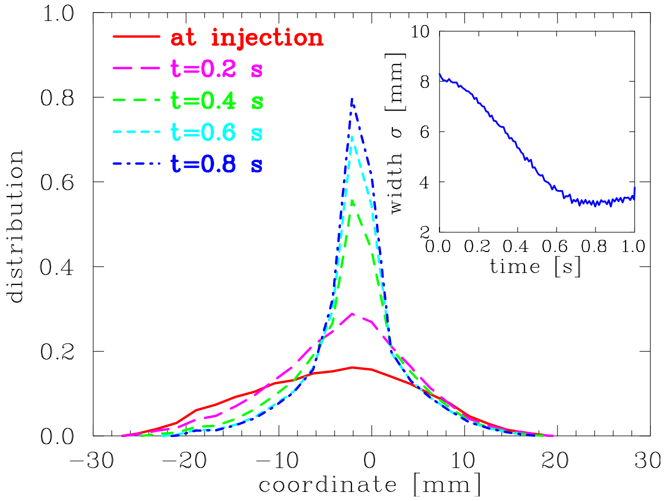

Figure 3.19: The profile during an electron cooling cooling process for an 11 MeV/u Ar^{18+} beam at the GSI synchrotron. Five profiles from the injection (broad peak bottom) to the maximal cooled profile recorded at different time during the cycle. The inlet shows the standard deviation of the profile as a function of time.

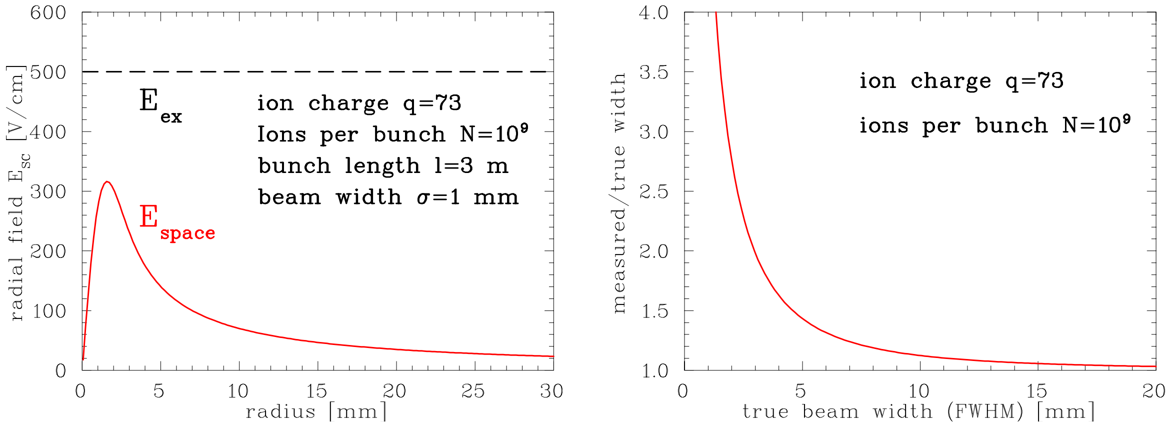

Figure 3.20: Model calculation of the beam broadening due to the space charge field of a U^{73+} with 10^9 particles per 3 m bunch length (left). The resulting relative broadening using a residual gas monitor with ion detection (right) is plotted for this current. The parameters are valid for an intense, cooled ion beam.

Ion detection: Resolution limit by the beam's space charge

The residual gas ions or electrons are accelerated toward the detector with an external electrical field. But the beam, made of charged particles, also carries an electrical field, the space charge field, which influences the trajectory in addition. The radial electrical field E_{space} of a round beam is given non-relativistically for a Gaussian distribution with standard deviation σ (FWHM=$2.35 \cdot \sigma$) by

$$E_{space}(r) = \frac{1}{2\pi\epsilon_0} \cdot \frac{qeN}{l} \cdot \frac{1}{r}\left(1 - e^{r^2/\sigma^2}\right). \tag{3.3}$$

The field is radially symmetric in this case. qeN/l is the number of particles in charge state q per unit length. For high current operation this field strength is comparable to the external field, see Fig. 3.20. The residual gas ions or electrons are accelerated by both fields, leading to a broadening of the measured profile, see Fig. 3.21. To get an estimation of the real beam size, the correction can be calculated via

$$\sigma_{beam}^2 = \sigma_{meas}^2 - \sigma_{corr}^2. \tag{3.4}$$

σ_{corr} is given in a first order approximation by the beam space charge and the external field according to

$$\sigma_{corr}^2 = \frac{e^2 \ln 2}{4\pi\epsilon_0 \sqrt{m_p c^2}} \cdot d_{gap} \cdot qN \cdot \sqrt{\frac{1}{eU_{ex}}}. \tag{3.5}$$

The correction is proportional to the number of particles N. It is inversely proportional to the square root of the external field (created by the static voltage U_{ex}) and therefore an increase of the external field has only a relatively weak influence on the broadening. A large distance d_{gap} between the two high voltage electrode results in a longer drift time and therefore in a prolonged influence of the space charge field. To calculate this correction for a real case, the beam has to have a Gaussian distribution or a self-consistent algorithm has to be used.

The initial velocity of the ions right after the ionizing atomic collision between the residual gas molecule and the beam particle is too low to affect the resolution (in contradiction to the electron detection scheme, see below). For electronic stopping collisions (Bethe-Bloch regime) the momentum transfer to the nucleus is quite small.

Electron detection in the presence of a magnetic field

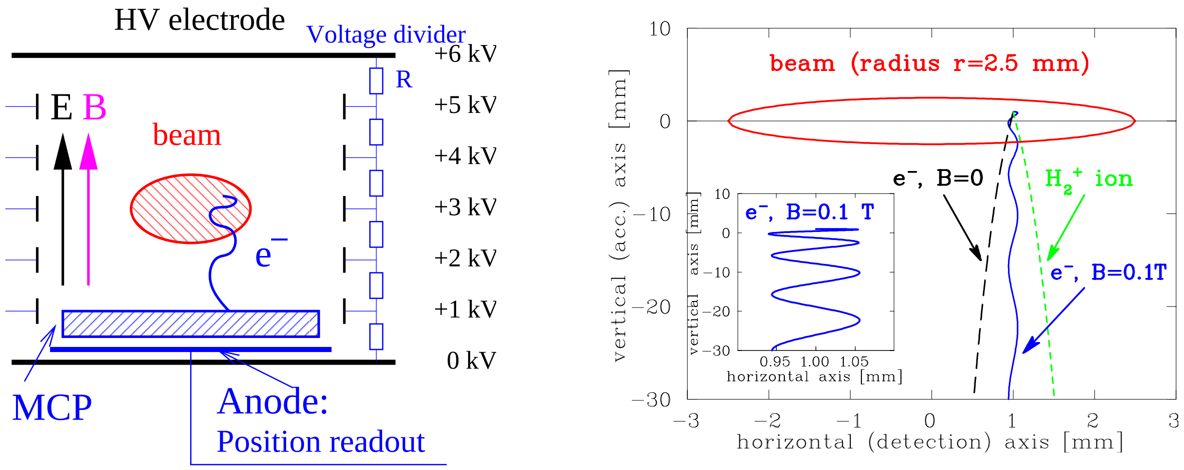

Figure 3.21: Schematic trajectory of an electron in a residual gas monitor with an additional magnetic field on the right. The comparison of the trajectories of an H_2^+-ion and an electron with and without a magnetic field on the left visualize the broadening due to the beam space charge field. By applying a magnetic field the electron is fixed to the field line, as shown in the insert. The beam parameters are: 10^9 U^{73+} in a 10 m long bunch with radius 2.5 mm.

For the measurement of intense beams, detection of electrons is more suited to overcome the space charge induced broadening, see Fig. 3.21. For this the HV is reversed, to accelerate now the negative electrons created by the beam interaction toward the detector. If an additional magnetic field B is applied parallel to the external electrical field, the electrons spiral around the magnetic field lines with the cyclotron radius $r_c = \sqrt{2m_e E_{kin}}/eB$ with E_{kin} being the kinetic energy fraction perpendicular to the field. This transverse kinetic energy is determined by the initial transverse velocity given by the kinematics of the atomic collision. The cross sections depends on the beam and residual gas molecule properties [44], resulting in kinetic energies for the emitted electron up to keV for the typical case. The cyclotron radius, and therefore the detector resolution, is mainly determined by this initial energy and is nearly independent of the beam space charge field. The projection of the trajectory in the plane perpendicular to the field is a circle with less than 0.1 mm radius (corresponding to the spatial resolution of the MCP) if a magnetic field of $B \simeq 0.1$ T is applied. The movement along the field is a linear acceleration with a typical time of flight of ~ 2 ns. The necessary magnetic field of about 0.1 T is generated in most cases with a dipole magnet of the same type as used for the beam bending, see e.g. [40].

3.6 Beam induced fluorescence monitor

By the collision of the beam particles with the residual gas, the molecules are not only ionized, but also excitation of internal energy levels can occur. The excitations decay electro-magnetically by light emission leading to fluorescence [45]. In particular, the excitation of N_2 results in a transition bands in the optical region. The band is originated by the decay of molecular ions N_2^+ excited by the collision with the beam ions in the wavelength range 390 nm $< \lambda <$ 470 nm, i.e., in the near UV to blue color. The lifetime is in the range of 60 ns (depending on the involved upper and lower molecular state). About 1 % of the energy loss in N_2 gas is converted to the optical wavelength interval [46]. The general scheme of a **B**eam **I**nduced **F**luorescence monitor (**BIF**) is shown in Fig. 3.22 and reviewed in [35].

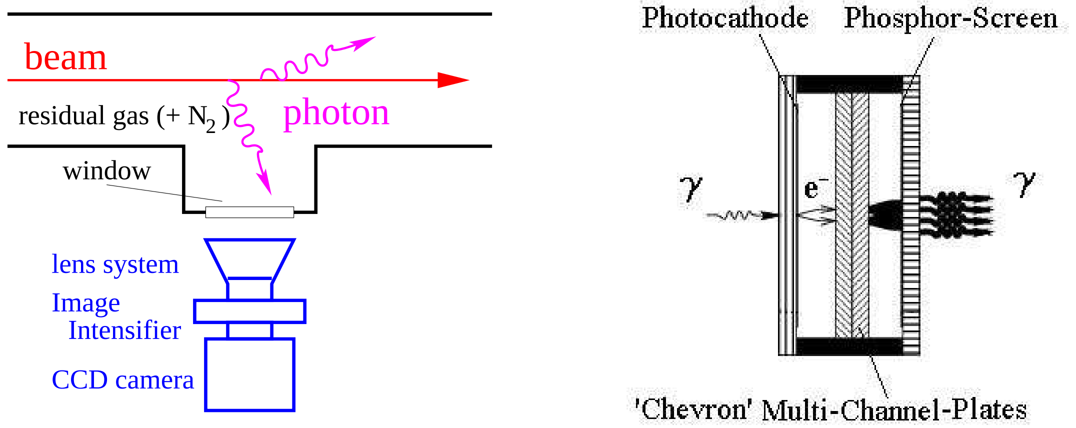

Figure 3.22: Left: General scheme of the profile determination via detection of the residual gas fluorescence. Right: Scheme of an image intensifier consisting a photo-cathode, a MCP and a phosphor screen.

In LINACs the most prominent vacuum constituent is N_2; if the signal strength is not large enough, a pressure bump of N_2 gas can be injected in the vacuum pipe with the help of a regulated gas valve. The fluorescence can be monitored by an image amplified CCD camera [47]. The advantage of this non-intercepting method is, that nothing has to be installed in the vacuum pipe and the commercially available CCD data acquisition can be used. The rate of photons N_{photon} for the detected light is given by

$$N_{photon} \propto \frac{dE}{ds} \Delta s \cdot p \cdot \frac{f}{h\nu} \cdot \frac{\Omega}{4\pi} \cdot \frac{I_{beam}}{qe} \tag{3.6}$$

where $\frac{dE}{ds}\Delta s$ is the energy loss of ions with charge state q in N_2 for an observation length s and the pressure p, $f \sim 1$ % the fraction of the light conversion to $h\nu$ and Ω the solid angle

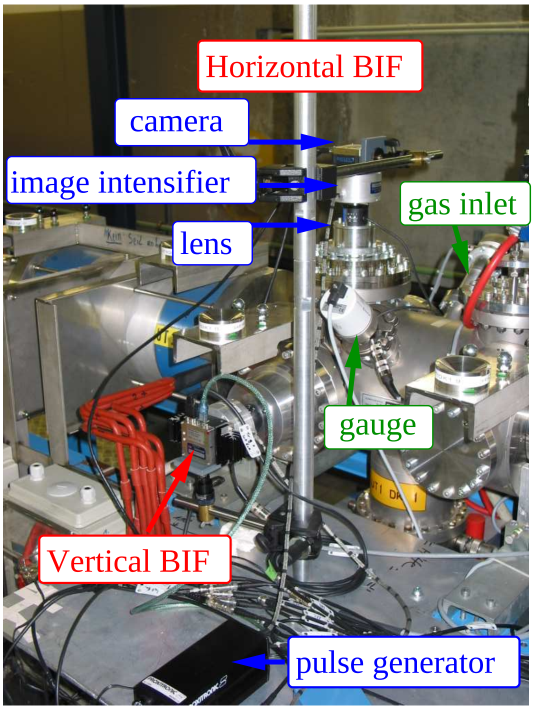

Figure 3.23: The installation of the BIF monitors at the GSI-LINAC consisting of two intensified cameras for the horizontal and vertical profile measurement, respectively.

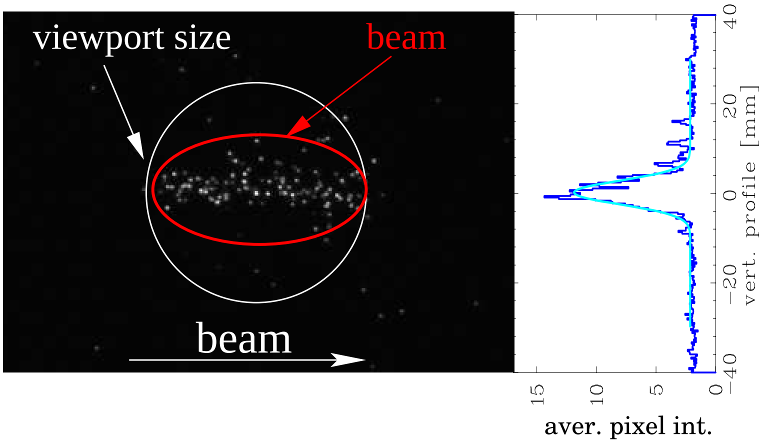

Figure 3.24: Image of a 250 μs Ar^{10+} beam of $I_{beam} = 2.5$ mA and a vacuum pressure of 10^{-5} mbar recorded at the GSI LINAC. The original image (recorded with a double MCP intensifier) is shown and the projection for the vertical profile [47].

converted by the CCD. In the image intensifier (see Fig. 3.22) the photons hit a photo-cathode and with a probability of about 20 %, electrons are created. Low noise photo-cathode materials are available having a matched wavelength sensitivity. The electrons are accelerated toward a MCP and amplified by a factor of maximally 10^6 as described above. A phosphor screen, with decay time of 100 ns converts the electrons back to photons, which are then imaged by the CCD camera via relay optics or fibers. The total conversion efficiency can be up to 15%, i.e. 15% of the arriving photons are visible as a light-spots in the image. An example is shown in Fig. 3.24 recorded at the pulsed LINAC at GSI with a Ar-beam. Single photon spots are visible on the image, but the projection along the longitudinal direction shows a profile with sufficient statistics [47]. The method is also applied for higher energy at CERN SPS [48].

3.7 Optical transition radiation screens

At electron accelerators, as well as at high energy proton synchrotrons, like the CERN SPS, the profile is determined from the electro-magnetic radiation at an intercepting thin metallic foil by the so called **O**ptical **T**ransition **R**adiation **OTR**. The OTR is a pure classical electrodynamic process including special relativity, as produced by a charged particle passes from one medium into another. At the vacuum in front of the foil, the particle has a certain electro-magnetic field configuration, which is different from the field inside the medium, because the foil has a (complex) dielectric constant different from vacuum. By approaching the foil, the particle's electro-magnetic field leads to a time-dependent polarization at the foil boundary. The change of this polarization emits the radiation, which combines coherently from different points at the foil to a characteristic intensity and angular distribution.

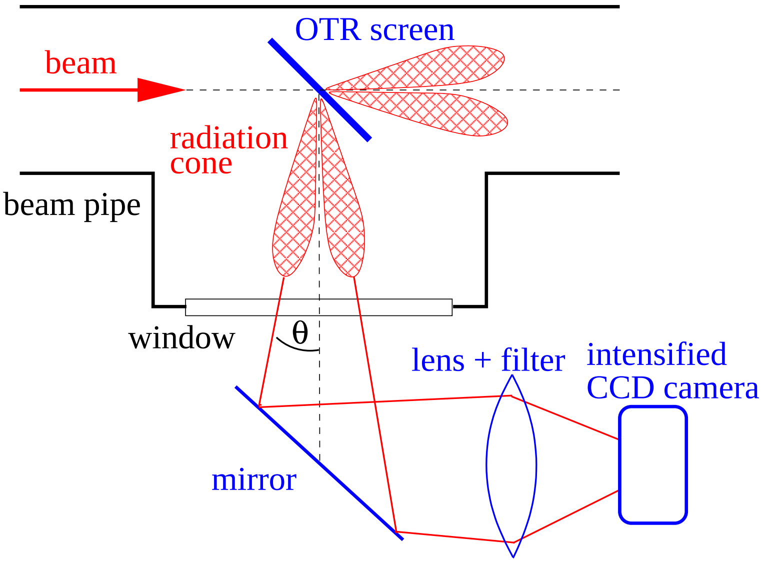

Figure 3.25: The scheme of an OTR screen measurement.

A typical setup of an OTR measurement is shown in Fig. 3.25. The foil is inserted under 45^o with respect to the beam path in most cases. The foil is made of Aluminum or Aluminum coated on Mylar with a thickness 1 μm or less. The light is emitted in the forward direction as well as at 90^o, because the metallic surface acts as a mirror. Depending on the particle energy, the angular distribution is peaked at the angle $\theta = 1/\gamma$ with γ the relativistic Lorentz factor, see below. For typical values, 100 to 1000 beam particles yield 1 photon in the optical wavelength range. With appropriate optics, an image of the foil is recorded with a CCD camera. In most cases an image amplified CCD device is used due to the relatively low number of photons.

The general process is treated in e.g. [12, 49, 50] leading to closed form, but extensive formulas. For relativistic beam particles and some other valid assumptions, the radiated energy dW into a solid angle $d\Omega$ per frequency interval $d\omega$ can be approximated by

$$\frac{d^2W}{d\Omega d\omega} = \frac{\mu_0 ce^2}{4\pi^3} \cdot \frac{\theta^2}{\left(\gamma^{-2} + \theta^2\right)^2} \tag{3.7}$$

with μ_0, c, e, γ are the permeability of the vacuum, the velocity of light, the elementary charge and the relativistic Lorentz factor, respectively. The observation is done at an angle θ perpendicular to the beam path, the so called specular angle, see Fig. 3.25. There is no difference of the radiated energy for electrons or protons, reflecting the fact that only the electro-magnetic fields of the beam particles are concerned. Note that the radiated energy doesn't depend on the frequency ω, i.e., the whole spectrum in covered. This is valid up to the plasma frequency of the metal, which is for most metals in the deep UV at about 10 eV. For higher photon energies than 10 eV, the behavior of the metal is not longer described by classical electrodynamics. The radiated energy of Eq. 3.7 is converted to the number of photons by $W = N_{photon} \cdot \hbar\omega$ observed within a wavelength interval from λ_{begin} to λ_{end} in the optical region by the CCD camera, yielding the number of photons per solid angle

$$\frac{dN_{photon}}{d\Omega} = N_{beam} \cdot \frac{\mu_0 c e^2}{4\hbar\pi^3} \cdot \log\left(\frac{\lambda_{begin}}{\lambda_{end}}\right) \cdot \frac{\theta^2}{(\gamma^{-2} + \theta^2)^2} \tag{3.8}$$

with N_{beam} is the number of beam particles. This function is plotted in Fig. 3.26 for three different values of γ. It is clearly seen that the radiation is more tightly focused for higher energies, having the advantage that a larger fraction of the photon reaches the CCD camera. For lower particle energies, like in most proton accelerators, the opening angle is too large for a practical application.

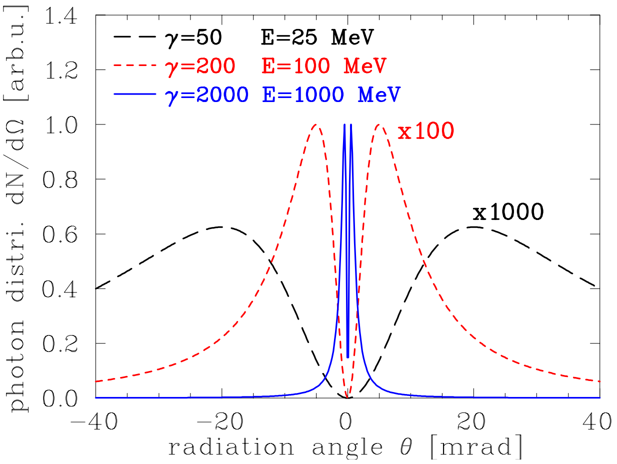

Figure 3.26: The intensity distribution of OTR as a function of the observation angle for three different value of γ. The corresponding beam energies for electrons are also given. The photon intensity is enhanced by a factor of 1000 for $\gamma = 50$ and 100 for $\gamma = 200$ in the plot.

The angular distribution in Eq. 3.8 is given for a single particle incidence. A real beam has an angle distribution for the beam particles, which have to be convolved to yield a realistic photon distribution. Assuming a Gaussian beam angular distribution with a standard deviation σ_{beam}, the photon angular distribution is modified by the convolution as

$$\frac{dN_{photon}}{d\Omega} = N_{beam} \cdot \frac{\mu_0 c e^2}{4\hbar\pi^3} \cdot \log\left(\frac{\lambda_{begin}}{\lambda_{end}}\right) \cdot \int_{-\infty}^{\infty} \frac{1}{2\pi\sigma_{beam}} \exp\left(\frac{-\theta'}{2\sigma_{beam}}\right)^2 \cdot \frac{(\theta-\theta')^2}{\left(\gamma^{-2} + (\theta-\theta')^2\right)^2} d\theta'. \tag{3.9}$$

This integral has to be evaluated numerically and can contribute significantly to the resolution for small beam sizes. In addition, the diffraction by the finite aperture of the optics can limit the resolution, as discussed e.g. in [51, 52].

For the profile observation, the focus of the CCD optics coincides with the OTR screen. For the measurement of the photon angular distribution, the focus is set to infinity. Using the latter setting, the angular distribution of the beam can be evaluated. Doing both types of measurements (focus on foils yield the profile, focus on infinity yield the beam angular distribution) a transverse emittance measurement can be performed, see e.g. [51]. Again, the Fraunhofer diffraction has to be taken int account, limiting the resolution of the emittance measurement.

The OTR profile determination has some advantages and disadvantages compared to a scintillating screen measurement [22]:

- It is based on a classical electrodynamic process, leading to a strict linearity between the number of photons and the beam intensity.
- The number of photons and their distribution is independent of the thickness of the foil. Therefore very thin foils down to 0.25 μm can be used. In most cases a pure Al foil or Al coated on Mylar is preferred.
- It is still an intercepting method, but a thin foil minimizes the influence on the beam due to the low scattering probability. It can be applied also at high beam power, because of the low energy loss in the thin, low Z material.
- A measurement of profile and beam angular distribution yield the emittance of the beam.
- It is mainly used for electron beams with energies above 100 MeV. For proton beams, the needed γ is only reached at the very high energy accelerators.
- The disadvantage is the contribution of the photon angular distribution in Eq. 3.8, which might limit the resolution. This is different for a scintillation screen, where an isotropic emission occurs and the diffraction starts to become important at much smaller beam sizes.
- The usable light of a OTR screen is orders of magnitude lower than for a scintillation screen. Therefore the more advanced and expensive techniques of image amplification have to be used.

3.8 Synchrotron radiation monitor

For electron accelerators, the effect of synchrotron radiation, emitted by accelerated electrons, can be used for a profile determination. As known from classical electrodynamics [12] the radiation power P_{synch} is given for a momentum change dp/dt of a particle with mass m_0 by

$$P_{synch} = \frac{e^2 c}{6\pi\varepsilon_0 (m_0 c^2)^2} \left[\frac{dp}{dt}\right]^2 . \tag{3.10}$$

For linear acceleration we have $dp/dt \sim dW/dx$. Taking typical values of $dW/dx = 15$ MeV/m for the energy gradient of a LINAC, we find that the radiated power is negligible. This is completely different in circular machines. Taking into account that $dp/dt = p \cdot v/R$ we obtain for the radiation power from a bending magnet

$$P_s = \frac{e^2 c}{6\pi\varepsilon_0 (m_0 c^2)^4} \frac{W^4}{R^2} . \tag{3.11}$$

For comparison of the radiation from electrons and protons for the same energy we have the ratio

$$\frac{P_{synch}^{electrons}}{P_{synch}^{protons}} = \left[\frac{931 MeV}{511 keV}\right]^4 \approx 10^{13} , \tag{3.12}$$

which means, that the power radiated by electrons is 10^{13} time higher than for protons of the same energy.

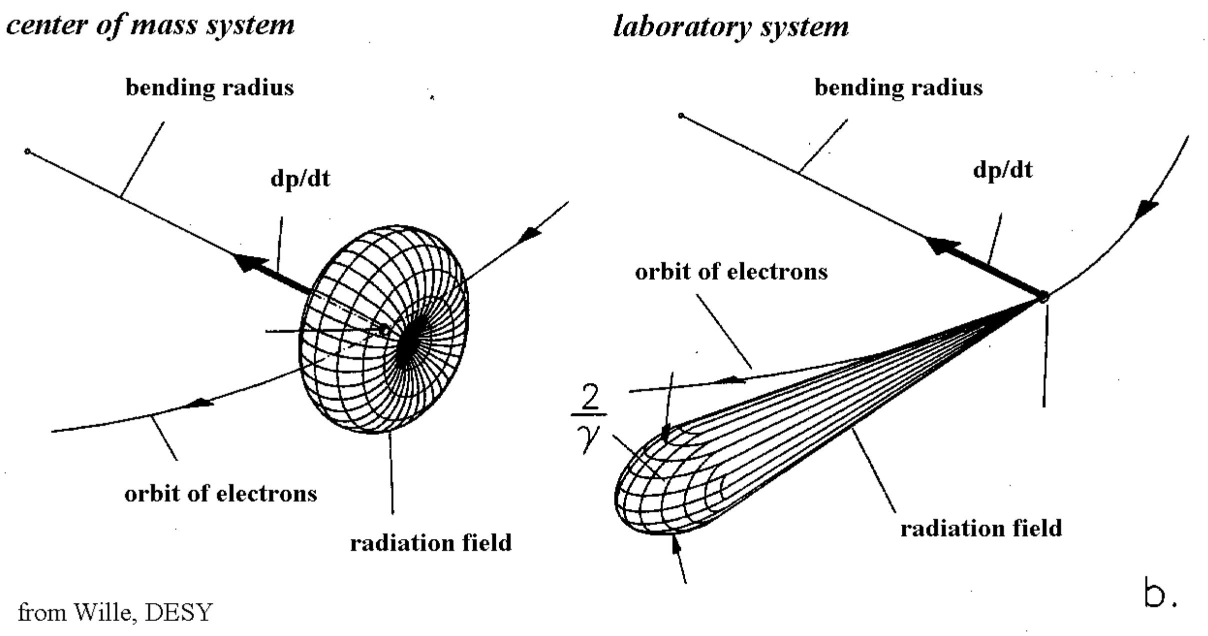

Figure 3.27: Forward peaked synchrotron radiation for relativistic particles from a bending magnet.

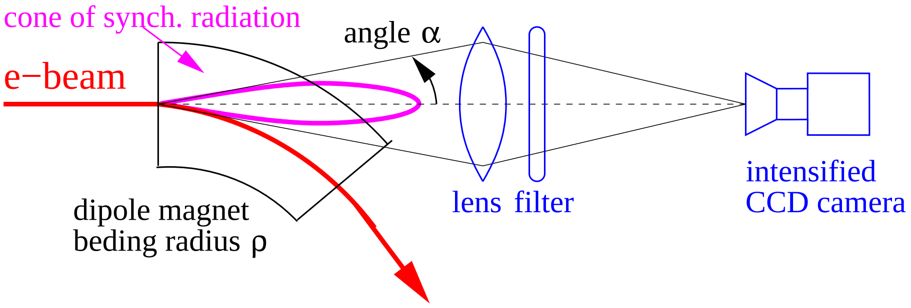

Figure 3.28: Scheme for a synchrotron radiation profile monitor observing the radiation from a dipole.

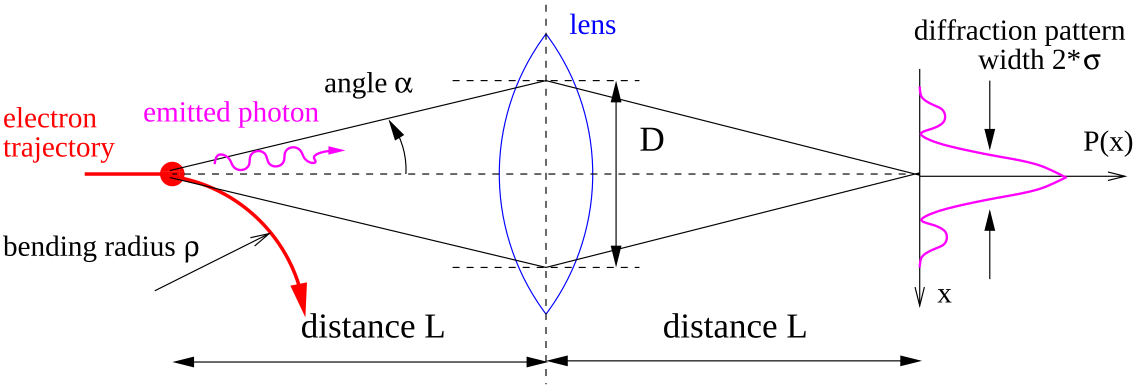

Figure 3.29: Scheme of the optical system for synchrotron radiation profile monitors and a 1:1 image explaining the diffraction limit.

In the center-of-mass system the radiation is perpendicular to the momentum change. The Lorentz transformation to the laboratory frame gives a factor of γ, yielding a forward peak distribution with opening cone of half angle γ. This is demonstrated in Fig. 3.27.

The light emitted by the electron's bend in a dipole magnet can be used to monitor its horizontal and vertical beam profile, as schematically shown in Fig. 3.28 and reviewed in [53]. For diagnostic purposes, the optical part of the emitted spectrum is observed in most cases by using optical bandpass filters. For this wavelength, high quality optics are available and standard CCD cameras can be used. For most accelerator applications, the required wavelength is longer than the so called critical wavelength, where the power spectrum falls off. Due to this we can apply some approximation, see e.g. [54]. For the horizontally polarized synchrotron light of wavelength λ the radiation by the electrons is emitted into a cone with opening angle of

$$\alpha = 0.41\,(\lambda/\rho)^{1/3}\,, \tag{3.13}$$

with ρ being the radius of the bending magnet. For the optical system a 1:1 image from the beam spot to the CCD camera is obtained by a focusing lens of diameter D separated by a distance L from the beam and from the CCD, see Fig. 3.29. More precisely, the finite emission angle α results in an image of size D on the lens. From the theory of Fraunhofer diffraction on a round aperture, the pattern on the image plane has a half width σ of

$$\sigma = \frac{\lambda}{2D/L} \quad . \tag{3.14}$$

Combining both equations together with the geometrical dependency $D \simeq 2\alpha L$ yields the resolution due to diffraction

$$\sigma \simeq 0.6\left(\lambda^2 \cdot \rho\right)^{1/3} \quad . \tag{3.15}$$

A small width of the diffraction pattern and therefore a good resolution is achieved for the given optical system by [55, 56]:

- using dipole magnets with small bending radius ρ; but this radius is fixed by the accelerator construction.
- a short wavelength; but due to technical reasons (optic components, CCD camera) it should not be shorter than near UV of $\lambda > 300$ nm.

Typical limits are in the order of ~ 100 μm, depending on the dipole bending radius. A higher resolution can be achieved by observing the light from wigglers or undulators, if they are installed in the synchrotron.

A realization of a synchrotron light profile monitor is shown in Fig. 3.30 at CERN LEP [57]. The bending radius is here 3.1 km and the diffraction gives the largest contribution to the resolution by about $\sigma \sim 300$ μm, which is comparable to the real electron beam size close to the final energy. The setup consists of a metallic mirror to deflect the light out of the plane of the beam. Due to the high power of the synchrotron radiation, the mirror has to be cooled and possible deformations can spoil the optical quality. With the help of some curved mirrors the light is focused and an optical filter selects the wavelength range of blue or UV light. The detector is an image intensified CCD camera. Even though the resolution is not too high, this relatively straight forward system can be quite helpful due to its non-destructiveness, as demonstrated in Fig. 3.31 from the synchrotron light source APS [58].

The diffraction limit can be compensated by using an interference technique by a double slit as known from astronomy. From the distance of the minima of the interference pattern, the beam width can be calculated. A scheme of this is presented in Fig. 3.32. Due to the non-coherent emission by an ensemble of electrons, the fringes fade-out for large beam sizes. A

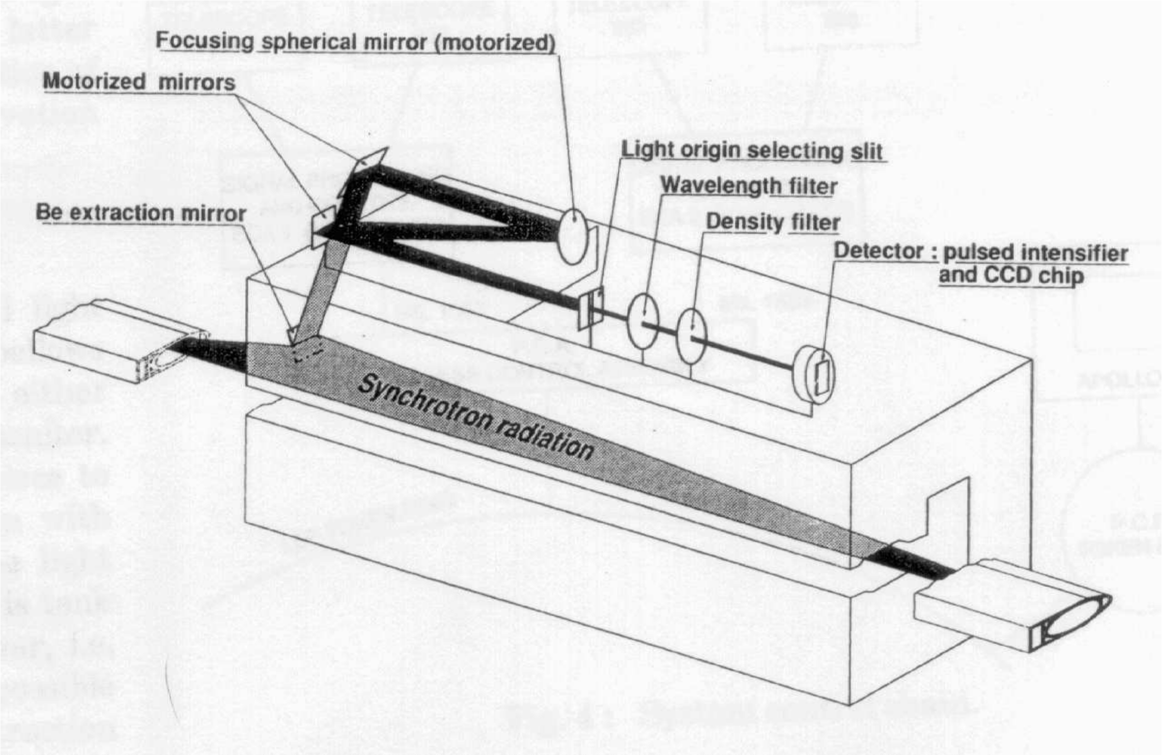

Figure 3.30: The synchrotron radiation profile monitor at LEP. The optical system is installed close to the 23 m long dipole magnet with bending radius of 3100 m, from [57]

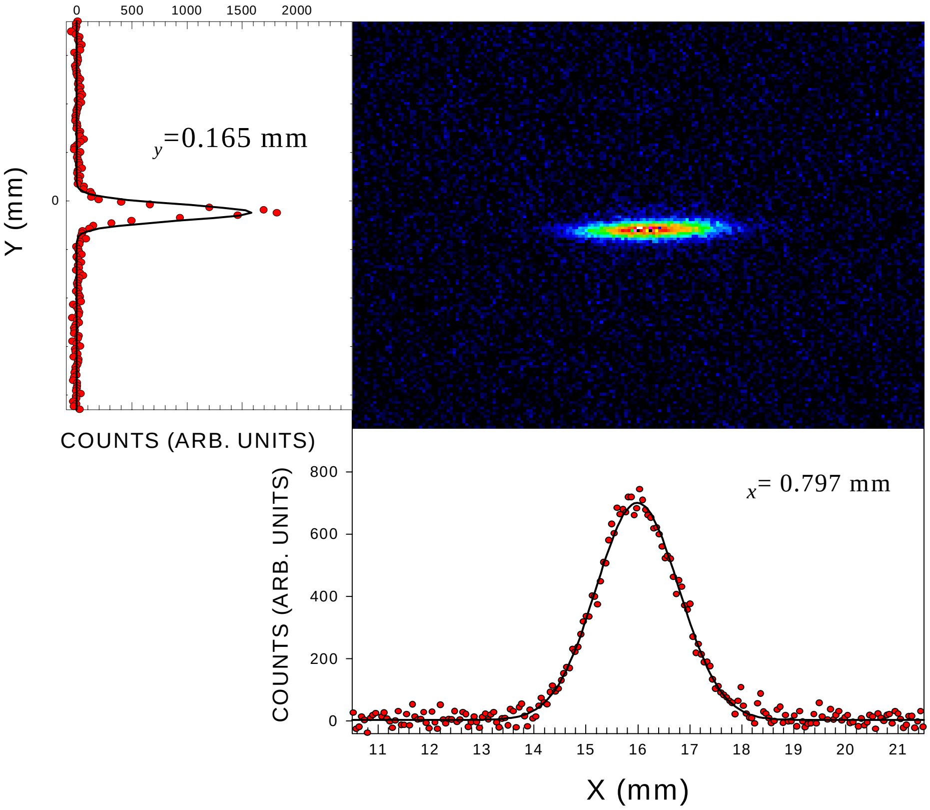

Figure 3.31: Image of the electron beam in the APS accumulator ring (Argonne National Lab.)by a synchrotron radiation monitor [58].

resolution down to the μm range has been realized with this method. For more details see e.g. [59].

A higher resolution can also be achieved by monitoring the profile at much shorter wavelengths. X-ray pin-hole cameras are used for this purpose. Only the emitted x-rays, scraped by a typically Ø1 mm aperture of high Z-material are recorded with a detector.

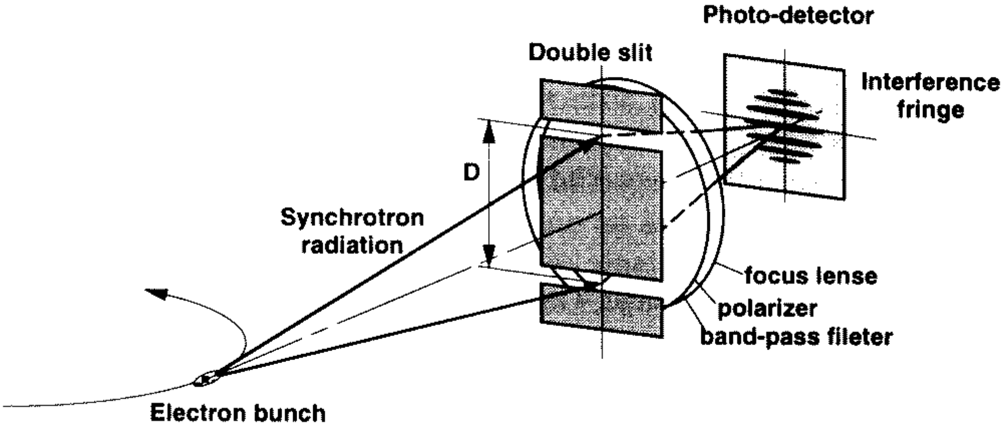

Figure 3.32: Schematics of a double slit synchrotron radiation interferometer.

Chapter 4

Measurement of transverse emittance

The emittance describes the quality of a beam. Its determination is based on profile measurements. It is unimportant what method of profile measurement is used, as long as it has an adequate resolution. In the following we start with a slit-grid and pepper-pot device, where the spatial coordinate is fixed by an aperture and the angle distribution is measured. This is suited for particles having a range in matter below ~ 1 cm i.e. proton or ions with $E_{kin} < 100$ MeV/u. The emittance can also be determined by fitting the beam envelope, measured at one location with different focusing conditions or at different locations. This can be applied to transfer lines for all particle conditions. But here it is problematic to include emittance growth due to space charge forces, i.e., blow-up of the transverse size due to the forces between the charged particles. A detailed review on the involved physics, technologies and data acquisition is given in [60].

In a synchrotron it is sufficient to measure the beam profile at one location only. The orientation of the ellipse, which is equivalent to the knowledge of the lattice functions dispersion $D(s)$ and β-function $\beta(s)$, is fixed (or can be measured separately). The emittance is calculated from the beam width σ via

$$\epsilon_x = \frac{1}{\beta_x(s)}\left[\sigma_x^2 - \left(D(s)\frac{\Delta p}{p}\right)^2\right] \qquad \text{and} \qquad \epsilon_y = \frac{\sigma_y^2}{\beta_y(s)} \tag{4.1}$$

4.1 Definition of the emittance

The motion of the beam particle can be described by a linear second order differential equation. This assumes the absence of any non-linear coupling, like space charge forces or beam-beam effects. The beam quality is given by the phase space volume, which is in this case a constant of the motion. The emittance for one plane is defined by

$$\epsilon_x = \frac{1}{\pi}\int_A dx dx', \tag{4.2}$$

where $A = \pi\epsilon$ is the area of the phase space occupied by the beam, see Fig. 4.1. A determination of the emittance is equivalent to the determination of the distribution of the spatial coordinate x (i.e. the beam profile), the distribution in angle x' and the correlation between x and x'.

The interpretation of an area assumes a hard-edge, homogeneous distribution. A more realistic case is the Gaussian density distribution $\rho(x, x')$ defined at the position of the vector

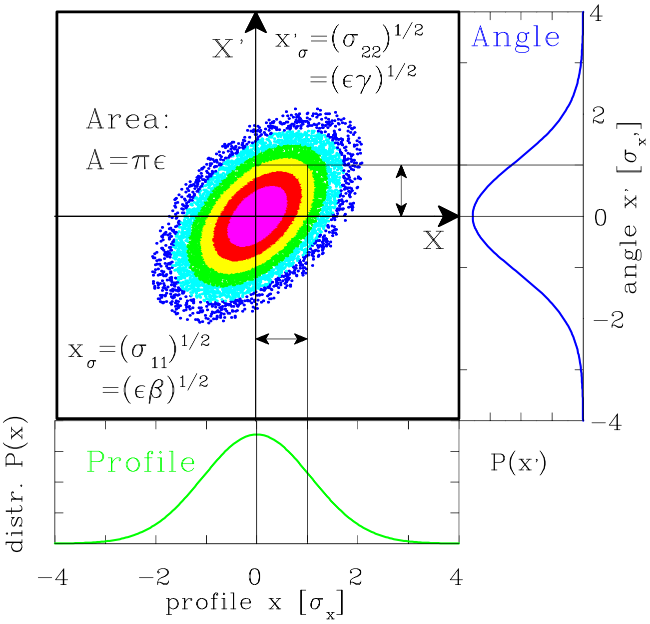

Figure 4.1: The emittance ellipse and the projection to space- and angle coordinates for a Gaussian density distribution. The values of the independent variables are given in units of the standard deviation.

$\vec{x} = (x, x')$. The value of emittance is then given by

$$\epsilon_x = \frac{1}{\pi} \int\limits_{-\infty}^{\infty} \int\limits_{-\infty}^{\infty} \rho(x, x') dx dx'. \tag{4.3}$$

and include 100 % of the particles. A Gaussian distribution $\rho(x, x')$ can be also expressed by $\vec{x} = (x, x')$ and the symmetric beam matrix σ

$$\sigma = \begin{pmatrix} \sigma_{11} & \sigma_{12} \\ \sigma_{12} & \sigma_{22} \end{pmatrix} \tag{4.4}$$

at one location s in the beam line. The beam matrix σ is a representation of the beam ellipse at this position s along the beam path. The 2-dim density is then

$$\rho(x, x') = \frac{1}{2\pi\epsilon_x} \exp\left[\frac{-1}{2} \vec{x}^T \sigma^{-1} \vec{x}\right] = \frac{1}{2\pi\epsilon_x} \exp\left[\frac{-1}{2 \det \sigma} \left(\sigma_{22} x^2 - 2\sigma_{12} x x' + \sigma_{11} x'^2\right)\right]. \tag{4.5}$$

The profile distribution $P(x)$ is obtained by integrating the density ρ over x' as $P(x) = \int \rho(x, x') dx'$ and the parameter $\sqrt{\sigma_{11}}$ is the standard deviation of this distribution. $\sqrt{\sigma_{22}}$ is the corresponding value for the angular distribution $P(x')$ obtained by integrating $\rho(x, x')$ over x as $P(x') = \int \rho(x, x') dx$. σ_{12} describes the correlation between x and x' and is related to the angle of the ellipse. The absolute value of the emittance can be defined using this notation as

$$\epsilon_x = \sqrt{\det \sigma} = \sqrt{\sigma_{11}\sigma_{22} - \sigma_{12}^2} \tag{4.6}$$

and corresponds to an occupation of 15 % of the full phase space area. The unit of this value is m·rad or more frequently mm·mrad. To be consistent with the geometrical interpretation of an area surrounded by an ellipse, the number is multiplied by π; in this case 39 % of the beam is inside the area of $\pi \cdot \sqrt{\sigma_{11}\sigma_{22} - \sigma_{12}^2}$.

Frequently the Twiss parameters are used, which are the beam matrix elements normalized by the emittance as

$$\alpha = -\sigma_{12}/\epsilon \qquad \beta = \sigma_{11}/\epsilon \qquad \gamma = \sigma_{22}/\epsilon. \tag{4.7}$$

The beam matrix is then

$$\sigma = \epsilon \cdot \begin{pmatrix} \beta & -\alpha \\ -\alpha & \gamma \end{pmatrix} \tag{4.8}$$

and the equation of the beam ellipse can be written as

$$\gamma x^2 + 2\alpha x x' + \beta x'^2 = \epsilon \qquad \text{with the normalization} \qquad \beta\gamma - \alpha^2 = 1. \tag{4.9}$$

The width of profile- and angular distribution is given by

$$x_\sigma = \sqrt{\sigma_{11}} = \sqrt{\epsilon\beta} \qquad \text{and} \qquad x'_\sigma = \sqrt{\sigma_{22}} = \sqrt{\epsilon\gamma}. \tag{4.10}$$

Their geometric meaning is one standard deviation of the transverse profile and angular distribution of the beam. The geometrical size of the phase space ellipse is changed along the beam pass s; therefore the parameters $\alpha(s)$, $\beta(s)$ and $\gamma(s)$ are functions on the position s. In particular, for a synchrotron $\beta(s)$ is called the beta-function, describing the beam size via $x_\sigma(s) = \sqrt{\epsilon \cdot \beta(s)}$.

For comparison to calculations one prefers analytical descriptions of the density distribution. One example is the Gaussian distribution of Eq. 4.5, other functions are discussed e.g. in [61]. But the beam doesn't always have a Gaussian shape. For any arbitrary phase space distribution the beam emittance can be calculated via the statistical moments of a 2-dim distribution $\rho(x, x')$ [1]. To describe the beam quality via the emittance the *rms* value (*r*oot *m*ean *s*quare) can be calculated as

$$\epsilon_{rms} = \sqrt{\det \begin{pmatrix} \langle x^2 \rangle & \langle xx' \rangle \\ \langle xx' \rangle & \langle x'^2 \rangle \end{pmatrix}} = \sqrt{\langle x^2 \rangle \langle x'^2 \rangle - \langle xx' \rangle^2} \tag{4.16}$$

---

[1] The first moments of a density distribution $\rho(x, x')$ is called expectation value and is defined as

$$\mu \equiv \langle x \rangle = \frac{\int_{-\infty}^{\infty}\int_{-\infty}^{\infty} x \cdot \rho(x,x')dx'dx}{\int_{-\infty}^{\infty}\int_{-\infty}^{\infty} \rho(x,x')dxdx'} \qquad \text{and} \qquad \mu' \equiv \langle x' \rangle = \frac{\int_{-\infty}^{\infty}\int_{-\infty}^{\infty} x' \cdot \rho(x,x')dxdx'}{\int_{-\infty}^{\infty}\int_{-\infty}^{\infty} \rho(x,x')dxdx'} \quad . \tag{4.11}$$

The n^{th} central moment of a density distribution $\rho(x, x')$ calculated via

$$\langle x^n \rangle = \frac{\int_{-\infty}^{\infty}\int_{-\infty}^{\infty} (x-\mu)^n \cdot \rho(x,x')dx'dx}{\int_{-\infty}^{\infty}\int_{-\infty}^{\infty} \rho(x,x')dxdx'} \qquad \text{and} \qquad \langle x'^n \rangle = \frac{\int_{-\infty}^{\infty}\int_{-\infty}^{\infty} (x'-\mu')^n \cdot \rho(x,x')dxdx'}{\int_{-\infty}^{\infty}\int_{-\infty}^{\infty} \rho(x,x')dxdx'} \quad . \tag{4.12}$$

Using the abbreviation $P(x) = \int \rho(x,x')dx'$ and $P(x') = \int \rho(x,x')dx$ as in Fig. 4.1 this is equivalent to

$$\langle x^n \rangle = \frac{\int_{-\infty}^{\infty} (x-\mu)^n \cdot P(x)dx}{\int_{-\infty}^{\infty} P(x)dx} \qquad \text{and} \qquad \langle x'^n \rangle = \frac{\int_{-\infty}^{\infty} (x'-\mu')^n \cdot P(x')dx'}{\int_{-\infty}^{\infty} P(x')dx'} \tag{4.13}$$

The second moments with $n = 2$ are called variance. If the variance is positive, its square root is the standard deviation $\sigma_x = \sqrt{\langle x^2 \rangle}$ and $\sigma_{x'} = \sqrt{\langle x'^2 \rangle}$.
The mixed quantity $\langle xx' \rangle$ is called covariance and is defined in an analog way via

$$\langle xx' \rangle = \frac{\int_{-\infty}^{\infty}\int_{-\infty}^{\infty} xx' \cdot \rho(x,x')dxdx'}{\int_{-\infty}^{\infty}\int_{-\infty}^{\infty} \rho(x,x')dxdx'} \quad . \tag{4.14}$$

A measurement leads to discrete values of the density distribution at distret steps $\rho(x_i, x'_j)$. The first moment is calculated for this case via

$$\mu \equiv \langle x \rangle = \frac{\sum_{i,j}\ x_i \cdot \rho(x_i, x'_j)}{\sum_{i,j}\ \rho(x_i, x'_j)} \qquad \text{and} \qquad \mu' \equiv \langle x' \rangle = \frac{\sum_{i,j}\ x'_j \cdot \rho(x_i, x'_j)}{\sum_{i,j}\ \rho(x_i, x'_j)} \tag{4.15}$$

and the other quantities in a corresponding manner.

and follows the same general mathematical role as Eq. 4.6.

For a Gaussian distribution the fraction f of the beam inside the certain value of the emittance can be expressed via the *rms* value as

$$\epsilon(f) = -2\pi\epsilon_{rms} \cdot \ln(1-f) \tag{4.17}$$

leading to the following table:

factor to ϵ_{rms}	$1 \cdot \epsilon_{rms}$	$\pi \cdot \epsilon_{rms}$	$2\pi \cdot \epsilon_{rms}$	$4\pi \cdot \epsilon_{rms}$	$6\pi \cdot \epsilon_{rms}$	$8\pi \cdot \epsilon_{rms}$
faction of beam f [%]	15	39	63	86	95	98

When a certain value of emittance is given for a beam one has to check carefully its meaning, because there is no common definition for the emittance around the different accelerator facilities to what level of beam fraction for a given emittance value is referring to.

The emittance is a quantity defined in the laboratory frame due to the definition of the divergence. When a beam is accelerated, the divergence shrinks ('adiabatic damping') due to the changing ratio of longitudinal velocity v_s to transverse velocity v_x: $x' = v_x/v_s$. To compare emittance for different longitudinal momenta $p_s = m_0 \cdot \gamma_{rel} \cdot v_s$, the normalized emittance ϵ_{norm}

$$\epsilon_{norm} = \frac{v_s}{c}\gamma_{rel} \cdot \epsilon \tag{4.18}$$

is referred to a value $v_s/c \cdot \gamma_{rel} = 1$, i.e. to a beam velocity $v_s = \sqrt{\frac{1}{2}} \cdot c = 0.71 \cdot c$. ($c$ is the velocity of light and $\gamma_{rel} = 1/\sqrt{1-(v_s/c)^2}$ is the relativistic Lorentz factor.) The normalized emittance is constant under ideal accelerating conditions.

A measurement of emittance means a determination of the numerical value of ϵ as well as the orientation and shape of the phase space distribution.

4.2 Slit-grid method

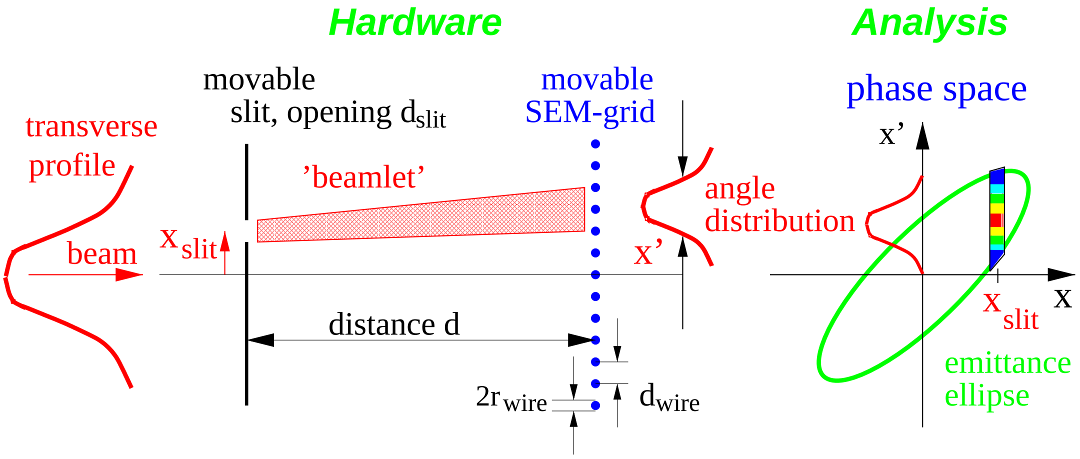

Figure 4.2: Scheme of a slit-grid emittance measurement device.

A popular method at proton/heavy ion LINACs with penetration depth below 1 cm is the slit-grid device. Here the position x is fixed for one direction with a thin slit having an opening of typically 0.1 to 0.5 mm. In the perpendicular direction the full beam is transmitted to get a large signal. The angle x' is determined with a SEM-grid having a distance from the slit of 10 cm to 1 m depending on the ion velocity. In the field-free drift space the trajectories of the particles, combined in a 'beamlet', are straight lines [62, 63]. The contribution to the emittance

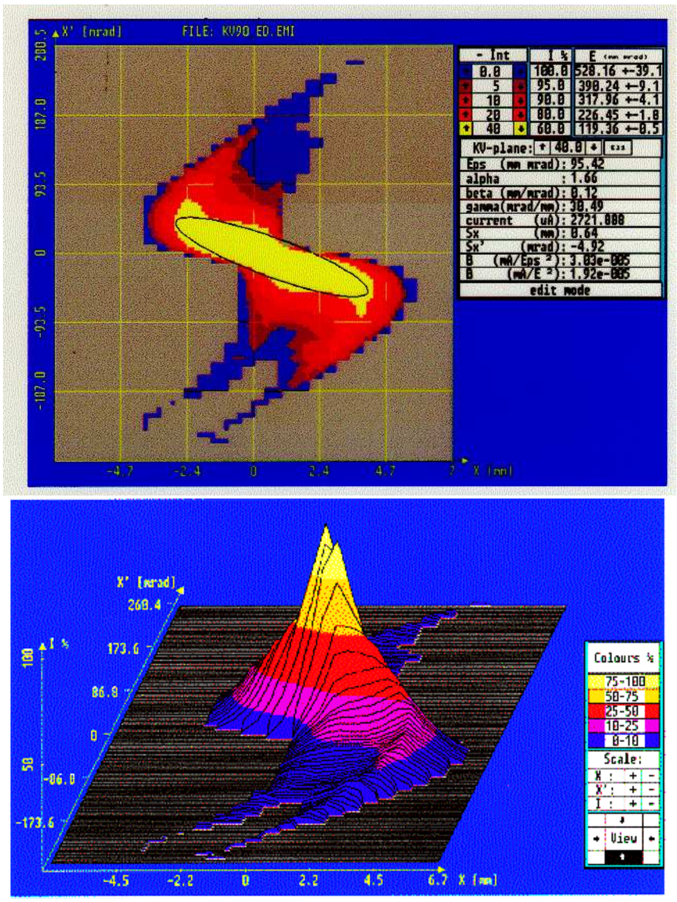

- Int	I %	E (mm mrad)
0.0	100.0	528.16 +-39.1
5	95.0	390.24 +-9.1
10	90.0	317.96 +-4.1
20	80.0	226.45 +-1.8
40	60.0	119.36 +-0.5

KV-plane: 40.0
Eps (mm mrad): 95.42
alpha : 1.66
beta (mm/mrad): 0.12
gamma(mrad/mm): 30.49
current (uA): 2721.000
Sx (mm): 0.64
Sx' (mrad): -4.92
B (mA/Eps ^{2}): 3.03e-005
B (mA/E ^{2}): 1.92e-005
edit mode

Figure 4.3: Emittance measurement using a slit-grid device with a low energy ion beam after the source.

plot in the phase space is given by the angle distribution at the slit location. The slit is then scanned trough the beam to get all positions. The data have to be normalized to a constant beam current as measured e.g. by the beam charges hitting the slit. After making the full scan, the emittance is plotted and the *rms*-value is calculated from the data. A fit with an elliptical shape is drawn to the data and the Twiss parameters can be calculated from this fit. An example is shown in Fig. 4.3 for a low energy ion beam as a contour or 3 dimensional plot. This method can also determine more pathological phase space distributions, not only Gaussian distributions. Close to an ion source this happens quite often due to the large space charge forces or the large profile width, where aberrations of the magnets start to play a role.

The resolution for the space coordinate Δx is limited by the slit width $\Delta x = d_{slit}$. The angle resolution $\Delta x'$, measured at the distance d, is given by the radius of the wire r_{wire} and the width of the slit resulting in $\Delta x' = (d_{slit} + 2r_{wire})/d$. The size of discrete elements in the phase space is given by $\Delta x \cdot \Delta x'$. This leads to a discretization error, in particular in the case of small beam sizes (focused beam) or small angle distributions (parallel beam). The resolution is improved by scanning the SEM-grid in steps lower than the distance of the wires d_{wire}, increasing the density of the discrete elements in the phase space analysis. This can lead to overlapping elements, because their size $\Delta x \cdot \Delta x'$ stays constant. The same holds for a movement of the slit with step sizes lower than the slit width.

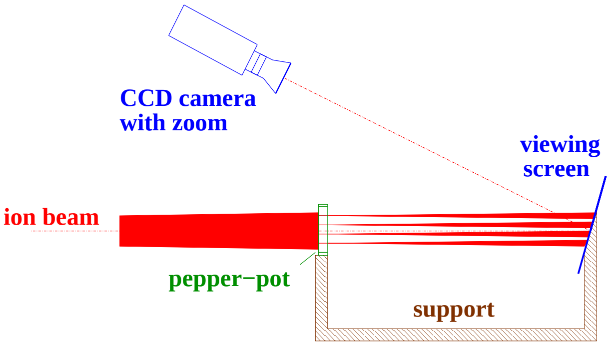

Figure 4.4: Scheme of a pepper-pot emittance measurement device.

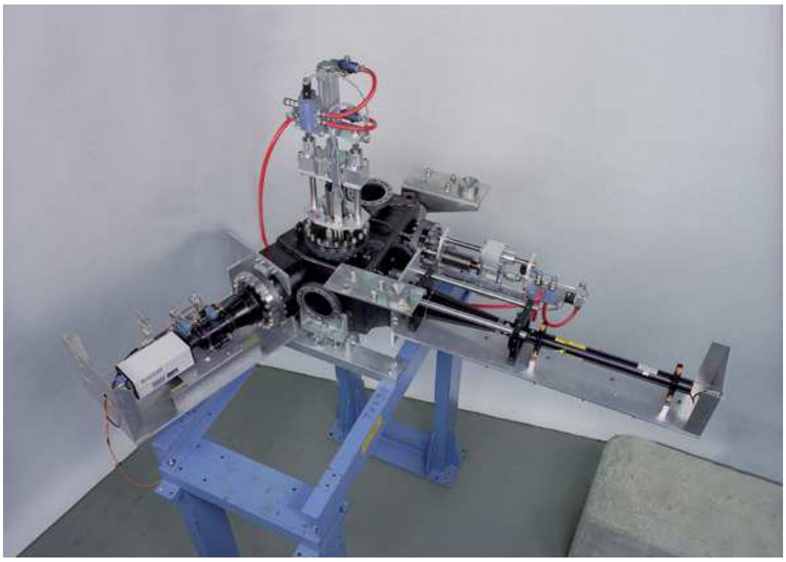

Figure 4.5: Photo of the hardware of a pepper-pot emittance device including the laser for calibration (right side), the CCD-camera (left), the pneumatic feed-through for the pepper-pot-screen support (right back) and the feed-through of the movable mirror for the laser light.

4.3 Pepper-pot device

Using a slit-grid device, the slit and the SEM-grid have to be scanned trough the beam, which takes some time: up to several minutes per plane. In particular for pulsed LINACs, only one step for the slit and the SEM-grid can be performed during a single pulse. Using a slit, the determinations for the two transverse planes have to be done separately. Having a matrix of holes in a plate, such a measurement can be performed within one shot. Moreover, if the ion sources may have fluctuations from pulse to pulse, the emittance is measured for a single beam setting. This is performed with a pepper-pot device [64, 65], shown in Fig. 4.4 schematically and a realization in Fig. 4.5. As an example, the pepper-pot plate of the GSI device has holes with 0.1 mm diameter and 3 mm spacing. To display a calibration grid on the screen, a HeNe laser beam illuminates the pepper-pot and the image is recorded with a CCD camera, as shown in Fig. 4.6 (top). This calibration has to be performed before each beam measurement to prevent errors from probable misalignments. Relative to this, the position and size of the beamlets' spots created by the holes are determined, see Fig. 4.6 (bottom). For the device used at GSI [64], the size of the pepper-pot is 50×50 mm^2 having 15×15 holes with 0.1 mm diameter. The distance between the pepper-pot and the viewing screen is 25 cm. The screen is made of pure Al_2O_3 due to the high beam intensities. Other materials can be used for the screen, e.g., the discussed phosphor screens.

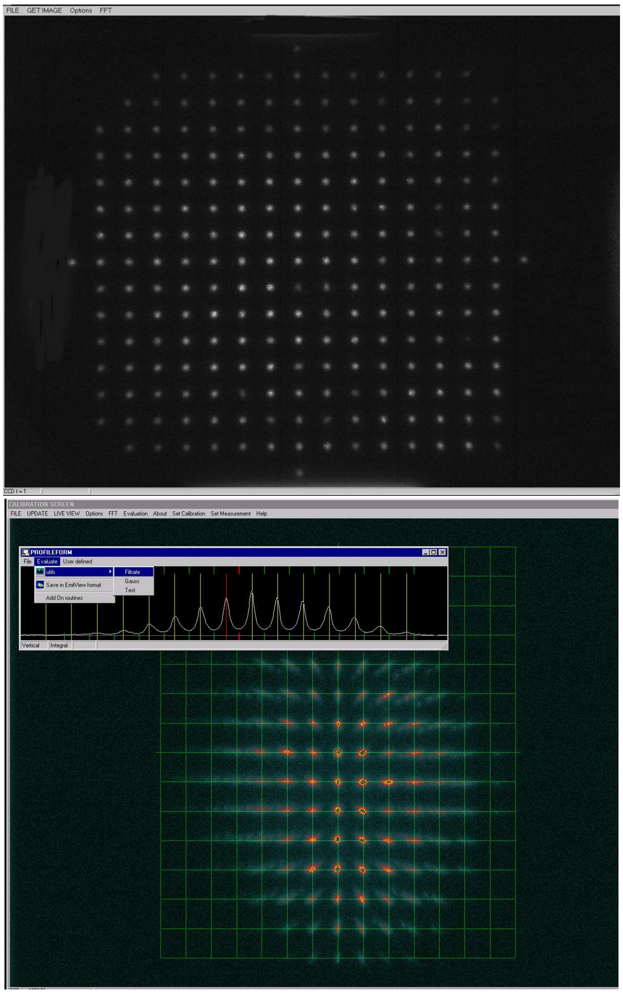

Figure 4.6: Screen shots of the pepper-pot device with a laser beam for calibration (top) and a single shot ion beam including the projection of the horizontal plane with a high current Ar^{1+} ion beam at 1.4 MeV/u (bottom), from [66].

The analysis for the emittance plot can be done by the evaluation of the individual spot's angle distributions; in this case even coupling of the two transverse planes would be detectable. Alternatively, the data are projected to both transversal planes, as shown in the insert of Fig. 4.6 (bottom). The analysis for the phase space plot is similar as for the slit-grid method. For an estimation of the resolution, the arguments are comparable to the one for the slit-grid device:

- A good spatial resolution is generated by the illumination of many holes having small distances. But one has to avoid overlapping of the beamlets at the screen to distinguish the contributions of the individual holes.
- The diameter of the holes should be small, but then the signal strength goes down.

In general, the resolution is inferior to the slit-grid, where the movable slit can have much smaller increments than the distance between the holes. Moreover, small holes lead to significant contribution of Fraunhofer diffraction of the laser light.

Like for every destructive measurement, one has to evaluate the total beam power to prevent melting of the uncooled pepper-pot aperture.

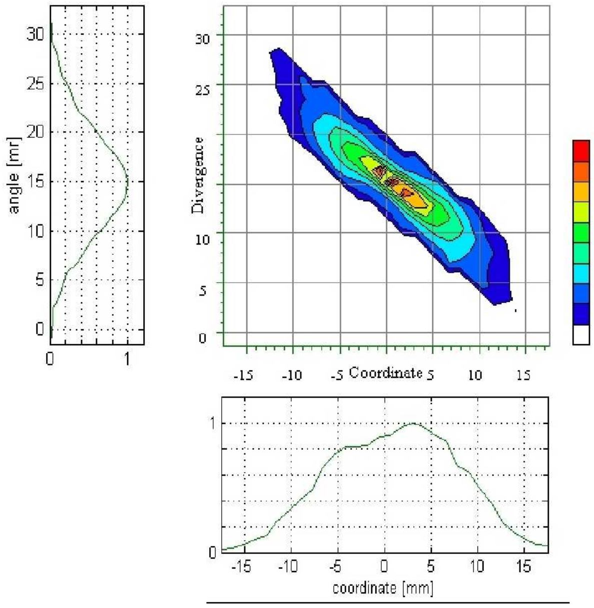

Figure 4.7: The horizontal emittance of the data above, including the projection to the axis.

4.4 Quadrupole variation

The emittance can be determined from a series of profile measurements, either by changing the focusing strength of a quadrupole, or by measuring at 3 or more positions along a transfer line, as schematically shown in Fig. 4.8 and Fig. 4.10. To derive the emittance from such a measurement, linear transformations are used. The described measurement is just the reverse of normal transport calculations with codes like TRANSPORT, MAD, WinAgile or MIRCO: Starting for a given emittance (size and orientation) at the input of a transport line, the beam envelope is calculated along the line. If the profile is measured, one calculates the emittance at the input of the line by using the same transformations in reverse (see below).

For LINACs with a straight, non-dispersive transfer line, the transformation from a location s_0 to s_1 is given by the 2×2 transfer matrix $\mathbf{R}$. Important examples for these matrices are:
Drift with length L:

$$\mathbf{R_{drift}} = \begin{pmatrix} 1 & L \\ 0 & 1 \end{pmatrix} \tag{4.19}$$

Horizontal focusing quadrupole with quadrupole constant k and effective length l:

$$\mathbf{R_{focus}} = \begin{pmatrix} \cos\sqrt{k}l & \frac{1}{\sqrt{k}}\sin\sqrt{k}l \\ -\sqrt{k}\sin\sqrt{k}l & \cos\sqrt{k}l \end{pmatrix} \tag{4.20}$$

Horizontal de-focusing quadrupole with quadrupole constant k and effective length l:

$$\mathbf{R_{defocus}} = \begin{pmatrix} \cosh\sqrt{k}l & \frac{1}{\sqrt{k}}\sinh\sqrt{k}l \\ -\sqrt{k}\sinh\sqrt{k}l & \cosh\sqrt{k}l \end{pmatrix}. \tag{4.21}$$

For an ideal quadrupole with field gradient $g = B_{pole}/a$, B_{pole} is the field at the pole and a the aperture, the quadrupole constant is $k = |g|/(B\rho)_0$ for a magnetic rigidity $(B\rho)_0$.

A determination of the emittance at the position s_0 is equivalent to the evaluation of the beam matrix $\sigma(0)$ at this position. The beam matrix is transformed to a second location s_1 with

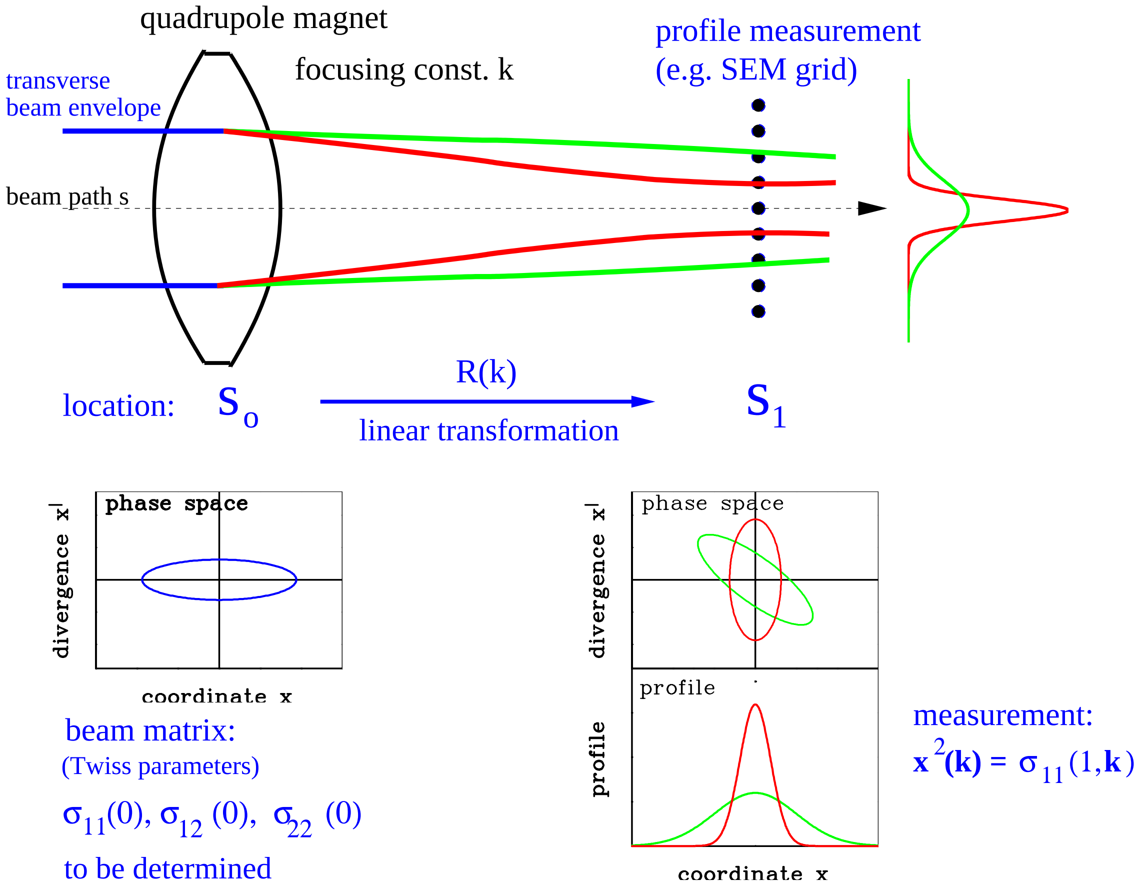

Figure 4.8: Variation of a quadrupole strength for the determination of the emittance at the location s_0.

the help of the product of transfer matrices for the individual elements $\mathbf{R} = \prod \mathbf{R_{elements}}$ via

$$\sigma(1) = \mathbf{R}\sigma(0)\mathbf{R}^{\mathbf{T}} \tag{4.22}$$

The beam width $x_{max}(1)$ is measured at s_1 and the equation for the element $\sigma_{11}(1)$ is given by

$$x^2_{max}(1) = \sigma_{11}(1) = R^2_{11}\sigma_{11}(0) + 2R_{11}R_{22}\sigma_{12}(0) + R^2_{12}\sigma_{22}(0). \tag{4.23}$$

This is a linear equation for the unknown three beam matrix elements $\sigma_{ij}(0)$ at location s_0, in Fig. 4.8 in front of the focusing quadrupole magnet.

To get a solution, we need at least three different settings of the quadrupole strength k_i, and therefore different transfer matrices $\mathbf{R}(k_i)$ leading to three different readings of the profile width as depicted in Fig. 4.8. Assuming $i = 1, 2...n$ different settings of the quadrupole strength $k_1, k_2...k_n$ and n measurements of the beam width $x^2_{max}(1, k_i) = \sigma_{11}(1, k_i)$ a redundant system of linear equations is obtained in the form

$$\begin{aligned}
\sigma_{11}(1,k_1) &= R^2_{11}(k_1)\cdot\sigma_{11}(0) + 2R_{11}(k_1)R_{22}(k_1)\cdot\sigma_{12}(0) + R^2_{12}(k_1)\cdot\sigma_{22}(0) \quad \text{focusing } k_1\\
\sigma_{11}(1,k_2) &= R^2_{11}(k_2)\cdot\sigma_{11}(0) + 2R_{11}(k_2)R_{22}(k_2)\cdot\sigma_{12}(0) + R^2_{12}(k_2)\cdot\sigma_{22}(0) \quad \text{focusing } k_2\\
&:\\
\sigma_{11}(1,k_n) &= R^2_{11}(k_n)\cdot\sigma_{11}(0) + 2R_{11}(k_n)R_{22}(k_n)\cdot\sigma_{12}(0) + R^2_{12}(k_n)\cdot\sigma_{22}(0) \quad \text{focusing } k_n
\end{aligned} \tag{4.24}$$

The solution of this system are the values of the beam matrix $\sigma_{ij}(0)$ (or equivalent the Twiss parameters) at the location s_0, the entrance of the quadrupole magnet. With theses values, the

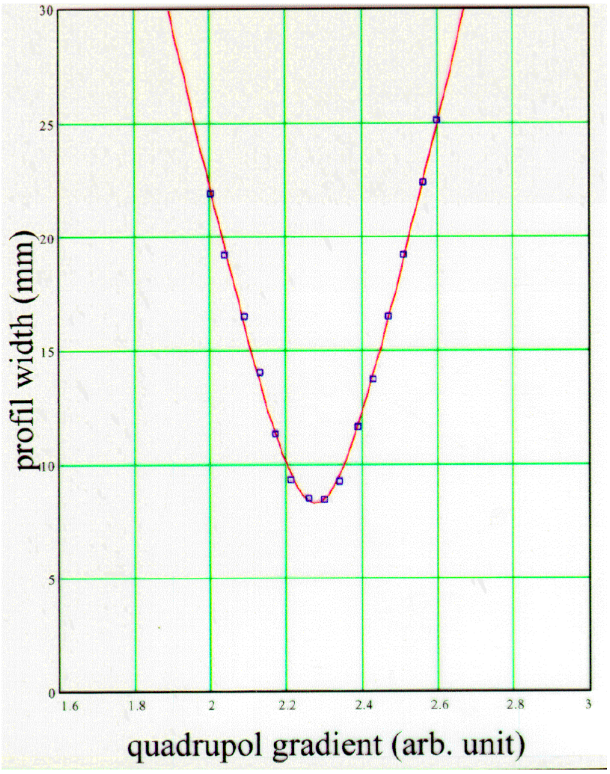

Figure 4.9: Profile width determined with a SEM-grid for a quadrupole variation and the parabolic fit.

size and orientation of the phase space ellipse is fixed. For three measurements (k_1, k_2, k_3) we can have a unique solution, but nothing is learned about the errors. Therefore more than 3 measurements have to be performed, leading to a redundant system of linear equations. The solution is reached by a least square fit to the best parameters of $\sigma_{ij}(0)$ or by solving the linear regression problem via so called normal equations. Both algorithms are described in textbooks of Linear Algebra or Numerical Mathematics.

An example is shown in Fig. 4.9 performed at the GSI LINAC. To get a small error for the emittance determination, it is recommended to pass a beam waist by the quadrupole variation. Only in this case a parabola can be fitted through the profile data with sufficient accuracy.

Instead of solving the redundant system of linear equations, one can start from the parabola fit of the beam size as a function of the quadrupole strength as shown in Fig. 4.9. The most frequently used case it a quadrupole follow by a drift toward the profile measurement location. A quadratic dependence is observed for the following reason: Assuming a thin lens approximation with a focal length f of the quadrupole action one can write the transfer matrix as:

$$\mathbf{R}_{\mathbf{focus}} = \begin{pmatrix} 1 & 0 \\ -1/f & 1 \end{pmatrix} \equiv \begin{pmatrix} 1 & 0 \\ K & 1 \end{pmatrix}. \tag{4.25}$$

After a drift of length L one gets the full transfer matrix

$$\mathbf{R} = \mathbf{R}_{\mathbf{drift}} \cdot \mathbf{R}_{\mathbf{focus}} = \begin{pmatrix} 1+LK & L \\ K & 1 \end{pmatrix}. \tag{4.26}$$

Inserting this matrix into Eq. 4.22 for the transformation of the beam matrix $\sigma(1) = \mathbf{R}\sigma(0)\mathbf{R}^T$ one gets for the measured beam matrix element $\sigma_{11}(1) = x^2_{max}(1)$:

$$\sigma_{11}(1) = L^2\sigma_{11}(0) \cdot K^2 + 2\left(L\sigma_{11}(0) + L^2\sigma_{12}(0)\right) \cdot K + L^2\sigma_{22} + \sigma_{11}. \tag{4.27}$$

This is the expected quadratic function in the quadrupole gradient K. From the beam width measurement for various quadrupole setting a parabola fit is performed as done in Fig. 4.9 with the fit-parameters a, b and c (this parametrization is chosen to yield a simple expression for the absolute value of the emittance as shown for Eq. 4.31 below)

$$\sigma_{11}(K) = a\,(K-b)^2 + c = aK^2 - 2abK + ab^2 + c. \tag{4.28}$$

A comparison of the coefficients of the last two Eqn. 4.27 and 4.28 yields

$$\begin{aligned} a &= L^2\sigma_{11}(0) \\ -ab &= L\sigma_{11}(0) + L^2\sigma_{12}(0) \\ ab^2 + c &= L^2 + 2L\sigma_{12}(0) + \sigma_{11}(0). \end{aligned} \tag{4.29}$$

These linear equations can finally be solved and the result are the requested matrix elements at the entrance of the optical system:

$$\begin{aligned} \sigma_{11}(0) &= \frac{a}{L^2} \\ \sigma_{12}(0) &= -\frac{a}{L^2}\left(\frac{1}{L} + b\right) \\ \sigma_{22}(0) &= \frac{1}{L^2}\left(ab^2 + c + \frac{2ab}{L} + \frac{a}{L^2}\right). \end{aligned} \tag{4.30}$$

The absolute value of the emittance is calculated from these fit parameters via

$$\epsilon = \sqrt{\det \sigma(0)} = \sqrt{\sigma_{11}(0)\sigma_{22}(0) - \sigma_{12}^2(0)} = \frac{\sqrt{ac}}{L^2} \quad . \tag{4.31}$$

Be aware, that the fit-parameters have some units as given in Eq. 4.28.

The described method is based on linear transformations and conservation of the emittance during the manipulation. Moreover, an elliptical shape of the emittance is assumed. This is a good assumption as long as non-linear effects, like space charge forces, are low. If the investigations are done with intense beams, an emittance blow-up may occur, depending on the particle density, i.e., on the beam size. But the size is to be changed and even a waist has to be created. For high intensity beams, self-consistent algorithms have to be applied to get an estimation of the emittance at the quadrupole entrance, see ,e.g. [67].

4.5 'Three grid' method

Instead of varying a quadrupole, the beam profiles at different locations along a transfer line can be measured with fixed magnet settings. This is easier to perform at long transfer lines, where the profile monitors are installed anyhow. There is no general restriction to the involved linear optics, e.g. dipoles can be included with their known transfer matrix $\mathbf{R_{dipole}}$.

The profile has to be measured at three or more locations, see Fig. 4.10. To get good accuracy, one profile monitor should be close to a beam waist. For the determination of the beam matrix elements $\sigma_{ij}(0)$ at the entrance of the line s_0, the profile widths and therefore the beam matrix elements $\sigma_{11}(n)$ are determined at n different locations s_n. A system of redundant linear equations for the entrance emittance $\sigma_{ij}(0)$ is given by

$$\begin{aligned} \sigma_{11}(1) &= R_{11}^2(1)\cdot\sigma_{11}(0) + 2R_{11}(1)R_{22}(1)\cdot\sigma_{12}(0) + R_{12}^2(1)\cdot\sigma_{22}(0) \qquad \mathbf{R}(1): s_0 \to s_1 \\ \sigma_{11}(2) &= R_{11}^2(2)\cdot\sigma_{11}(0) + 2R_{11}(2)R_{22}(2)\cdot\sigma_{12}(0) + R_{12}^2(2)\cdot\sigma_{22}(0) \qquad \mathbf{R}(2): s_0 \to s_2 \\ &\vdots \\ \sigma_{11}(n) &= R_{11}^2(n)\cdot\sigma_{11}(0) + 2R_{11}(n)R_{22}(n)\cdot\sigma_{12}(0) + R_{12}^2(n)\cdot\sigma_{22}(0) \qquad \mathbf{R}(n): s_0 \to s_n \end{aligned} \tag{4.32}$$

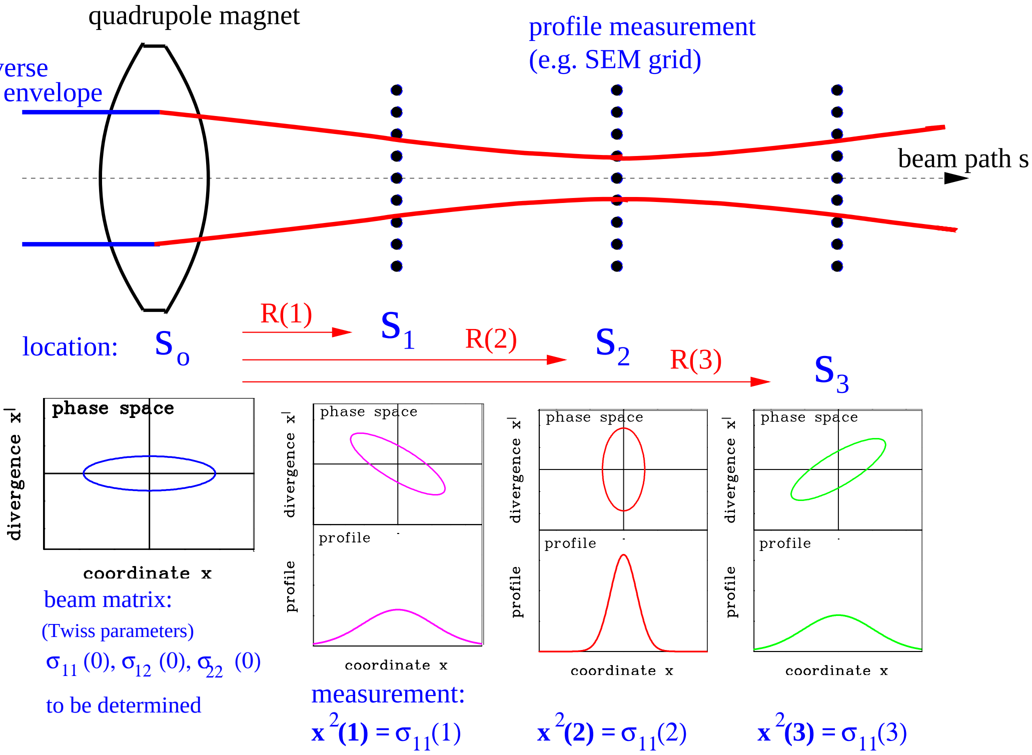

Figure 4.10: Scheme for the emittance determination at a transfer line using a profile measurement at three locations.

This is a similar formula as for the quadrupole variation (Eq. 4.24), but the transfer matrix $\mathbf{R}(i)$ describes now the beam transport from the starting point of the transfer line s_0 to the location of the individual measurements s_i. The algorithm of the emittance calculation (least square fit or normal equations) is the same as for the quadrupole scan. Such a measurement is shown in Fig. 4.11, compared to the fitted beam envelope, to visualize also the possible errors. In practice the parameters of the entrance ellipse are fitted to match the measured profiles using a linear optics code (e.g. TRANSPORT, MAD, WinAgile) for this line.

To get a reliable measurement, the transfer matrix $\mathbf{R}(n)$ should be an adequate description of the action of the optical elements on the beam. In particular, one has to make sure that the beam center passes the quadrupoles on their magnetic axes, i.e. no 'steering' of the quadrupoles is present. This might be a source of errors in practical situations. As discussed before, no emittance growth, e.g. due to space charge forces, is assumed here.

The algorithm is not limited to straight transport lines. If a dipole magnet is present in addition, one has to take its action on the beam also into account. This results in a dispersion D, i.e., a coupling between the momentum spread $\delta = \Delta p/p$ and the transverse beam size with $\Delta x = D \cdot \Delta p/p$. For the transport matrix we get an additional matrix element R_{13}. Also, a dipole has an influence of the angular distribution called angular dispersion, resulting in a additional matrix element R_{23}. The single particle trajectory is now made of a 3-dim vector $\vec{x} = (x, x', \Delta p/p)$ and the transfer matrix $\mathbf{R}$ is now a 3×3 matrix. The effect of dispersion has to be included into the symmetric beam matrix σ with three new elements σ_{13}, σ_{23} and σ_{33} . To determine the values of these beam matrix elements, at least 6 profile measurements have to be done, resulting in at least 6 equations in the (redundant) system of linear equations for $\sigma_{ij}(0)$ in Eq. 4.24 and Eq. 4.32.

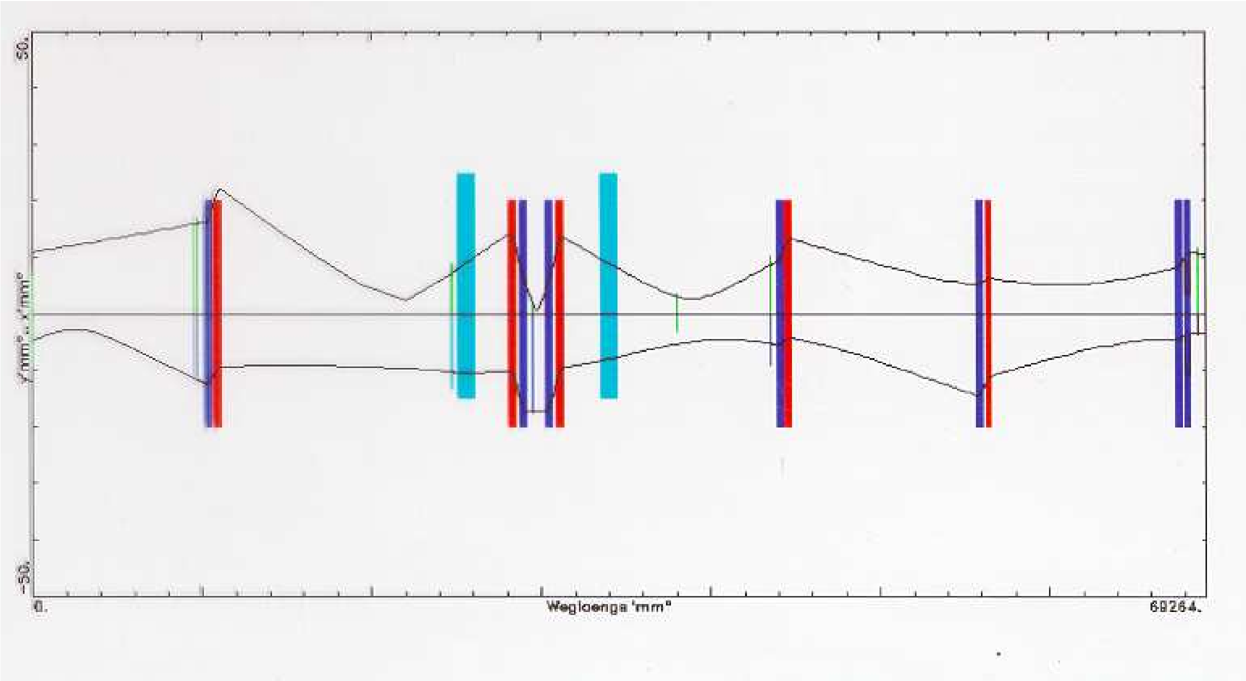

Figure 4.11: Determination of the beam envelope by linear transformations in horizontal (top curve) and vertical (bottom curve) direction using different profile measurements. The width of the profile is shown as green lines, performed at a transfer line at GSI.

Chapter 5

Pick-ups for bunched beams

The longitudinal bunch shape as well as the position of a beam is usually determined with pick-up plates. The idea is to measure on an insulated metal plate the charges induced by the electric field of the beam particles, see Fig. 5.1. Because the electric field of a bunched beam is time dependent, an ac signal is seen on the plate and the coupling is done using rf technologies. The principle signal shape, as well as the most often used types of pick-ups are described. The application is the determination of the beam position (center-of-mass). To this end, four pick-up plates are installed and the difference of the signals yields the center-of-mass in both transverse axes. This installation is called a **B**eam **P**osition **M**onitor **BPM**. In a synchrotron, the closed orbit is determined by the BPMs. Measurements based on this position information are discussed, namely the determination of the tune and the lattice functions of a synchrotron.

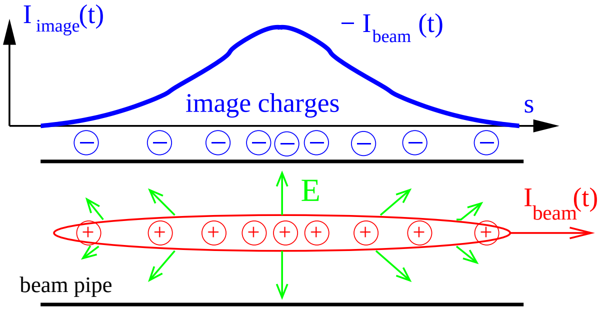

Figure 5.1: The beam current induces a wall current of the same magnitude but reversed polarity.

5.1 Signal treatment of capacitive pick-ups

As shown in Fig. 5.2, a capacitive pick-up consists of a plate or a ring inserted in the beam pipe. Here the induced image charge of the beam is coupled via an amplifier for further processing. The plate at a distance a from the beam center has an area of A and a length in longitudinal direction of l. The current I_{im} driven by the image charge Q_{im} is

$$I_{im}(t) \equiv \frac{dQ_{im}}{dt} = \frac{A}{2\pi a l} \cdot \frac{dQ_{beam}(t)}{dt}. \tag{5.1}$$

Having a beam with velocity β we can write for the derivative of the beam charge $dQ_{beam}(t)/dt$

$$\frac{dQ_{beam}(t)}{dt} = \frac{l}{\beta c}\frac{dI_{beam}}{dt} = \frac{l}{\beta c} \cdot i\omega I_{beam}(\omega) \tag{5.2}$$

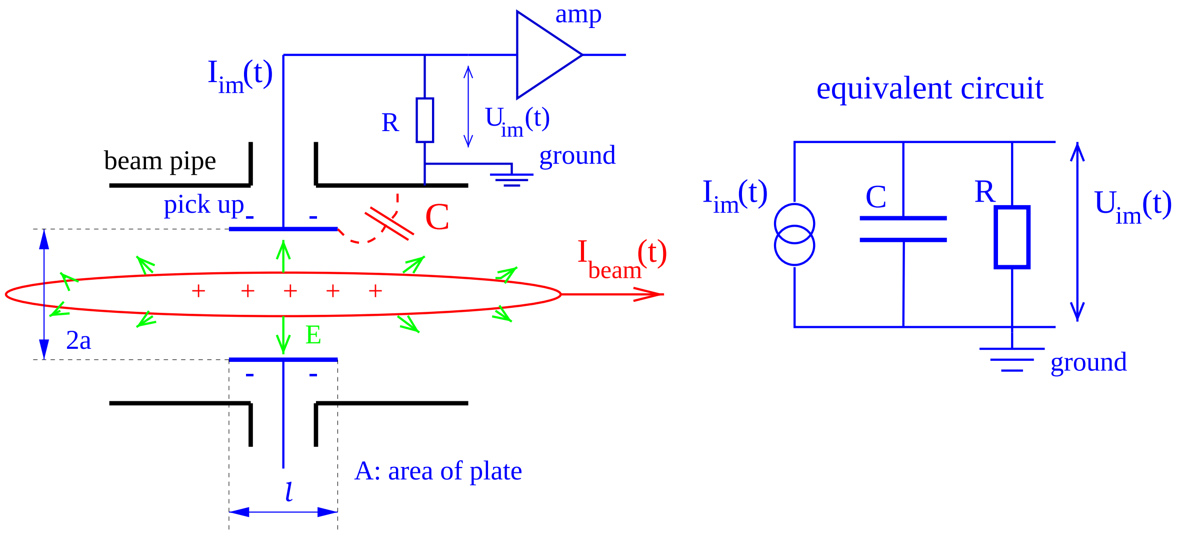

Figure 5.2: Scheme of a pick-up electrode and it's equivalent circuit.

where the beam current is expressed in the frequency domain as $I_{beam} = I_0 e^{i\omega t}$ [1]. As the signal we use the voltage drop at a resistor R

$$U_{im}(\omega) = R \cdot I_{im}(\omega) = Z_t(\omega, \beta) \cdot I_{beam}(\omega) \tag{5.3}$$

For all types of pick-up plates, the general quantity of longitudinal transfer impedance $Z_t(\omega, \beta)$ is defined in the frequency domain according to Ohm's law. For more detailed discussion see [68, 69, 70].It describes the effect of the beam on the pick-up voltage and it is dependent on frequency, on the velocity of the beam particles β and on geometrical factors. It is very helpful to make the description in the frequency domain, where the independent variable is the angular frequency ω, related to the time domain by Fourier transformation [2].

The capacitive pick-up of Fig. 5.2 has a certain capacitance C, which is determined by the distance of the plate with respect to the beam pipe and a capacitance contributed by the cable between the plate and the amplifier input. This amplifier has a input resistor R. Using a current source to model the beam and the parallel connection of the equivalent circuit we can write its impedance Z as

$$\frac{1}{Z} = \frac{1}{R} + i\omega C \qquad \Longleftrightarrow \qquad Z = \frac{R}{1 + i\omega RC} \tag{5.6}$$

Therefore the transfer function of the pick-up is

$$U_{im} = \frac{R}{1 + i\omega RC} \cdot I_{im} = \frac{1}{\beta c} \cdot \frac{1}{C} \cdot \frac{A}{2\pi a} \cdot \frac{i\omega RC}{1 + i\omega RC} \cdot I_{beam} \equiv Z_t(\omega, \beta) \cdot I_{beam}. \tag{5.7}$$

---

[1] More precisely: The derivative of a function df/dt can be expressed as a multiplication of its Fourier transformation $\tilde{f}(\omega)$ with $-i\omega$.

[2] The frequency domain function $\tilde{f}(\omega)$ is calculated from the time domain function $f(t)$ by Fourier transformation as

$$\tilde{f}(\omega) = \frac{1}{\sqrt{2\pi}} \int_{-\infty}^{\infty} f(t) e^{i\omega t} dt \quad . \tag{5.4}$$

By inverse transformation the time domain function can be recovered as

$$f(t) = \frac{1}{\sqrt{2\pi}} \int_{-\infty}^{\infty} \tilde{f}(\omega) e^{-i\omega t} d\omega \tag{5.5}$$

if the given integral for $\tilde{f}(\omega)$ exists. Normally the absolute value $|\tilde{f}(\omega)|$ and the phase $\tan\varphi = Re(\tilde{f})/Im(\tilde{f})$ of this complex (in mathematical sense) function is displayed.

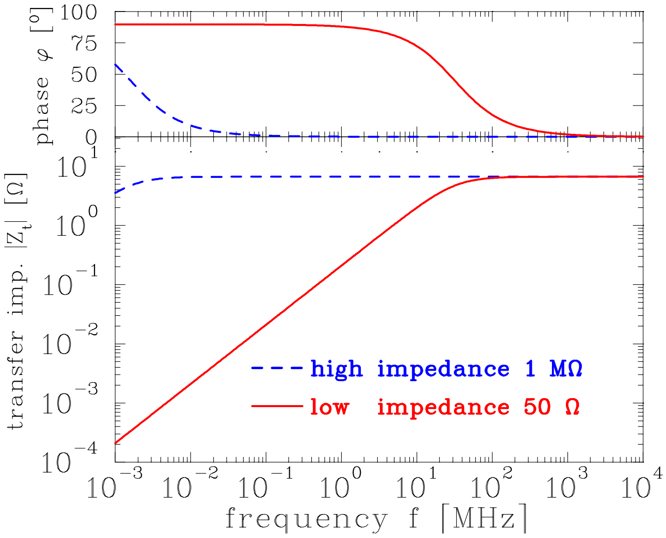

Figure 5.3: Absolute value and phase of the transfer impedance for a $l = 10$ cm long round pick-up with a capacitance of $C = 100$ pF and an ion velocity of $\beta = 50\%$ for high (1 MΩ) and low (50 Ω) input impedance of the amplifier. The parameters are typical for a proton/heavy ion synchrotron. The high-pass characteristic is clearly seen corresponding to a signal decreasing for low frequencies.

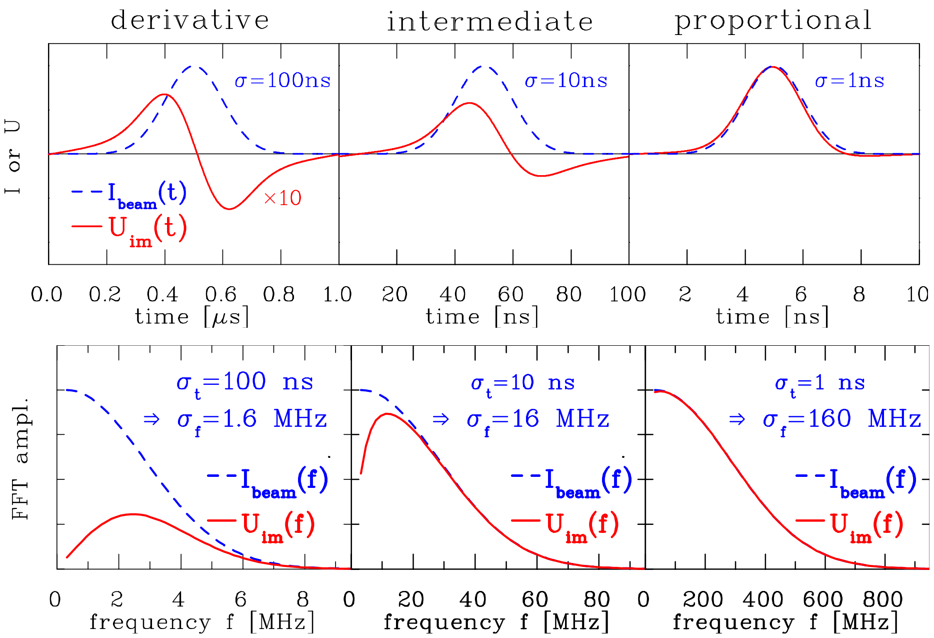

Figure 5.4: Simulation of the image voltage $U_{im}(t)$ for the values of the pick-up used in Fig. 5.3 terminated with $R = 50\ \Omega$ for three different bunch lengths of Gaussian distribution with σ of 100 ns, 10 ns and 1 ns, respectively. The cut-off frequency f_{cut} is 32 MHz. Note the different time scales. (The bunch length in the last case is artificially short for a proton synchrotron.) The shape of U_{im} is generated by the following steps: Given $I_{beam}(t) \rightarrow$ FFT yields $\tilde{I}_{beam}(\omega) \rightarrow$ multiplying by $Z_t(\omega)$ yields $\tilde{U}_{im}(\omega) = Z_t(\omega) \cdot \tilde{I}_{beam}(\omega) \rightarrow$ inverse FFT yields $U_{im}(t)$. The Fourier transformations are shown in the lower plots. Note, that a Gaussian function in time domain of width of σ_t has a Fourier transformation described by a Gaussian function of width $\sigma_f = 1/(2\pi\sigma_t)$ centered at $f = 0$.

This is a description of a first-order high-pass filter with a cut-off frequency $f_{cut} = \omega_{cut}/2\pi = (2\pi RC)^{-1}$. For the case of the so called linear cut pick-ups used at proton synchrotrons (see below), a typical value of the capacitance is $C = 100$ pF with a length of $l = 10$ cm. The high-pass characteristic is shown in Fig. 5.3 for a 50 Ω and a high impedance 1 MΩ amplifier input resistor. In the figure the absolute value

$$|Z_t| = \frac{1}{\beta c} \cdot \frac{1}{C} \cdot \frac{A}{2\pi a} \cdot \frac{\omega/\omega_{cut}}{\sqrt{1+\omega^2/\omega_{cut}^2}} \quad \text{and the phase relation} \quad \varphi = \arctan\left(\omega_{cut}/\omega\right) \tag{5.8}$$

is shown. A pick-up has to match the interesting frequency range, which is given by the accelerating frequency and the bunch length. In a proton synchrotron typical values of the accelerating frequency are in the range from 1-10 MHz, while for LINACs and electron synchrotrons typically 100 MHz to 3 GHz are used. We can distinguish two different cases for the transfer impedance, namely:

- **high frequency range** $\omega \gg \omega_{cut}$**:** Here we have

  $$Z_t \propto \frac{i\omega/\omega_{cut}}{1 + i\omega/\omega_{cut}} \longrightarrow 1. \tag{5.9}$$

  The resulting voltage drop at R is for this case

  $$U_{im}(t) = \frac{1}{\beta c C} \cdot \frac{A}{2\pi a} \cdot I_{beam}(t). \tag{5.10}$$

  Therefore the pick-up signal is a direct image of the bunch time structure with no phase shift, i.e. $\varphi = 0$. To get a low cut-off frequency $\omega_{cut} = 1/RC$, high impedance input resistors are used to monitor long bunches, e.g. in the proton synchrotron. The calculated signal shape is shown in Fig. 5.4 (right). Note that in the figure a 50 Ω termination is considered, leading to a large value of the cut-off frequency $f_{cut} = 32$ MHz. In the application of a proton synchrotron, high impedance (~ 1 MΩ) termination yielding a much lower value of the cut-off frequency, $f_{cut} = 10$ kHz in this case. A typical signal from this circuit is given in Fig. 5.5.

- **low frequency range** $\omega \ll \omega_{cut}$**:** The transfer impedance is here

  $$Z_t \propto \frac{i\omega/\omega_{cut}}{1 + i\omega/\omega_{cut}} \longrightarrow i\frac{\omega}{\omega_{cut}}. \tag{5.11}$$

  Therefore the voltage across R is in this case

  $$U_{im}(t) = \frac{R}{\beta c} \cdot \frac{A}{2\pi a} \cdot i\omega I_{beam} = \frac{R}{\beta c} \cdot \frac{A}{2\pi a} \cdot \frac{dI_{beam}}{dt} \tag{5.12}$$

  using again the frequency domain relation $I_{beam} = I_0 e^{i\omega t}$. We see that the measured voltage is proportional to the derivative of the beam current. This can also be seen from the phase relation of the high-pass filter in Fig. 5.3, where a phase shift of 90^o corresponds to a derivative. The signal is bipolar, as shown in Fig. 5.4 (left). A measurement from the GSI-LINAC is shown in Fig. 5.6.

The signal at the amplifier output depends on the frequency range as compared to the cut-off frequency. Of course the bunches are not pure sine waves, and therefore it might be that a mixture of proportional and derivative components are present, see Fig. 5.4 (middle).

With respect to the different limits of the transfer impedance, two important applications are discussed:

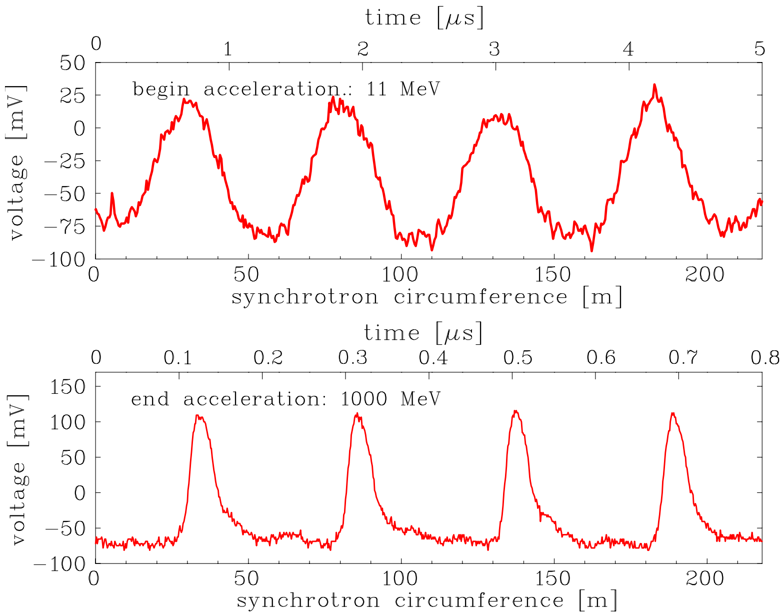

Figure 5.5: Bunch signals from a shoe-box pick-ups for 1 MΩ termination. The upper curve shows the bunches along the synchrotron circumference at the begin of the acceleration, the lower curve after reaching the final energy. Note the different time scales on top of the plots.

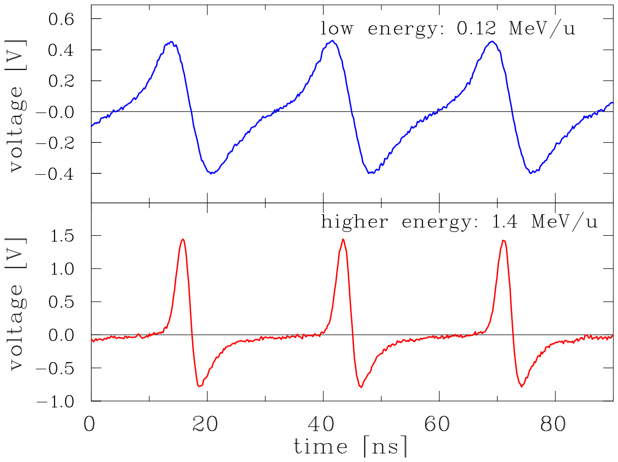

Figure 5.6: Bunch signal from a capacitive pick-up with 0.12 MeV/u (top) and 1.4 MeV/u (bottom) energy at the GSI-LINAC. The derivative behavior is caused by 50 Ω termination to achieve a large bandwidth of the amplifier. The accelerating frequency is 36 MHz.

- **Range $\omega \gg \omega_{cut}$ realized by a *low* ω_{cut} due to high impedance:**
  In a proton/heavy ion synchrotron a low frequency (1-10 MHz) is used for acceleration, resulting in bunches of several meters in length. In these machines, large apertures are necessary of more than $a = 10$ cm lowering the transfer impedance due to $Z_t \propto 1/a$. To get a larger sensitivity, the length of the pick-up in beam direction is increased, typically $l \sim 10$ cm due to $Z_t \propto l$. Note that the pick-up length is still much shorter than the bunch length. To have a flat curve of the sensitivity, i.e., a large bandwidth, a low $\omega_{cut} = 1/RC$ is used by feeding the signal into a high impedance FET transistor as the first step of the amplifier. A bandwidth of the amplifier circuit of 100 MHz can be reached, but it is very difficult to build them with larger bandwidth. To prevent for signal degeneration due to the limited amplifier bandwidth the application of high impedance amplifiers is restricted to proton/heavy ion

synchrotrons with less than $\sim$ 10 MHz acceleration frequency. (The observation of the contribution in the bunch spectrum from the tenth harmonic is sufficient.) As stated above and shown in Fig. 5.5 a direct image of the bunch is seen in this case.

- **Range $\omega \ll \omega_{cut}$ realized by a high ω_{cut} due to 50 Ω impedance:**
  At LINACs, the bunches are short, in the mm range, due to the higher accelerating frequencies (100 MHz to 3 GHz). First, one does not gain signal strength by making the length l larger. Second, a 50 Ω termination is used to prevent reflections and to get smooth signal processing with a large bandwidth up to several GHz. The short l, and therefore a lower capacitance C, and the $R = 50$ Ω leads to a high ω_{cut} and the derivative of the bunches is seen as displayed in Fig. 5.6.

The foregoing discussion does not take into account the effect of the frequency response of the associated cables. See [69] for a more detailed discussion. Moreover, at the high frequencies the excitation of standing wave modes might be possible.

5.2 LINAC pick-up for longitudinal bunch observation

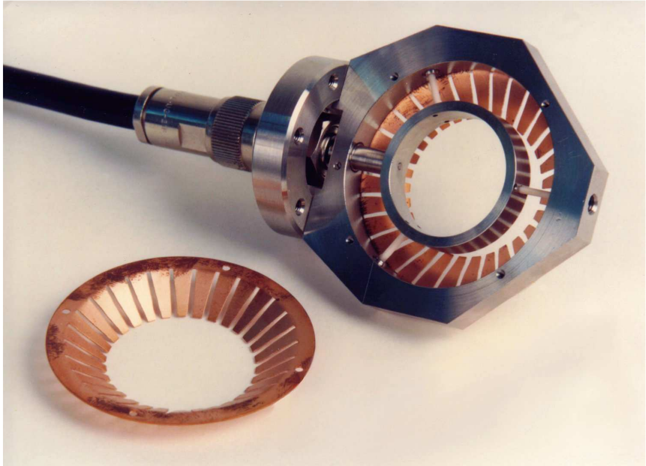

Figure 5.7: Capacitive pick-up in 50 Ω geometry as used for the longitudinal bunch observation at the 108 MHz GSI-LINAC. The inner diameter is 35 mm.

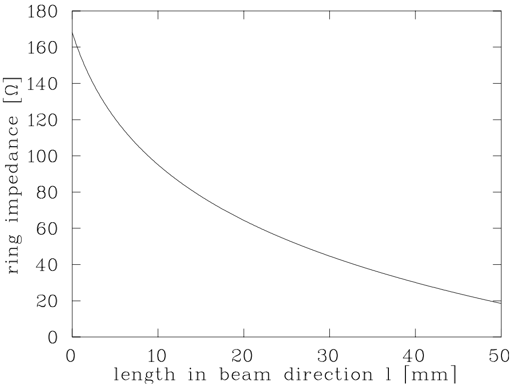

Figure 5.8: Calculation of the impedance of a ring pick-up as a function of the length in beam direction.

The observation of the bunches is an important parameter for the settings of a LINAC, to visualize the bunch shape, to setup the right phases between different accelerating structures and to measure the energy via time-of-flight in the case of proton/heavy ion LINACs; this is discussed in Chapter 6. Normally, 50 Ω is used as the input impedance of the amplifier, because a bandwidth of several GHz is needed [74]. A frequency of 1 GHz corresponds to a wavelengths of 30 cm in free space (TEM-mode), so the signal transit times can not be neglected. In case of the pick-up shown in Fig. 5.7 the 50 Ω is realized between the inner ring shaped electrode and the outer ring at ground potential. To calculate the impedance, one can take advantage of formulas given for the design of strip-lines. The capacitive pick-up is a strip-line bent around the beam pipe axis and its impedance Z_0 is given by

$$Z_0(l) = \frac{87}{\sqrt{\varepsilon_r + 1.4}} \ln\left(\frac{5.98h}{0.8l + d}\right) \tag{5.13}$$

where ε_r is the relative permeability, h is the distance between inner and outer conductor, d is the thickness of the inner ring and l is the length of the inner ring in beam direction. The diagram of Fig. 5.8 holds for $\varepsilon_r = 1$, $d = 3\,\text{mm}$ and $h = 10\,\text{mm}$. The induced signal can travel along two ways to the output cable corresponding to a parallel circuit of two transmission lines. The pick-up ring shown in Fig. 5.7 is designed for an impedance of $100\,\Omega$, to match the $50\,\Omega$ signal transmission via the coax-cable. A typical bunch signal measured with such a pick-up is shown in Fig. 5.6.

5.3 Position measurement with a capacitive pick-up

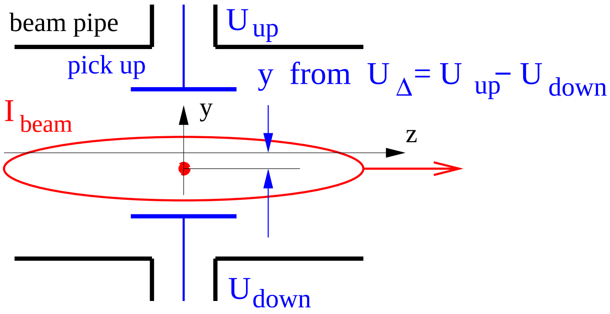

Figure 5.9: Schematics of a BPM for the vertical position reading using the proximity effect.

The deviation of the beam center with respect to the center of the vacuum chamber can be monitored using four isolated plates or buttons by determining the difference voltage $\Delta U_x = U_{right} - U_{left}$ or $\Delta U_y = U_{up} - U_{down}$ of opposite plates. The closer distance to one of the plates leads to a higher induced voltage. This is called the 'proximity effect' and schematically shown in Fig. 5.9. Normalizing to the total signal $\Sigma U_x = U_{right} + U_{left}$, the horizontal displacement x can be obtained via

$$x = \frac{1}{S_x} \cdot \frac{U_{right} - U_{left}}{U_{right} + U_{left}} = \frac{1}{S_x} \cdot \frac{\Delta U_x}{\Sigma U_x} \quad \text{(horizontal)} \tag{5.14}$$

which is independent of the beam intensity. For the vertical plane the position y is given by

$$y = \frac{1}{S_y} \cdot \frac{U_{up} - U_{down}}{U_{up} + U_{down}} = \frac{1}{S_y} \cdot \frac{\Delta U_y}{\Sigma U_y} \quad \text{(vertical).} \tag{5.15}$$

This position measurement is the most frequent application of pick-ups, hence they are called **B**eam **P**osition **M**onitor **BPM**. The proportional constant S_x respectively S_y between the measured normalized voltage difference and the beam displacement is called **position sensitivity**

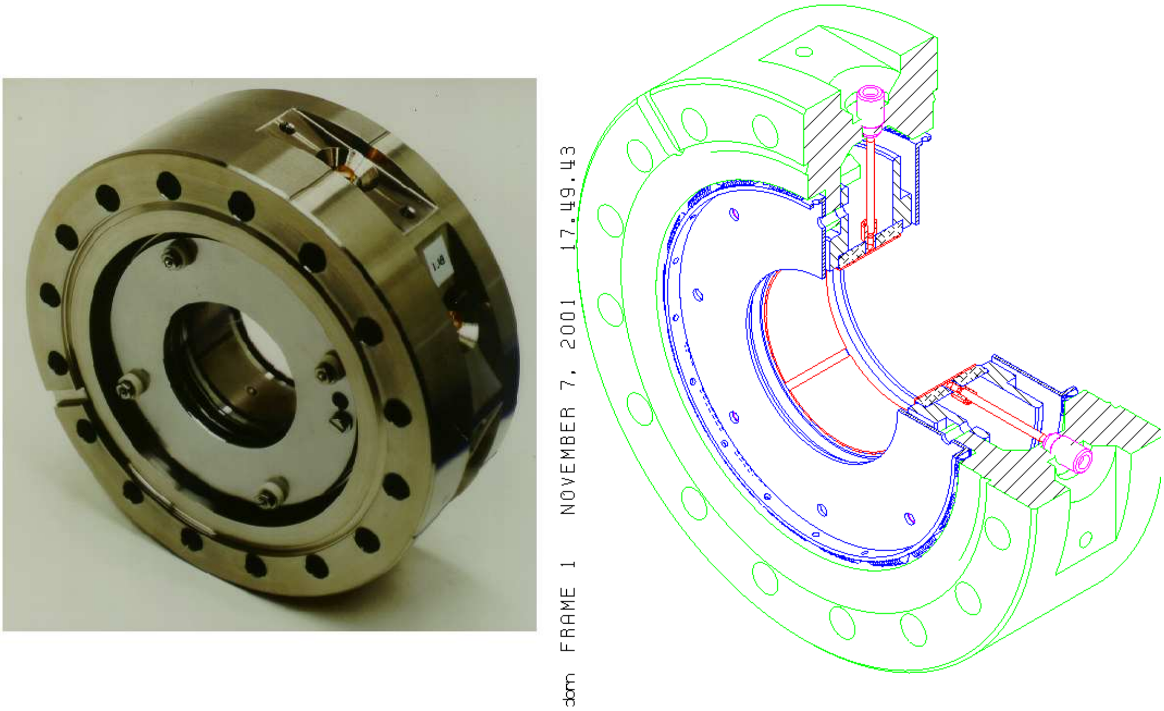

Figure 5.10: Photo and schematic drawing of a capacitive position sensitive pick-up at the GSI-LINAC. The aperture is 50 mm and the electrode length 20 mm.

and its unit is $S = [\%/mm]$. It is possible that the position sensitivity additionally depends on the beam position itself, corresponding to a non-linear voltage response for a large beam displacement. Moreover, S can also depends on the evaluation frequency.

Like in the case of longitudinal coupling, we can define the transverse transfer impedance $Z_\perp$as

$$\Delta U_x = Z_\perp \cdot x I_{beam} \tag{5.16}$$

for an off-center position x and a beam current I_{beam}; the product xI_{beam} is sometimes called the dipole moment of the beam. $Z_\perp$ can be written as a product of the longitudinal transfer impedance Z_t and a geometric non-linear function $g(x)$ as

$$Z_\perp = \frac{Z_t}{g(x)}. \tag{5.17}$$

An example of a capacitive pick-up used at the GSI-LINAC is shown in Fig. 5.10. The plates consist of (nearly) a quarter cylinder segment with radius a. For typical displacements up to $x < 1/2 \cdot a$ the function $g(x) = a$ is sufficiently constant. For larger displacements, the response is non-linear and a correction algorithm has to be applied to the digitized signals. For the device shown, the aperture is 50 mm and a relatively large length of $l = 20$ mm in the beam direction is used to attain a large signal strength.

5.4 Position measurement using button pick-ups

For a round arrangement of buttons, a simple 2-dimensional electro-static model can used to calculate the voltage difference as a function of beam displacement. According to Fig. 5.11 we assume a thin, 'pencil' beam of current I_{beam} which is located off-center by the amount r at an

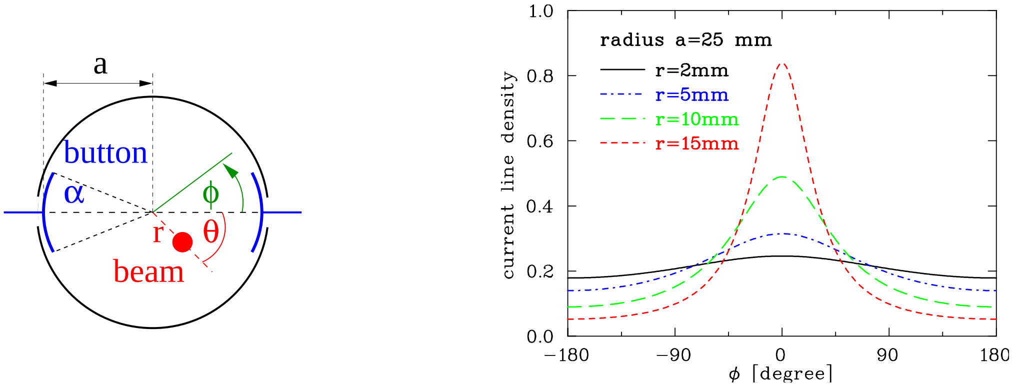

Figure 5.11: Schematics for a button BPM and the image current density generated by a 'pencil' beam at different displacements r for an azimuth $\theta = 0$.

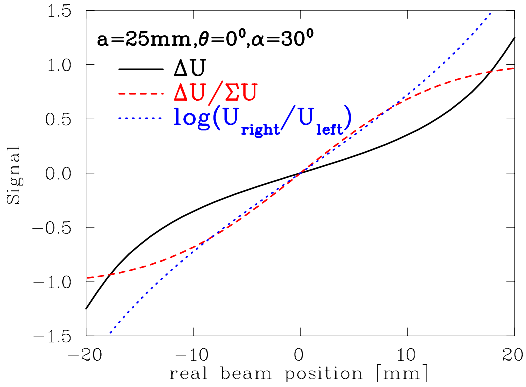

Figure 5.12: Difference voltage, normalized difference and logarithmic ratio for a button BPM arrangement of angular coverage $\alpha = 30^o$ as a function of horizontal beam displacement i.e. $\theta = 0$ for a beam pipe radius $a = 25$ mm.

angle θ. The wall current density j_{im} at the beam pipe of radius a is given as a function of the azimuthal angle ϕ as

$$j_{im}(\phi) = \frac{I_{beam}}{2\pi a} \cdot \left(\frac{a^2 - r^2}{a^2 + r^2 - 2ar \cdot \cos(\phi - \theta)} \right) \tag{5.18}$$

and is depicted in Fig. 5.11; see [75] for a derivation of this formula.

As discussed above, this represents the proximity effect, where the current density depends on the distance with respect to the beam center. The buttons covering an angle α and the image current I_{im} is recorded as given by:

$$I_{im} = a \int_{-\alpha/2}^{+\alpha/2} j_{im}(\phi) d\phi \quad . \tag{5.19}$$

The resulting signal difference for opposite plates as a function of horizontal beam displacement (corresponding to $\theta = 0$) shows a significant non-linear behavior as displayed in Fig. 5.12. It can be seen, that for the normalized difference $\Delta U / \Sigma U$ the linear range continues to larger beam offsets. The non-linearity increases if the beam center moves outside the horizontal axis, which is depicted in Fig. 5.13 for different values of the azimuthal orientation θ as a function of horizontal displacement according to Eqs. 5.18 and 5.19. For an orientation along the diagonal line, a significant deviation from linearity starts for this case even at about 1/4 of the beam pipe

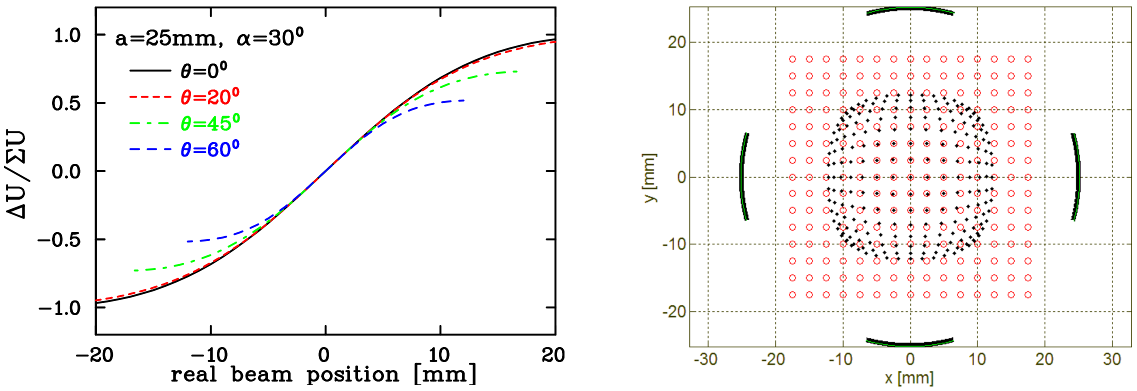

Figure 5.13: Left: Horizontal position calculation for different azimuthal beam orientation θ for the parameters of Fig. 5.12. Right: In the position map the open circles represent the real beam position and the dots are the results of the $1/S \cdot \Delta U/\Sigma U$ algorithm with $S = 7.4$ %/mm for the central part.

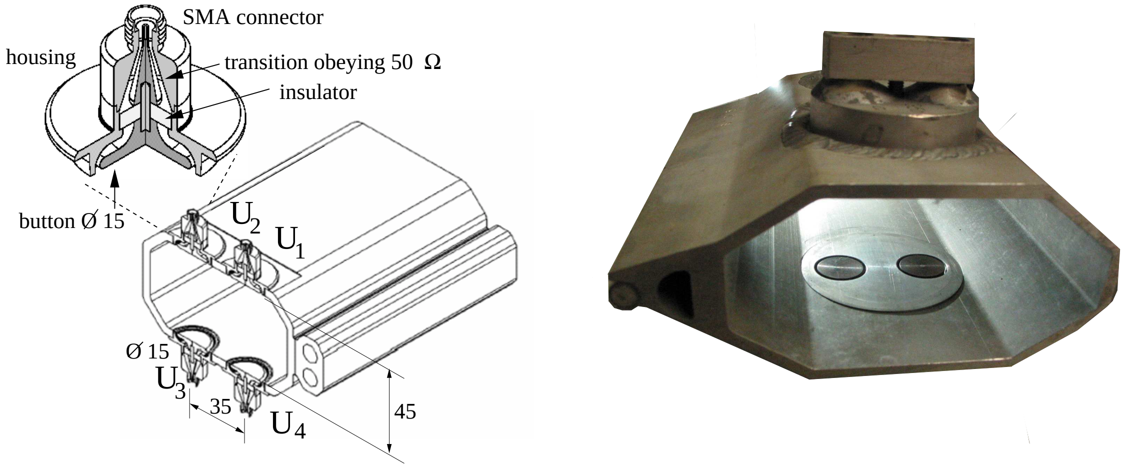

Figure 5.14: Right: Typical button BPM arrangement within a vacuum chamber at a synchrotron light source, from [79]. Right: Photo of the realization at HERA, DESY.

radius. However, in the central part the reading is nearly independent of the orientation leading to a universal position sensitivity S. The dependence between the horizontal and vertical plane is better depicted in the position map of Fig. 5.13, right: Here the real beam positions with equidistant steps are plotted as well as the results using $1/S \cdot \Delta U/\Sigma U$ calculations with S fitted at the central part.

Button pick-ups are the most popular devices for electron accelerators. They consist of a circular plate of typically 1 cm diameter mounted flush with the vacuum chamber as shown in Fig. 5.14. The cross section of the chamber is not changed by this insertion, to avoid excitation of wake fields by the beam. The button itself should have a short vacuum feed-through with a smooth transition to the 50 Ω cable, to avoid excitation of standing waves and to reach a bandwidth up to 10 GHz. Fig. 5.14 shows a typical setup used at electron accelerators, where the buttons are not mounted in the horizontal plane to avoid synchrotron light hitting the feed-through. According to Fig. 5.15 the position is calculated via

$$\text{horizontal:}\quad \frac{\Delta U_x}{\Sigma U_x} = \frac{(U_2+U_4)-(U_1+U_3)}{U_1+U_2+U_3+U_4} \qquad \text{vertical:}\quad \frac{\Delta U_y}{\Sigma U_y} = \frac{(U_1+U_2)-(U_3+U_4)}{U_1+U_2+U_3+U_4} \tag{5.20}$$

using all four pick-up voltages for the position determination. This geometry leads to a non-

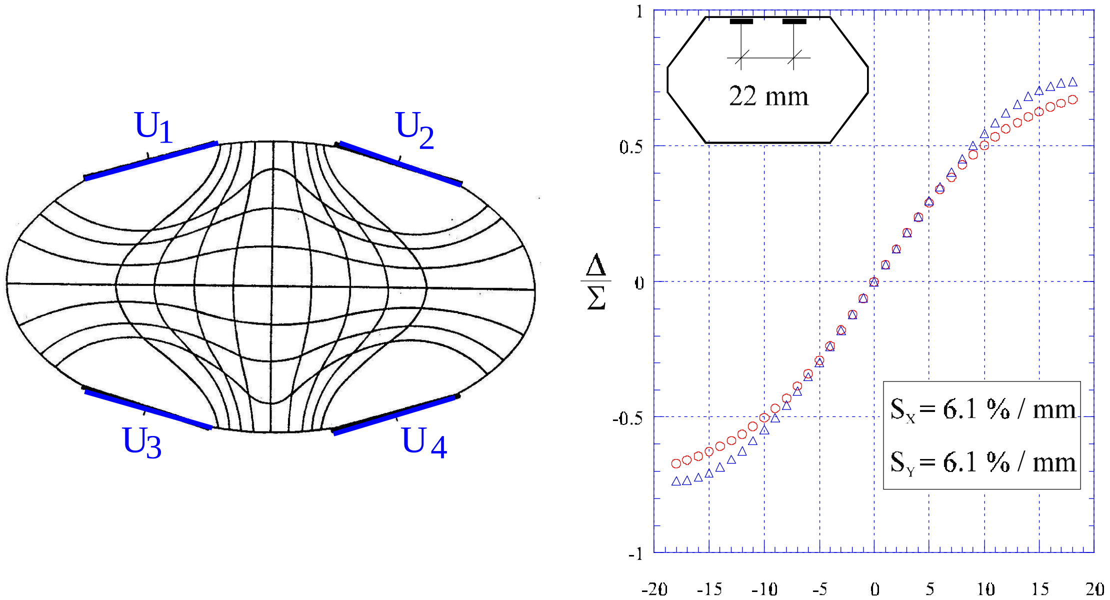

Figure 5.15: Iso-level curves for an arrangement of button pick-ups are shown on the left. On the right: The calculated accuracy for the difference voltage over the sum Δ/Σ as a function of beam displacement (horizontal o, vertical $\triangle$) for the displayed button arrangement [81].

linear position sensitivity (i.e. non linear $g(x)$ in Eq. 5.17). The iso-levels for this geometry are shown. A displacement of the beam center on one of these lines lead to the same reading in the difference voltage of the desired plane. A good location of the buttons for a linear sensitivity has to be calculated numerically (see e.g. [80, 81]). The optimized location depends on the size and distances of the pick-ups, as well as the chamber cross section. The result for such an optimized setting is shown in Fig. 5.15.

5.5 'Shoe box' pick-ups using the so-called linear cut

Due to the long bunches at proton/heavy ion synchrotrons, one can use long plates of typically 20 cm to enhance the signal strength. A box-like device is used normally, to get a precise linear dependence with respect to the beam displacement, see Fig. 5.16. For the previously discussed pick-up geometries, the signal of the plate closer to the beam's center-of-mass is larger than that

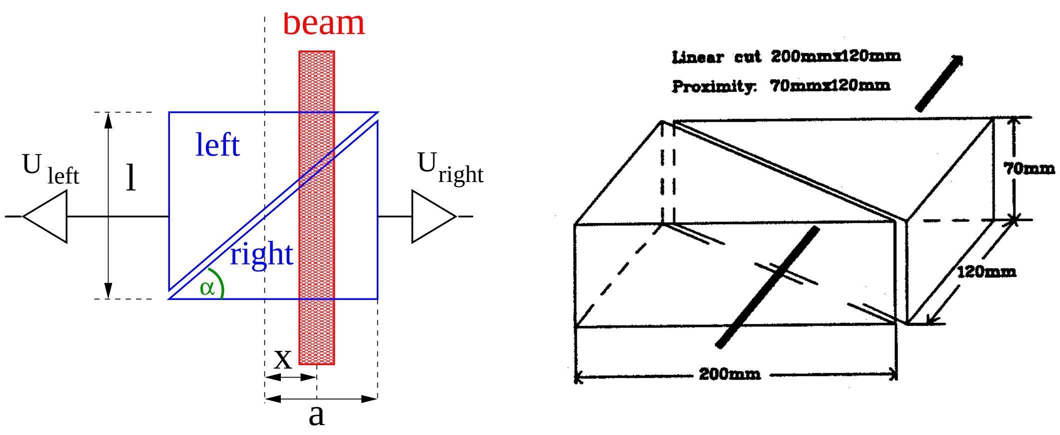

Figure 5.16: Scheme of the position measurement using the so-called linear cut and an example of an electrode arrangement for the horizontal plane.

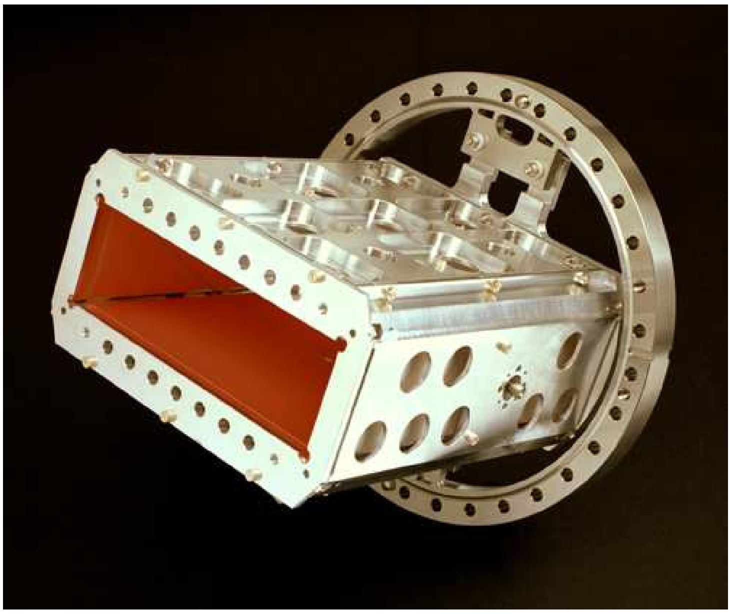

Figure 5.17: Linear cut position pick-up from the GSI synchrotron ring.

of the more distant plate; this is called the proximity effect. In contrary to that, the shoe-box pick-ups have another principle: The influenced signal is proportional to the actual plate length at the beam center position. For a given beam displacement x the electrode's image voltage U_{im} is proportional to the length l of the beam projected on the electrode surface as shown for the horizontal direction in Fig. 5.16, left. For triangle electrodes with half-aperture a one can write:

$$l_{right} = (a + x) \cdot \tan\alpha \qquad \text{and} \qquad l_{left} = (a - x) \cdot \tan\alpha \qquad \Longrightarrow \qquad x = a \cdot \frac{l_{right} - l_{left}}{l_{right} + l_{left}} \quad . \tag{5.21}$$

The position reading is linear and can be expressed by the image voltages as

$$x = a \cdot \frac{U_{right} - U_{left}}{U_{right} + U_{left}} \equiv \frac{1}{S_x} \cdot \frac{\Delta U_x}{\Sigma U_x} \qquad \Longrightarrow \qquad S_x = \frac{1}{a} \tag{5.22}$$

which shows that the position sensitivity for this ideal case is simply given by the inverse of the half-aperture. Compared to other types of pick-ups, the position sensitivity is constant for nearly the full range of displacements, i.e. nearly no corrections due to non-linearities have to be applied [82]. This is demonstrated in Fig. 5.18. The electrode arrangements is shown in Fig. 5.16 and the analog signal in Fig. 5.5.

5.6 Signal treatment of a stripline pick-up

When the bunch length becomes comparable to the length of a capacitive pick-up, the signal is distorted. In the discussion above, the pick-up was treated as a grounded prolongation of the beam pipe. Now we want to take the signal propagation via a transmission line into account. The stripline pick-up is used for short bunches with relativistic velocities. In a collider, the system offers the possibility of the signal suppression from one of the counter-moving beams, due to their directional characteristic (see below).

A stripline pick-up consists of a transmission line of several cm length l, having at both ends a feed-through with a impedance of R_1 and R_2, normally 50 Ω, see Fig. 5.19. The stripline is installed in a cylindrical chamber with radius r at a distance from the beam center a covering an angle of α. This line has a certain impedance Z_{strip} depending on the parameters r, a, α

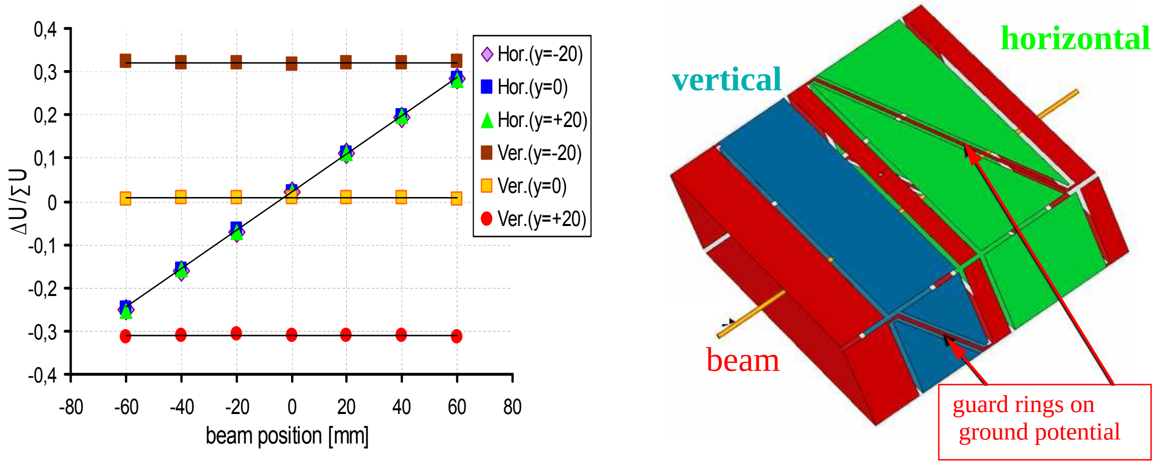

Figure 5.18: Numerical calculation of the position reading $\Delta U/\Sigma U$ as a function of beam displacement for the horizontal plane. The plot also includes the calculations for a beam offset in the vertical direction and proves the decoupling of both planes [82]. It is performed for the pick-up shown right and in Fig 5.17 with a 200×70 mm^2 cross section and 350 mm length.

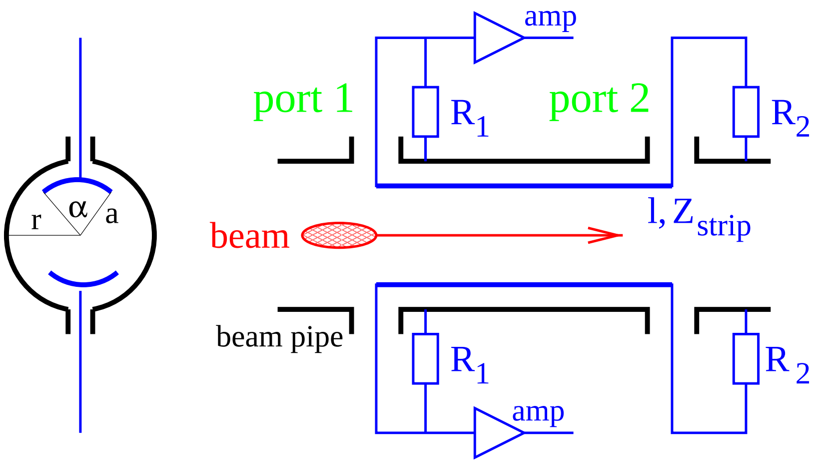

Figure 5.19: Scheme of a stripline pick-up.

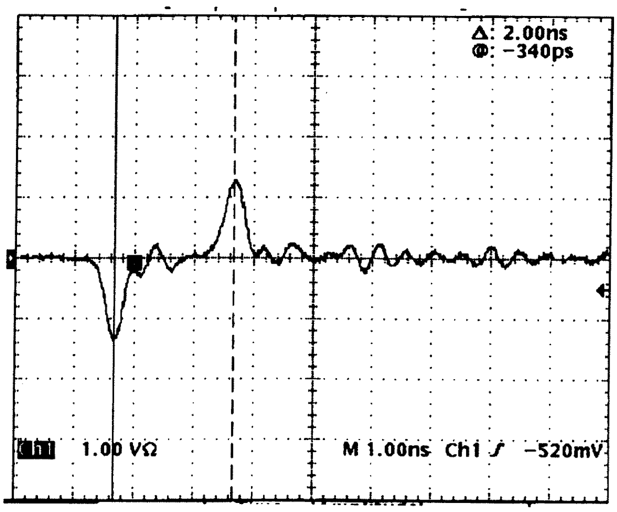

Figure 5.20: Single shot signal from from a 30 cm stripline pick-up recorded at the ALS synchrotron light facility for a single bunch with 1 ns/div [71].

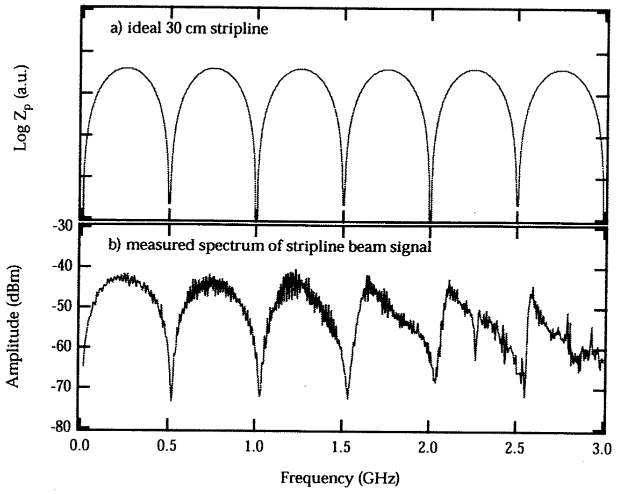

Figure 5.21: Calculated transfer impedance of an ideal 30 cm stripline (a) and and a measurement (b) with a spectrum analyzer for a single bunch signal [71]. The frequency range is 0 to 3 GHz.

[78]. The stripline is matched to the outer resistor $Z_{strip} = R_1 = R_2$. In the following, a beam velocity $\beta = 1$ and a bunch length much shorter than the stripline are assumed. When the beam enters the upstream port 1 of the stripline, a fraction of the image charge of the wall current acts as a current source. Due to the matching of the voltage divider $Z_{strip} = R_1$ half of this signal travels toward the feed-through 1 and half of it travels down the stripline. Assuming a TEM mode with a phase velocity c, this signal travels in phase with the beam. At the downstream port 2 the image charge leaves the stripline, generating an equal and opposite current source and it is split in half due to $Z_{strip} = R_2$. However, the image current is leaving the detector and has the opposite sign to that of the upstream port. Therefore, this half of the signal cancels the signal traveling with the beam created at the upstream port 1. The other half travels now back toward the upstream port and arrives there at the time $2l/c$. A signal recorded with this device is shown in Fig. 5.20.

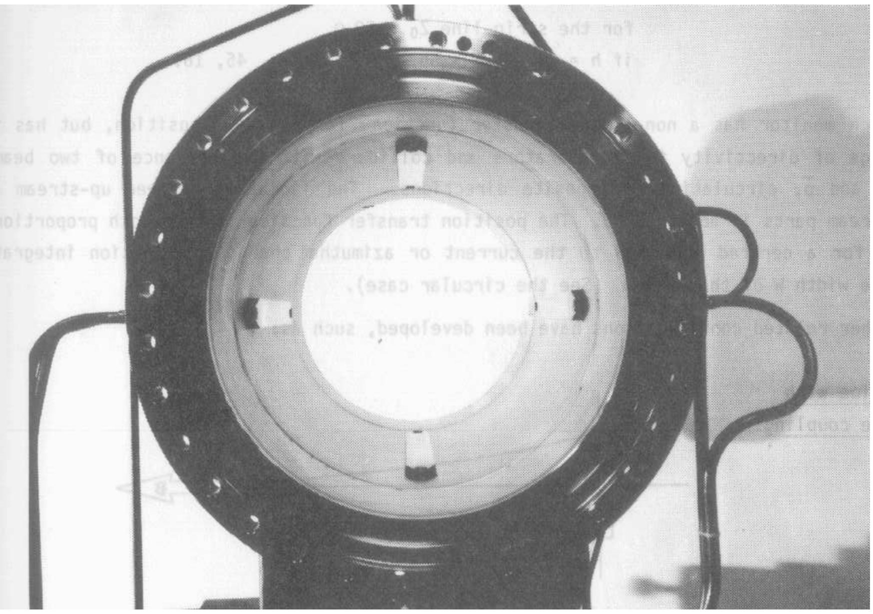

Figure 5.22: Photo of a stripline pick-up at the CERN SPS, from [78].

We can write the behavior at port 1 as

$$U_1(t) = \frac{1}{2} \cdot \frac{\alpha}{2\pi} \cdot R_1 \left(I_{beam}(t) - I_{beam}(t - 2l/c) \right) \ . \tag{5.23}$$

For very short bunches, i.e., $I_{beam}(t) \to \delta(t)$, it can be shown via Fourier transformation that the corresponding transfer impedance Z_t is [70, 73, 72]

$$Z_t(\omega) = Z_{strip} \cdot \frac{\alpha}{2\pi} \cdot \sin\left(\omega l/c\right) \cdot e^{i(\pi/2 - \omega l/c)} \tag{5.24}$$

The absolute value of Z_t compared to a measurement is shown in Fig. 5.21, as recorded for a 30 cm matched detector at the ALS synchrotron light facility [71].

The transfer impedance shows some interesting features:

- $|Z_t|$ shows a maximum for $l = c/4f = \lambda/4$, where λ is the wave length. Therefore it this called a quarter wave coupler.
- The length l is chosen to work close to the maximum sensitivity.
- The sensitivity is zero for $l = \lambda/2$. This means no signal is present when the spacing between bunches are equal to $2l$, because the interference between following bunches is destructive.
- The phase for Z_t are straight lines with a zero phase shift at the maximum sensitivity $l = \lambda/4$. For this frequency, the recorded signal is a direct image of the bunch.
- In contrast with capacitive pick-ups, short bunches can be monitored without signal deformation (working at the maximum sensitivity).

Matching the stripline with good accuracy is a difficult task, due to the high desired frequency range. To prevent reflections at the downstream port, ferrite absorbers can be used [77]. In colliders, the directional coupling can be very useful to distinguish between the position of the two counter-rotating beams within a common vacuum chamber. An example of a realization at CERN SPS is shown in Fig. 5.22.

For the position measurement other techniques are also used, including monitors measuring the magnetic field (so called inductive pick-ups) or the excitation of cavity modes. Further descriptions can be found in [78, 90, 91].

5.7 Electronic treatment for position determination

To get the position of the beam, the signals from the electrodes have to be compared. For this comparison, the signal shape (differentiation or proportional behavior) is of minor importance. The electronics used for this purpose are described only very briefly. A detailed review is given in [83]. For the position resolution, the signal-to-noise ratio is important. Beside the stray fields from the rf cavities, the broadband amplifier noise, as well as the electronic noise of the following devices contribute. Therefore a minimum bunch current is needed for a reliable position measurement. Two different principles are commonly used: the so called broadband and narrowband processing:

In the broadband case, as shown in Fig. 5.23, the signals from the individual plates are amplified (or even attenuated) to adapt the signal strength to the ADC input level. The sum and difference signal is then calculated from the digital values. For noise reduction and alias-product suppression, a lowpass filter is used matched to the sample rate of the ADC. In older installations fast sampling was not possible and an external trigger, as generated from the

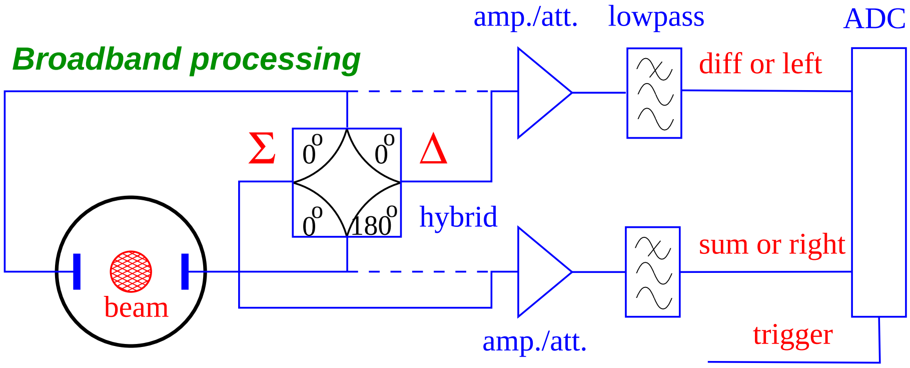

Figure 5.23: Scheme of a broadband signal processing. The plate signals are either fed directly to the amplifier (dashed line) or via a hybrid the sum and difference is generated in an analog manner (solid line).

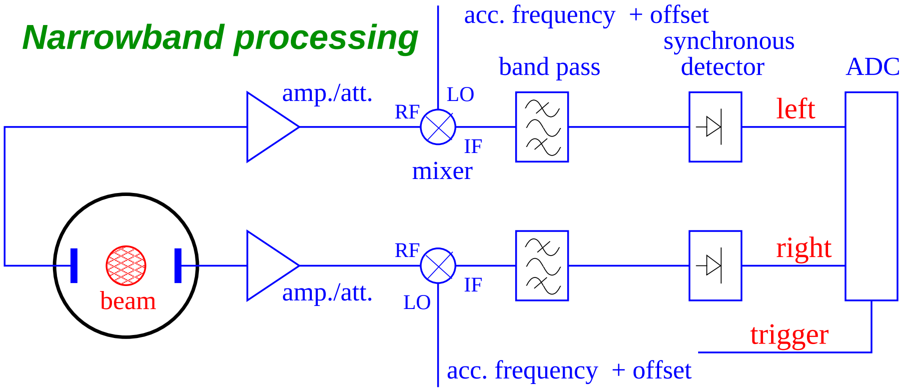

Figure 5.24: Schematic signal analysis for a narrowband treatment.

bunch passage in an analog manner forced the digitalization. In many applications the sum and difference voltages are analogously generated by a 180^o hybrid or a differential transformer. Because they are pure passive devices, they can be mounted quite close to the BPM plates even in case of high radiation. The resulting sum and difference signals are then stored in the ADC. The difference signal, which is normally lower by at least a factor of 10, can be amplified by a higher amount than the sum signal to exploit the full ADC range. (An overview of standard rf components can be found in [84].) The analog electronics is required to match the signal shape to the properties of the ADCs and an appropriate trigger is used for the digitalization. Modern installations do not use these types of analog electronics, instead the signal is directly digitized by a fast ADCs or digital receivers, which are even commercially available [85]. With the help of high speed digital signal processing the bunch signal is than reduced to one value per bunch and the beam position is calculated from the sum and difference value [86, 87]. The precision of this method is lower as compared to the narrowband processing described below. For electron machines, with small beam size, a resolution of 100 μm can been achieved by this broadband processing. The advantage is the possibility to do a bunch-by-bunch analysis (i.e. measuring the position of always the same bunch rotating in a synchrotron) by using an appropriate trigger setting or precise digital signal processing.

The narrowband processing is used to get a higher precision of the position reading, attaining 1 μm in electron machines here. The better signal-to-noise ratio is achieved by reducing the bandwidth of the signal processing by several orders of magnitude. As an illustrative example the Fourier-Transformation of the signal form the GSI-LINAC pick-up is shown in Fig. 5.25. The spectral power of the signal is mainly available at the bunch repetition harmonics nf_0. The

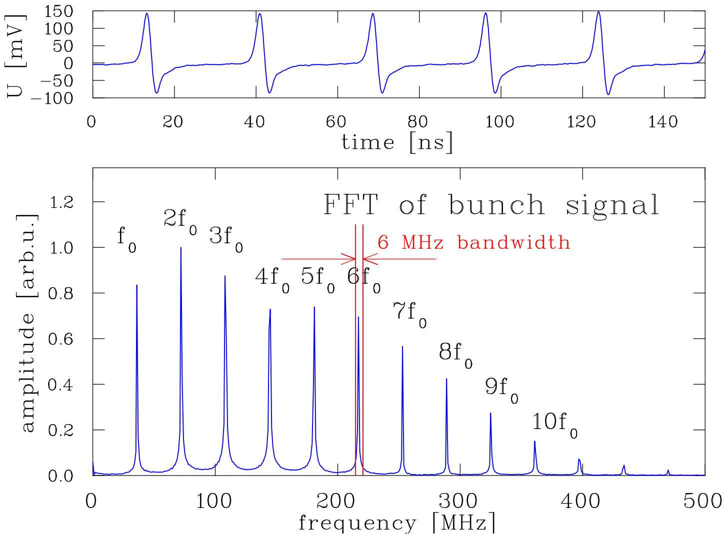

Figure 5.25: Bunch signal (top) and its Fourier transformation (bottom) at the GSI-LINAC of a 1.4 MeV/u beam. In the Fourier spectrum each line corresponds to the indicated harmonics of the 36 MHz accelerating frequency. The position evaluation is done at $6f_0 = 216.8$ MHz by a 6 MHz narrowband processing as indicated by the red lines.

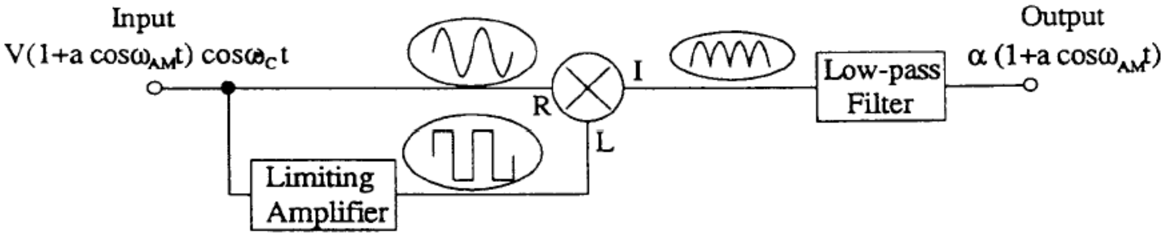

Figure 5.26: Scheme of a synchronous detector to rectify an rf signal: The rf signal is split and one branch is fed into a limiter amplifier driven into saturation, which transforms the signal to a bipolar rectangular pulse. This signal is mixed with the original signal to yield a unipolar waveform (corresponding to the square). It is passed through a low-pass filter and can then be digitized by a low sampling ADC.

position evaluation uses only this large signal power within the band of frequency span Δf, while the thermal noise is reduced as $U_{eff} \propto \sqrt{\Delta f}$. Technically, the pick-up signal is mixed with the accelerating frequency. A mixer is a passive rf-device multiplying the two waves at the port RF (for radio frequency) and LO (for local oscillator). The product is available at port IF (for intermediate frequency). From a mathematical point of view, the mixer multiplies the two waves at LO and RF and we get from a trigonometric theorem [3]

$$A_{IF}(t) = A_{RF} \cdot A_{LO} \cos\omega_{RF}t \cdot \cos\omega_{LO}t = \frac{1}{2}A_{RF} \cdot A_{LO}\left[\cos(\omega_{RF} - \omega_{LO})t + \cos\left(\omega_{RF} + \omega_{LO}\right)t\right]. \tag{5.25}$$

Typically 10.7 MHz, or one of its harmonics (due to it's large use in telecommunication), is filtered out by a narrow bandpass filter. The signal is rectified by a so called synchronous detector, for which the schematics are shown in Fig. 5.26.The resulting quasi-dc signal is then digitized and the position is calculated via software. In general, this technique is called heterodyne mixing and the same principle is used in a spectrum analyzer. The mixing is equivalent to an average over many turns leading to much higher precision in the position reading. But this method does not allow a turn-by-turn observation. For a proton/heavy ion synchrotron at non-relativistic ve-

---

[3] $\cos x \cdot \cos y = 1/2 \cdot [\cos(x - y) + \cos(x + y)]$

Soll-Delay: 10.000 ms Rampenlänge: 1578.00 ms Flattoplänge: 4509.00 ms

Figure 5.27: Example of a position measurement done at the GSI synchrotron for a partly misaligned beam during the acceleration. The top plot shows the position around the ring at a certain time, the lower left is the position for one pick-up and the lower right is the sum signal power $\propto U_\Sigma^2$ during the ramp for the same single pick-up.

locities, this method can also be applied, because the varying accelerating frequency is changed in phase with the bunch signal, resulting in a constant intermediate frequency. Such a system is commercially available [88]. Modern systems use digital filtering and data reduction with a Digital Signal Processor [89]. Other, more complex techniques suited for large accelerators are described in [83].

5.8 Closed orbit measurement

In a synchrotron, several pick-ups for the determination of the closed orbit are installed. A good choice is to have four pick-ups per tune value separated approximately by about $\mu \simeq 90^o$ betatron phase advance. The pick-ups should be located at position with a large value of the betatron function to have a reasonable spatial resolution even for smaller average beam excursions. The closed orbit is the central beam path along the machine, taking the existing imperfections into account. The closed orbit might differ from the ideal path, defined by the center of the quadrupole magnets. Only for a good alignment the real beam behave as expected from beam optics calculations, e.g. no beam steering by the quadrupole magnets occurs. An example for the use of a position measurement is displayed in Fig. 5.27 during the acceleration in the SIS synchrotron.

The position reading of the pick-ups around the ring can be used as the input of a feedback loop to do an active beam correction, see e.g. [93]. Such a feedback system is installed in most synchrotrons, but a description is out of the scope of this lecture.

5.9 Tune measurement

One very important parameter of a synchrotron is its tune. For machines running at high current, the incoherent tune spread, related to the space charge of the beam, is of interest to find a large stable region in the working diagram. For these parameters, the tune as a function of stored current has to be evaluated. Pick-ups measure the center of the bunched beam. First we define the betatron frequency f_β as

$$f_\beta = Q \cdot f_0 \tag{5.26}$$

as the tune Q expressed in relation to the revolution frequency f_0. The tune itself is the number of betatron oscillations per turn. The idea of a tune measurement related to pick-ups is to excite a coherent transverse betatron oscillation, whose frequency gives the tune.

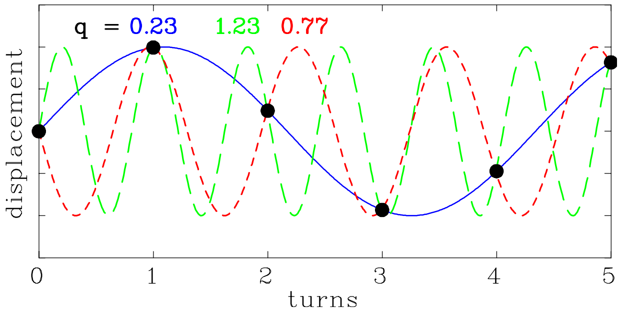

Figure 5.28: Schematic of the tune measurement for six subsequent turns determined with one pick-up, together with with the three lowest frequency fits.

The tune value can be split in two parts as $Q = Q_n + q$ with Q_n is the integer part and q fractional part. Most measurement methods can only determine the fractional part q. The integer number of oscillations Q_n cannot be seen, but this is normally of no interest, as it is known from calculations. This behavior is schematically shown in Fig. 5.28 for the case of a turn-by-turn reading of one pick-up: Having the position reading, a sine function can be drawn through the data, but one cannot distinguish between the lowest frequency (here $q = 0.23$) and higher values, leading to the fact that the fractional part is only uniquely defined for $0 < q < 0.5$. To distinguish between a value below or above 0.5, the focusing by the quadruples (i.e. the tune) can be slightly changed and the direction of the shift of q can be observed. The calculation of q is done by a Fourier analysis of the time domain data.

Most methods used today are based on a frequency domain treatment. Before discussing this, a simpler excitation method is described first, using a time domain point of view.

5.9.1 The kick method, time domain method

Coherent betatron oscillations are excited by a fast kick. This kick has to be much shorter than the revolution time $1/f_0$ and is provided in most cases by the injection or extraction kicker installed in the machine anyhow. The strength of the kick has to be chosen with care, so the beam is not lost. To get a reasonable resolution, the pick-up should be located at lattice point with a large value of the betatron function. The beam position is monitored turn-by-turn (broadband processing only) and it is stored as a function of time. The Fourier transformation of the displacements gives the fractional part q of the tune and the width of the Fourier line give the tune spread with $\Delta q = \Delta Q$ (assuming a sufficient resolution). An example from the GSI synchrotron is shown in Fig. 5.29.

To understand the limitation of this method, one has to look at the single particle behavior. At the time of the kick, the particles start a free betatron oscillation with the same phase, but

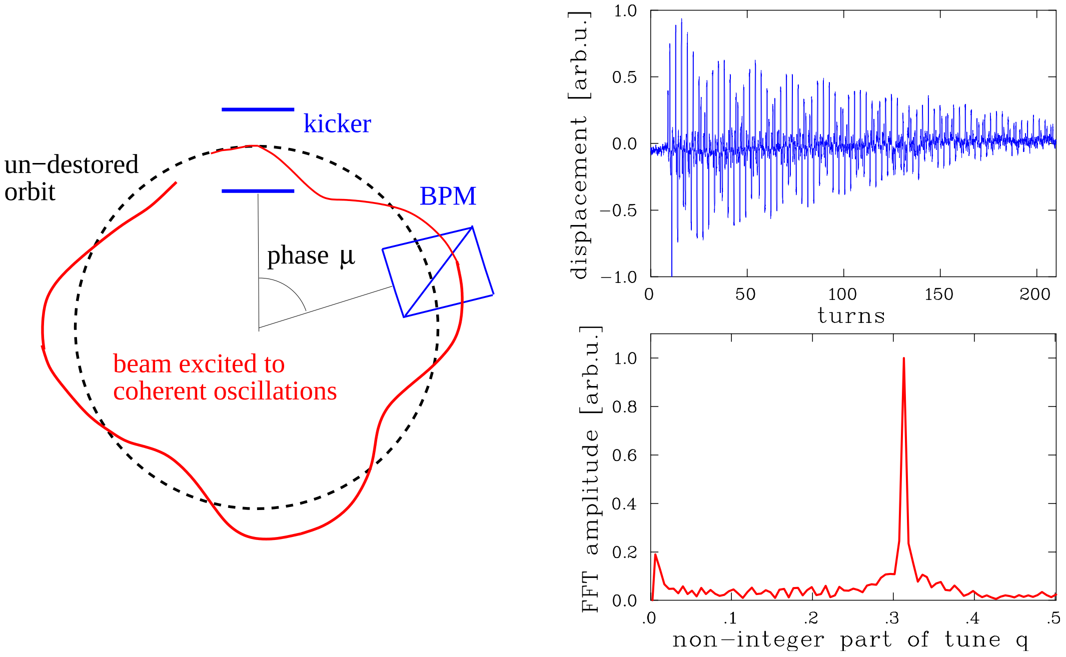

Figure 5.29: Beam oscillations after a kick excitation recorded in the time domain for 200 turns (top) and its Fourier transformation for q determination (bottom) at the GSI synchrotron.

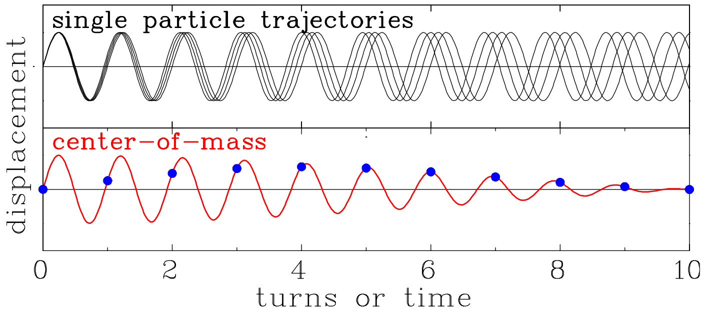

Figure 5.30: Plot of the individual trajectories of four particles after a kick (top) and the resulting coherent sum signal as measured by a pick-up (bottom). (The tune spread is much to large for a real machine.)

each particle has a slightly different betatron frequency due to the tune spread. Even if the individual oscillations last for a long time, the coherent motion detected by a pick-up is damped as a consequence of the de-coherence of the individual motion given by the time of the inverse betatron frequency spread, see Fig. 5.30. A description is given in the frame of Landau damping. This damping limits the observation time and therefore the precision of the tune determination by this method. The tune is calculated from the position reading via Fourier transformation: A limited series of position measurements $x_1, x_2, ..., x_N$ of N consecutive turns with non-vanishing displacements are taken into account. The distribution function of the tune $P(q_i)$ is calculated via discrete Fourier expansion from the displacement reading via

$$P(q_i) = \frac{1}{N}\sum_{n=1}^{N} x_n e^{-2\pi i n q_i} \quad . \tag{5.27}$$

The discretization of the obtained peak is generally related to the number of position samples N by

$$\Delta q = \frac{1}{2N} \tag{5.28}$$

according to the Nyquist theorem. Therefore the peak in the distribution function $P(q_i)$ has at least this width. To achieve an adequate resolution of typically $\Delta q \simeq 10^{-3}$ at least $N = 500$ turns of non-vanishing displacements are needed. In a lot of practical cases the de-coherence time is shorter than this border as demonstrated in Fig. 5.29. Therefore this straightforward method is not very precise. But there exists some improved analysis methods using digital filters to achieve a better precision, see e.g. [95].

An additional drawback of such a measurement is a blow-up of the transverse emittance of the stored beam, because the excitation of the individual particles are damped much slower than the coherent motion as depicted in Fig. 5.30.

5.9.2 Beam transfer function measurement

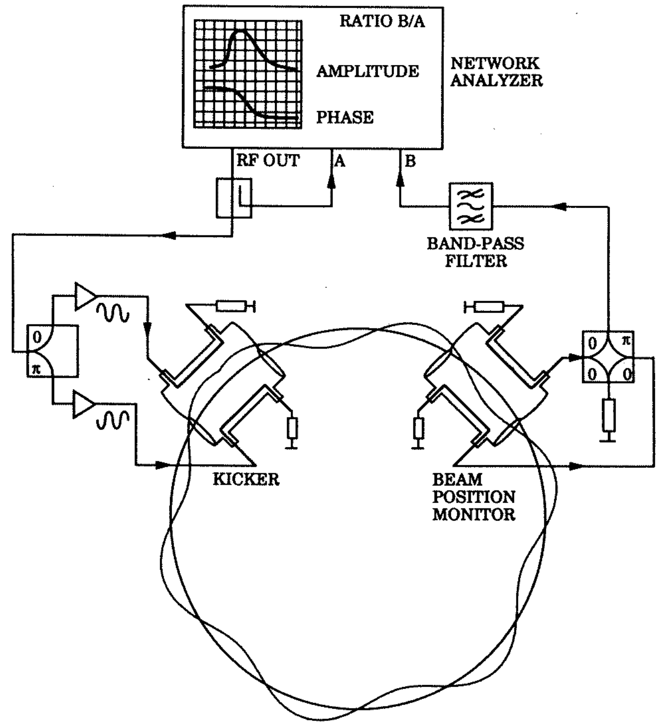

Figure 5.31: Scheme of a beam transfer function (BTF) measurement.

An rf method for tune determination uses a beam excitation driven by a continuous sine wave stimulus. This wave is swept slowly within seconds over a certain band and the response of the beam is measured in coincidence. The device used in rf engineering for this purpose is a network analyzer, see [94]. It provides a frequency scan over an user-given range, which is amplified and applied to the beam via an rf exciter. The exciter is built like a pick-up. The normalized difference signal U_Δ/U_Σ from the pick-up is fed to the input of the network analyzer as shown in Fig 5.31. Here the amplitude and phase relative to the excitation are measured precisely and displayed. The horizontal axis of the display correspond to the frequency band for the beam excitation. The displayed spectrum represents the beam transfer function (BTF), which can be defined as the transverse velocity response to the given acceleration by the kicker. Due to practical reasons, a harmonics of the revolution frequency f_0 is used for the excitation and the resulting resonance line is expressed in terms of this harmonics. An example of such a measurement with an excitation around the $h = 25^{th}$ revolution harmonics is shown in Fig. 5.32. The beam reacts as a driven oscillator with a resonance as given by the tune value. Because only the fractional part can be measured, this resonance is located at $f_h^\pm = (h \pm q) f_0$ on both

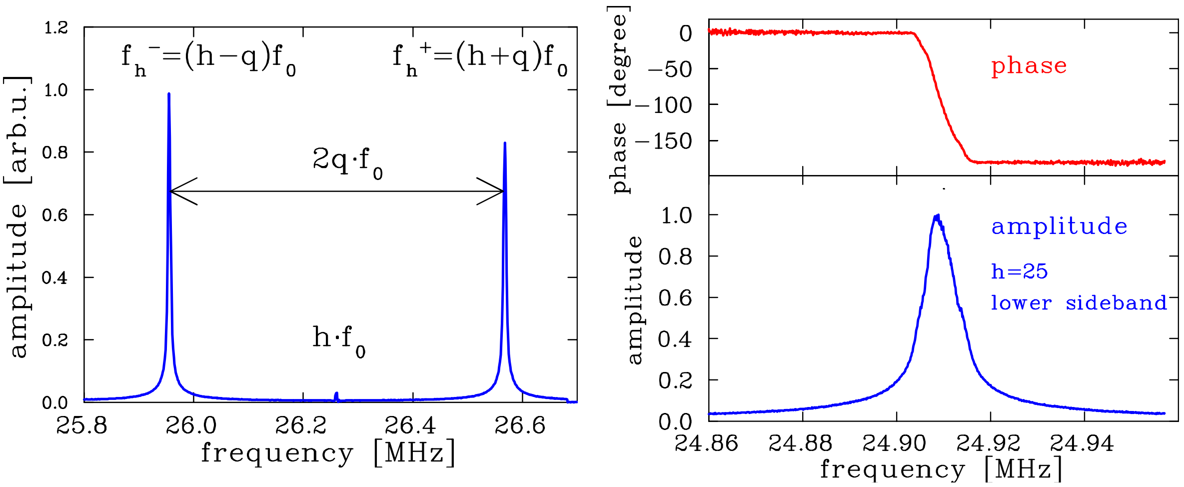

Figure 5.32: BTF measurement at the GSI synchrotron with a 500 MeV/u U^{73+} beam having a revolution frequency of $f_0 = 1.048$ MHz. The wide scan around the $h = 25^{th}$-harmonics is shown left and a scan around the lower sideband centered at f_{25}^- on the right. The fractional tune is $q = 0.306$ for these data.

sides of the revolution frequency and are called lower and upper sideband. From the distance of the sidebands, the fractional part of the tune q is determined. The resonance nature of the BTF measurement can also be seen from the phase shift of 180^o during resonance crossing, as shown in on the right side of Fig. 5.32. An analytic expression for the BTF can be found in [96] based on the theory of a driven oscillator including Landau damping. From the width of a sideband the tune spread can roughly be estimated as $\Delta q \simeq \frac{\Delta f}{h f_0}$. For a more detailed evaluation of of the sideband-width for beams with low space charge contributions i.e. for the validity of linear beam optics, one has to take the longitudinal momentum into account, resulting in a more complex description of the sideband width (see Eq. 7.24) as discussed in the frame of transverse Schottky analysis in Chapter 7. Due to the driving force for BTF measurements, the signal strength is several orders of magnitude higher as compared to a Schottky scan.

With this method a high precision of the tune value q up to 10^{-4} can be reached. Such a measurement might takes some time (up to several minutes), because the frequency has to be swept and the response to one single frequency is measured at a given time. The resolution is determined by the sweep velocity, i.e. a slow sweep yields a better resolution. In addition, the sweep velocity has to be slow enough to allow the transient beam response to die out and a steady state response to be attained. Using a sensitive pick-up, the measurement can also be done with an un-bunched beam.

5.9.3 Noise excitation of the beam

Instead of single frequency excitation, a wide band rf signal can be applied. The beam is excited by the same frequency spectrum as delivered by a network analyzer, but here the excitation takes place for all frequencies at the same time, using white noise of adequate bandwidth being larger than the tune variation. The position reading is done in the time domain using a fast ADC recording each bunch. The data are Fourier analyzed and the tune is drawn. An example is shown in Fig. 5.33 from the GSI synchrotron during acceleration [97], see also [98] for a comparable measurement. The resolution for the tune is given by the inverse of the averaging time for one FFT calculation (here in the order of 5 ms, corresponding to 2048 turns), leading to about $\Delta Q \sim 5 \cdot 10^{-3}$ for one single scan. The power applied to the beam is much lower than for a BTF measurement using a network analyzer and the beam is much less disturbed.

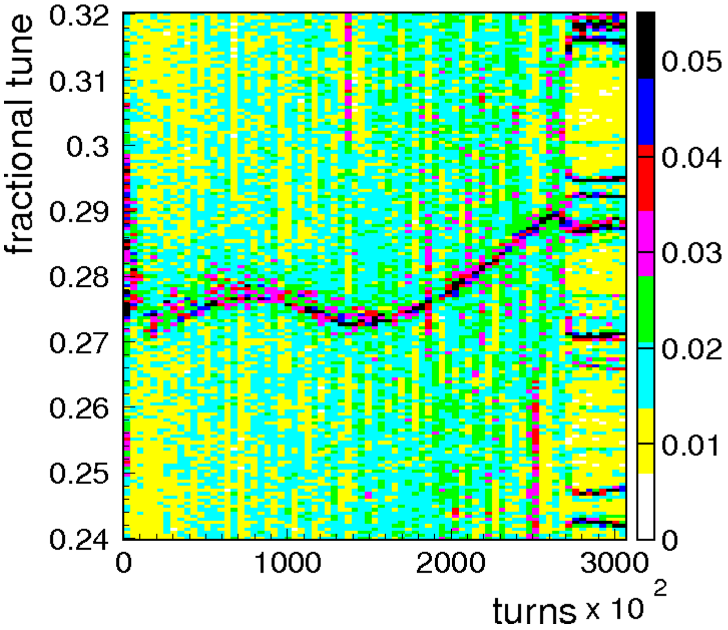

Figure 5.33: Measurement of the tune at the GSI synchrotron during about 0.5 s acceleration [98]. Displayed is the Fourier transformation of displacements of 2048 successive individual bunches during acceleration as a function of the turns on the horizontal axis. The maxima of the FFT are color-coded.

5.10 Measurement of lattice functions

The technique of beam excitation can also be used to determine parameters of the beam optics. In particular, local values of dispersion and beta-function as well as the chromaticity has been measured with this technique. A knowledge of these parameters is of importance during the commissioning of a new machine, the control of mechanical misalignments, as well as a check of critical settings, e.g. close to a low-beta insertion. If required, the values of the local lattice function can be corrected by applying correction magnets inside the synchrotron.

The dispersion function $D(s)$ at a position s in the synchrotron is defined as

$$x(s) = D(s)\frac{\Delta p}{p} \tag{5.29}$$

with $x(s)$ being the displacement for a given momentum deviation Δp from the nominal momentum p. $D(s)$ can be determined at the pick-up location by a slight momentum change with the help of a frequency detuning of an accelerating cavity. Several position measurements are plotted as a function of the momentum deviation and D is given by the slope.

Having a turn-by-turn readout of several pick-ups, the coherent betatron oscillation of a single bunch can be monitored. The position reading at a pick-up i located at s_i for turn number k is given by

$$x_{ik} = \hat{x}_i \cdot \cos\left(2\pi Qk + \mu_i\right) = \hat{x}_0 \cdot \sqrt{\frac{\beta(s_i)}{\beta(s_0)}} \cos\left(2\pi Qk + \mu_i\right) \tag{5.30}$$

with $\hat{x}_i$ the amplitude at the pick-up i, $\hat{x}_0$ the amplitude at a reference pick-up at s_0, $\beta(s_i)$ and $\beta(s_0)$ the beta-functions at these pick-ups, Q the tune and μ_i the betatron phase at s_i with respect to the reference location.

The ratio of the beta-functions can be determined by a comparison of the amplitudes at these two locations

$$\frac{\beta(s_i)}{\beta(s_0)} = \left(\frac{\hat{x}_i}{\hat{x}_0}\right)^2 . \tag{5.31}$$

The accuracy of such a measurement might not be too good, because the absolute calibration of the pick-up enters the calculation.

The phase advance between two locations can be determined by this measurement as

$$\Delta\mu = \mu_i - \mu_0 \tag{5.32}$$

with a high accuracy by fitting a sine function to the measured data, as schematically plotted in Fig. 5.34.

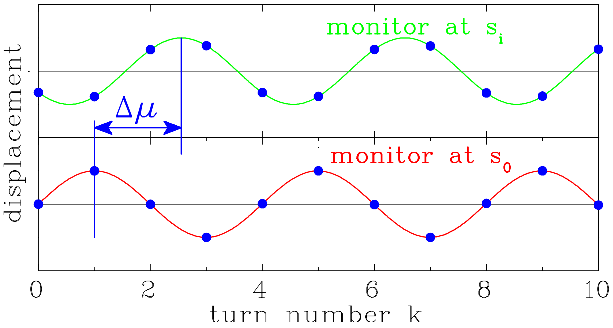

Figure 5.34: Scheme of the individual measurements at two pick-ups for a phase advance $\Delta\mu$ determination. A sine function can be fitted through the data points.

This leads to another way of beta-function measurement using the betatron phase difference $\Delta\mu$ between the two locations s_0 and s_i using the relation

$$\Delta\mu = \int_{s_0}^{s_i} \frac{ds}{\beta(s)}, \tag{5.33}$$

where the measured value $\Delta\mu$ is compared to the result using the theoretical beta-function.

The focusing of a quadrupole is dependent of the particle momentum, resulting in a change of the tune for different momenta. It is described by the chromaticity ξ defined as

$$\frac{\Delta Q}{Q} = \xi \frac{\Delta p}{p} \quad . \tag{5.34}$$

This value can be determined directly by a slight momentum change using a detuned rf-frequency, as shown in Fig. 5.35. The tune is then measured as discussed above and plotted as a function of the momentum deviation; the value of ξ is given by the slope. A linear behavior between $\Delta p/p$ and $\Delta Q/Q$ is only valid in a small momentum interval (here $\Delta p/p = \pm 0.1\%$). For larger deviations, non-linear forces from the synchrotron magnets contribute significantly. Instead of changing the rf-frequency one can also change the magnetic field of the main dipole magnets, because this type of measurement is based on the detuning between ideal closed orbit and revolution frequency.

The chromaticity can also be determined locally by comparing the measured betatron phase advance using Eq. 5.30 with the tune Q as a fit parameter (the beta-function has to known of course). These measurements have to be repeated for different Δp. Real examples and further references are given in [99].

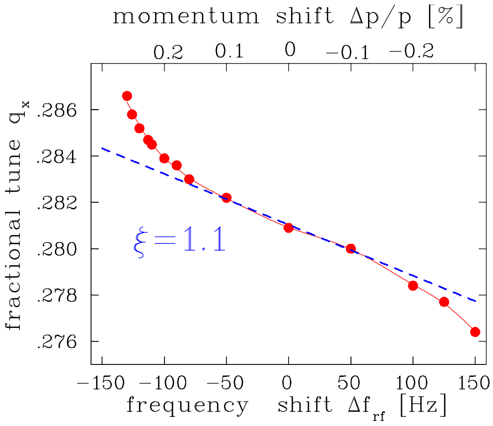

Figure 5.35: Measurement of the chromaticity at LEP. The horizontal tune is determined for different setting of the acceleration frequency and therefore of the momentum of the circulating beam. The chromaticity is fitted through the linear part of the data [100].

Chapter 6

Measurement of longitudinal parameters

Longitudinal parameters are as important as the transverse ones, but the way of their measurements are not described as often. The longitudinal phase space is spanned by:

- The longitudinal spread of the bunch l is given in units of time (ns) or phase (^{o} degrees), see Fig. 6.1. The mean value is the center of the bunch relative to the rf or relative to the ideal reference particle. The corresponding transverse value is the transverse beam profile. For a un-bunched dc beam, e.g. in a proton or heavy ion storage ring, the quantity is of no meaning.
- The momentum spread $\delta = \Delta p/p$ is the deviation relative to the momentum p of the reference particle. In proton or heavy ion LINACs sometimes the quantity is related to the beam energy $\Delta W/W$ or even only ΔW is given. The corresponding transverse value is the beam divergence.

The value of emittance ϵ_{long} is given by the the product of the two quantities

$$\epsilon_{long} = \frac{1}{\pi}\int dl d\delta. \tag{6.1}$$

More precisely, using a phase space density distribution $\rho(l,\delta)$ the emittance is

$$\epsilon_{long} = \frac{1}{\pi}\int \rho(l,\delta) dl d\delta. \tag{6.2}$$

Linear transformations can be applied in the same way as for the transverse case (see Chapter 4.1). The normalized longitudinal emittance

$$\epsilon_{long}^{norm} = \frac{v_s}{c}\gamma_{rel}\cdot\epsilon_{long} \tag{6.3}$$

is preserved under ideal conditions (v_s is the longitudinal velocity and γ_{rel} is the relativistic Lorentz factor).

Using a pick-up, the projection of the phase space on the time axis is determined, resulting in the bunch position and width. A determination of the emittance by linear transformation is possible. Some conditions have to be fulfilled for a capacitive pick-up to guarantee an adequate interpretation: First, the bunch has to be much longer in the longitudinal direction than the pick-up. For bunches with a length comparable to the pick-up, a second condition is that the beam must be sufficiently relativistic, so that the beam's electric field is essentially transverse.

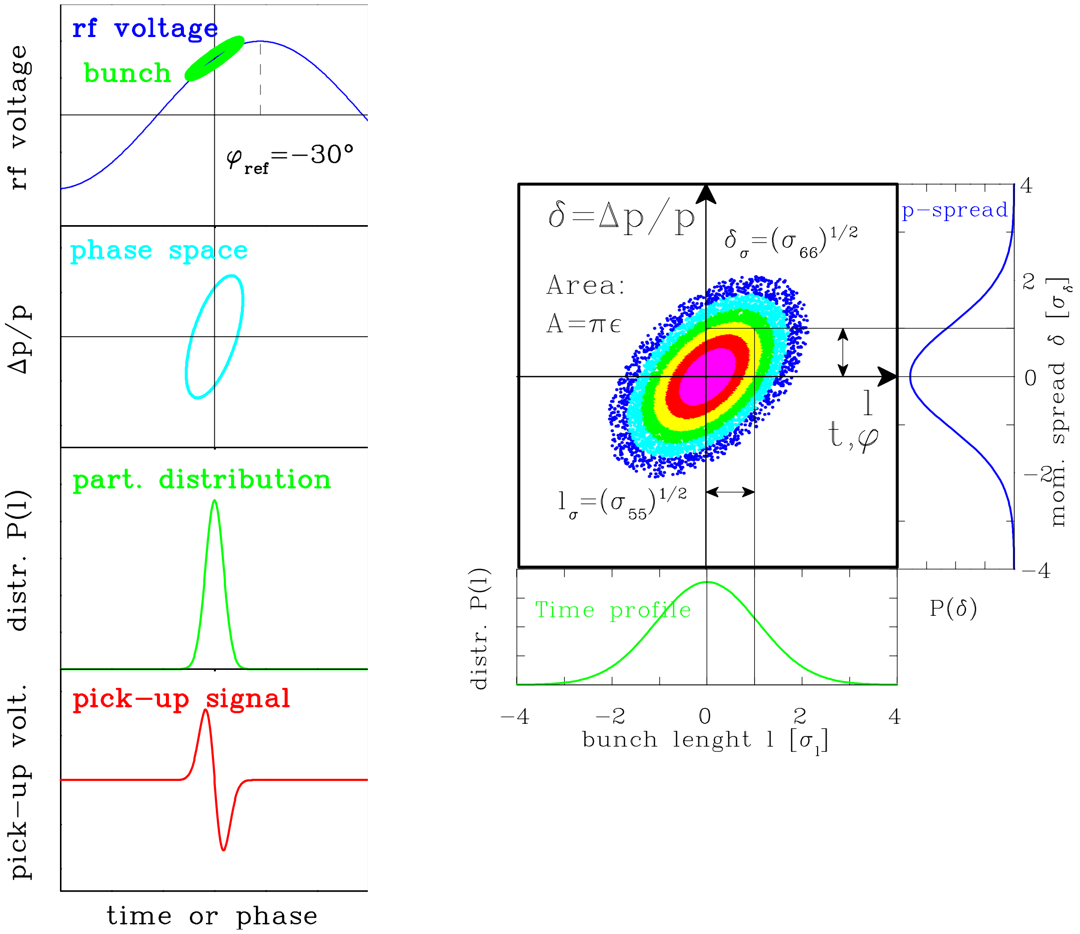

Figure 6.1: Left: The relation between the rf voltage and the longitudinal emittance as well as the time distribution of the bunches as measured with the differentiated pick-up signal. Right: The longitudinal phase space plot of a Gaussian distribution.

For the transverse electric field component $\vec{E}_\perp$, relativity gives an enhancement in the lab-frame compared to the rest-frame of moving charge by

$$E_{\perp,lab} = \gamma E_{\perp,rest} \quad , \tag{6.4}$$

see also Fig. 6.2. In the case of a slow beam from a proton/heavy ion LINAC, the last condition is not fulfilled and other methods have to be applied. For bunches shorter than the capacitive pick-up, the signal does not reflect the longitudinal bunch shape. Stripline pick-ups can still be used. For electron beams, the bunch length is so short that the bunch structure is smeared out by integration on the pick-up capacitance, i.e. by the limited bandwidth. Here the monitoring of synchrotron radiation is used in connection with the fast optical method of streak cameras.

A measurement of the energy- or momentum spread $\delta = \Delta p/p$ is not discussed in detail here. A magnetic spectrometer can be used for this purpose, having point-to-point focus in connection with small slits located at appropriate locations. This is discussed in textbooks on beam optics [101].

6.1 Electric fields of a relativistic charge

Due to the finite velocity of light, the electric field of a moving charge is modified. This effect for different velocities β of the moving charge is shown in Fig. 6.2, where the longitudinal electrical field $E_{\parallel}(t)$ in the lab-frame has been calculated for a single particle with a charge of $1e$ traveling in empty space. It is calculated by the relativistic Lorentz-boost including the transformation of the time coordinate [12] to be

$$E_{\parallel,lab}(t) = -\frac{e}{4\pi\varepsilon_0} \cdot \frac{\gamma\beta ct}{\left[R^2 + (\gamma\beta ct)^2\right]^{3/2}} \tag{6.5}$$

R is the distance of closest approach and $\gamma = \left(1-\beta^2\right)^{-1/2}$ the relativistic Lorentz factor. The transversal field component $E_{\perp}$ in the lab-frame is given by

$$E_{\perp,lab}(t) = \frac{e}{4\pi\varepsilon_0} \cdot \frac{\gamma R}{\left[R^2 + (\gamma\beta ct)^2\right]^{3/2}} \tag{6.6}$$

The formula is a bit different from the simple one of Eq. 6.4 as $E_{\perp,lab}(t_{lab}) = \gamma E_{\perp,rest}(t_{rest})$ due to the additionally required transformation of the time coordinate $t_{rest} \rightarrow t_{lab}$. The above formulas are valid for a free particle and are modified by the boundary condition of the metallic surface e.g. of the beam pipe or the pick-up plates. A beam bunch consist of many particles distributed within a certain area; to calculate the accompanying electric field one has to integrate of this distribution. For low velocities the electric field arrives earlier at the pick-up and does not reflect the charge distribution of the bunch, see Chapter 6.7 for more details.

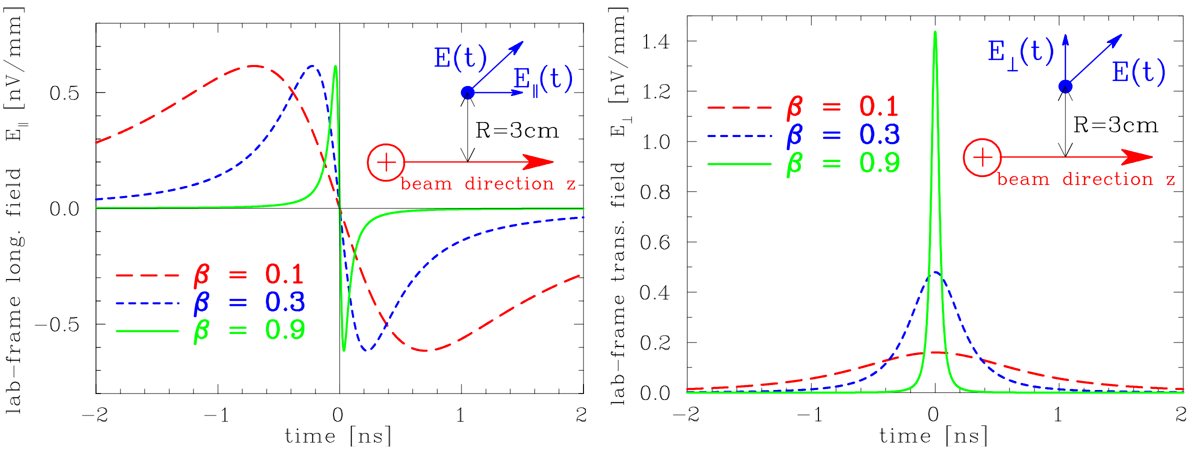

Figure 6.2: Effect of the advanced longitudinal (left) and transverse (right) electric field at an observation point $R = 30$ mm from the beam axis for different velocities of a point-like charge. For $t = 0$ the closes approach is reached.

6.2 Determination of phase position

The corresponding quantity to the transverse beam position is the center-of-mass of a bunch relative to the accelerating rf sine-wave. For the matching of successive LINAC modules, the right phase relation has to be determined with a beam-based measurement. A typical plot is shown in Fig. 6.3 for a slow 1.4 MeV/u ion beam. Due to the differentiated beam signal the center of the bunch is well determined. There is an arbitrary, but fixed phase shift between the signals due to the different cable lengths.

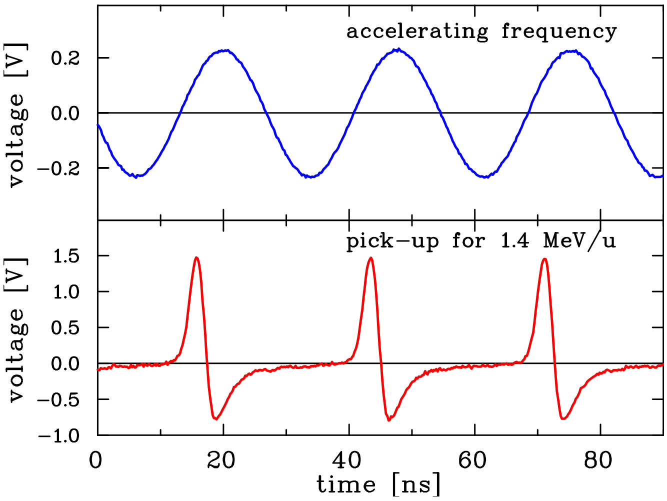

Figure 6.3: The pick-up signal from a 1.4 MeV/u ion beam and the corresponding LINAC module frequency for the determination of the bunch position.

6.3 Determination of non-relativistic mean energy

The final energy of a LINAC module is sensitive to the actual setting of the rf amplitude and the phase relative to the preceding modules. Therefore, an energy determination is important. Because of dispersion, the bending radius of a magnetic system can be used for this, but the resulting profile is a mixture of the transverse and longitudinal parameters. An independent measurement can be performed for non-relativistic energies using two pick-ups separated by the distance L and a time-of-flight (TOF) measurement, see e.g. [37, 102]. As displayed in Fig. 6.4, two pick-ups are installed in a straight section with a typical distance of several meters. This distance L has to be known precisely, to within 1 mm. The bunch center-of-mass can be read from the oscilloscope or the correlation function between the two signals can be calculated. A typical measurement is displayed in Fig. 6.5. As shown in the schematic, several bunches are between the pick-ups and a coarse estimate of the velocity is needed. This is normally known, but in case of trouble, a third pick-up has to be installed much closer to one of the others. The velocity is calculated for the measured time t_{scope} via

$$\beta c = \frac{L}{NT + t_{scope}} \tag{6.7}$$

with N bunches between the pick-ups and the bunch repetition time of $T = 1/f_{rf}$.

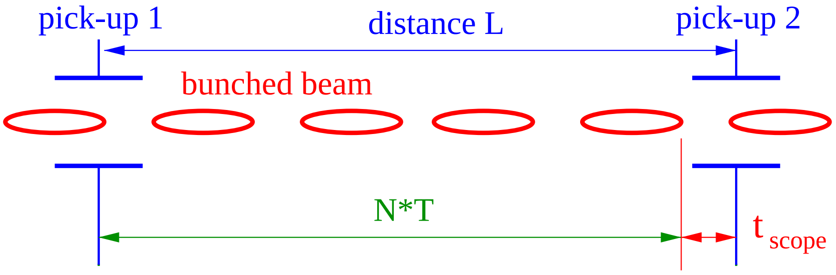

Figure 6.4: Principle of a TOF measurement using two pick-ups.

The precision of such a velocity measurement $\Delta\beta/\beta$ is given by the uncertainty of the distance

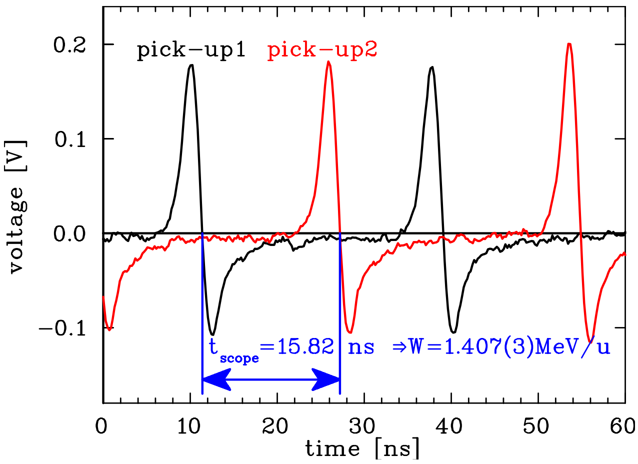

Figure 6.5: Time-of-flight signal from two pick-ups with $W \simeq 1.4$ MeV/u at the GSI-LINAC. The frequency is $f_{rf} = 36.136$ MHz $\Leftrightarrow T = 27.673$ ns. For the distance of $L = 1.629$ m between the pick-ups $N = 3$ bunches are between the pick-ups. Inserting the time difference of $t_{scope} = 15.82$ ns in Eq. 6.7, the velocity $\beta = 0.05497(7)$ and the corresponding beam energy $W = 1.407(3)$ MeV/u is calculated. The error is given by Eq. 6.8 with the uncertainties of $\Delta t = 0.1$ ns and $\Delta L = 1$ mm.

ΔL and the scope reading Δt to be

$$\frac{\Delta\beta}{\beta} = \sqrt{\left(\frac{\Delta L}{L}\right)^2 + \left(\frac{\Delta t}{NT + t_{scope}}\right)^2} \tag{6.8}$$

An accuracy better than 0.1 % for the energy spread $\Delta W/W = 2\Delta\beta/\beta$ can be reached, assuming a precision of $\Delta L = 1$ mm and $\Delta t = 100$ ps for the time measurement; the parameters used at the GSI-LINAC are summarized in Table 6.1.

location (GSI-slang)		RFQ	IH1	IH2	AL4
energy W	[MeV/u]	0.12	0.75	1.4	11.4
velocity β	%	1.6	4.0	5.5	15.5
total TOF	[ns]	677	271	197	70
bunch spacing $\beta c/f_{rf}$	[cm]	13	33	45	129
resolution $\Delta W/W$	%	0.07	0.10	0.12	0.22

Table 6.1: The energy resolution for a TOF measurement with a pick-up distance of 3.25 m for some GSI LINAC modules. The rf-frequency is $f_{rf} = 36.14$ MHz and the assumed time accuracy is 100 ps.

The final energy of a LINAC module depends on the applied amplitude and phase of the accelerating rf. This is depicted in Fig. 6.6 for an ion beam of 1.400 MeV/u nominal energy. This nominal energy is reached only in a small interval, for the displayed case the allowed amplitude range is below ±2 % and the phase should be aligned within $\pm 10^o$. This corresponds to a relatively small range and it calls for a precise beam alignment and a very large precision in the TOF measurement, as demonstrated by the small error bars in Fig. 6.6. Matching the nominal beam energy of a LINAC module is an important task, because the energy acceptance of the following module is typically restricted within several percent and a sufficient beam transmission through a chain of LINAC modules is only achieved if all modules produces the right energy increase. Moreover, the longitudinal emittance depends strongly on the right rf amplitude and phase setting, as shown in Chapter 6.7.2.

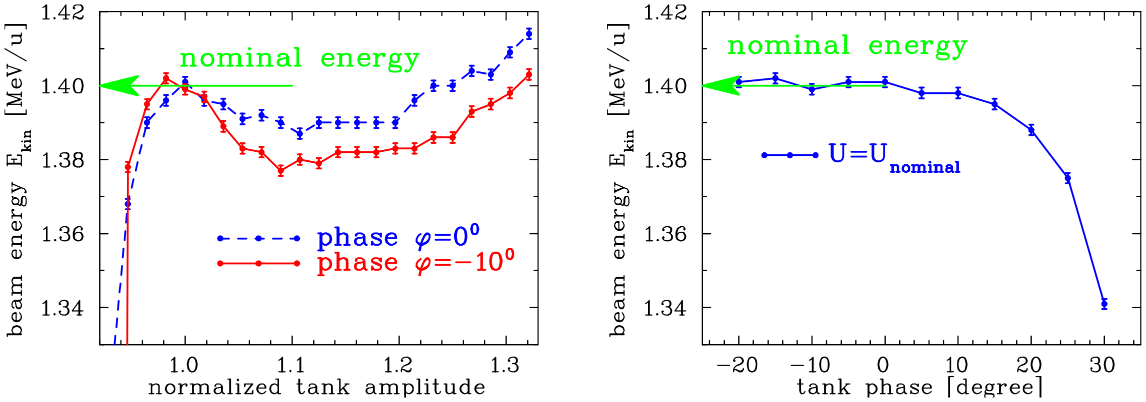

Figure 6.6: The output energy of the GSI-LINAC as a function of the applied rf-amplitude inside the tank (left) and phase for the nominal amplitude (right) as recorded like displayed in Fig. 6.5. The required energy of this module is 1.400 MeV/u. The distance between the pick-ups is in this case $L = 1.97$ m with $N = 4$ bunches between.

Even though the TOF method is performed for energy measurements, it is basically a velocity determination. For electron beams this method can not be applied, because electrons are relativistic after the first LINAC modules. Acceleration of electrons is more related to an increase of their momentum and therefore the energy determination by the bending power of a dipole magnet is more appropriated in this case.

6.4 Longitudinal emittance from linear transformation

There are many cases where the length of the bunches fits the length of the capacitive or stripline pick-ups to get a reliable information of the bunch structure. The longitudinal emittance can then be determined from linear transformations, like in the transverse case as described in Chapter 4.4 and 4.5. The quadrupole variation corresponds to the change of the longitudinal focusing performed by a buncher, see Fig. 6.7. The phase of a buncher is adjusted to 0^o, so no acceleration is present. By varying the amplitude, the bunch can be longitudinally focused, i.e. compressed. The action is described in the longitudinal sub-space $(l, \delta = \Delta p/p)$, which is a part of the full 6-dim phase space describing both transverse and the longitudinal planes. The transfer matrices $\mathbf{R}$ have 6×6 elements, as does the beam matrix σ. Disregarding any transverse-longitudinal coupling (e.g. by a dipole magnet), the longitudinal phase space corresponds to the 'lower right' part of the full 6×6 matrices, having the indices 5 and 6. The reduced 2×2 transfer matrix of a buncher $\mathbf{R}_{buncher}$ is given in the thin lens approximation by

$$\mathbf{R}_{buncher} = \begin{pmatrix} 1 & 0 \\ -1/f & 1 \end{pmatrix}. \tag{6.9}$$

The focal length f is

$$\frac{1}{f} = \frac{2\pi q U_0 f_{rf}}{A p v^2} \tag{6.10}$$

with the amplitude U_0 at a frequency f_{rf} for a particle of charge q and mass A with velocity v and momentum p. The transfer matrix for a drift space of length L is given by

$$\mathbf{R}_{drift} = \begin{pmatrix} 1 & L/\gamma_{rel}^2 \\ 0 & 1 \end{pmatrix}. \tag{6.11}$$

γ_{rel} is the relativistic Lorentz factor. As for the transverse case, the emittance can be determined by an amplitude variation U_0 of the buncher leading to different longitudinal focusing.

A measurement of the bunch length at the pick-up location s_1 has to be performed for at least three settings of the buncher. The beam matrix $\sigma(0)$ at the buncher location s_0 has to be determined. For the bunch width $l_{max}(1, f_k) = \sqrt{\sigma_{55}(1, f_k)}$ at the pick-up location s_1, a system of linear equations for $\sigma_{ij}(0)$ in the form

$$\begin{aligned}
\sigma_{55}(1, f_1) &= R_{55}^2(f_1) \cdot \sigma_{55}(0) + 2R_{55}(f_1)R_{66}(f_1) \cdot \sigma_{56}(0) + R_{56}^2(f_1) \cdot \sigma_{66}(0) \quad \text{focusing } f_1 \\
\sigma_{55}(2, f_2) &= R_{55}^2(f_2) \cdot \sigma_{55}(0) + 2R_{55}(f_2)R_{66}(f_2) \cdot \sigma_{56}(0) + R_{56}^2(f_2) \cdot \sigma_{66}(0) \quad \text{focusing } f_2 \\
&\vdots \\
\sigma_{55}(n, f_n) &= R_{55}^2(f_n) \cdot \sigma_{55}(0) + 2R_{55}(f_n)R_{66}(f_n) \cdot \sigma_{56}(0) + R_{56}^2(f_n) \cdot \sigma_{66}(0) \quad \text{focusing } f_k
\end{aligned} \tag{6.12}$$

is obtained for $k = 1, 2...n$ measurements with $f_k = f_1, f_2...f_n$ different settings of the buncher. This redundant system of linear equations has to be solved as discussed in Chapter 4.4. A measurement is shown in Fig. 6.8. For the method it is of no importance which device is used for determination, as long as it reflects the actual bunch shape of the beam.

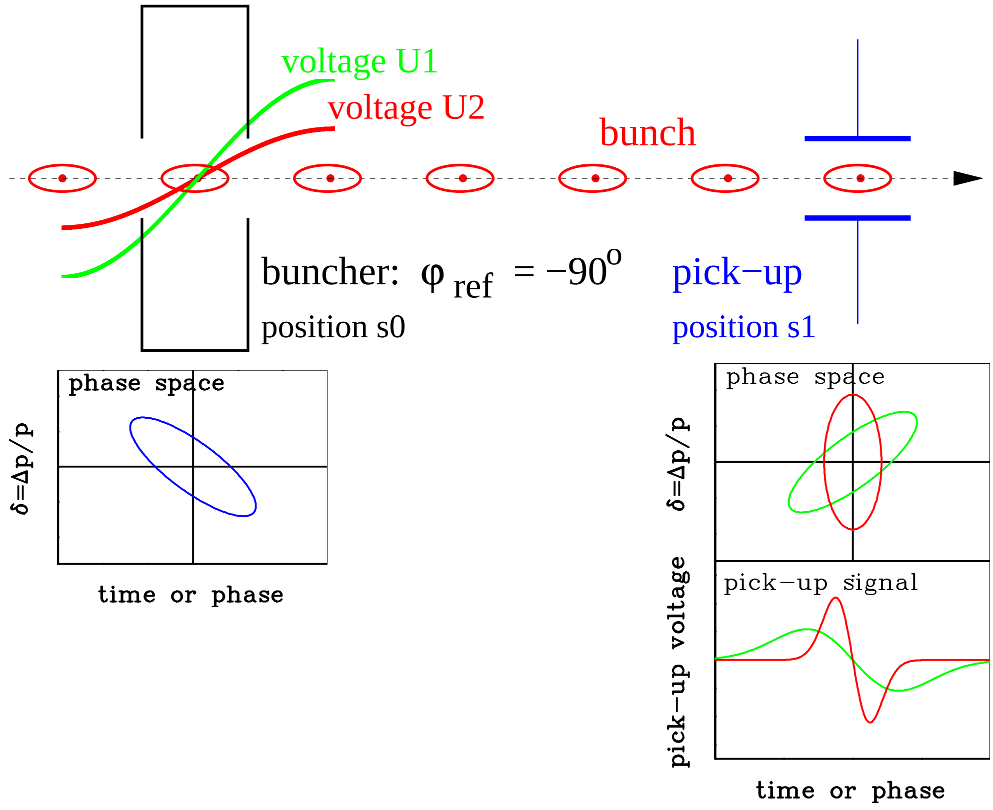

Figure 6.7: Scheme for a longitudinal emittance measurement using a buncher and one pick-up.

Corresponding to the 'three grid method', the bunch width can also be determined from a series of measurement along a transfer line, see Fig. 6.9. As in the transverse case Chapter 4.5 we get a redundant system of linear equations for the transformation $\mathbf{R}(k)$ from the buncher to the pick-up at s_k of the form

$$\begin{aligned}
\sigma_{55}(1) &= R_{55}^2(1) \cdot \sigma_{55}(0) + 2R_{55}(1)R_{66}(1) \cdot \sigma_{56}(0) + R_{56}^2(1) \cdot \sigma_{66}(0) \quad \mathbf{R}(1) : s_0 \to s_1 \\
\sigma_{55}(2) &= R_{55}^2(2) \cdot \sigma_{55}(0) + 2R_{55}(2)R_{66}(2) \cdot \sigma_{56}(0) + R_{56}^2(2) \cdot \sigma_{66}(0) \quad \mathbf{R}(2) : s_0 \to s_2 \\
&\vdots \\
\sigma_{55}(n) &= R_{55}^2(n) \cdot \sigma_{55}(0) + 2R_{55}(n)R_{66}(n) \cdot \sigma_{56}(0) + R_{56}^2(n) \cdot \sigma_{66}(0) \quad \mathbf{R}(n) : s_0 \to s_n
\end{aligned} \tag{6.13}$$

For a precise determination, a longitudinal focus has to be placed close to one pick-up.

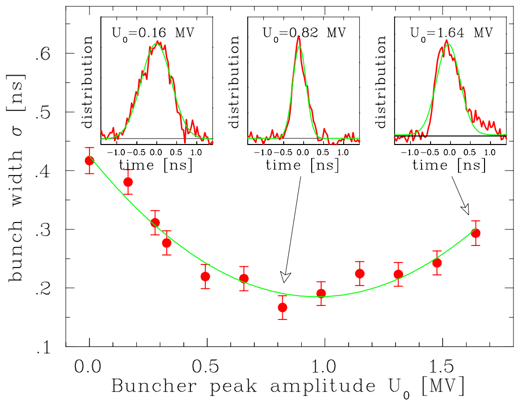

Figure 6.8: Measurement of the bunch width (one standard deviation) as a function of the buncher voltage 31 m upstream. The bunch shape is not measured by a pick-up, but a specially design monitor for low energetic beams [103].

As discussed for the transverse case, the restrictions are the presence of Gaussian phase space distributions, linear beam manipulations and the lack of non-linear space charge forces. In addition, one has to underline, that the above methods are mainly used at LINACs. For beam extracted from a synchrotron, the variation of the bunch length within the beam transfer line is negligible in most cases, due to the low synchrotron frequency (up to ∼ 10 kHz) of the bunches formed in the synchrotron. Therefore the measurement inside the synchrotron is sufficient.

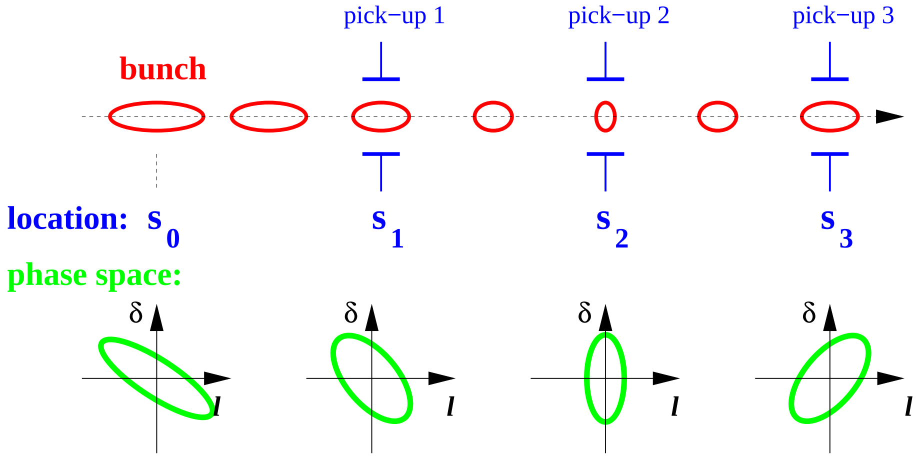

Figure 6.9: Scheme for a longitudinal emittance measurement using pick-ups in a transfer line.

6.5 Longitudinal emittance using tomographic reconstruction

In a proton/heavy ion synchrotron the bunch length is much longer than the typical pick-up size or the gap of a resistive wall current monitor (see Chapter 6.6). This allows the recording of a true image of the bunch shape. Observation and control of the longitudinal behavior at injection, acceleration and possible bunch manipulations, like combining or splitting of bunches, can be performed.

In recent years, an innovative analysis method has been developed at CERN [104] to determine the longitudinal emittance and bucket filling from a measurement of the bunch shape on a turn-by-turn basis. The idea is based on the well known tomographic reconstruction used as an imaging technique in medicine for x-ray and nuclear spin tomography.

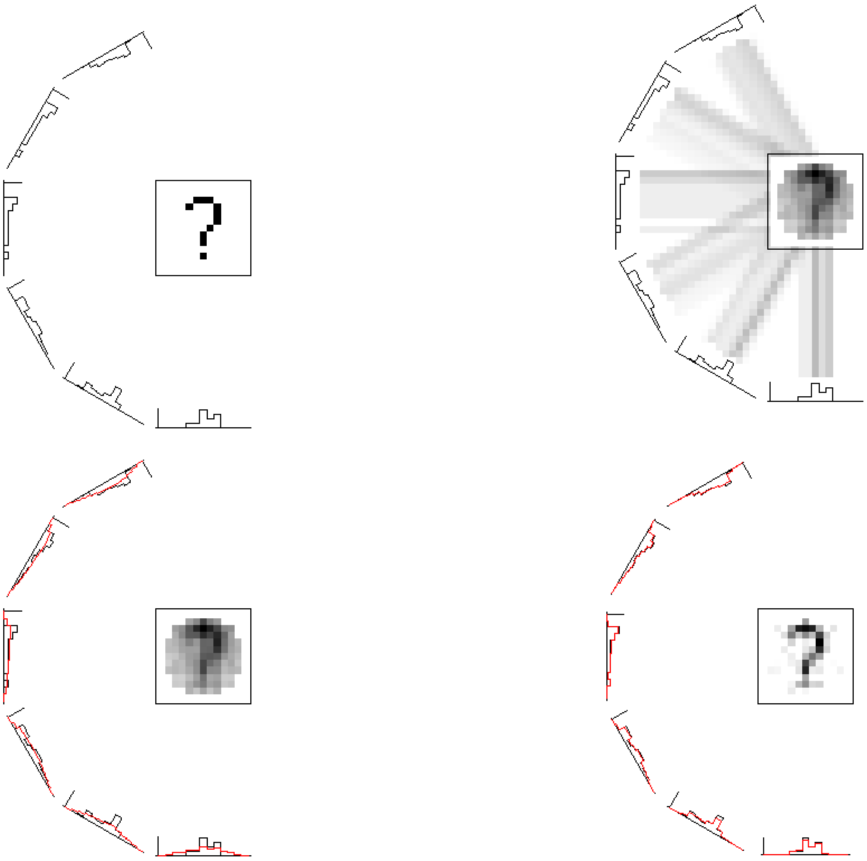

Figure 6.10: Schematic plots for the tomographic reconstruction technique [105]. The original 2 dimensional image and the 1-dim projections are shown to the left. A first back projection is shown top right. The first iteration step for the generation of the differences in the projected data is plotted bottom left. After ~ 50 iterations, the original image can be reconstructed.

The underlying principle of tomography is to combine the information in a sufficiently large number of projections to unambiguously reconstruct the fuller picture with the extra dimension reinstated. The application of tomography to longitudinal phase space in an accelerator becomes obvious once it is realized that a bunch of particles performing synchrotron motion is analogous to a patient rotating in a stationary body scanner. On each turn around the machine, a longitudinal pickup provides a "snapshot" of the bunch projected at a slightly different angle. It suffices to combine such profiles tomographically to obtain a two-dimensional picture of phase space density. Also non-linear emittance growth can be included [104]. A general, well fulfilled condition is that the synchrotron frequency is much lower than the revolution frequency. At least half a synchrotron period has to be recorded, corresponding to a 180^o degree image of the patient body in the medical application.

The general idea for tomography is based on algebraic reconstruction techniques (described in textbooks on medical physics) as depicted in Fig. 6.10 from [105]. The contents of the bins of a one-dimensional histogram are redistributed over the two-dimensional array of cells which comprise the reconstructed image. Given no a-priori knowledge of the original two-dimensional distribution, the contents of one bin are spread over all the cells that could have contributed to that bin. The back projection of all bins of all profiles yields a first approximation to the original distribution. Back projection of the bin-by-bin difference between the original set of profiles and this new one yields an improved approximation. Further iterations converge more rapidly if any cell whose contents have become negative is reset to zero. A more detailed description is found

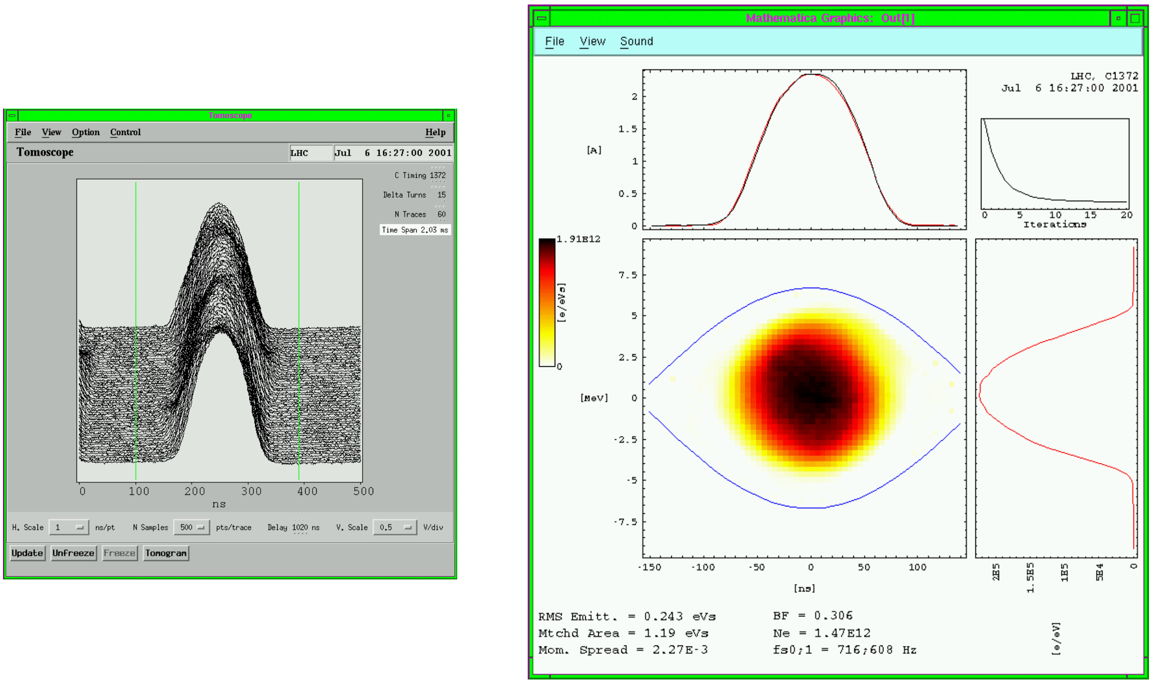

LHC Jul 6 16:27:00 2001

C Timing 1372
Delta Turns 15
N Traces 60
Time Span 2.03 ms

H. Scale 1 ns/pt
N Samples 500 pts/trace
Delay 1020 ns
V. Scale 0.5 V/div

LHC, C1372
Jul 6 16:27:00 2001

RMS Emitt. = 0.243 eVs
Mtchd Area = 1.19 eVs
Mom. Spread = 2.27E-3
BF = 0.306
Ne = 1.47E12
fs0;1 = 716;608 Hz

Figure 6.11: The recorded bunch shape at CERN PS using a resistive wall current monitor for 500 turns (left) and the reconstructed longitudinal phase space. The bucket size is shown in the phase space and the projections to the time axis (top) and energy (right) are displayed. From [106].

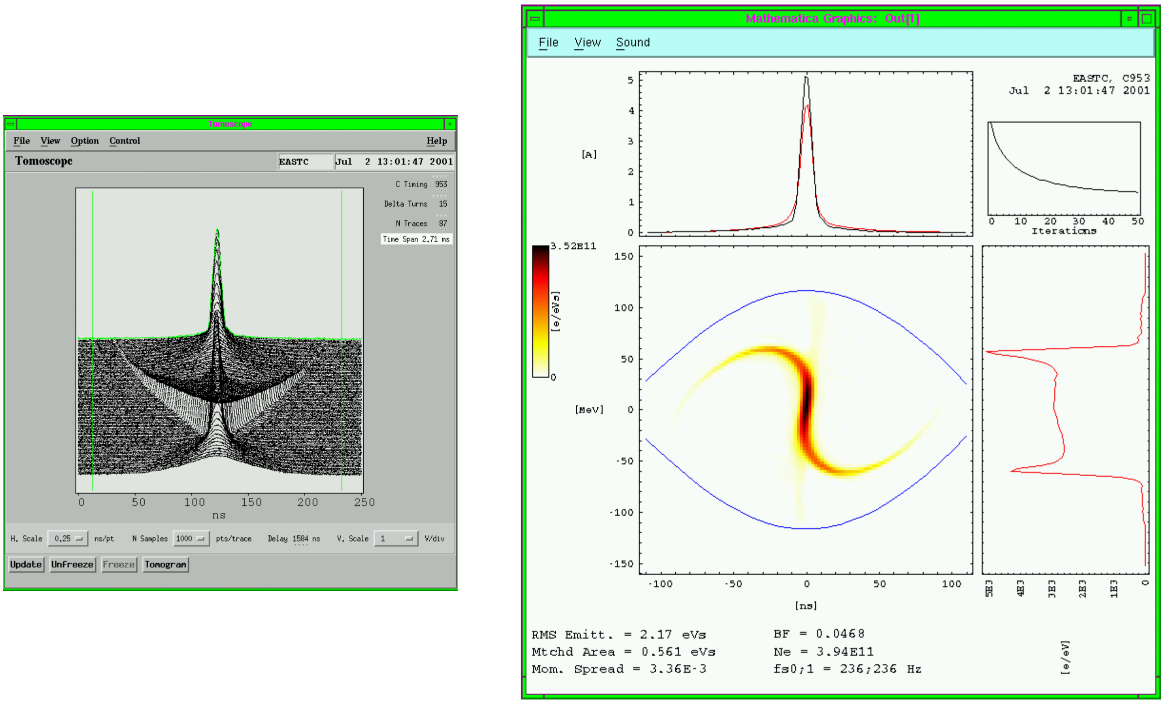

EASTC Jul 2 13:01:47 2001

C Timing 953
Delta Turns 15
N Traces 87
Time Span 2.71 ms

H. Scale 0.25 ns/pt
N Samples 1000 pts/trace
Delay 1584 ns
V. Scale 1 V/div

EASTC, C953
Jul 2 13:01:47 2001

RMS Emitt. = 2.17 eVs
Mtchd Area = 0.561 eVs
Mom. Spread = 3.36E-3
BF = 0.0468
Ne = 3.94E11
fs0;1 = 236;236 Hz

Figure 6.12: Same as Fig. 6.11 but for a mismatched bunch. The complex rotation of the bunch width is seen left and the reconstructed phase space density (right) for one specific time slice. The filamented distribution rotates to yield varying bunch shapes. Form [106].

in [104].

Two examples [106] demonstrate the high analyzing power of tomography. The first, displayed in Fig. 6.11 is a standard, constant bunch shape recorded with a digital scope. The reconstruction of the first time slice shows a good filling of the bucket. The second example in Fig. 6.12 is a mismatched bunch. In phase space (as shown for a small bunch width) the distribution rotates at the synchrotron frequency, resulting in varying bunch shapes as a function of time. The bucket is filled badly.

6.6 Resistive wall current monitor

For the observation of the bunches and their structure, a large bandwidth is required. With a resistive **W**all **C**urrent **M**onitor **WCM**, a bandwidth up to several GHz can be reached [107]. The beam always induces an image current flowing along the vacuum pipe, having the same magnitude and the same time structure. To measure this image current, the vacuum pipe is interrupted by a ceramic gap, as displayed schematically in Fig. 6.13. The gap is bridged by typically n =10 to 100 resistors with a low resistivity on the order of R =10 to 100 Ω leading to a total value of $R_{tot} = R/n \sim 1\ \Omega$. The resistors are azimuthally distributed on a printed circuit board, so that the signal amplitude is independent of the actual beam position. At several locations, the signal is connected to a coaxial cable, feeding an amplifier. The voltage across the resistors U_{tot} is given by

$$U_{tot} = \frac{R}{n} \cdot I_{beam}. \tag{6.14}$$

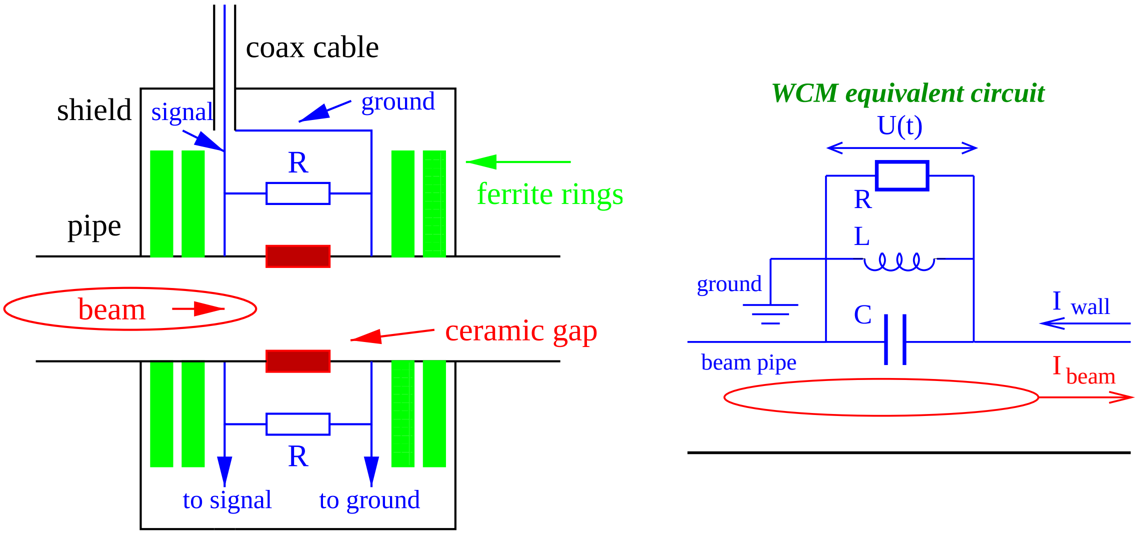

Figure 6.13: Schematics of a wall current monitor used for fast bunch observations and its equivalent circuit.

The resistors have to be shielded carefully against noise from the surroundings as caused, e.g. by ground currents from the rf-system. The shield also acts as a short circuit for low frequencies. In addition, ferrite rings are mounted across the vacuum pipe to force the image current through the resistors by damping the high frequencies penetrating the rings. Using high permeability ferrites, the lower cut-off frequency $f_{low} = 2\pi \cdot R_{tot}/L$ can be decreased. Values of about $f_{cut} \sim 10$ kHz are typical and allow un-differentiated bunch structure observation. The upper cut-off frequency is given by the capacitance of the gap to be $f_{high} = 2\pi \cdot R_{tot} \cdot C$. Several GHz are realizable with a careful design of all rf-components. The equivalent circuit is the same as for a passive transformer and hence its properties as discussed in Chapter 2.1.1. The only

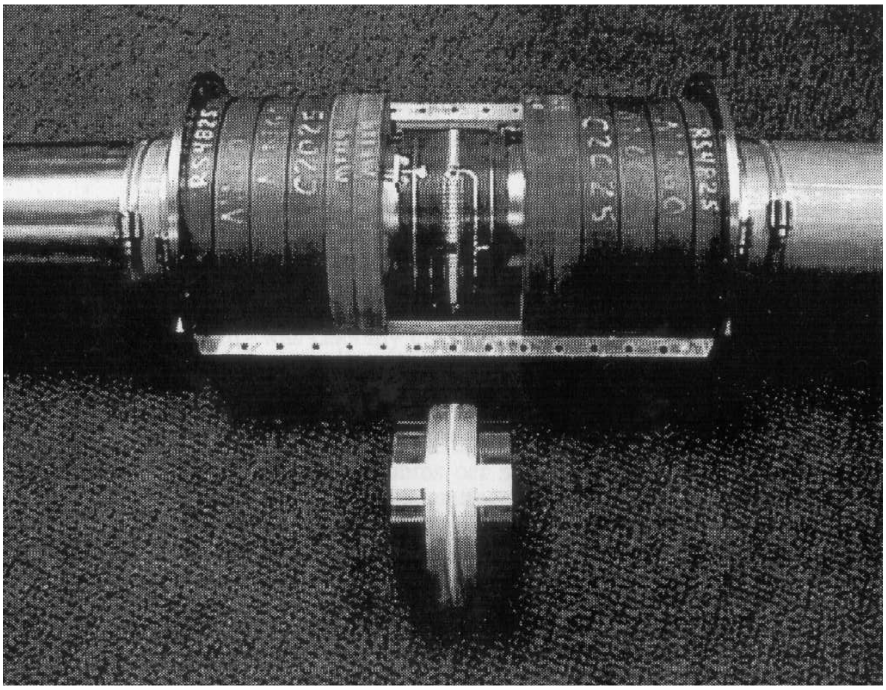

Figure 6.14: Photo of the wall current monitor used at FERMI-Lab for protons, from [107]. The ceramic gap is shown separately. The ferrite rings and the printed circuit with the resistors are visible.

exception is that the capacitance for the WCM is given by the ceramic gap, which is larger than any stray capacitance. The wall current monitor is well suited for broadband bunch shape observations at proton synchrotrons with bunch lengths down to the ns region.

6.7 Bunch structure for non-relativistic energies

For non-relativistic energies, the electric field of a bunch has a significant longitudinal component, as calculated for Fig. 6.2. This longitudinal field is seen by the pick-up, leading to a smearing of the signal. The structure of a bunch can not be monitored with a pick-up, as demonstrated in Fig. 6.15 for a 1.4 MeV/u ion beam corresponding to $\beta = 5.5$ %. In addition, the required resolution of 1^o in phase, or less than 50 ps in time, corresponds to an band-width of more than 10 GHz, which is hardly achieved by rf technologies. Other method have to be applied for such a measurement. The result is important for the adjustment of the LINAC modules, including bunchers for the injection to following accelerators, and the comparison of measurements and calculations, e.g. during a commissioning phase of a new accelerator. The bunch width and structure enters the numerical codes in the same manner as the transverse parameters, e.g. for the estimation of emittance growth by space charge forces. Moreover, as is shown below, a Gaussian distribution is not a good approximation for the bunch structure at these low energies. Three different devices are discussed below.

6.7.1 Coaxial Faraday cups for bunch shape observation

Faraday cups, as described in Chapter 2.4, are used to monitor the structure of bunches for non-relativistic protons or heavy ions at LINACs up to an energy of about 100 MeV/u and a bunch length of down to 1 ns. This should be a direct measurement of the beam charges arriving at the metallic surface of the cup. The electric signal is than guided via a 50 Ω matched transition

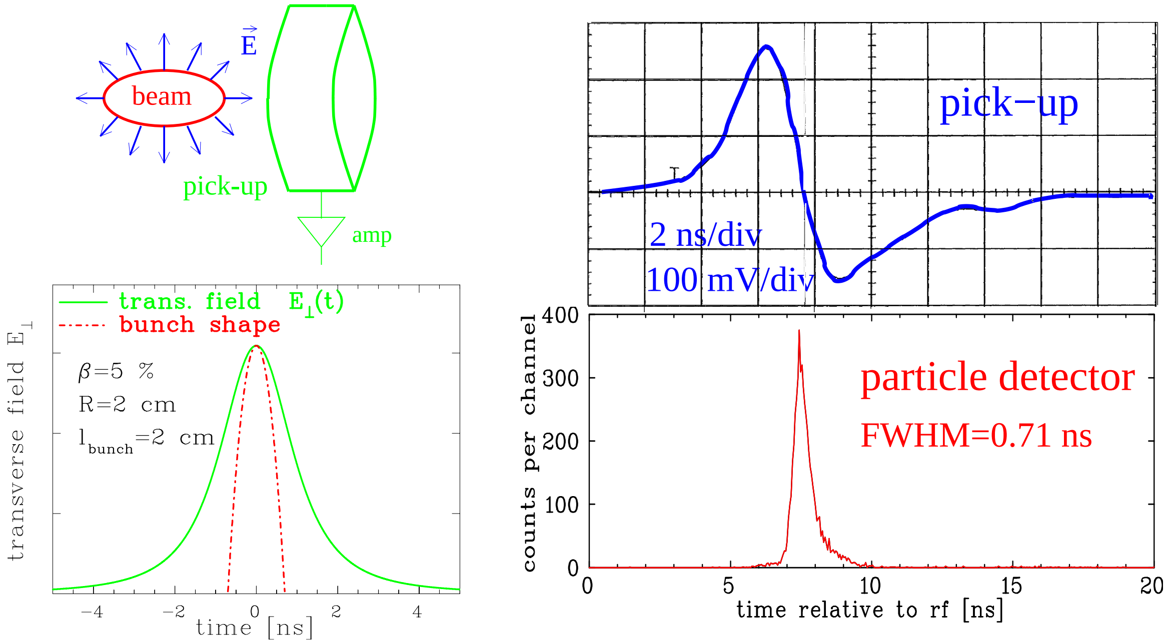

Figure 6.15: The comparison of a pick-up signal to the bunch structure measured with a particle detector at the GSI LINAC with 1.4 MeV/u on the right. The broadening of the pick-up signal due to the longitudinal field component is clearly seen. On the left, the time evolution of transverse electric field as seen by the pick-up is simulated for the for a bunch with $\cos^2$-distrubution.

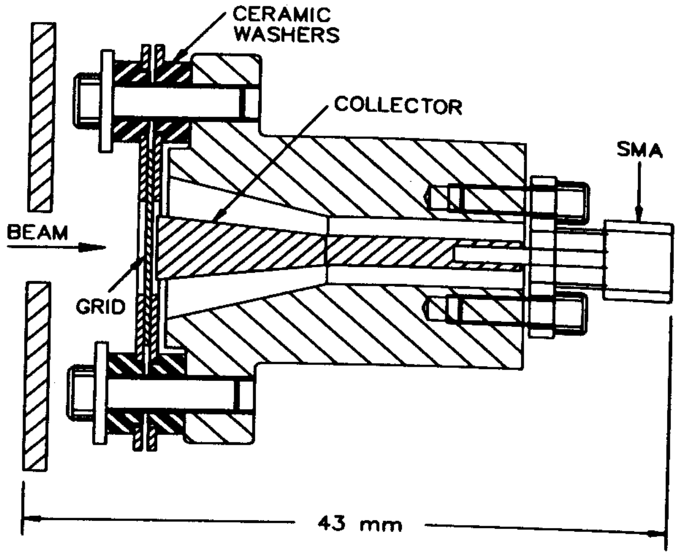

Figure 6.16: Scheme of a 50 Ω cup. A smooth transition to the SMA connector, maintaining 50 Ω impedance, is used. The grid for minimizing the advanced electrical field component is mounted close to the collector [108].

line to a broadband amplifier. All components of this electrical chain must have a bandwidth of ∼ 1 GHz for an un-distorted image of the bunch shape, which is not easy achievable. In Fig. 6.16 the schematics of a coaxial Faraday cup is shown: The beam hits a collector, which is mounted in a rotational symmetric configuration inside an outer conductor leading to a 50 Ω transmission line. To ensure the large bandwidth of 1 GHz and prevent for signal reflection, it is necessary to keep a constant ratio of the collector radius r_{coll} and the outer radius of the

Figure 6.17: Head of a coaxial Faraday cup. The grid for shielding of the advanced field and suppression of secondary electrons is shown in the middle. The collector including the ceramic cooling water feed-through is seen on the right hand side.

shield r_{shield}. The impedance Z of a coaxial transmission line should be 50 Ω everywhere and is given by

$$Z = \frac{Z_0}{2\pi} \cdot \ln \frac{r_{coll}}{r_{shield}} \quad . \tag{6.15}$$

The constant Z_0 is the 'impedance of the vacuum' and is given by $Z_0 = \sqrt{\mu_0/\epsilon_0} = 377\ \Omega$. If the impedance is not constant, part of the signal is reflected, leading to a deformation of the beam image [1].

---

[1] A measure of the matching quality is the voltage reflection coefficient ρ_V of a transmission line, defined by

$$U_{back} = \rho_V \cdot U_{forward} \tag{6.16}$$

with $U_{forward}$ the input voltage and U_{back} the reflected voltage. Expressed in terms of the transmission line impedance Z_1 and the impedance of the load Z_2 the voltage reflection coefficient ρ_V is

$$\rho_V = \frac{Z_2 - Z_1}{Z_2 + Z_1}. \tag{6.17}$$

There are three important cases:

- $Z_2 = Z_1 \Rightarrow \rho_V = 0$ the matching is perfect, no signal is reflected.
- $Z_2 = 0 \Rightarrow \rho_V = -1$ corresponding to a short circuit, the reflected signal has the same amplitude but opposite sign.
- $Z_2 = \infty \Rightarrow \rho_V = 1$, corresponding to an open circuit, the reflected signal comes back with the same amplitude and sign.

Another description of the matching is the so-called 'Voltage Standing Wave Ratio' which is defined as

$$\text{VSWR} = \frac{Z_2}{Z_1} = \frac{1 + \rho_V}{1 - \rho_V} \quad . \tag{6.18}$$

Most coaxial Faraday cups have a relatively small collector area, comparable with the size of the transmitting coaxial cable; in Fig. 6.16 it is only a few mm. In this case only the central part of the beam hits the collector. This does not influence the bunch shape measurement, because normally no correlation between the transverse and longitudinal plane exists.

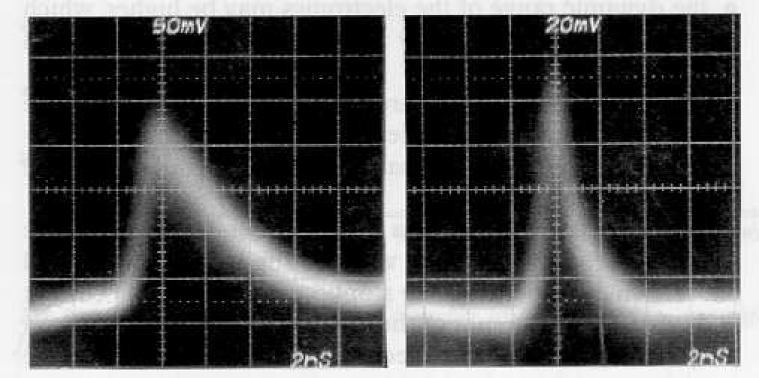

Figure 6.18: Observed bunch signal from a coaxial Faraday cup. Left: without suppressor voltage on the grid, right: -500 Volts on the grid.

Due to the creation of secondary particles, Faraday cup can only be used for protons or ions with energies below about 100 MeV/u. For this non-relativistic velocities $\beta < 40\%$ the advanced electric field, as calculated in Chapter 6.1, leads to an induced voltage on the collector prior to the arriving particles. Therefore a grid is mounted very close to the collector plate, which acts as an equi-potential surface shielding the collector. In addition one has to prevent for the escape of secondary electrons. By supplying a negative voltage, the secondary electrons are repelled back to the collector in connection to the shielding of the advanced electrical field. Figure 6.17 shows all important parts of the cup, including the grid. Fig. 6.18 gives an example of measured bunch signals with and without voltage on the grid. The signal from the coaxial cup is recorded with an oscilloscope in most cases. These devices have a bandwidth limitation of $\sim$ 1 GHz. Therefore the time resolution of this method is limited and sometimes insufficient for the application.

6.7.2 Time-of-flight using particle detectors

Particle detectors can have a fast response to a hit by a single beam particle. The signal width from such a single particle detector output can be less than 1 ns with a rise time of 100 ps and therefore a precise timing corresponding to bandwidth of larger than 10 GHz can be reached easily. Examples for adequate detectors are synthetic diamond counters [110], which work like solid state detectors, or Multi-Channel-Plates equipped with an anode in 50 Ω-geometry [115], where the anode shape is similar to that discussed for 50 Ω Faraday cups (Chapter 6.7.1). The arrival of a beam particle with respect to the accelerating rf frequency reflects the bunch structure with a time resolution of several tens of picoseconds.

The principle of such a setup [109, 66] is shown in Fig. 6.19. It can work with less than one ion hit per rf-period due to the use a of single hit particle detector. In the setup used at the GSI-LINAC, this reduction is done by Rutherford scattering in a 210 μg/cm^2 tantalum foil ($\sim$ 130 nm thickness) at a scattering angle of 2.5^o defined by a collimator with 16 cm distance and Ø0.5 mm apertures to give a solid angle of $\Delta\Omega_{lab} = 2.5 \cdot 10^{-4}$. The parameters are chosen to get an attenuation of $\sim 10^{-8}$ of the beam current, see Fig. 6.20. The calculated value is nearly independent of the ion species due the transformation from the center-of-mass frame (where the scattering cross section has the Rutherford-scaling $\sigma_{ruther} \propto Z^2 W_{beam}^{-2} \sin^{-4} \theta/2)$ to the lab frame (where the ratio of the projectile and target mass enters). A high target mass is preferred, so the additional energy spread by the scattering is lower than the required resolution. A contribution

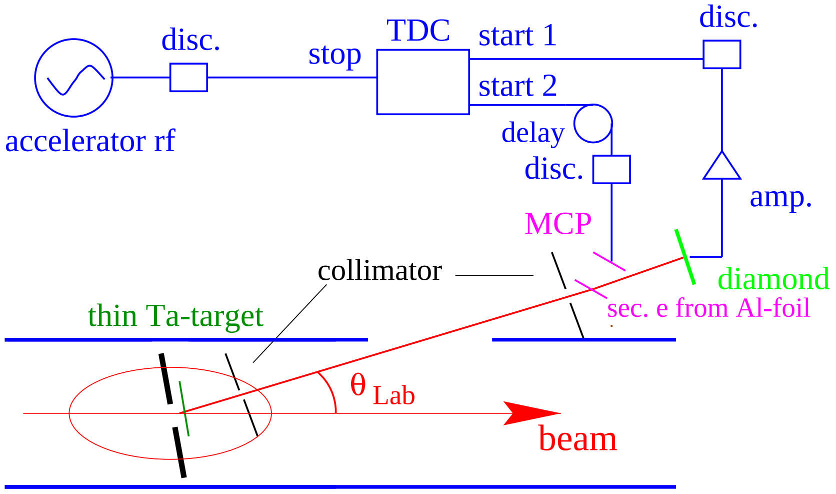

Figure 6.19: Principle of a particle detector using the TOF-technique for bunch structure and longitudinal emittance measurement.

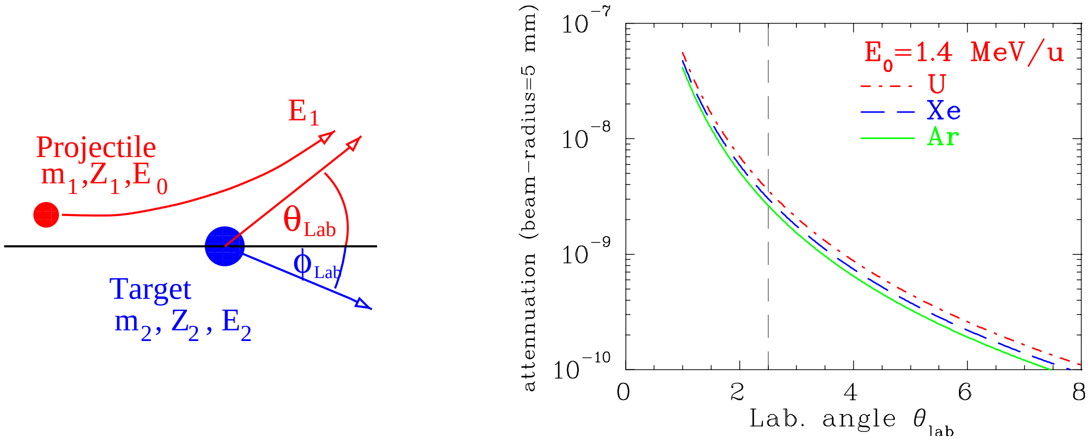

Figure 6.20: Calculated attenuation of a 1.4 MeV/u ion beam by Rutherford scattering in a 130 nm Ta foil for 1.4 MeV/u ions as a function of the angle in the lab-frame.

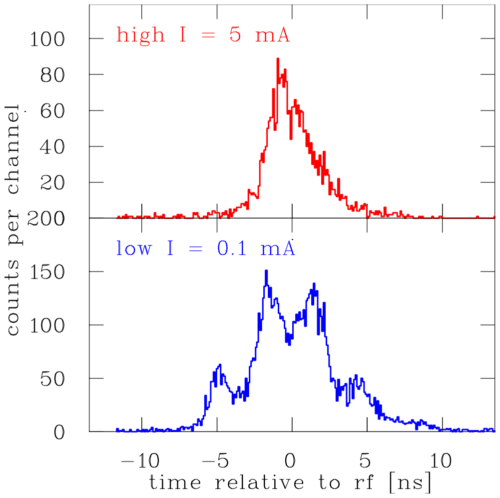

Figure 6.21: The bunch structure measured at the GSI LINAC with a 120 keV/u Ar^{1+} beam for different currents inside the RFQ [66]. The influence of the beam's space-charge to the longitudinal emittance is demonstrated by it. One rf-period is shown.

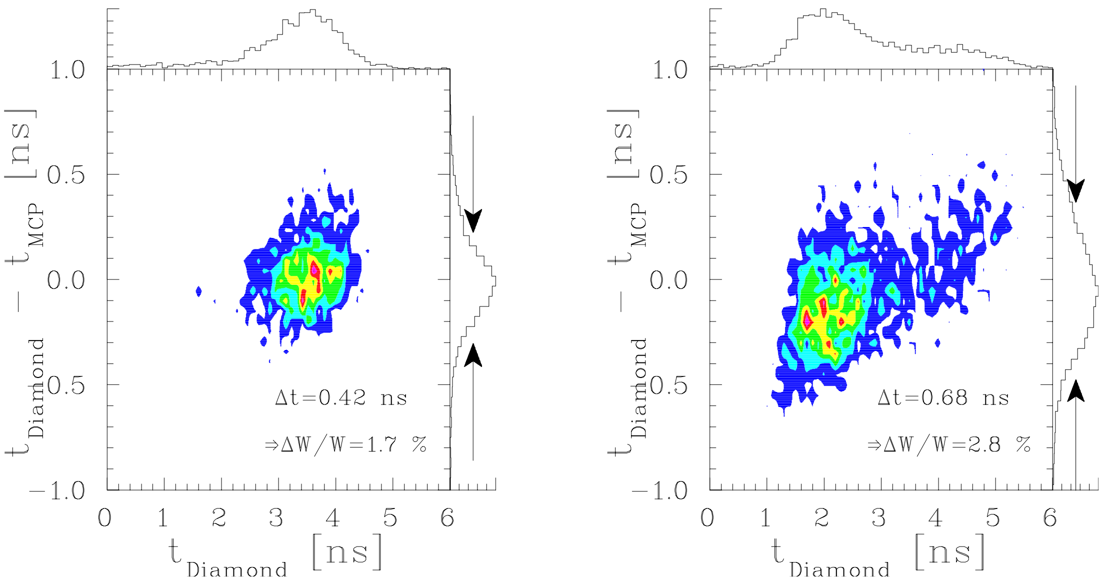

Figure 6.22: Phase space plot recorded with two detectors in coincidence at the GSI LINAC [66]. The time relative to the rf is plotted along the horizontal axis, the time difference of the individual particles on the vertical axis corresponding to the energy distribution. The low current ($I_{beam} = 0.1$ mA) results are plotted left. For a high current beam ($I_{beam} = 5$ mA) the emittance is asymmetrically broadened by space charge forces (right).

to the energy spread might arise from the electronic stopping power in the foil. After a drift space of ∼ 1 m the scattered particles hit the detector. Its output pulse is converted to a logic pulse with a special discriminator and the time relative to the accelerating rf is determined. A resolution of 25 ps, corresponding to 0.3^o rf-phase is attained here.

A typical measurement behind a low energy LINAC module is shown in Fig. 6.21, which acts also as an example for the probable non-Gaussian shape typically created in high current proton/heavy ion LINACs. The two measurements for high (top) and low (bottom) current show a quite different bunch shapes. A larger width corresponding to a filamented phase space distribution for the low current case is observed. Particle tracking calculation for this case confirm the strong ion current dependence for the longitudinal emittance. The applied rf-power in the cavity counteracts the space charge force for a high current beam. For a low current, filamentation occurs due to the missing damping by the space charge, which has to be corrected by a lower rf-power.

There are not many method to determine the longitudinal emittance at low energies, because this requires correlated time and energy spread measurements. With particle detectors, it is possible to measure the longitudinal emittance using a coincidence technique. As shown in Fig. 6.19, a second detector can be moved into the path of the scattered ions. For the GSI setup, this consists of a 15 μg/cm^2 Aluminum foil (∼ 50 nm) where several secondary electrons per ion passage are generated. These electrons are accelerated by an electric field of 1 kV/cm toward a micro channel plate equipped with a 50 Ω anode. The time relative to the accelerating rf, as well as the arrival time of the same particle at the diamond detector located 80 cm behind the MCP, are measured. From the difference in time of the individual particles (TOF method), the energy can be calculated and the phase space can be spanned.

An example of such a measurement is given in Fig. 6.22 for low (left) and high (right) current Ar beam. The arrival times at the diamond detector are used as the phase (or time) axis having a width of 1.4 ns, corresponding to 18^o phase, for the plotted case. The time difference between diamond and MCP is plotted on the vertical axis. The width for the low current operation is about 0.4 ns (FWHM), corresponding to an energy spread of $\Delta W/W = 1.7$ %. For a high current beam a double structure is visible in the bunch profile and an energy broadening to $\Delta W/W = 2.8$ % with a clear correlation in the phase space. This demonstrates the emittance growth due to the very high space charge forces.

6.7.3 Time structure using secondary electrons

In several low energy proton/heavy ion LINACs, a device for the bunch structure observation is installed, based on the observation of secondary electrons liberated from a single wire intersecting the beam, as shown in Fig. 6.23 and reviewed in [111, 112]. The beam hits a wire, which is held on a negative potential of typically 10 kV. By this field, the liberated secondary electrons are accelerated toward a thin slit on the side of the vacuum chamber. Here they pass a pair of plates, where an rf-field is applied having the same frequency as the accelerating rf or a higher harmonics of it. This field deflects the electrons and the different arrival times are transformed via varying deflection angles to a difference in space, i.e. this deflector acts as a 'time-to-space converter'. (The same principle is used in a non-resonant way in an analogue oscilloscope.) After a drift of typically 0.5 m, the electrons are detected with a Faraday cup or a secondary electron multiplier with a small slit in front. (A secondary electron multiplier is just the same as a photo-multiplier, but without a photo-cathode.) For a fixed slit position, the phase of the deflecting rf relative to the accelerating rf can be changed to transmit electrons representing different time slots of the beam bunches, to get a full image of the bunch structure.

The resolution of this device is better than 1^o in phase, independent of the frequency of the rf, up to several hundred MHz. It is known that the emission of secondary electrons is a fast process with a time difference of less than 1 ps between the hit of the beam particle and the electron emission, i.e. much faster than the required resolution. The rf deflector is built as a resonator to get an electric field high enough for typically 100 mrad deflection to have an appropriate separation at the detector ~ 0.5 m apart. A careful design is required to prevent multi-pactoring. In addition, the electrons have to be focused transversally. A constant dc-

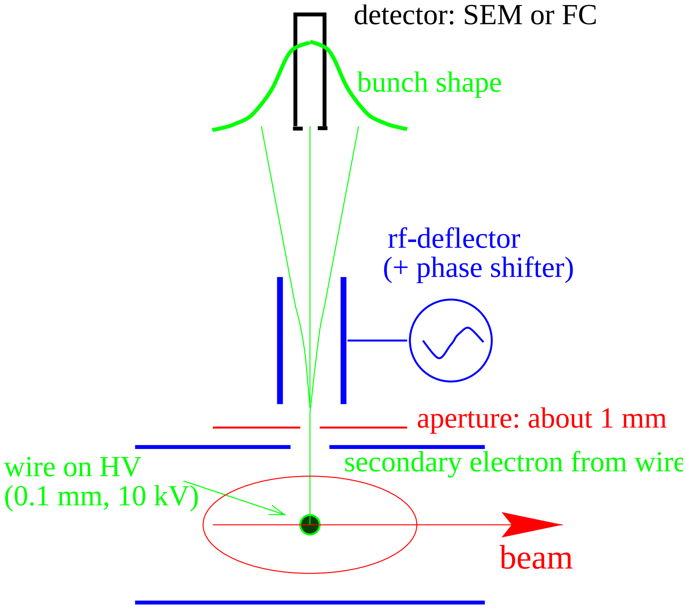

Figure 6.23: Principle of a deflector technique for bunch structure observation. SEM means secondary electron multiplier.

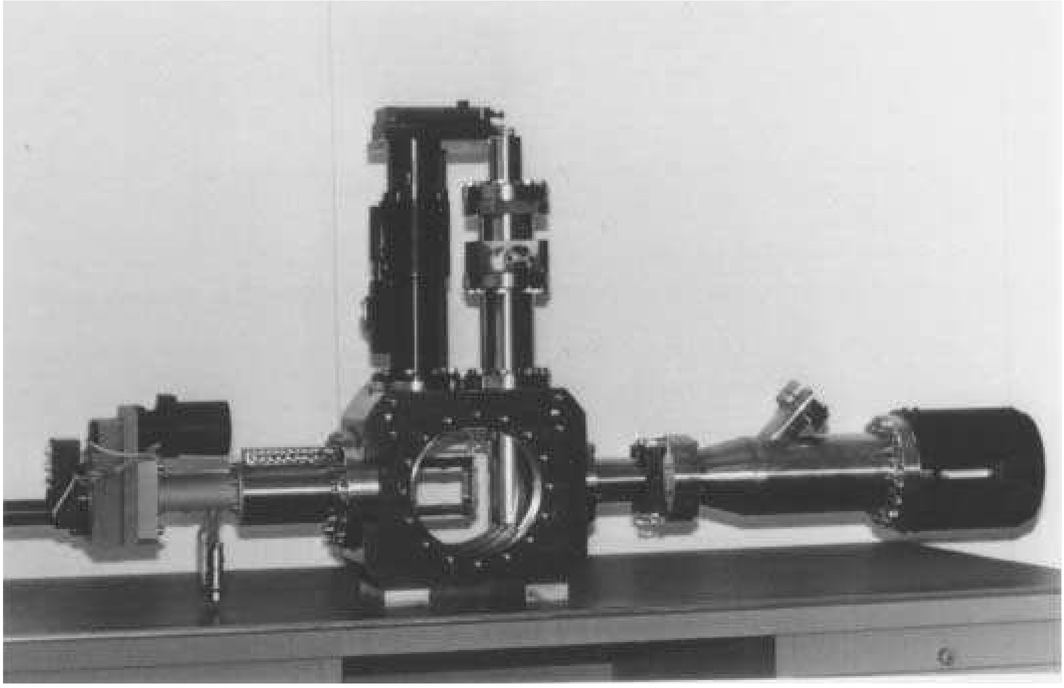

Figure 6.24: The bunch shape monitor (BSM) installed at CERN LINAC 2 [111]. The vacuum feed-through on the left side is the support for the high voltage wire. The rf-deflector is installed on the vertical flange and the detector is mounted on the right.

voltage applied to the deflector plates serves as an electrostatic lens. The HV-wire is movable, so the bunch shape can be measured for different horizontal locations and it is possible to do a measurement with a high current beam by intercepting the beam edge with low power deposition.

6.8 Bunch structure for relativistic electron beams

In most cases, longitudinal diagnostics at electron accelerators is not done using pick-ups, although, due to the relativistic velocities, it would be possible. However, the bunch length is typically only of the order of several hundred ps, so that even a pick-up bandwidth of several GHz is insufficient to reproduce the detailed bunch structure. Here we profit from the emission of synchrotron light at a dipole, or preferably from a insertion device. A review on this technique is given in [113].

The principle of such a measurement is shown in Fig. 6.25. The synchrotron light emitted by the electrons is filtered to get a small wavelength band (about $\Delta\lambda \simeq 10$ nm width). It is focused and scraped by a pin hole onto the photo-cathode of a streak camera. A streak camera is a commercially available device [115], which allows visible light observations with a time resolution down to 1 ps. The secondary electrons from the photo-cathode are accelerated and pass a fast deflector, driven by a frequency in the 50 to 300 MHz region. The general scheme is similar to the discussed 'time-to-space converter' in Chapter 6.7.3. For synchronization, this deflection is locked to the accelerating rf. After a certain drift space, the electrons are amplified by a MCP and converted to photons by a phosphor screen. With a standard CCD camera, the image from the phosphor is stored. The different arrival time of the synchrotron light, and therefore the bunch structure, is converted to a difference in space with a full scale of typically 500 ps and a

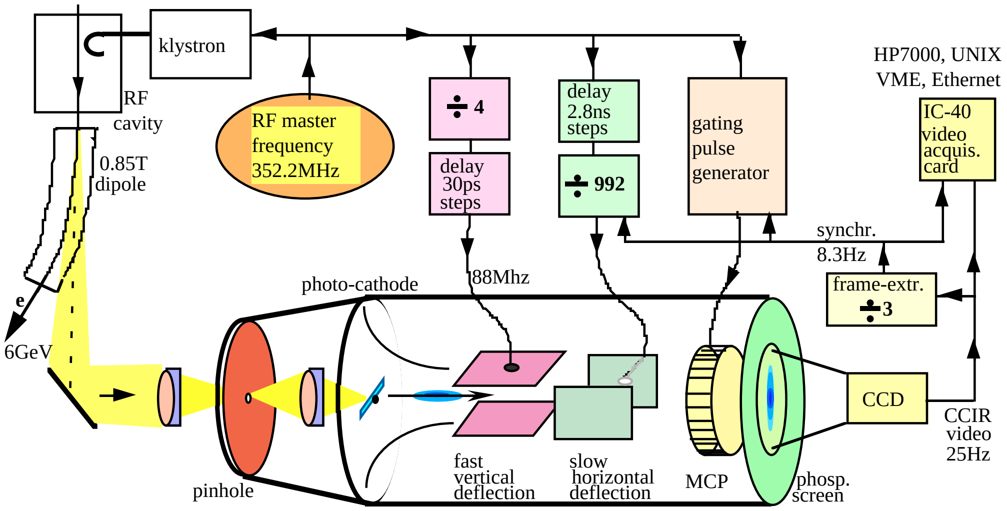

Figure 6.25: Principle of a streak camera measurement for bunch width determination at electron accelerators (here ESRF), from [114].

resolution in the ps range. A second, perpendicular pair of plates is driven with a much lower frequency to separate the images from the individual bunches.

Fig. 6.26 is an example of such a measurement, performed with synchrotron radiation from a wiggler [116]. The slow scan for the separation of the individual bunches is the horizontal axis. The vertical axis has a full scale of 800 ps and the bunch width is only 60 ps (FWHM), demonstrating the high resolution of such a system. Short bunches are needed by synchrotron radiation users for time resolved spectroscopy. A large voltage is applied to the synchrotron rf cavities to produce and maintain these short bunches together. In Fig. 6.27 the bunch width is plotted for different rf voltages. The achievable bunch length depends on the stored electron current, as displayed. Counteracting the rf bunching force, non-linear processes like wake-fields and instabilities increase for higher currents. Effects like head-tail oscillations are visible with the help of the streak camera measurements, see e.g. [113].

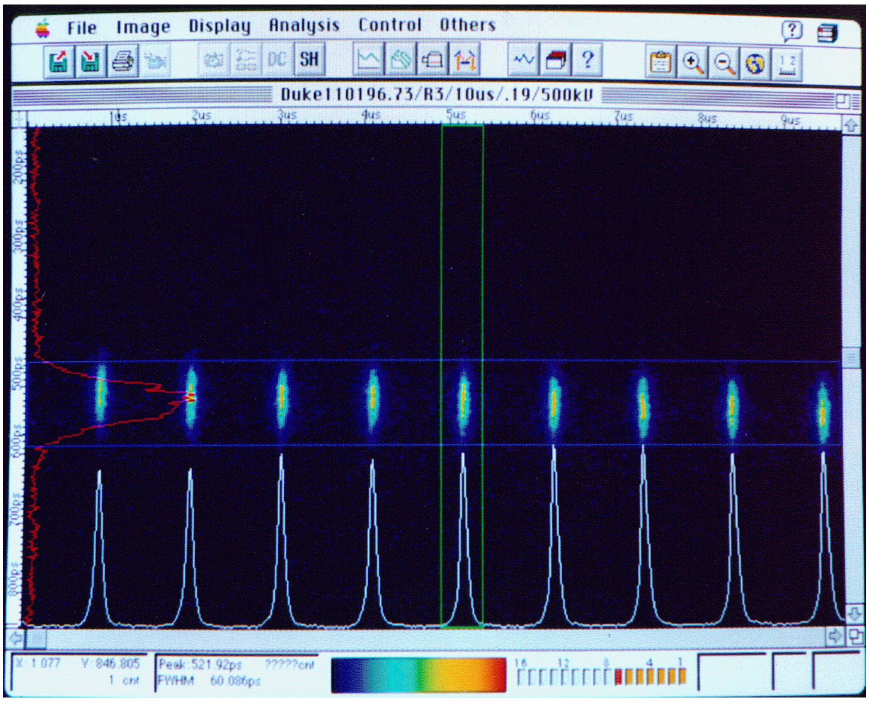

X: 1.077 Y: 846.805
1 cnt

Peak:521.92ps ?????cnt
FWHM 60.086ps

Figure 6.26: Bunch length measurement with a streak camera, using synchrotron light from a wiggler at the Duke storage ring [116]. The horizontal axis is 10 μs for the bunch repetition and the vertical axis is 800 ps full scale for the bunch structure. The bunch width is 60 ps (FWHM). A low current beam was used and the wavelength of 450 nm is transmitted to the photo-cathode.

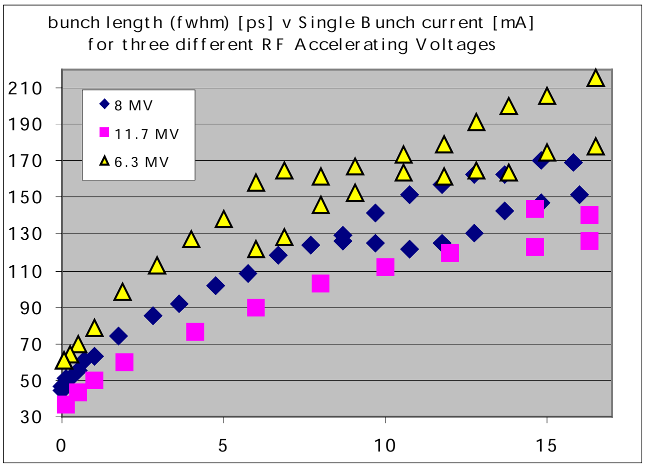

Figure 6.27: Example of the use of a streak camera at the synchrotron light facility ESRF [113]: The bunch-length is recorded as a function of the current per bunch for different accelerating voltages.

Chapter 7

Schottky noise analysis

The beam in an accelerator consists of a finite number of particles. A current created by a finite number of charge carriers always has some statistical fluctuation. This was investigated first by W. Schottky in 1918 [117]. The detection of these fluctuations with a sensitive spectrum analyzer allows a non-destructive and precise measurement of several parameters, like momentum distribution, tune, transverse emittance and chromaticity. The method is mainly used for coasting (de-bunched) beams in proton/heavy ion synchrotrons and storage rings. At LINACs the method is not applicable. The strength of the detected incoherent signals is orders of magnitude lower than those produced by the coherent motion of bunched beams described in Chapter 5. Nevertheless, due to the high sensitivity, a Schottky scan with very low currents can be performed, in particular with electron- or stochastically cooled beams.

For the following description we recall some basic formulas of accelerator optics in circular machines:

$$\frac{\Delta C}{C_0} = \alpha \frac{\Delta p}{p_0} \quad \text{Definition of momentum compaction factor} \tag{7.1}$$

$$\alpha = \frac{1}{\gamma_{tr}^2} \quad \text{Momentum compaction factor and } \gamma\text{-transition} \tag{7.2}$$

$$E_{tr} = \gamma_{tr} m_0 c^2 \quad \text{Transition energy} \tag{7.3}$$

$$\frac{\Delta f}{f_0} = -\frac{\Delta T}{T_0} = -\eta \frac{\Delta p}{p_0} \quad \text{Definition of frequency dispersion} \tag{7.4}$$

$$\eta = \frac{1}{\gamma_{tr}^2} - \frac{1}{\gamma^2} = \alpha - \frac{1}{\gamma^2} \quad \text{Frequency dispersion and } \gamma\text{-transition} \tag{7.5}$$

$$\frac{\Delta Q}{Q_0} = \xi \frac{\Delta p}{p_0} \quad \text{Definition of chromaticity} \tag{7.6}$$

$$f_s = \frac{1}{2\pi}\sqrt{\frac{\zeta e}{C A m_0 \gamma} \cdot \frac{f_{rf}}{f_0} \cdot |\eta| \cdot U_{rf} \cos\varphi} \quad \text{Synchrotron frequency} \tag{7.7}$$

With C_0 circumference of the synchrotron, p_0 momentum, f_0 revolution frequency, T_0 revolution time, Q_0 the tune for the reference particle, γ relativistic factor, A the mass of the particle with charge ζ and f_{rf} the frequency of the acceleration rf with amplitude U_{rf} and a phase φ for the reference particle realtive to the crest.

7.1 Spectrum analyzer

A spectrum analyzer is used to determine the amplitude of a frequency component of a time varying signal. In principle, it is an analogue equivalent to a Fourier transformation. A tunable

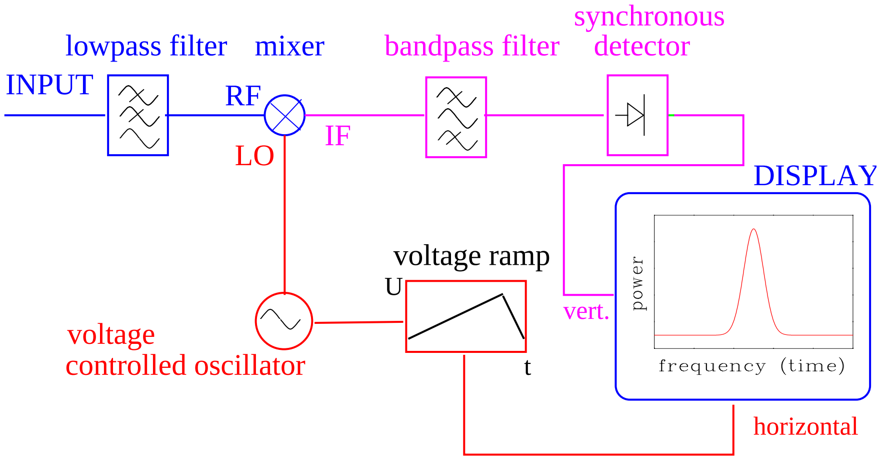

Figure 7.1: Principle of a spectrum analyzer.

bandpass filter could be used, where the center frequency is swept. But this is difficult to realize. Instead, a mixer in the input port of the spectrum analyzer is used. See Eq. 5.25 for a description of a mixer.

The simplified principle of a spectrum analyzer is shown in Fig. 7.1. The input signal passes a low-pass filter, which limits the bandwidth of the device. Typical values for the bandwidth of high performance models are 100 Hz to 3 GHz. The filtered signal is then mixed with a tunable frequency of constant amplitude, applied to the LO port of the mixer. This frequency can be ramped and its maximum value is twice the maximum input frequency (in this case from 3 to 6 GHz). The wave with the difference frequency is filtered by a narrow bandpass filter. A linear synchronous detector rectifies the signal to get the amplitude (or power) of the mixed signal. The amplitude or the power is displayed as a function of the LO frequency. The described principle is that of a heterodyne receiver. In commercial devices several steps of mixers are used.

Four main parameters can be chosen by the operator:

- the frequency range for the LO sweep
- the sweep time i.e. the time needed for the frequency sweep
- the reference level i.e. the power of the LO wave
- the resolution bandwidth corresponding to the width of the bandpass filter.

Short, excellent descriptions of the functionality of spectrum- and network analyzers are given in [94]. For a fixed LO frequency this principle was also discussed in Chapter 5.7 for the narrowband position pick-up processing.

For a Schottky scan, typical values of an LO frequency range is 10 to 100 kHz with a sweep time of 0.1 to 1 s. One should be aware that due to the relatively long sweep time, possible changes of the beam parameters during this time are displayed in a wrong manner. Instead of using a spectrum analyzer one can also use an ADC recording the data in the time domain and apply an FFT, see e.g. [118]. In modern applications, this is a cheaper alternative if the frequencies of interest are not too high.

7.2 Longitudinal Schottky signals for a coasting beam

We first consider a single particle with charge [1] ζe in a storage ring with a revolution period T_0 and a revolution frequency $f_0 = 1/T_0$. The current at a fixed location is given by the passing of the particle at time $t = 0, 1 \cdot T_0, 2 \cdot T_0, ...$ is

$$I(t) = \zeta e f_0 \sum_{h=1}^{\infty} \delta(t - hT_0) = \zeta e \sum_{h=-\infty}^{\infty} e^{2\pi i h f_0 t}. \tag{7.8}$$

A real detector can only measure positive frequencies. Or in other words, the phase information is lost, when detecting a real signal using an ADC or a spectrum analyzer. Therefore the current of a single charge is

$$I(t) = \zeta e f_0 + 2\zeta e f_0 \sum_{h=1}^{\infty} \cos\left(2\pi h f_0 t\right) \tag{7.9}$$

The first term is the dc part of the current $I_{dc} = \zeta e f_0$, while the sum gives the Schottky signal, as we will see. The Fourier transformation is given by

$$I(f) = \zeta e f_0 \cdot \delta(0) + 2\zeta e f_0 \sum_{k=1}^{\infty} \delta(f - k f_0) \tag{7.10}$$

which is a line spectrum with peaks at all harmonics of the revolution frequency f_0, with finite height for a real beam and a real equipment, see Fig. 7.2.

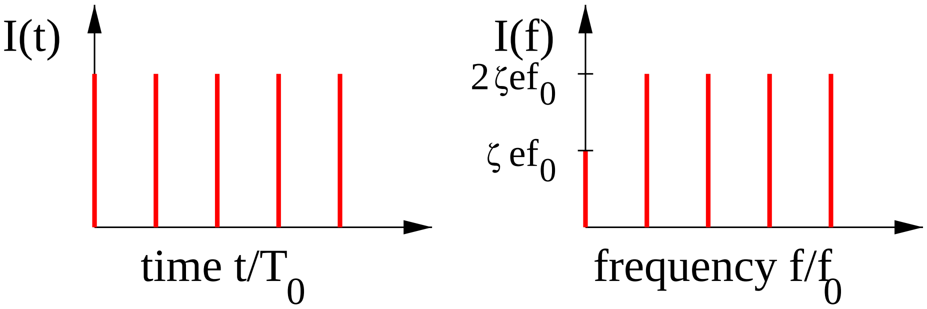

Figure 7.2: The time domain signal of a single particle in a storage ring and its frequency spectrum made of single lines.

Now consider a coasting (debunched) beam of N particles randomly distributed along the storage ring at an angle θ_n with slightly different revolution frequencies f_n. One can rewrite Eq. 7.9 for the N particles as

$$I(t) = \sum_{n=1}^{N} \zeta e f_0 \cos\theta_n + 2\zeta e f_0 \sum_{n=1}^{N} \sum_{h=1}^{\infty} \cos\left(2\pi h f_n t + h\theta_n\right) \tag{7.11}$$

A spectrum analyzer measures the power density spectrum, which is given for the frequency band of the harmonic h by the rms (root-mean-square) current $\langle I^2 \rangle$ as

$$\begin{aligned} \langle I^2 \rangle &= \left(2\zeta e f_0 \sum_{n=1}^{N} \cos h\theta_n\right)^2 = (2\zeta e f_0)^2 \cdot (\cos h\theta_1 + \cos h\theta_2 + ... + \cos h\theta_N)^2 \\ &= (2\zeta e f_0)^2 \cdot N/2 \end{aligned} \tag{7.12}$$

---

[1] Here ζ is used as the abbreviation for the charge to distinguish it from the non-integer part of the tune q.

because all terms of the from $\cos^2 h\theta_i$ are positive. Or, in other words the term in brackets is

$$(\cos h\theta_1 + \cos h\theta_2 + ... + \cos h\theta_N)^2 = N\langle\cos^2 h\theta_i\rangle = N/2. \tag{7.13}$$

This means that only the dc part remains. All others cancel due to averaging. The rms signal is finally

$$I_{rms} = \sqrt{\langle I^2\rangle} = \zeta e f_0 \sqrt{2N} \tag{7.14}$$

This total current per band is proportional to the square root of the number of particles due to its incoherent distribution. It is independent of the harmonic number h. This is different from the coherent beam signal recorded with a pickup for bunched beam, having $I \propto N$. A more stringent treatment can be found in [96, 119, 120].

A pick-up, as described in Chapter 5, is used to monitor the signal. The measured current I_{rms} has to be transformed with the help of the transfer impedance Z_t to voltage $U = Z_t \cdot I_{rms}$.

A measurement using a spectrum analyzer shows the power spectrum density $P(f)$ within a frequency range Δf, which is given by

$$P(f) = Z_t \frac{I^2_{rms}}{\Delta f}. \tag{7.15}$$

Because the total power within a band is constant, the Schottky lines become broader for a increasing harmonic number h and their heights decrease. This is shown in Fig. 7.3. The width of all harmonics corresponds to the spread in the revolution frequency. Using the frequency dispersion η (Eq. 7.4), this can be transformed to the momentum distribution $\Delta p/p$. From the center frequency at each harmonic f_h and the width Δf_h, one can calculate the momentum width as

$$\frac{\Delta p}{p} = -\frac{1}{\eta} \cdot \frac{\Delta f_h}{f_h} = -\frac{1}{\eta} \cdot \frac{\Delta f_h}{h f_0}. \tag{7.16}$$

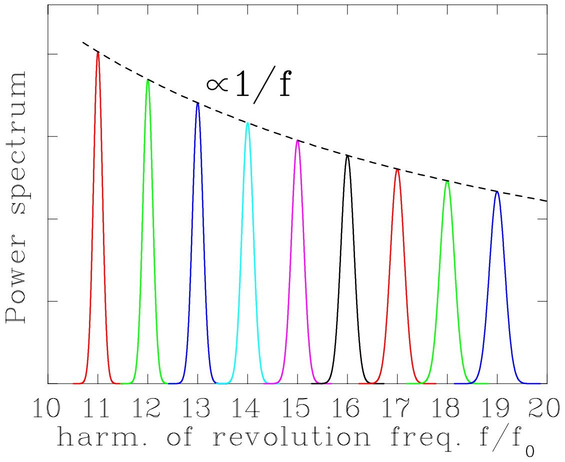

Figure 7.3: Hypothetical longitudinal Schottky lines for a Gaussian momentum distribution with $\Delta p/p = 1$ % and an artificial small value of $\eta = -0.005$. The different peaks correspond to the different harmonics.

The plot in Fig. 7.3 uses a momentum width of 1%, but an artificially small value of $\eta = -0.005$ to get unusually broad lines. From the figure we can see, that the lines from ascending harmonics starts to overlap for

$$h > \frac{|\eta|}{2} \cdot \frac{p}{\Delta p} \tag{7.17}$$

which happens for real beams only at very high harmonics. Schottky lines at lower harmonics are well separated, because $\Delta p/p < 10^{-3}$ and an absolute value of η close to unity are typical values for the injection to a synchrotron. The resolution is larger for higher harmonics due to a wider peak. On the other hand, the signal-to-noise ratio is better for a lower harmonic number due to the required lower bandwidth Δf and the scaling of the noise voltage $U_{noise} \propto \sqrt{\Delta f}$. At most proton/heavy ion synchrotrons with a typical revolution time of 1 μs (corresponding to $f_0 = 1$ MHz), harmonic numbers between 10 and 30 are used. The typical frequency range for a scan of the distribution is less than 100 kHz.

In proton/heavy ion synchrotrons or storage rings, cooling is very often used to achieve highly brilliant beams by transverse emittance and momentum distribution shrinkage. This is important for high resolution experiments or for the increase of the number of stored particles using stacking methods. This is performed by electron cooling (see e.g.[42]) or stochastic cooling (see e.g. [43]), in most cases with an un-bunched beam. Schottky diagnostics are an essential tool to control the cooling process. An example is given in Fig. 7.4, where the momentum width of an ion beam is reduced by two orders of magnitude within seconds by electron cooling.

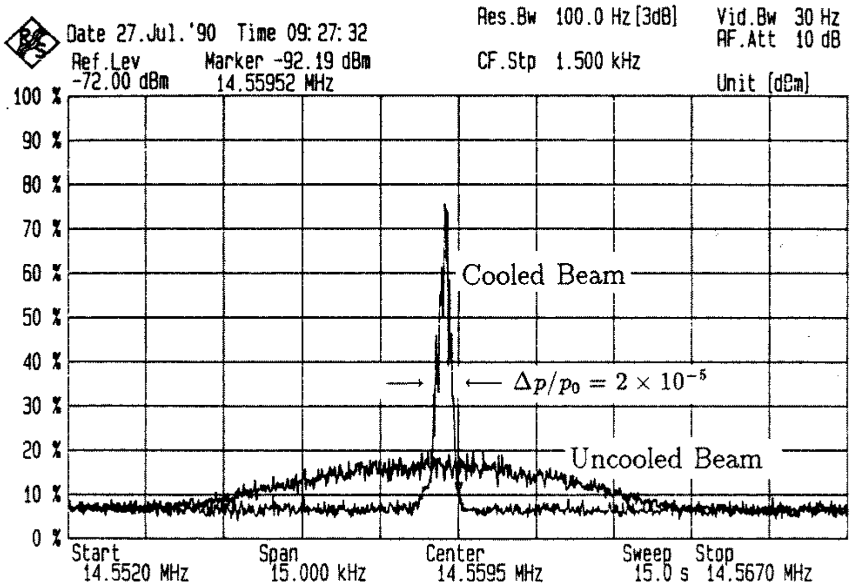

Figure 7.4: Longitudinal Schottky scan at the 10^{th} harmonic of Ar^{18+} at the GSI storage ring. The broad curve is the frequency spectrum at injection with $\Delta p/p = 1 \cdot 10^{-3}$ and the narrow curve is recorded after electron cooling down to a momentum width of $\Delta p/p = 2 \cdot 10^{-5}$.

The pick-up installed at the ESR at GSI is shown in Fig. 7.5. The device can also be used for transverse Schottky diagnostics (see below). For each direction, a pair of plates is installed. The edges are bent to get a constant position sensitivity, independent of the orbital offset perpendicular to the direction under investigation.

7.3 Longitudinal Schottky signals for a bunched beam

For a bunched beam, the Schottky spectrum splits into several lines for the following reason: In addition to the discussed fluctuations because of their finite number, the beam particles oscillate with the synchrotron frequency. This corresponds to a modulation in time of the particles' passage through the pick-up. Therefore, the spectrum becomes more complicated since each harmonic line $h \cdot f_0$ (center of the Schottky bands) gets sidebands from the synchrotron oscillation.

The passage of the particles at the pick-up is modulated by the synchrotron frequency f_s for particle n with $\tau_n = \hat{\tau}_n \sin(2\pi f_s t + \varphi_n)$. The synchrotron frequency is much lower than the

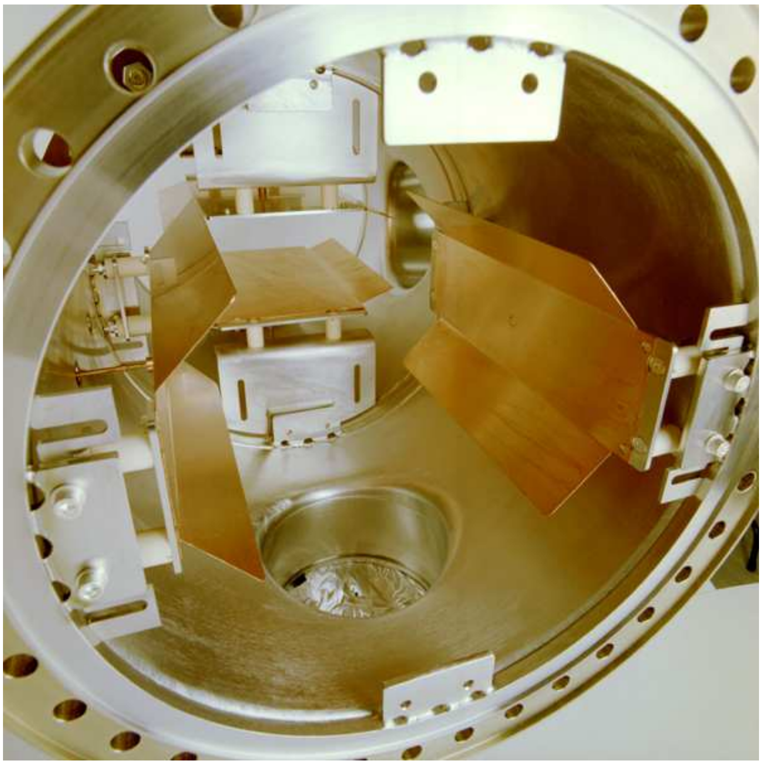

Figure 7.5: Photo of the Schottky pick-up installed at the storage ring at GSI. It can be used for longitudinal as well as for transversal diagnostics. In front we see the plates for the horizontal, at the back for the vertical direction. The flange diameter is Ø 350 mm.

revolution frequency. It can be shown [96], that this leads to a modulation of the un-bunched peak according to the Bessel functions J_p of order p. The second term of Eq. 7.11 has to be modified for each harmonic as

$$I_h(t) = 2\zeta e f_0 \cdot \mathrm{Re}\left[\sum_{n=1}^{N}\sum_{p=-\infty}^{\infty} J_p(h\omega_n\hat{\tau}_n)e^{i(h\omega_n t + h\theta_n + p\omega_s t + p\varphi_n)}\right] \tag{7.18}$$

The distance between the maxima is given by the synchrotron frequency. The sidebands decrease symmetrically with respect to the center and get broader. The number of sidebands above the noise increases for increasing harmonics. A measurement is shown in Fig. 7.6. The synchrotron frequency can be determined with this method.

7.4 Transverse Schottky signals for a coasting beam

As in the case of a beam position pick-up, one can use the difference signal of opposite electrodes for the monitoring of transverse noise signals. The finite number of particles perform betatron oscillations around the beam center (and the electrical center of the pick-up) with

$$x_n(t) = A_n\cos(2\pi q f_0 t + \mu_n) = A_n\cos(2\pi f_\beta t + \mu_n) \tag{7.19}$$

where A_n is the betatron amplitude of the particle n with an individual phase μ_n and q is the non-integer part of the tune and $f_\beta = qf_0$ the betatron frequency. The difference Schottky signal,

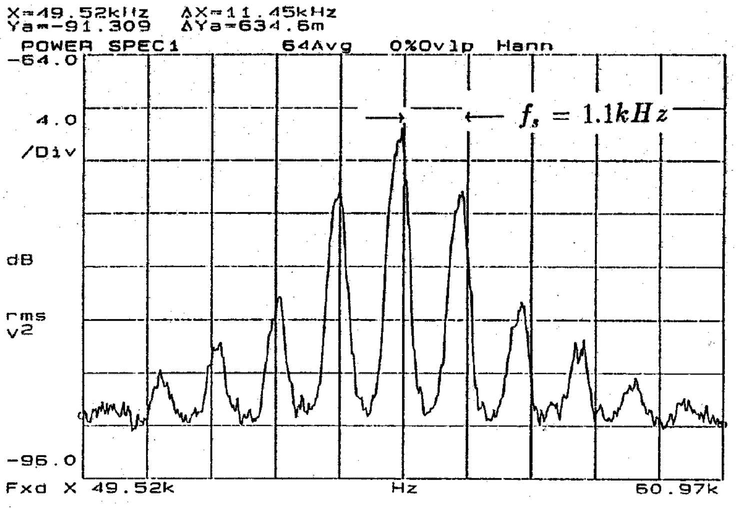

Figure 7.6: Schottky spectrum of a bunched ion beam at the GSI storage ring. f_s is the synchrotron frequency.

which corresponds to the dipole moment d_n of the beam, is a composition of the longitudinal noise and a transverse modulation. For one particle and a harmonic h, the dipole moment $d_n(t)$ is

$$\begin{aligned} d_n(t) &= \zeta e f_0 \cdot A_n + 2\zeta e f_0 \cdot A_n \sum_{h=1}^{\infty} \cos\left(2\pi q f_0 t\right) \cdot \cos\left(2\pi h f_0 t\right) \\ &= \zeta e f_0 \cdot A_n + \zeta e f_0 \cdot A_n \sum_{h=1}^{\infty} \cos\left[2\pi(h-q) f_0 t\right] \cdot \cos\left[2\pi(h+q) f_0 t\right] \qquad (7.20) \end{aligned}$$

as given by a theorem of trigonometry [2]. In the frequency domain this corresponds to a splitting into two sidebands for each harmonic, distributed symmetrically at $h - q$ and $h + q$. In electro-engineering this is called a frequency modulation. This is schematically shown in Fig. 7.7. The reason for the two bands arises from the fact that the Fourier transformation is defined for frequencies from $-\infty$ to $+\infty$, while a real device can only measure positive frequencies.

As in the longitudinal case, a coasting beam of N particles randomly distributed around the ring and with random betatron phase μ_n is considered. The rms value per band is

$$\begin{aligned} d_{rms}^2 = \langle d^2 \rangle &= (\zeta e f_0)^2 \cdot A_{rms}^2 \cdot N/2 \\ &= (\zeta e f_0)^2 \cdot \epsilon \cdot \beta(s) \cdot N/2. \qquad (7.21) \end{aligned}$$

The average of the individual betatron amplitudes A_n gives the beam width. The square of the width is related to the beam emittance ϵ times the value of the beta-function $\beta(s)$ at the location of the pick-up. A first result is that from the total power of the transverse band one can deduce the emittance. In particular, one can monitor transverse cooling with the help of the transverse Schottky noise. This is demonstrated in Fig. 7.8, where the time evolution of the beam during stochastic cooling is shown. The curves are recorded every 80 ms. One clearly sees the decrease of the power within the sidebands due to the shrinking emittance (and not due to particle losses). To get the absolute value of the emittance, a calibration is needed with respect to a residual gas monitor or a scraper, because too many inaccurately known device properties of the pick-up contribute to the spectrum. (A precise knowledge of the transverse

---

[2] $\cos x \cdot \cos y = 1/2[\cos(x-y) + \cos(x+y)]$

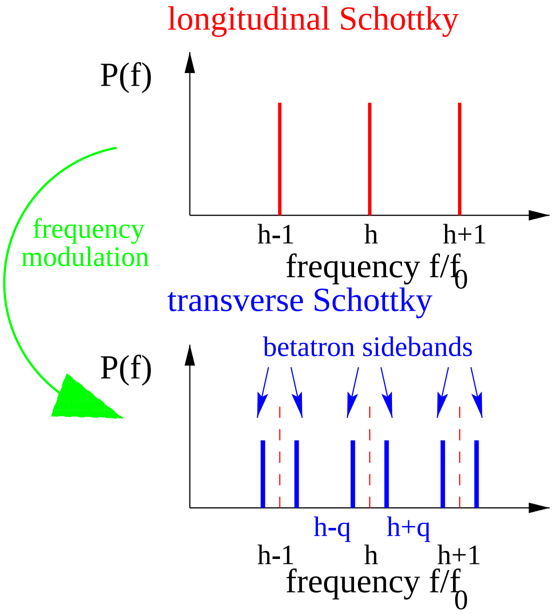

Figure 7.7: Schematic plot of the line splitting of a transverse Schottky scan as compared to the longitudinal case.

transfer impedance $Z_\perp(\omega)$ Eq. 5.16 is needed, because the voltage $U = Z_\perp d$ is measured.) The middle peak of the figure is the longitudinal signal, which should vanish according to the theory above. But here the beam was not perfectly centered in the pick-up. The increase of its height is due to longitudinal cooling.

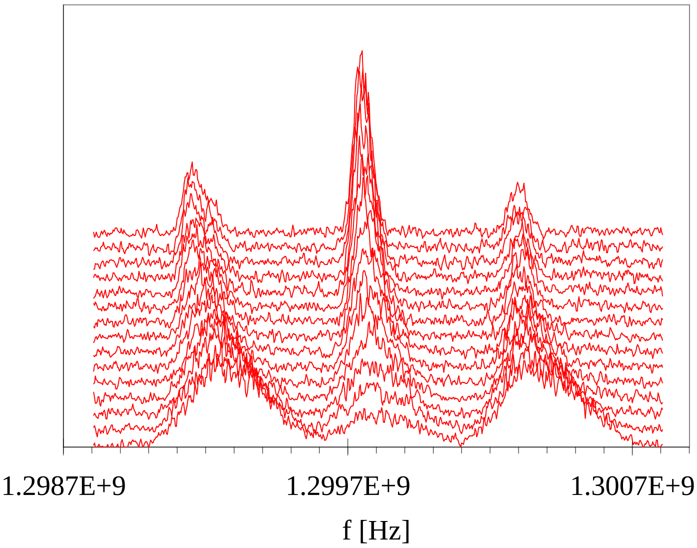

Figure 7.8: Transverse Schottky spectra recorded every 80 ms during stochastic cooling at the GSI storage ring at a high harmonic.

Another widely used application of transverse Schottky is the tune measurement of coasting beams. The maxima of the two sidebands for the same harmonic are located at $f_h^- = (h-q)f_0$ and $f_h^+ = (h+q)f_0$. The non-integer part of the tune is calculated via

$$q = h \cdot \frac{f_h^+ - f_h^-}{f_h^+ + f_h^-}. \tag{7.22}$$

With this method, one can easily get the incoherent value of the tune without any beam influence.

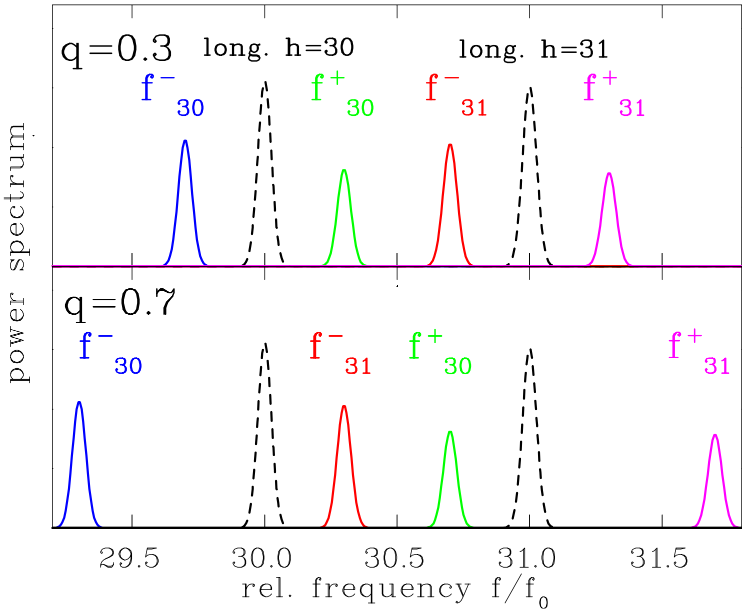

Figure 7.9: Transverse Schottky spectra for the harmonics 30 and 31. The plot on top shows the frequency position for $q = 0.3$. Here the sidebands are close to the longitudinal peak. The lower plot is for $q = 0.7$ and here the position are interchanged. The parameters for the calculation are: $f_0 = 1$ MHz, $\Delta p/p = 2 \cdot 10^{-3}$, $\eta = -1$, $\xi = -1$, $Q = 4.3$ or 4.7. The sideband for other harmonics are not shown.

This is in contrast to a measurement via BTF discussed in Chapter 5.9, where the beam is excited gently. Moreover, for the BTF the coherent tune is determined, which might differ from the incoherent one, if space charge forces are significant.

Looking at a transverse Schottky scan, it is not directly evident where the two sidebands of one harmonic are located. The ordering of the lines can be interchanged. This is demonstrated in Fig. 7.9 for $q < 0.5$ (top) and $q > 0.5$ (bottom). Like described for the BTF, this can be checked by a small variation of the tune while watching the direction of the line center shift.

From the width of the sidebands, the chromaticity can be deduced. From the position of the sidebands $f_h^{\pm} = (h \pm q) f_0$ and the product rule of the frequency derivative for the frequency distribution and the tune q one gets

$$\Delta f_h^{\pm} = \Delta f_0 (h \pm q) \pm \Delta q f_0. \tag{7.23}$$

Inserting the definition of frequency dispersion Eq. 7.4 and chromaticity Eq. 7.6, this leads to

$$\begin{aligned} \Delta f_h^{-} &= \eta \frac{\Delta p}{p} \cdot f_0 \left(h - q + \frac{\xi}{\eta} Q \right) \quad \text{lower sideband} \\ \Delta f_h^{+} &= \eta \frac{\Delta p}{p} \cdot f_0 \left(h + q - \frac{\xi}{\eta} Q \right) \quad \text{upper sideband.} \end{aligned} \tag{7.24}$$

First, one can see that the widths of the sidebands are not equal. Which band is broader depends on the sign of the chromaticity ξ (in most case negative), on q and the harmonic number. In Fig. 7.9 this is not clearly seen due to the large scale, but the height is lower for the left sideband corresponding to a large width, because the integral power is equal for both sidebands. From the width of the sideband, we have a measurement of the chromaticity without any beam excitation. Of course the other parameters $\Delta p/p$, η (or γ_{tr}) and q have to be measured independently.

7.5 Some further remarks to Schottky analysis

- The transverse Schottky signals can also be observed for a bunched beam. Like in the longitudinal case, the sidebands are modulated due to synchrotron oscillations. This can make the spectrum quite complex.
- No space charge effects are considered in the discussion above. In particular, we assume that the tune is independent of the single particle betatron amplitude and the tune spread is only given by the chromaticity. If this is not the case, the tune can be evaluated using a slightly more complex method, see e.g. [121].
- The longitudinal spectrum can be significantly deformed by observing cooled beams, perverting the interpretation of the width as the momentum spread. For cold and sufficiently dense beams, the signal shows a splitting related to plasma waves, see e.g. [120].
- We did not discuss the device noise level contribution to the spectra. In general, for the transverse case, the signal-to-noise is at least two orders of magnitude worse as compared to the longitudinal.
- If very low currents have to be observed (like for anti-protons) the signal strength can be raised by an external resonator.

Chapter 8

Beam loss detection

In a real accelerator, the transmission from the source to the target is never 100 %. The fraction of beam particles lost has to be controlled carefully to achieve optimal transmission. The lost beam particles cause some activation of the accelerator components by nuclear reactions. Moreover, the surrounding material can be destroyed by the radiation, as well as by the heating due to the particles' energy loss. The important processes leading to secondary particles are reviewed briefly. A large variety of **B**eam **L**oss **M**onitors **BLM** exists. Most of them are particle counters, detecting secondary reaction products. At nearly every high current accelerator facility, these monitors are installed for the protection of the accelerator components. They are mounted outside of the vacuum pipe at crucial locations and are relatively cheap instruments. The signal is an important information to prevent unwanted loss during the operation, e.g., caused by malfunctions of components. A careful analysis of the location and time structure of possible losses has to be performed before the choice of the suitable types of beam loss monitors can be made, see [122] for a review. Beam loss monitors are very sensitive devices, which detect even a very small fraction of losses, therefore they are also used for machine tuning. Two examples are presented in the last section.

8.1 Secondary particle production

When a high energy particle hits the vacuum pipe or any other material, secondary particles are generated. The relevant processes are described e.g. in [123, 124, 125]. Here only a brief overview is given:

- **Interaction of electrons**
  For electron energies above ~ 100 MeV, Bremsstrahlung dominates the slow-down process in materials, as shown in Fig. 2.23. The created high energy photons give rise to further particles via $e^+ - e^-$ pair production. If the energy of the γ is high enough, other particles, like $\mu^\pm, \pi^\pm$... can also be produced. An electro-magnetic shower is then generated. Moreover, the nucleus can be excited to so called giant resonances. This is a collective nuclear excitation, where the neutrons oscillate against the protons. The dipole mode of these giant resonances has a threshold of about 6 MeV for typical materials. The de-excitation proceeds with high probability via neutron emission as a (γ, n) reaction. For higher energies also (γ, p) and (γ, np) channels are open.
  When the electron is slowed down below ~ 10 MeV, ionization loss by electronic stopping dominates, resulting in soft x-rays, which are absorbed within a short distance.

- **Interaction of protons**
  Beside electronic stopping, as shown in Fig. 2.22, nuclear interactions are possible. First

we define the term 'thick target' when the interaction length is comparable to the range as given by the electronic stopping. In these thick targets, the probability of a nuclear reaction rises to nearly 100 % for energies above 1 GeV, see Fig. 8.1. Most of the final channels of these nuclear reactions include neutron emission. As an example, for the stopping of 1 GeV proton in copper or iron, $\sim$ 10 fast neutrons are liberated. The neutron yield scales approximately with E_{kin} for energies above 1 GeV. In addition, hadron showers (by the strong interaction at the quark level) are possible, resulting in various species of 'elementary' particles.

- **Interaction of ions**
  Beside the interactions also valid for the protons, an ionic projectile can be fragmented or fission can be induced, leading to radioactive nuclei and fast proton and neutron emission. Simple scaling laws don't exist due to the complex nuclear physics involved.

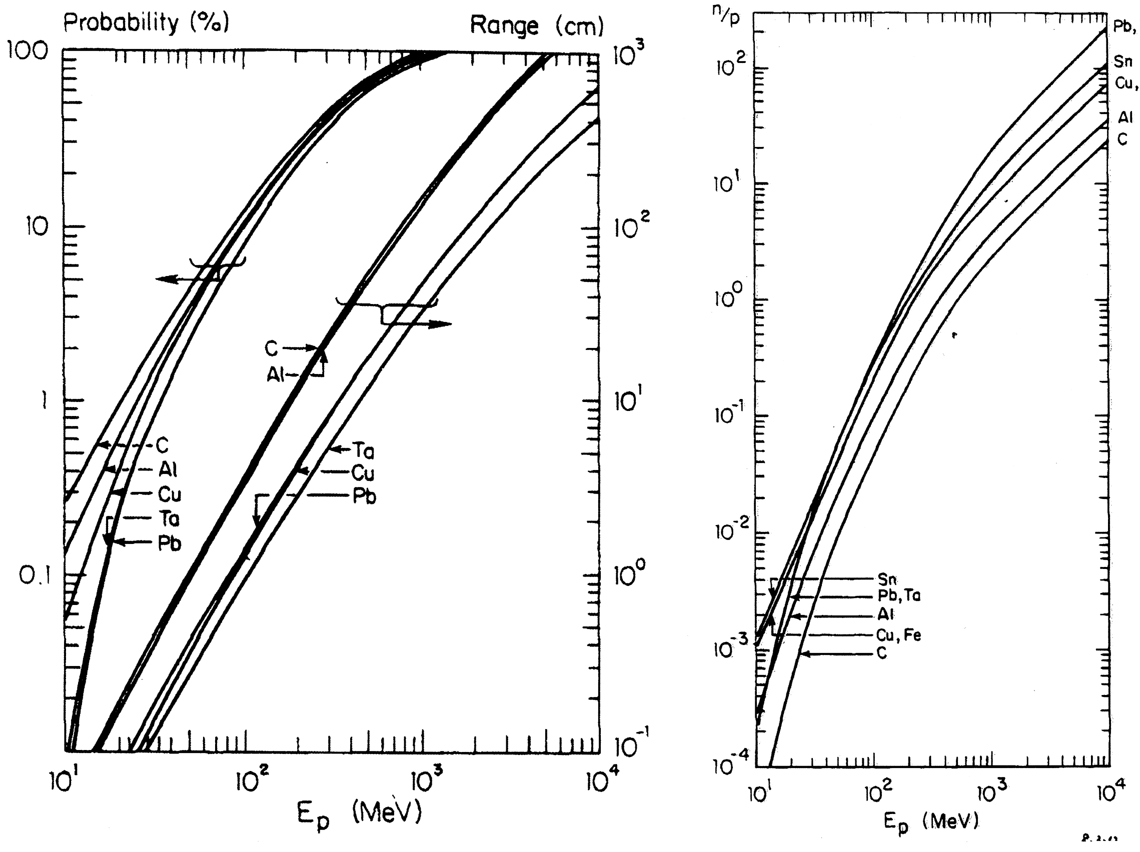

Figure 8.1: Left: The ranges of protons in various metals and the probability of an inelastic nuclear reaction within the range as a function of the proton energy. Right: The total number of neutrons per proton incident on a thick target of various metals as a function of the proton energy. From [125].

Common to all interactions is the production of radioactive nuclei leading to activation of the accelerator components. The emitted charged particles are relatively quickly stopped by the surrounding material. But the neutrons, produced by most primary interactions, can travel long distances. Some of the beam loss monitors are therefore sensitive to these neutrons. Except for the production of radioactive nuclei, all processes are fast, compared to the timescale of interest in accelerator physics, i.e. faster than $\sim$ 10 ns. In this sense, a beam loss monitor reacts promptly to the particle loss. Due to the kinematics of the primary interaction, the secondaries are emitted into a (more or less) forwardly peaked angular distribution. This leads to a spatial resolution of the loss detection by the monitor position close to the loss point.

8.2 Types of beam loss monitors

The task for beam loss monitors is to localize position and time of the loss. Their signals should be proportional to the amount of loss at this position. A high sensitivity is needed to measure low losses. A high dynamic range is required to deal with a sudden loss of a sizable fraction of the beam. Depending on the application, a bunch-to-bunch resolution on a ~ 10 ns time scale is needed, as well as up to 100 ms for a slow detection. All loss monitors are installed outside of the vacuum pipe, detecting mostly secondary particles. These can be neutrons, which are not much absorbed by the surrounding material, or charged particles like protons, e^- and e^+ or γ-rays. Fig. 8.2 shows a photo of some frequently used types as tested at the GSI synchrotron. An overview of the different types is given in [126].

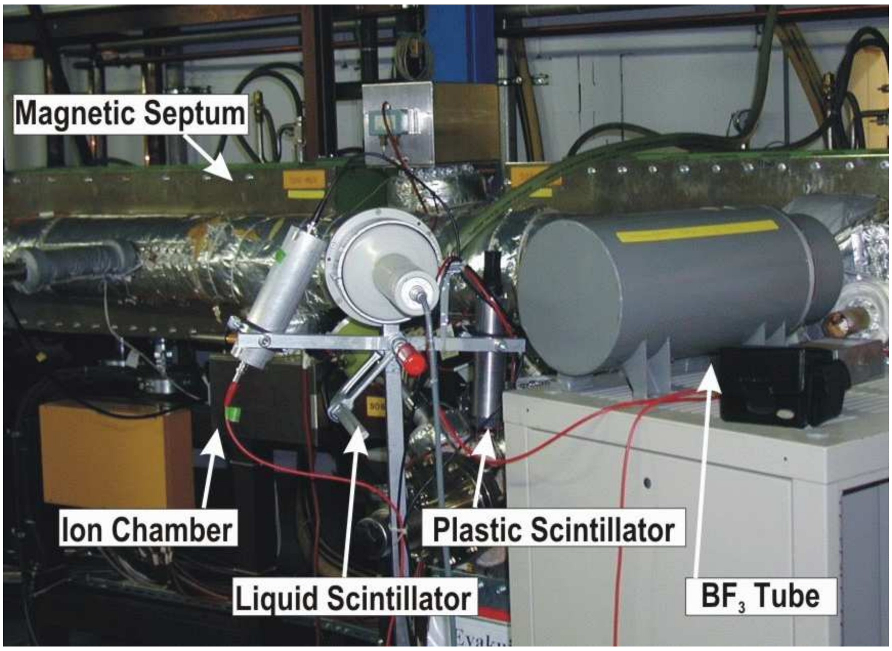

Figure 8.2: The tested beam loss detectors installed at the extraction from the GSI heavy ion synchrotron [127].

8.2.1 Plastic scintillators

Plastic scintillators detect charged particles due to their electronic stopping, as discussed in Chapter 2.7.1 as well as γ-rays. Moreover, they are also sensitive to neutrons due to their elastic scattering on the hydrogen atoms of the polymers [11]. Due to the neutron scattering, a fast proton travels through the scintillator material, leading to light emission by its electronic stopping. The light is guided to a photomultiplier, converted to electrons and amplified. The readout of the resulting electronic signal can be effected by digitizing the analog voltage using a relatively small photomultiplier gain. Or a particle counting mode can be used for higher sensitivity and larger dynamic range. A typical output for the counting mode is shown in Fig. 8.3 showing analog pulses of ~ 20 ns length. Due to the wide spectrum of particle species and related energies, the pulse height distribution is quite broad. (This should be compared to the narrow pulse height distribution of single energetic particles in Fig 2.32.) In the counting mode, the plastic scintillators have a very large dynamic range, from single particle counting up to a count rate of 10^7 s^{-1}. In most cases the scintillation monitors are located in the crucial areas, like the injection or extraction devices, or close to scrapers. The disadvantage is the low radiation hardness of the plastic materials due to the complex chemical composition of the polymers from the plastic matrix. A very rough number of the destruction threshold is 1 Mrad $= 10^4$ Gy. At this dose, the light transmission is reduced by a factor $1/e = 0.37$. Typical sizes of plastic scintillators are cylindrical rods of 2 cm diameter and 10 cm length. Sometimes also long fibers of plastic or inorganic materials are used.

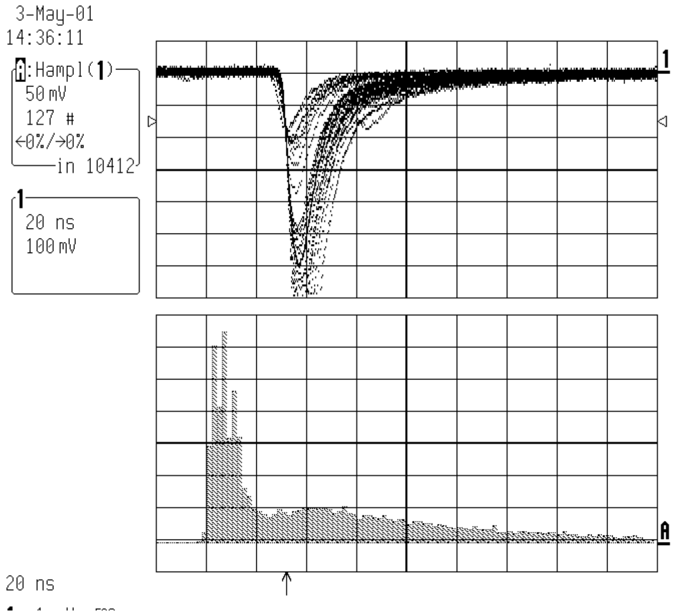

Figure 8.3: Typical pulses from a plastic scintillator (top, 100 mV/div and 20 ns/div) and their pulse height distribution (bottom, 50 mV/div) as measured at the GSI heavy ion synchrotron.

8.2.2 Liquid scintillator

A scintillator material within a liquid solvent of about 1 liter is used. The device is also sensitive to charged particles, $e^{\pm}$, γ and neutrons by the same mechanisms as discussed for the plastic scintillators. A comparable pulse height distribution is observed. The pulse length of the scintillation process is about 1 order of magnitude longer and therefore the dynamic range is a factor of 10 lower for the counting mode. Due to the microscopic light creation, a discrimination between γ-rays and neutron can be performed using special electronics, the so called pulse shape discrimination [11]. The liquid is about a factor of 10 more radiation hard than the plastics, due to the simpler chemical composition of the solvent.

8.2.3 Aluminum coated Electron Multiplier

An Aluminum Coated Electron Multiplier (ACEM) is a photomultiplier, where the photocathode is replaced by an Aluminum surface. Secondary electrons are liberated by the interaction of the radiation and amplified by the dynodes. It offers a fast rise time and high dynamic range, but a sensitivity much lower as scintillators.

8.2.4 PIN diode

Solid state detectors can be used as particle counters. In the -typically 100 μm thick- depletion layer of the doped Si-crystal, electron-hole pairs are generated. For a minimum ionizing particle

(MIP), say, a charged hadron at the minimum of its electronic stopping power, about 10^4 electron-hole pairs are generated. This signal has to be amplified by a charge sensitive pre-amplifier and can then be counted. Two face-to-face mounted PIN diodes are used in coincidence to count only the charged particles and not the low energy photons, as emitted at electron accelerators by synchrotron radiation, see Fig. 8.4. These photons are absorbed in one PIN diode and do not arrive at the second. The detection efficiency is relatively low due to the small active area of typically 10×10 mm^2 and the 0.1 mm depletion depth. A device made of two PIN diodes including the amplifier and the counter is commercially available [5].

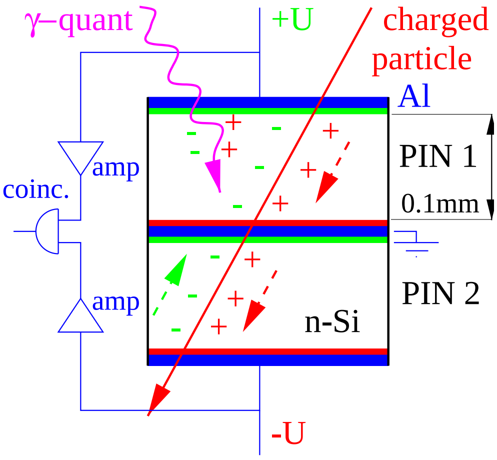

Figure 8.4: Scheme of a two PIN diodes driven in coincidence.

8.2.5 BF_3 proportional tube

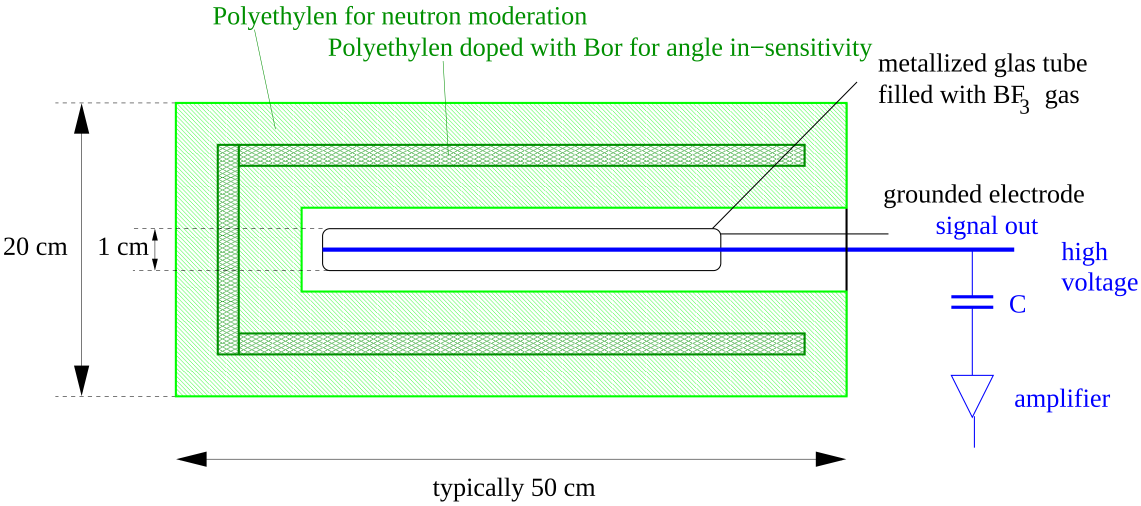

Figure 8.5: Scheme of a BF_3 proportional tube as used for beam loss detection. The proportional tube is filled with BF_3 gas surrounded by polyethylene for the moderation of the neutrons.

To have the possibility to measure only neutrons, a cylindrical proportional tube (typical diameter 10 mm and length 500 mm) filled with the gas BF_3 can be used [11]. For thermal neutrons, the reaction $^{10}\mathrm{B}+\mathrm{n} \rightarrow {}^{7}\mathrm{Li} + \alpha$ has a high cross section ($\sim$ 1 kbarn) and is exothermic by a Q-value (total kinetic energies of Li and α) of 2.3 MeV. The gas-filled tube is surrounded by concentric layers of polyethylene with an outer diameter of $\sim$ 200 mm. The neutrons from the primary beam interaction are slowed down by elastic collisions with the hydrogen nuclei of the polyethylene. Special precautions are taken to get a flat detection efficiency as a function of the angle. Normally these detectors are used at nuclear power plants for neutrons with an energy up to 10 MeV, but the thermalization yield of the neutrons can be extrapolated at least up to 100 MeV. The count rate is limited to several 10^4 s^{-1} due to the time needed for recharging the inner wire of the proportional tube.

Sometimes comparable types are used, but filled with ^{3}He, having a comparable cross section of thermal neutron absorption by the reaction ${}^3_2\mathrm{He} + \mathrm{n} \rightarrow {}^3_1\mathrm{H} + {}^1_1\mathrm{H}$.

8.2.6 Ionization chamber

Ionization chambers measure the amount of secondary charges created in a gas volume (see also Chapter 2.7.2). Fig. 8.6 shows such a round ionization chamber filled with Ar or N_2 gas. Typically, a sealed glass tube contains ~ 100 cm^3 of gas between an outer high voltage electrode and an inner grounded and readout electrode [128]. The output current is measured with a sensitive current-to-voltage or current-to-frequency converter [129]. The IC is not sensitive to neutrons and has a low detection efficiency for γ-rays. Mainly charged hadrons and $e^{\pm}$ are detectable. By definition, the signal strength gives directly the absorbed dose in Gy. Because an inert, single or diatomic gases like Ar, N_2 or air are used in the detection volume, the device is very radiation hard. The signal strength is orders of magnitude lower than for detectors in a particle counting mode. In addition the IC does not react as fast as the scintillators, because the gas ions, created by the radiation, need ~ 100 μs to reach the electrode. This time constant leads to a convolution of the primary signal. The readout of the IC current by the digital electronic is therefore not faster than 1 ms in typical applications.

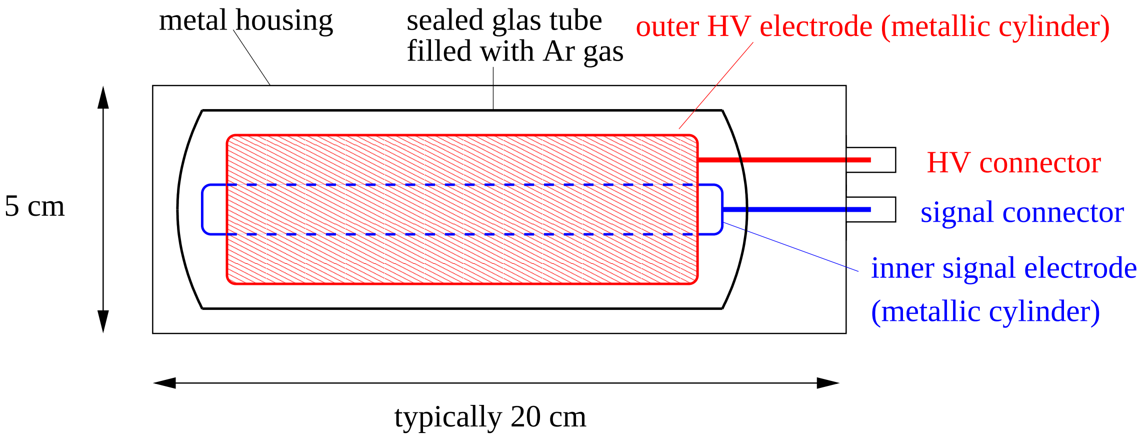

Figure 8.6: Scheme of an ionization chamber as used for beam loss detection.

8.2.7 Optical fiber

All discussed devices so far are particle counters. A totally different scheme uses the material modification by the absorbed dose. Optical fibers, like those used in tele-communication, can be fabricated in nearly arbitrary length at low cost. A fiber is installed close to the beam pipe with up to several km length [130]. Due to radiation destruction, secondary particles modify this fiber by creating color centers. This leads to a change in light transmission of the fiber and to a noticeable amount of reflected light. As used in tele-communication, the quality of a fiber is tested by an optical time domain reflector (OTDR), see Fig. 8.7: A ~ 1 ns laser pulse is coupled to the fiber and travels along the fiber. If the optical properties of the fiber are modified due to the radiation, part of the light is reflected. Its intensity, as well as the arrival time with respect to the input pulse is measured. Due to the known velocity of light in fiber of $\sim 0.66c$, this can be converted to a distance. With this arrangement, a good spatial resolution can be achieved and critical loss regions can be identified. The fiber can be partly repaired by an annealing process, either by time, or by heating the fiber to about 150^{o}C. Special doping of the fibers makes them sensitive to different beam loss mechanisms. This monitor has a slow time response of more than 1 s due to the use of the OTDR.

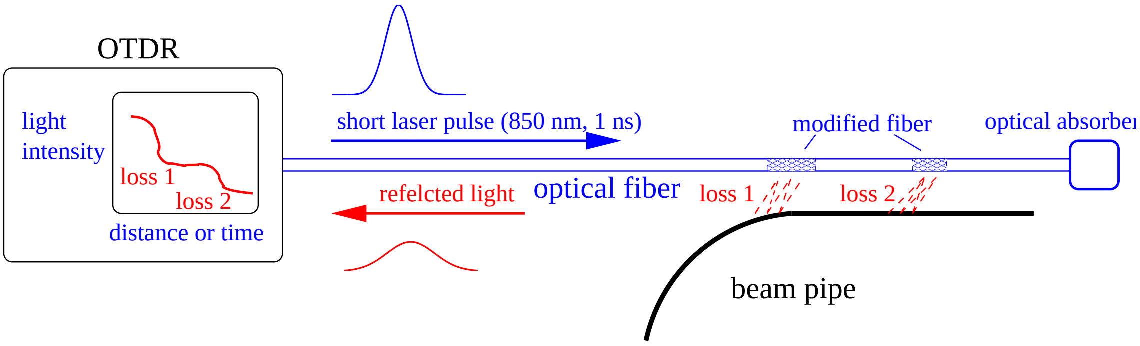

Figure 8.7: Principle of an OTDR beam loss detection with optical fibers.

8.2.8 Comparison of different beam loss monitors

Several of the described types are tested at the extraction septum magnets at the GSI synchrotron [127]. A typical example is shown in Fig. 8.8 for a O^{8+} beam accelerated from 11.4 MeV/u to 800 MeV/u and then extracted slowly over 3 s. The maximum number of stored particles was 4×10^{10}. The signal as a function of time seen at the figure is displayed together with the signal for the synchrotron dc-transformer (top, arbitrary units) and a reference signal proportional to the extracted current measured at the experiment location (second plot, using a secondary electron monitor in arbitrary units, see Chapter 2.7.3). The general feature is that the signals for the different loss monitors are showing the same time behavior. This is not a-priori evident due to the different detection mechanisms. This shows the predominant role of the 'prompt' radiation (prompt within a time scale of ms) whatever the type of secondary radiation is. The signals of all detectors are background-free, showing the minor role of permanent activation compared to the signals induced during the beam delivery.

The linearity of the different detectors is shown in Fig. 8.8 right, where the total counts for one spill are shown as a function of the current detected at the experiment. The count-rate is quite different: The plastic scintillator shows the maximum rate, about a factor of 30 more than the BF_3-tube, due to the detection of more categories of secondary particles. The liquid scintillator shows a lower rate; the saturation for the highest rate is due to the slow integrating pre-amplifier. The signal strength of the IC is lower by a factor of 200 as compared to the plastic scintillator. The dynamic range is highest for the plastic scintillator.

The PIN diode is not shown here, but the count rate would have been about 3 orders of magnitude below that of the plastic scintillator.

8.3 Machine protection using beam loss detectors

The most frequent application of beam loss monitors is the protection of the accelerator components. The high energy stored in the beam can lead to damage of the surroundings when the projectiles hit its materials. In particular, the vacuum pipe can be destroyed by the temperature rise due to the energy release of the particles, leading to a vacuum leakage. Also other materials, like electrical feed-through, the isolation of the magnet coils or any electronic devices can be destroyed due to the modification of the material by the radiation. As discussed in Chapter

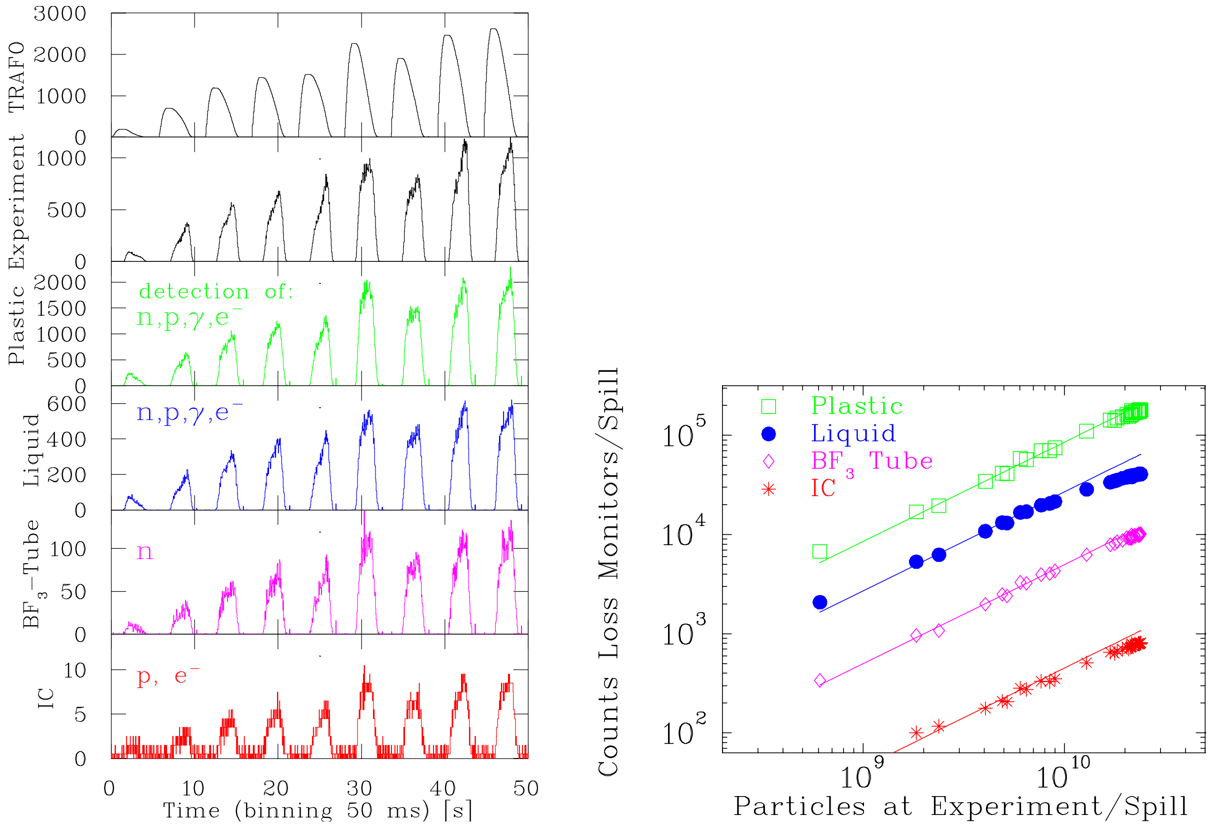

Figure 8.8: Left: Typical example from different beam loss monitors for a O^{8+} beam accelerated from 11 to 800 MeV/u with up to 4×10^{10} particles per spill [127]. Right: Linearity of the loss monitors as a function of the current for the same parameters. The lines are linear fits.

8.1, the nuclear interaction leads to radioactive nuclei, which have lifetimes of hours or more. An activation of the accelerator components is the result, preventing the access of persons into the accelerator tunnel and maintenance is strongly hampered. As a general rule, the power dissipation of the beam losses should be below 1 W/m to enable 'hands-on maintenance'. Another important application of beam loss monitors is the quench protection of super-conducting magnets and cavities. Even a small amount of loss can heat up the super-conducting material above the critical temperature causing a quench, i.e. a transition to normal conductivity. This dangerous situation is always controlled by loss monitors. They create an interlock: as soon as a critical count rate or dose is reached, the beam is kicked out of the accelerator immediately. The design criteria of an interlock system are discussed in [129]. Last but not least the reason for low losses is the protection of the environment and an efficient transfer of particles to the experiment. In the control room of most high current accelerator facilities, the loss rate at sensitive locations is monitored online to visualize the full functionality of the machine.

We discuss briefly two categories of losses:

- **Irregular or fast losses** occur by a malfunction of an accelerator device, like magnets- or rf cavities power supplies, leading to a beam with wrong parameters. Also a misalignment of their settings (e.g., the beam is not centered inside a quadrupole leading to steering, or wrong kinetic energy of the beam by a wrong rf cavity phase or amplitude) results in a mismatch of beam at the following stages of the accelerator and part of the beam might be lost. The task of the beam loss monitors is to localize these losses, warning the operator or triggering an interlock to stop the beam delivery.

- **Regular or slow losses** are known losses, e.g. at aperture limits of a collimator system, or losses due to the finite lifetime of the beam in a synchrotron. Most of them are unavoidable, but an increase of the loss rate shows a malfunction. In addition, beam loss monitors can be used to find the right parameters, e.g. for an emittance reducing collimator.

It is obvious, by looking in particular to the first item, that a beam loss monitor system should have a high sensitivity as well as a very large dynamic range. The high sensitivity is needed to get a usable signal when only a very small fraction of the beam is lost. Using scintillators or PIN diodes, single particle counting can be performed with a very low detection threshold. Detecting the lost particles directly gives a much higher sensitivity than looking at the lost fraction of the total signal by a current transformer. The high dynamic range is mainly needed for the detection of irregular losses, because the losses at one location can easily vary by several orders of magnitude, e.g. due to a power failure of a magnet or cavity. The monitoring has to work over several orders of magnitude without changing the full-scale-range, to prevent the saturation of the signal for large losses. Here, a particle counting mode delivers this high dynamic for rates ranging from 10 s^{-1} up to 10^7 s^{-1}. Close to a collimator, scintillators offer the high dynamic range which is needed for the sensitive detection of the tails in the transverse particle distribution. For other regular losses, the required dynamic range is not so large, due to the slower time variation. For the detection of those, ionization chambers are often used.

Beam loss monitors are relatively cheap instruments and are installed outside the vacuum. At most facilities, they are mounted at many locations along the accelerator to have a good spatial coverage. Beside special insertions they are mostly mounted closed to the focusing quadrupoles, because the beam has normally its maximum transverse size there. This also offers the possibility to distinguish between horizontal and vertical losses. The required time resolution depends very much on the application: For a bunch-to-bunch diagnostics, fast responding detectors (reaction time less than 100 ns), like scintillators or PIN diodes, are needed. Ionization chambers are much slower having only $\sim 100\ \mu$s time response.

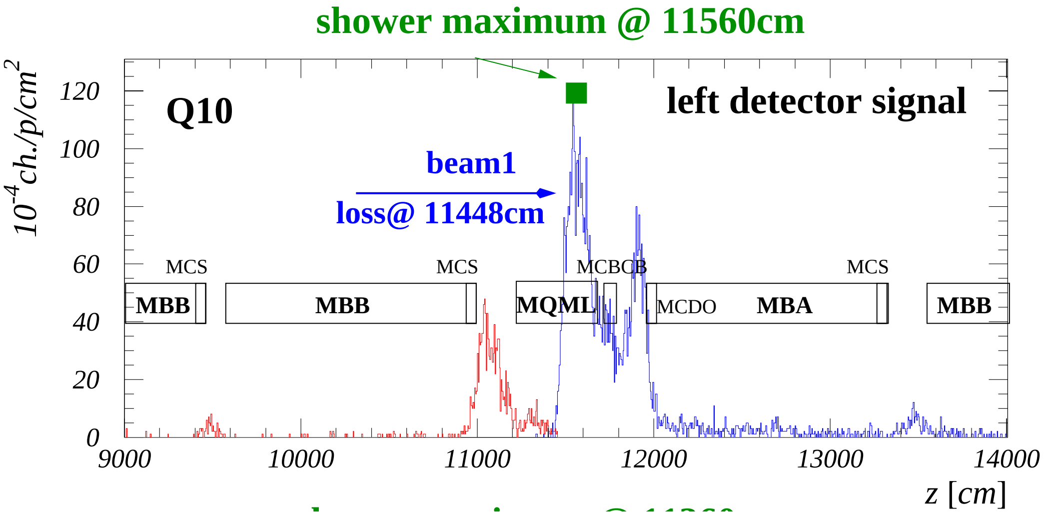

Figure 8.9: Simulation of a secondary particle distribution (hadron shower) due a proton loss inside a quadrupole for the LHC and 7 TeV protons [131]. The maximum of the shower is about 1 m from the loss point.

The position of the beam loss monitors should be well chosen. For highest sensitivity, the distribution of the secondary particles should have a maximum at this location. The secondary particle distribution has to be calculated using an adequate software code. For high energies, the well known code `GEANT` [132] is used in most cases, as shown in Fig. 8.9 for the case of the LHC beam. Of course, an assumption of the primary particle loss is needed. A loss at a quadrupole

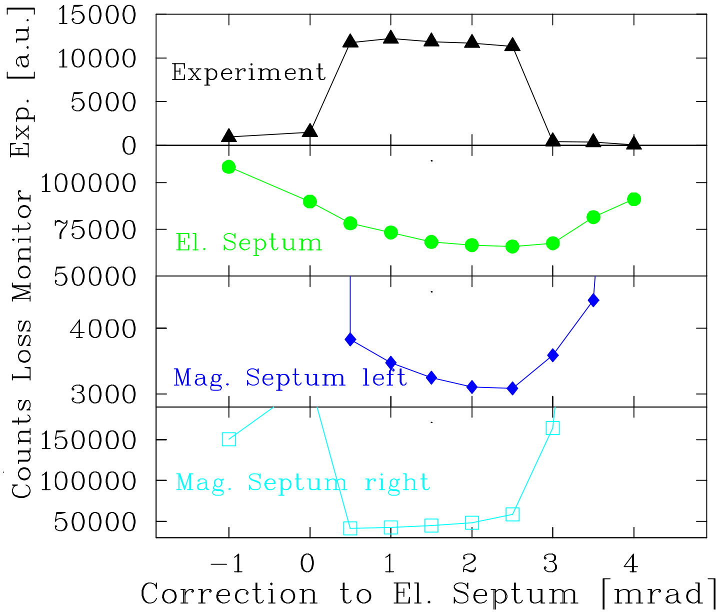

Figure 8.10: Counts per spill from three loss monitor locations and the current at the experiment as a function of the angle electrostatic septum at the GSI synchrotron [127].

is assumed in Fig. 8.9. This is the most probable location, because the beam has the largest width there.

8.4 Beam loss monitoring for alignment

Beam loss monitors have two main advantages, namely the large sensitivity and the fact that these monitors can be installed at many locations. For the alignment of the beam at critical positions having small beam pipes, beam loss monitors can be mounted densely. An example for the slow extraction at the GSI synchrotron is shown in Fig. 8.10. Here, the septum elements, used to kick the beam, have small pipe diameters, comparable to the actual beam size. If the angle at the input of the septum magnets is slightly wrong, part of the beam is lost there. Therefore the angle kick at the first element (here the electro-static septum) has to be aligned carefully in small steps to find the minimal loss rate. Using beam loss monitors, the alignment procedure works better than by looking at the transmitted current, as demonstrated by the top curve in Fig. 8.10.

To have a stable beam stored inside a synchrotron, the tune has to be chosen quite carefully to avoid tune-resonances resulting in transverse beam blow-up. The mechanical alignment and the settings of the various magnets is never in perfect agreement with the theory, therefore the optimal setting for the beam has to be found experimentally. The beam blow-up can be measured precisely by putting a scraper close to the transverse beam tail inside the vacuum tube. The amount of beam particles hitting this scraper can be determined by a beam loss monitor mounted close to the scraper. In Fig. 8.11, the loss rate normalized to the circulating current is determined as a function of the machine tune. The tune is varied by changing the main quadrupoles slightly. At certain settings, the loss rate increases. By a beam-optics theory aided alignment of all important elements, the beam loss is minimized and an optimal storage is performed [133]. More advanced experiments can be realized, for example, to get information about the beam lifetime limitations due to the interaction between the individual beam particles by Coulomb-scattering (i.e. intra beam interaction by multiple Coulomb scattering leading to a transverse or longitudinal beam enlargement) or Touschek scattering (i.e. transfer of transverse

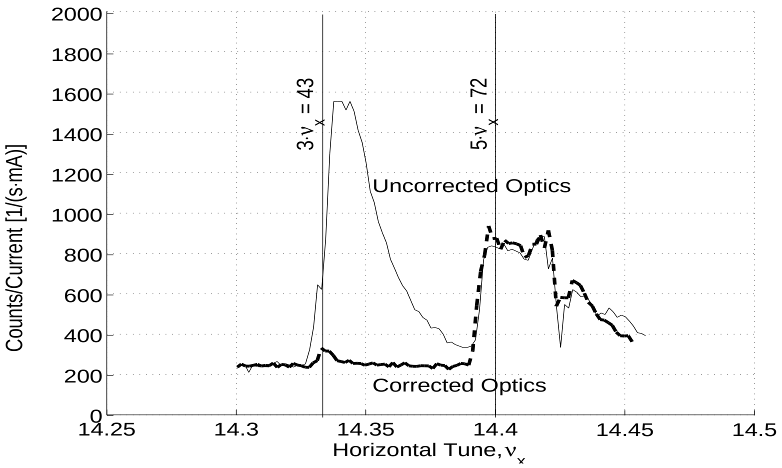

Figure 8.11: Tune scan at the ALS synchrotron light source [133]. For a fixed vertical tune, the horizontal tune is varied and the loss rate, as measured with a scintillator at a collimator is plotted. By changing the setting of some quadrupole, one resonance ($3 \cdot \nu_x$) can be avoided.

particle momentum to the longitudinal plane by a single scattering process). A longitudinal increase of $\Delta p/p$ by Touschek scattering can be monitored by a scraper located at a dispersive region due to the coupling of $x = D \cdot \Delta p/p$, while at locations with $D = 0$ only the transverse effect is seen [134].

Frequently used abbreviations

ac	alternating current
ACCT	alternating current current transformer
ADC	analog-digital converter
amp	amplifier (electronic device)
BIF	beam induced fluorescence monitor
BLM	beam loss monitor
BSM	bunch shape monitor
BTF	beam transfer function
BW	band-width for electrical devices
CCD	charged coupled device for a camera
dc	direct current
DCCT	direct current current transformer
DTL	drift tube LINAC
DSO	digital signal oscilloscope
DSP	digital signal processor
FFT	fast Fourier transformation
FWHM	full width half maximum
Grid	identical with SEM-grid for profiles
Harp	identical with SEM-grid for profiles
HV	high voltage above ~ 1 kV
IC	ionization chamber
IF	intermediate frequency for a rf-mixer
IPM	ionization profile monitor, identical with RGM
IR	infra red light
LO	local oscillator for rf-mixer
MCP	micro channel plate
mw	micro waves with 1 GHz $< f <$ 100 GHz
MWPC	multi wire proportional chamber for profiles
NWA	network analyzer
op-amp	operational amplifier (electronic chip device)
OTR	optical transition radiation for profiles
PHD	pulse height distribution for particle detectors
PMT	photo-multiplier tube
pre-amp	first stage amplifier direct behind detector (fully equipped electronic device)
rf	radio frequency with 100 kHz $< f <$ 1 GHz
RFQ	radio frequency quadrupole LINAC
RGM	residual gas (profile) monitor, identical with IPM
SEEM	secondary electron emission monitor, identical with SEM
SEM	secondary electron (emission) monitor, identical with SEEM
SEM-grid	secondary electron emission grid for profiles, identical to harp
SLM	synchrotron light monitor
SPA	spectrum analyzer
SR	synchrotron radiation
SRM	synchrotron radiation monitor
TOF	time-of-flight
UV	ultra violet light
WCM	wall current monitor

Acknowledgment

The large and complex field of beam diagnostics can not be covered without participating in the open discussions held in the community of accelerator physicists, where one gets in contact with new and exciting physics and technologies. This is gratefully acknowledged.

A very clear description of diagnostics is given H. Koiziol (CERN); I learned a lot from him.

This lecture was prepared under the guideline of Peter Strehl (GSI), who performed previous JUAS lectures. I have to thank him for the release of his materials and ideas.

The members of the GSI beam diagnostic group were always open for discussion sharing their knowledge and were willing to prepare many good figures. In particular I have to express my thanks to A. Bank, T. Giacomini, T. Hoffmann, W. Kaufmann and H. Reeg. Also thanks to W. Barth, M. Kirk and V. Kornilov from GSI for the release of some data.

The careful and critical reading of the script and the intense discussion on all subjects by A. Peters (GSI) is gratefully acknowledged.

A careful prove reading was done by Jeroen Belleman (CERN), many thanks for his hard work and his important improvements.

Last but not least, thanks are given to my wife Elisabeth Forck and my children for their understanding and patient during a lot of long evenings I was working for this lecture.

The high quality photos of the GSI devices are made by G. Otto and A. Zschau.

Bibliography

[1] **General readings on Beam Diagnostics**

1. D. Brandt (Ed.), *Beam Diagnostics for Accelerators, Proc. CERN Accelerator School CAS,* Dourdan, to be published (2008).
2. H. Koziol, *Beam Diagnostic for Acclerators, Proc. CERN Accelerator School CAS,* Uni. Jyväskylä, Finland, p. 565 **CERN 94-01**, http://schools.web.cern.ch/Schools/CAS/CAS_Proceedings.html (1993).
3. J. Bohrer, R. Jung, Diagnostics, *Proc. CERN Accelerator School CAS,* Geneva, p. 385, **CERN 84-15** (1984).
4. J. Bosser (Ed.), *Beam Instrumentation*, **CERN-PE-ED 001-92, Rev. 1994**
5. P. Strehl, *Beam Instrumentation and Diagnostics*, Springer-Verlag, Berlin 2006.
6. S-I. Kurokawa, S.Y. Lee, E. Perevedentev, S. Turner (Eds.), *Proceeding of the School on Beam Measurement,* Proceeding Montreux, World Scientific Singapore (1999).
7. J.M. Month, S. Turner (Eds.), *Frontiers in Particle Beams; Observation, Diagnosis and Correction,* Proceeding Anacapri, Lecture Notes in Physics 343, Springer-Verlag, (1988).
8. M.G. Minty and F. Zimmermann, *Measurement and Control of Charged Particle Beams,* Springer-Verlag, Berlin 2003.
9. These JUAS lecture notes are available at www-bd.gsi.de/conf/juas/juas.html.

[2] **Conferences**

1. *Dedicated beam diagnostics conferences:*
   - *Europe:* European Workshop on Beam Diagostics and Instrumentation at Particle Accelerators (DIPAC)
     Basel 2009, Venice 2007, Lyon 2005, Mainz 2003, Genoble 2001, Chester 1999, Franscati 1997, Travemünde 1995, Montreux 1993.
     Proceedings since 1999 are available: http://www.jacow.org.
   - *America:* Beam Instrumentation Workshop (BIW)
     Lake Tahoe 2008, Batavia 2006, Knoxville 2004, Brookhaven 2002, Cambridge (MA) 2000, Standford 1998, Argonne 1996, Vancouver 1994 and earlier.
     Proceedings for BIW 2008 on http://www.jacow.org.
     Proceedings for other BIW are not available on the web.
2. *General Accelerator conferences:*
   - *Europe:* European Particle Accelerator Conference (EPAC)
     Genoa 2008, Edinburgh 2006, Lucerne 2004, Paris 2002, Vienna 2000, Stockholm 1998, Sitges 1996, London 1994, Berlin 1992, Nice 1990, Rome 1988.
   - *America:* Particle Accelerator Conference (PAC)
     Vancouver 2009, Albuquerque 2007, Knoxville 2005, Portland 2003, Chicago 2001, New York 1999, Vancouver 1997, Dallas 1995, Washington 1993 and earlier.

   Proceedings are available: http://www.jacow.org.

[3] M. Bai et al., Nucl. Instrum. Meth. **A 499**, 372 (2003).

[4] M. Arinaga et al., Nucl. Instrum. Meth. **A 499**, 100 (2003).

[5] Company Bergoz, www.bergoz.com

[6] R.C. Webber, *Proc. Beam Instr. Workshop BIW 94,* Vancouver, p. 3 (1994).

[7] H. Reeg, *Proc. Diag. Instrum. Part. Acc. Conf. DIPAC01,* Grenoble, p. 120 (2001).

[8] R. Bär et al, *Proc. Euro. Part. Acc. Conf. EPAC98,* Stockholm, p. 499 (1998).

[9] K. Unser, IEEE Trans. Nucl. Sci., NS-28, p. 2344 (1981).

[10] W.R. Leo, *Techniques for Nuclear and Particle Physics Experiment,* Springer-Verlag Berlin (1994).

[11] G. F. Knoll, *Radiation Detection and Measurement*, John Willey, New York (1999).

[12] J.D. Jackson, *Classical Electrodynamics*, John Wiley & Sons (1998).

[13] F. Ziegler, J.P. Biersack *SRIM*, see *The stopping and Ranges of Ions in Solids*, Pergamon Press (1985) and www.SRIM.org.

[14] R.W. Müller, P. Strehl, *Nucl. Instrum. Meth.* **A 415**, 305 (1998).

[15] P. Finocchiaro et al., *Proc. Diag. Instrum. Part. Acc. Conf. DIPAC 97,* Frascati, p. 53 (1997).

[16] P. Forck et al., *Proc. Diag. Instrum. Part. Acc. Conf. DIPAC 97,* Frascati, p. 165 (1997).

[17] P. Forck et al., *Proc. of Beam Instrum. Workshop BIW 96,* Argonne, p. 422 (1996).

[18] F. Sauli, *Prinziple of operation of multiwire and drift chambers,* CERN77-09 (1977).

[19] H. Reeg, *Proc. Diag. Instrum. Part. Acc. Conf. DIPAC 99,* Chester, p. 141 (1999).

[20] G. Ferioli, R. Jung, *Proc. Diag. Instrum. Part. Acc. Conf. DIPAC 97,* Frascati, p. 168 (1997).

[21] A. Peters et al., *Proc. of Beam Instrum. Workshop BIW 98,* Stanford, p. 163 (1998) and A. Peters *Proc. Diag. Instrum. Part. Acc. Conf. DIPAC 99,* Chester, p. 109 (1999).

[22] R. Jung, G. Ferioli, S. Hutchins *Proc. Diag. Instrum. Part. Acc. Conf. DIPAC 03,* Mainz, p. 28 (2003) and R. Jung, *Proc. Diag. Instrum. Part. Acc. Conf. DIPAC 93,* Montreux, p. 4 (1993).

[23] E. Gütlich et al., *Proc. of Beam Instrum. Workshop BIW 08,* Lake Tahoe (2008).

[24] T.J. Shea et al., *Proc. Part. Acc. Conf. PAC 97,* Vancouver, p. 2215 (1997).

[25] A. Peters et al., *Proc. Diag. Instrum. Part. Acc. Conf. DIPAC 01,* Grenoble, p.123 (2001).

[26] M. Plum, *Beam Instrum. Workshop, Knoxville, AIP Conf. Proc. 732*, p. 23 (2004).

[27] S. Burger et al., *Proc. Diagn. Instrum Part Acc. Conf. DIPAC 03*, Mainz, p. 122 (2003).

[28] C. Fischer et al., *Proc. Euro. Part. Acc. Conf. EPAC 88,* Rome, p. 1081 (1988).

[29] U. Raich, *Proc. Diag. Instrum. Part. Acc. Conf. DIPAC 05,* Lyon, p. 1 (2005).

[30] R.J. Colchester, R. Jung, *Proc. Part. Acc. Conf. PAC 97, Vancouver IEEE Trans. Nucl. Sci.,* Vol NS-32 p. 1917 (1985).

[31] C. Field, *Nucl. Instrum. Meth.,* A360, p. 467 (1995).

[32] M. Matoba et al.,m *IEEE Trans. Nucl. Sci.,* Vol NS-32 p. 541 (1985).

[33] M. Benedikt et al., *Proc. Diag. Instrum. Part. Acc. Conf. DIPAC 01,* Grenoble, p. 189 (2001).

[34] C. Bovet et al., *Proc. Euro. Part. Acc. Conf. EPAC 98,* Stockholm, p. 1488 (1998).

[35] P. Forck et al., *Proc. Diag. Instrum. Part. Acc. Conf. DIPAC 05,* Lyon, p. 221 (2005).

[36] T. Giacomini et al., *Beam Instrum. Workshop, Knoxville, AIP Conf. Proc. 732*, p. 286 (2004) and T. Giacomini et al. *Proc. Diag. Instrum. Part. Acc. Conf. DIPAC 05,* Lyon, p. 150 (2005).

[37] P. Forck, P. Strehl, *Proc. Diag. Instrum. Part. Acc. Conf. DIPAC 99,* Chester, p. 42 (1999) and P. Forck, A. Peters, P. Strehl, *Proc. Beam Instr. Workshop BIW 2000,* Cambridge AIP 546, p. 606 (2000).

[38] R. Connolly et al., *Proc. Beam Instr. Workshop BIW 2000,* Cambridge AIP 546, p. 330 (2000).

[39] K. Smith, Position-sensitive particle detection with microchannel-plate electron multiplier, *Experimental Methods in phys. science, Academic Press* Vol. 29A, p. 253 (1995).

[40] G. Ferioli et al., *Proc. Diag. Instrum. Part. Acc. Conf. DIPAC 01,* Grenoble, p. 201 (2001).

[41] F. Nolden et al., *Proc. Euro. Part. Acc. Conf. EPAC 2000,* Vienna p. 1262 (2000).

[42] D. Möhl, Stochastic cooling, in *CERN Acc. School,* CERN 95-06, p. 587 (1995) http://cas.web.cern.ch/cas/CAS_Proceedings.html.

[43] J. Bosser, Electron cooling, in *CERN Acc. School,* CERN 95-06, p. 673 (1995).

[44] A. Allisy (Ed.), *Secondary Electron Spectra from charged Particle Interaction*, International Commission on Radiation Units and Measurement Report No. 55 (1996).

[45] D. P. Sandoval et al., *Proc. Beam Instr. Workshop BIW 93,* Santa Fe, p. 273 (1993) and references their in.

[46] M.A. Plum et al., *Nucl. Instrum. Meth.* **A 492,** 74 (2002).

[47] P. Forck, A. Bank, *Proc. Euro. Part. Acc. Conf. EPAC 2002, Paris*, p. 1885 (2002) and A. Bank, P. Forck, *Proc. Diagn. Instrum Part Acc. Conf. DIPAC03*, Mainz, p. 137 (2003).

[48] G. Burtin et al., *Proc. Euro. Part. Acc. Conf. EPAC 2000, Vienna*, p. 256 (2000).

[49] Wartski et al., J. Appl. Phys. **46**, 3644 (1975).

[50] J. Bosser et al., Nucl. Instrum. Meth. **A 238**, 45 (1985).

[51] M.A. Tordeux and J. Papadacci, *Proc. Euro. Part. Acc. Conf. EPAC 2000, Vienna*, p. 1818 (2000).

[52] P. Catravas et al., *Proc. Part. Acc. Conf. PAC 99, New York*, p. 2111 (1999).

[53] G. Kube, *Proc. Diagn. Instrum Part Acc. Conf. DIPAC 07*, Venice, p. 6 (2007).

[54] M. Wilke, *Proc. Beam Instr. Workshop BIW 94,* Vancouver, p. 128 (1994).

[55] A. Hoffmann, F. Meot, *Nuncl. Instrum. Meth.* **203**. p. 483 (1982).

[56] G. Kube et al., *Proc. Diagn. Instrum Part Acc. Conf. DIPAC 05*, Lyon, p. 202 (2005).

[57] C. Bovet et al., *Proc. Part. Acc. Conf. PAC 91,* San Francisco, p. 1160 (1991).

[58] B.X. Yang et al., *Proc. Part. Acc. Conf. PAC 97,* Vancouver, p. 2215 (1997).

[59] T. Mitsuhashi, Beam size measurement by use of SR interferometers, in *Proceeding of the School on Beam measurement,* Montreux, p. 399 World Scientific Singapore (1999) and T. Mitsuhashi, *Proc. Beam Instr. Workshop BIW 2004,* Knoxville, AIP Conf. Proc. 732, p. 3 (2004).

[60] J.M. Stockli, *Proc. Beam Instr. Workshop BIW 2006,* Batavia (Illinois), AIP Conf. Proc. 868, p. 25 (2006).

[61] M. Reiser, *Theory and Design of charged Particle Beams*, J. Wiley Publishing New York (1994).

[62] K.T. McDonald , D.P. Russell, *Methods of Emittance Measurement,* Proc. Anacapri, Lecture Notes in Physics 343, Springer-Verlag, p. 122 (1988).

[63] G. Riehl et al., *Proc. Diag. Instrum. Part. Acc. Conf. DIPAC 95,* Travemünde, DESY M9507, p. 6 (1995).

[64] M. Dolinska et al., *Proc. Diag. Instrum. Part. Acc. Conf. DIPAC 99,* Chester, p. 161 (1999) and T. Hoffmann et al., *Proc. Beam Instr. Workshop BIW 2000,* Cambridge AIP 546, p. 432 (2000).

[65] M. Crecenti, U. Raich, *Proc. Diag. Instrum. Part. Acc. Conf. DIPAC 95,* Travemünde, DESY M9507, p. 66 (1995).

[66] P. Forck et al., *Proc. Linear Accel. Conf. LINAC 2000,* Monterey, p. 166 (2000).

[67] M.E. Schultz et al., *Proc. Linear Accel. Conf. LINAC 2000,* Monterey, p. 575 (2000) and W.P. Lysenko et al., *Proc. Linear Accel. Conf. LINAC 2000,* Monterey, p. 809 (2000).

[68] R.E. Shafer, *Proc. Beam Instr. Workshop BIW 89,* Upton, p. 26, available e.g. at www.bergoz.com/products/MX-BPM/MX-BPM-downloads/files/Shafer-BPM.pdf (1989).

[69] S.R. Smith, *Proc. Beam Instr. Workshop BIW 96,* Argonne AIP 390, p. 50 (1996).

[70] G.R. Lambertson, *Electromagnetic Detectors,* Proc. Anacapri, Lecture Notes in Physics 343, Springer-Verlag, p. 380 (1988).

[71] J.M. Byrd, Bunched Beam Signals in the time and frequency domain, in *Proceeding of the School on Beam measurement,* Montreux, p. 233 World Scientific Singapore (1999).

[72] L. Vos, *Proc. Diag. Instrum. Part. Acc. Conf. DIPAC 95,* Travemünde, DESY M9507, p. 20 (1995).

[73] .R. Lambertson, Dynamic devices-Pickups and Kickers, in *Proc. of SLAC and FERMILAB Summer School*, Stanford, AIP Conf. Proc. 153, p. 1413 (1985).

[74] J.F. Power et al., *Proc. Beam Instr. Workshop BIW 2000,* Cambridge AIP 546, p. 535 (2000).

[75] B.G. Pine, *CARE-ABI Workshop Lüneburg 2006,* see adweb.desy.de/mdi/CARE/Lueneburg/ABI-Lueneburg.htm (2006).

[76] T.J. Shea, R.L. Witkover, *Proc. Beam Instr. Workshop BIW 98,* Stanford AIP 451, p. 145 (1998).

[77] P.R. Cameron et al., *Proc. Part. Acc. Conf. PAC 95,* Dallas, p. 2458 (1995).

[78] J. Borer, R. Jung, *Proc. CERN Acc. School,* Geneva, CERN84-15, p.385 (1983).

[79] N. Kurita et al., *Proc. Part. Acc. Conf. PAC 95,* Dallas, p. 2512 (1995).

[80] C.K. Ng et al, *Proc. Part. Acc. Conf. PAC 95,* Dallas, p. 2485 (1995).

[81] A. Labrador et al., *Proc. Euro. Part. Acc. Conf. EPAC 98,* Stockholm, p. 1547 (1998).

[82] P. Kowina et al., *Proc. Diag. Instrum. Part. Acc. Conf. DIPAC 2005,*, Lyon, p. 114 (2005).

[83] G. Vismara, *Proc. Beam Instr. Workshop BIW 2000,* Cambridge AIP 546, p. 36 (2000) and G. Vismara, *Proc. Diag. Instrum. Part. Acc. Conf. DIPAC 99,* Chester, p. 11 (1999).

[84] R. Garoby, Low Level R.F. Building Blocks, in *CERN Acc. School,* CERN 93-03, p. 428 (1992), http://cas.web.cern.ch/cas/CAS_Proceedings.html.

[85] Company I-Tech, www.i-tech.si.

[86] J.M. Belleman, *Proc. Diag. Instrum. Part. Acc. Conf. DIPAC 05,* Lyon, p. 137 (2005).

[87] A. Galatis et al.,*Proc. Diag. Instrum. Part. Acc. Conf. DIPAC 07,* Venice, (2007).

[88] K. Unser, *Proc. Beam Instr. Workshop BIW 96,* Argonne AIP 390, p. 527 (1996) and www.bergoz.com.

[89] V. Schlott et al., *Proc. Euro. Part. Acc. Conf. EPAC 2000,* Vienna p. 1809 (2000) and www.i-tech.si.

[90] M. Wendt, J.R. Maidment, *Proc. Beam Instr. Workshop BIW 2000,* Cambridge AIP 546, p. 614 (2000).

[91] R. Lorenz, *Proc. Beam Instr. Workshop BIW 98,* Stanford AIP 451, p. 53 (1998).

[92] B. Dehning et al., *Proc. Euro. Part. Acc. Conf. EPAC 98,* Stockholm, p. 430 (1998).

[93] J.D. Fox, E. Kikuzani, Bunch feedback system and signal processing, in *Proceeding of the School on Beam measurement,* Montreux, p. 579 World Scientific Singapore (1999).

[94] J.M. Byrd, Spectrum and network analyzser, in *Proceeding of the School on Beam measurement,* Montreux, p. 703, World Scientific Singapore (1999).

[95] R. Bartolini et al., *Proc. Euro. Part. Acc. Conf. EPAC 96,* Sitges, p. 1329 (1996).

[96] D. Boussard, Schottky noise and Beam Transfer Function Diagnostics, in *CERN Acc. School,* CERN 95-06, p. 749 (1995), http://cas.web.cern.ch/cas/CAS_Proceedings.html.

[97] U. Rauch et al., *Proc. Diag. Instrum. Part. Acc. Conf. DIPAC 09,* Basel (2009).

[98] J. Dietrich, I Mohos, *Proc. Diag. Instrum. Part. Acc. Conf. DIPAC 99,* Chester, p. 146 (1999) and J. Dietrich, I Mohos, *Proc. Beam Instr. Workshop BIW98,* Stanford AIP 451, p. 454 (1998).

[99] S. Meyer, Performance related Measurements on LEP, *Proceeding of the School on Beam measurement,* Montreux, p. 484, World Scientific Singapore (1999).

[100] H. Burkhardt (CERN), private commmunications.

[101] H. Wollnik, *Optics of charged particles,* Academic Press (1987).

[102] J.C. Dooling et al., *Proc. Linear Accel. Conf. LINAC 2000,* Monterey, p. 193 (2000).

[103] P. Forck et al., *Proc. Diag. Instrum. Part. Acc. Conf. DIPAC 05,* Lyon, p. 48 (2005).

[104] S. Hancock, M. Lindroos, S. Koscielniak, *Phys. Rev. Special Topic Acc. Beam,* **3**, 124202 (2000) and CERN-PS-2000-068-OP (2000).

[105] S. Hancock et al., http://cern.ch/tomography.

[106] S. Hancock, J.L. Sanchez Alvarez,
CERN PS/RF Note 2001-010, http://cern.ch/tomography.

[107] B. Fellenz, J. Crisp, *Proc. of Beam Instrum. Workshop BIW 98,* Stanford, p. 446 (1998).

[108] W.R. Rawnsley et al., *Proc. Beam Instr. Workshop BIW 2000,* Cambridge AIP 546, p. 547 (2000).

[109] P. Forck et al., *Proc. Diag. Instrum. Part. Acc. Conf. DIPAC 99,* Chester, p. 176 (1999).

[110] RD 42 Collaboration at CERN, E. Berdermann et al., *Proc. XXXVI Int. Winter Meeting of Nucl. Phys., Bormio* (1998).

[111] A.V. Feschenko, *Proc. Part. Acc. Conf. PAC 2001,* Chicago, p. 517 (2001).

[112] N. E. Vinogradov et al., *Nucl. Instrum. Meth* **A 526**, p. 206 (2004).

[113] K. Scheidt, *Proc. Euro. Part. Acc. Conf. EPAC 2000,* Vienna, p. 182 (2000).

[114] K. Scheidt, *Proc. Euro. Part. Acc. Conf. EPAC 96,* Sitges, p. 1624 (1996).

[115] e.g. Campany Hamamatsu, www.hamamatsu.com

[116] A.H. Lumpkin et al., *Proc. Part. Acc. Conf. PAC 97,* Vancouver, p. 874 (1997).

[117] W. Schottky, *Annalen der Physik,* p. 57 (1918).

[118] L. Parker, *Proc. Beam Instr. Workshop BIW 2004,* Knoxville, AIP Conf. Proc. 732, p. 393 (2004).

[119] S. Cattopadhyay, Some fundamental aspects of fluctuation and coherence in charged particle beams in storage ring, CERN 84-11 (1984).

[120] F. Nolden, *Proc. Diag. Instrum. Part. Acc. Conf. DIPAC 01,* Grenoble, p. 6 (2001).

[121] S. van der Meer, *Diagnostics with Schottky Noise* , Proc. Anacapri, Lecture Notes in Physics 343, Springer-Verlag, p. 423 (1988).

[122] K. Wittenburg, *Proc. Euro. Part. Acc. Conf. EPAC 2002,* Paris, p. 109 (2002).

[123] P. Berkvens, *JUAS lecture notes on radiation and safety* (2003).

[124] A.H. Sullivan, *A Guide to Radiation and Radioactivity Level near high Energy Particle Accelerators*, Nuclear Technology Publishing, Ashford (1992).

[125] R.H. Thomas, *Radiation effects and protection,* in *A.W. Chao, M. Tigner (Eds.), Handbook of Acceleration Physics and Engeneering,* World Scientific (1999).

[126] R.E. Shafer, *Proc. Beam Instr. Workshop BIW 2002,* Brookhaven AIP 648, p. 44 (2002).

[127] P. Forck and T. Hoffmann, *Proc. Diag. Instrum. Part. Acc. Conf. DIPAC 2001,* Grenoble, p. 129 (2001).

[128] R.E. Shafer et al., *Proc. intern. Conf. High Energy Acc.*, Batavia, p. 609 (1983) and D. Gassner et al., *Beam Instrum. Workshop BIW 2000*, Cambridge, p. 392 (2000).

[129] B. Dehning, *Proc. Diag. Instrum. Part. Acc. Conf. DIPAC 2005,*, Lyon, p. 117 (2005).

[130] H. Henschel et al., *Proc. Diag. Instrum. Part. Acc. Conf. DIPAC 2001,* Grenoble, p. 73 (2001), H. Henschel et al., *Proc. Beam Instr. Workshop BIW 2000,* Cambridge AIP 546, p. 647 (2000).

[131] E. Gschwendtner et al., *Proc. Euro. Part. Acc. Conf. EPAC 2002,* Paris, p. 1894 (2002).

[132] http://wwwinfo.cern.ch/asd/geant4/

[133] D. Robin et al., *Proc. Euro. Part. Acc. Conf. EPAC 2000,* Vienna, p. 136 (2000).

[134] P. Kuske, *Proc. Diag. Instrum. Part. Acc. Conf. DIPAC 2001,* Grenoble, p. 31 (2001).